



UNIVERSITÀ DEGLI STUDI DI TRIESTE

e

UNIVERSITÀ CA' FOSCARI DI VENEZIA

XXXI CICLO DEL DOTTORATO DI RICERCA IN

CHIMICA

**SINTHESYS OF CARBON DOTS FOR MEDICAL
AND PHOTOCATALYTIC APPLICATIONS**

Settore scientifico-disciplinare: CHIM/06

**DOTTORANDO / A
SIMONE CAILOTTO**

Ph.D. student
Name - Surname

**COORDINATORE
PROF. BARBARA MILANI**

Ph.D. program Coordinator
Barbara Milani

**SUPERVISORE DI TESI
PROF. ALVISE PEROSA**

Thesis Supervisor
Prof. Name - Surname

ANNO ACCADEMICO 2017/2018

Abstract

Carbon dots (CDs) are a novel carbon-based nanomaterial that draws a great attention in the last decade. The easy way of synthesis and the cheapest nature of the precursors used, stimulated a lot of scientist to propose new way of synthesis and applications. Notwithstanding the number of paper published, a systematic and reproducible way of synthesis is not yet been achieved, as well as a common definition of the resulting nanomaterials and their properties. In this thesis, the synthetic protocols and the characterization procedures used for the CDs will be deeply investigated in order to apply the nanomaterials in different applications. In particular, carbon dots synthesized from fully biocompatible precursors such as glucose, fructose and ascorbic acid, are characterized and employed for drug loading applications. The study reveals that the choice of the precursors is a crucial step because it affects the structural properties of the nanomaterials and the biological properties, revealing an unexpected toxicity for the fructose derived CDs, ascribable to its thermal degradation pathway. Furthermore, the drug loading capabilities were found to be correlated to the morphology of the nanoparticles, revealing the crucial role of the π - π interactions in achieving a loading up to 28 %_{wt} for the glucose-based CDs. A second study was carried out on citric acid based CDs, in order to determine the best synthetic approach for photocatalytic applications. The nanoparticles synthesized both by hydrothermal and pyrolysis treatment, from sole citric acid and in combination with a nitrogen doping agent, were deeply characterized. The analysis reveals the difference in chemical, structural, and optical properties between the two synthetic methods. The photoreduction of methylviologen (MV) was used as model reaction to study the photocatalytic ability of the CDs, and the results reveal a relationship between the synthetic methods employed, the structural and optical properties of the CDs and their ability to act as a sensitizer. The amorphous nitrogen doped CDs reveals to be the best choice for this application with an initial rate conversion comparable to other reported in literature. The same CDs were also tested for the photocatalytic cleavage of C-O bonds in activated esters without the use of metals. The study reveals that CDs can successfully catalyze the reaction, with complete conversion and almost total selectivity. In addition, the CDs employed, shows different reactivity depending on the precursors and synthetic methods employed for their synthesis, with the same trend displayed for the MV photoreduction. This study highlights the ability of CDs to act as photosensitizer, without the addition of metals, in an organic reaction, opening a new scenario in the use of this nanomaterial in photocatalytic applications.

Sommario

I Carbon Dots (CDs) sono una nuova classe di nanomateriali a base di carbonio che hanno attratto una grande attenzione nell'ultimo decennio. La facilità di sintesi e il basso costo dei materiali di partenza hanno stimolato molti scienziati a proporre nuove vie di sintesi e applicazioni ma, una procedura di sintesi sistematica e riproducibile non è ancora stata individuata, come anche una precisa definizione delle sue proprietà. In questa tesi, le procedure di sintesi e le tecniche di caratterizzazione usate, verranno indagate per progettare il miglior nanomateriale da usare per specifiche applicazioni. Un primo set di CDs sintetizzati da risorse biocompatibili quali glucosio, fruttosio e acido ascorbico, è stato caratterizzato e poi studiato per il caricamento con un farmaco. Lo studio ha rivelato che la scelta del precursore è una fase cruciale nella progettazione di un sistema basato sui CDs, in quanto essa porta a cambiamenti nella struttura del nanomateriale e differenze nelle proprietà biologiche dei rispettivi CDs, infatti i campioni derivanti dal fruttosio sono risultati essere estremamente tossici a causa delle molecole formate durante la sua termolisi. La morfologia delle nanoparticelle inoltre influenza la capacità di caricare il farmaco, in particolare le interazioni π - π sono risultate essere molto importanti per questo scopo nei CDs derivanti dal glucosio. Una seconda famiglia di CDs sono stati sintetizzati e caratterizzati per studiare quale approccio sintetico sia il migliore per creare un sistema fotocatalitico. Le nanoparticelle sono state ottenute sia per via idrotermale che pirolitica dal solo acido citrico e anche in combinazione con dopante a base di azoto. Dalle caratterizzazioni è emerso che i 4 campioni hanno diverse proprietà chimiche, strutturali e ottiche. Per verificare l'abilità dei CDs di agire come fotocatalizzatori, sono stati impiegati nella riduzione del metilviologeno (MV), i risultati hanno evidenziato una correlazione tra il metodo di sintesi, le proprietà dei CDs e la loro efficienza nel ridurre il MV. I CDs amorfi dopati azoto, mai studiati finora, sono risultati essere i più attivi per questa applicazione con una velocità iniziale comparabile con i migliori riportati finora in letteratura. Gli stessi CDs sono stati poi utilizzati nella foto scissione del legame C-O di esteri picolinici senza l'impiego di metalli. Lo studio ha dimostrato come i CDs catalizzino, con buone conversioni e selettività totale, la rottura del legame. I diversi CDs testati hanno dimostrato una diversa reattività che rispecchia quella evidenziata nella riduzione del MV. Inoltre, mediante studi di voltammetria ciclica è stato possibile spiegare la diversa reattività dei CDs e degli esteri. La possibilità di eseguire semplici reazioni organiche impiegando solo un materiale a basso

costo e prodotto da precursori facilmente reperibili può aprire un nuovo scenario nell'ambito della fotocatalisi.

List of abbreviations

ACE	Angiotensin-Converting Enzyme
BE	Binding Energy
CA	Citric Acid
CDs	Carbon Dots
CNPs	Carbon Nanoparticles
CQDs	Carbon Quantum Dots
CV	Cyclic Voltammetry
CVD	Chemical Vapor Deposition
DDS	Drug Delivery System
DETA	Diethylentriamine
DMF	DiMethylFormamide
DOSY	Diffusion Ordered Spectroscopy
DOX	Doxorubicine
ESI-MS	Electron Spray Ionization- Mass Spectrometry
FDCA	2,5 FuranDiCarbAldehyde
FRET	Fluorescence Resonance Energy Transfer
FT-IR	Fourier Transformed InfraRed
GC-MS	Gas Chromatography- Mass Spectroscopy
HeLa	Henrietta Lacks
HMF	Hydroxy Methyl Furfural
HOMO	High Occupied Molecular Orbital
HTT	HydroThermal Treatment
HV	Hydroxyl Value
IPCA	Imidazo[1,2-a]Pyridine-7-CarboxylicAcid, 1,2,3,5-tetrahydro-5-oxo

LUMO	Lower Unoccupied Molecular Orbital
MV	Methyl Viologen
MW	Molecular Weight
MWCNTs	Multi Walled Carbon NanoTubes
MWCO	Molecular Weight Cut Off
NHE	Normal Hydrogen Electrode
NIR	Near InfraRed
NMP	N-MethylPicolinium
NMR	Nuclear Magnetic Resonance
PEG	Poly Ethylene Glycol
PET	Photo Electron Transfer
PRPG	Photo Releasable Protecting Group
PYR	Pyrolysis
PL	Photoluminescence
TEM	Transmission Electronic Microscopy
TOF	Turn Over Frequency
UV-Vis	UltraViolet-Visible
QY	Quantum Yield
XPS	X-ray Photoelectron Spectroscopy

Summary

1. Introduction: Carbon Dots.....	1
1.1. Nanomaterials.....	1
1.2. Methods of synthesis.....	5
1.2.1. Top Down syntheses.....	5
1.2.2. Bottom Up syntheses.....	6
1.3. Structure of the CDs.....	12
1.4. Photoluminescence.....	16
1.5. Applications.....	21
1.5.1. Drug delivery.....	22
1.5.2. Photocatalysis.....	24
1.6. Aim and structure of the thesis.....	27
2. Synthesis of CDs.....	28
2.1. Monosaccharides and Ascorbic acid derived CDs.....	28
2.1.1. Hydrothermal syntheses.....	29
2.1.2. Pyrolytic synthesis.....	32
2.2. Citric Acid derived CDs.....	36
2.2.1. Non-doped CDs.....	36
2.2.2. N-doped CDs.....	40
2.3. Experimental.....	43
2.3.1. Material and instrumentation.....	43
2.3.2. DOSY-NMR.....	43
3. Results: Carbon dots for drug delivery.....	44
3.1. Introduction.....	44
3.2. Synthesis and Characterization.....	47
3.3. Toxicity of the CDs.....	54
3.4. Drug uptake experiments.....	55
3.5. Conclusions.....	58
3.6. Experimental.....	59
3.6.1. Hydroxyl Value.....	59
3.6.2. Electrophoresis.....	60
3.6.3. Cytotoxicity.....	60

3.6.4.	Stern-Volmer method	60
3.6.5.	Job's plot method	60
4.	Results: Carbon dots for photocatalytic applications	61
4.1.	Introduction.....	61
4.2.	Characterization	63
4.2.1.	a-CDs and g-CDs.....	64
4.2.2.	a-N-CDs and g-N-CDs.....	69
4.3.	Quenching measurement	74
4.4.	MV reduction.....	80
4.5.	Conclusion	83
4.6.	Experimental	84
4.6.1.	XPS measurement	84
4.6.2.	Mass absorption coefficient.....	84
4.6.3.	CDs-Viologen quenching measurements	85
4.6.4.	Photocatalytic experiments	86
4.6.5.	ζ -potential	86
5.	Results: Photoreductive cleavage of C-O bond.....	86
5.1.	Introduction.....	86
5.2.	Synthesis of CDs	87
5.3.	Synthesis of esters	90
5.4.	Reactivity	90
5.4.1.	Photodeprotection of the octanoic ester	91
5.4.2.	Scope of the substrate	97
5.5.	Cyclovoltammetry study.....	99
5.5.1.	Cyclovoltammetry measurements on CDs.....	100
5.6.	Conclusion	105
5.7.	Experimental	106
5.7.1.	Reagents and instrumentation	106
5.7.2.	Synthesis of esters and cleavage products	106
5.7.2.1.	Octanoic acid protection	106
5.7.2.2.	Benzoic acid protection	108
5.7.2.3.	p-nitrobenzoic acid protection.....	111
5.7.2.4.	Synthesis of 1,4-dimethylpyridin-1-ium iodide	113

5.7.2.5.	Synthesis of 4-(hydroxymethyl)-1-methylpyridin-1-ium iodide	113
5.7.1.	Photocatalytic study	114
5.7.1.1.	Quantification of acid formed by the reaction.....	114
5.7.2.	Cyclovoltammetry	114
5.7.2.1.	Reagents	114
5.7.2.2.	Instrumentations and electrodes for electrochemical experiments	115
5.7.2.3.	Sample preparation	115
6.	Conclusion	115
7.	References.....	116
8.	Appendix	A1

1. Introduction: Carbon Dots

1.1. Nanomaterials

The term nanotechnology is relatively new in the field of chemistry research, but the use of nanomaterials and the exploitation of their properties is known for centuries. Indeed, Au NPs were used in China as an inorganic dye to introduce red color into their ceramic porcelains more than thousand years ago¹. Or simply we can just think of the colloidal dispersion of gold prepared by Faraday in 1857.² What changed from these case to the modern nanotechnology is the learned ability to manipulate, investigate and create nanomaterials as we want in order to obtain desired properties for new application. The first time that the term nanomaterials was mentioned, as we know it today, date back in the 1959 during the famous lecture of the Nobel Prize Richard P. Feynman "There's Plenty of Room at the Bottom"³. The key point of the lecture is that the nanoscale is small enough for the extreme minimization but larger enough to arrange sufficient atoms and obtain a structural complexity that can give raise at new and interestingly properties. Since then a lot of effort and discovery were made in this fields and new family of nanomaterials were synthesize and characterized. As an example the evolution of the electronic devices has seen a decrease year by year of their dimension following a law presented by Moore back in the 1965⁴ which predicts the halving of the dimension every 18 years (Figure 1). To date, anyway, the definition of nanomaterials is an open debate but, in general for a material in order to be called in such way, it needs to possess at least one dimension lower than 100 nm that is defined as nanoscale.⁵ The choice of this dimension lies in the observation that, in general, under these value new properties can arise from the materials⁶ such as new optical properties like fluorescence⁷, physical properties such as decreasing of melting point in crystal⁸ or semiconductor that become insulator when they reach the nanometer scale⁹. During the years different class of nanomaterials were defined on the base of how many dimensions are in the nanoscale such as nanoparticles, with all the three dimensions under 100 nm, or nano-fiber with two dimensions in the nanoscale and then nano-plate with only one dimension under 100 nm¹⁰. Due to the great number of nanomaterials synthesized in the last years a classification was introduced in order to better distinguish the materials to research on.

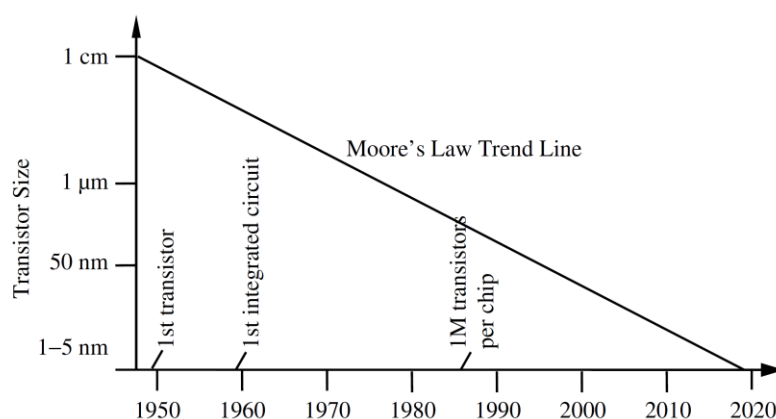


Figure 1. Moore's Law plot of transistor dimensions

The main difference in which the nanomaterials can be divided is based on their composition and on the choice of starting material: metals or carbon-based materials. Metal nanoparticles was the first family that received attention, and several applications have been developed with these materials. As example, the previously mentioned gold nanoparticles are well known for their versatility and wide use in the modern life; in particular as sensor for different compounds like alkali and alkaline earth metal ions, heavy metal ions and also small organic molecules¹¹ or in drug delivery system¹² (DDS). A plethora of other metal-based nanoparticles and nanomaterials were developed and studied in the recent years. The most successful and worldwide diffuse nanomaterial is for sure the titanium dioxide nanoparticles. It finds application in several fields, from food industry to personal care use¹³, and more over in photocatalytic application¹⁴ and in electronic device¹⁵. Despite, their outstanding property and unique features, the use of metal nanoparticles in human application give raise to many question related to their toxicity and to the possible accumulation of metals in the cells. Many studies were conducted to assess the healthy of this nanoparticle but up to date a clear answer is yet to be reached¹⁶. Anyway, some studies highlight the possible toxicity of silver nanoparticles, Handrup *et al.* analyze the effect of the accumulation of ions due to the use of silver nanoparticles. They found out that the silver seems to be distributed with the highest levels in the intestine and stomach and to induce a blue–grey discoloration termed argyria to the skin. This and other effects induced by particulate silver are suggested to be mediated via silver ions that are released from the particle surface. In order to reduce or avoid the use of metals both in nanomedicine and in the nanotechnologies in general, a new class of nanomaterials were emerged, the carbon-based nanoparticles (CNPs). In this fields, the first to be discovered was the monolayer graphene. Monolayer graphene is an sp^2 hybridized hexagonal carbon network discovered by H. P. Boehm in

1962¹⁷, indeed at that time the research wasn't focused on this nanomaterial but more on 3D graphite structures. In the years after, the progression in surface science, led to the studies of carbon cluster and to the discovery of cluster composed only by even number of carbon atoms, especially 60 or 70. The reason of this occurrence was soon explained by Kroto, Smalley, and Curl in the 1985 that proposed the formation of large highly symmetrical molecules called fullerenes, with 60 carbons at the vertices of a regular truncated icosahedron similar to the structure of a soccer ball¹⁸. Following the great success of the discovery of this nanomaterial, many other types of fullerenes were synthesized and characterized changing the number of carbon atoms and starting to derivatize the surface of the fullerenes¹⁹ (Figure 2). Many applications were developed with this class of CNPs; one of the major properties exploited in the fullerenes is their high superconductibility, especially if doped with alkali metals.

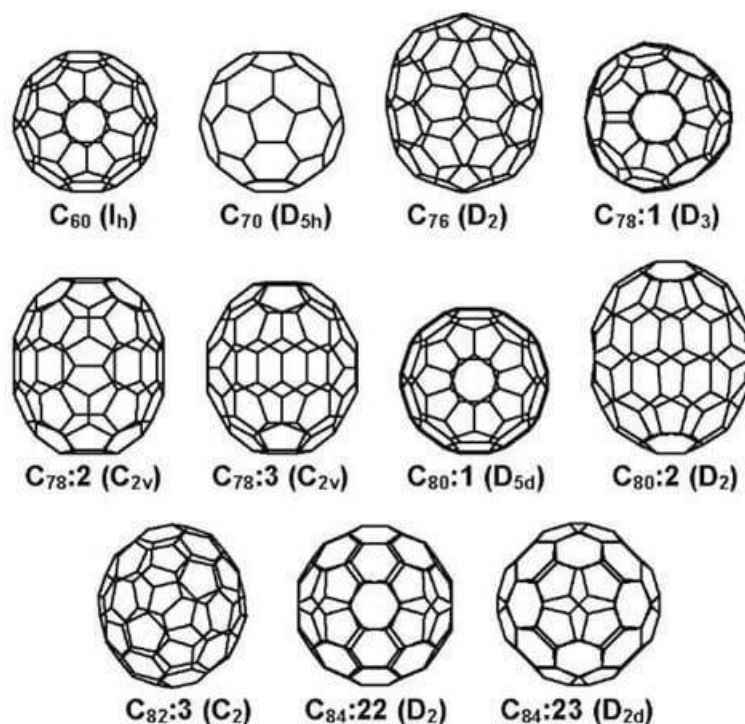


Figure 2. Different type of fullerenes

Up to date the fullerenes found a great number of applications in many branches of chemistry, and the study on this material is far from be over^{20,21}. As example, derivatized fullerenes were recently employed as inhibitors towards the infection of cell by virus Ebola, as reported by Martin *et al.*²² Other carbon-based materials were then discovered and among the others, carbon nanotubes, gave the best results and find more applications. This nanomaterial was first discovered in the 1991, and

since then they have been the focus of considerable research. The material has incredible properties such as thermal conductivity higher than diamond²³, high thermal stability²⁴ and resilience²⁵. This material derives from the fullerene but presents a dimension, the length, longer than 100nm and the walls could be formed by one-atom-thick sheets of carbon, called graphene or also by a multilayer of graphene sheets as illustrated in Figure 3. Accordely, they can be classified in single-wall nanotubes (SWNTs) and multi-wall nanotubes (MWNTs). These nanomaterials are used in a great number of application regarding different fields. As example the nanotubes are used in solar cells²⁶ and in many electronic devices.^{27,28}

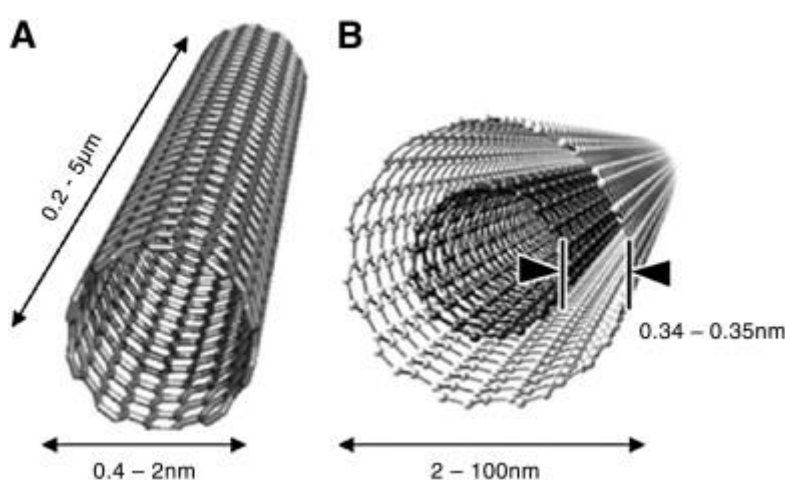


Figure 3. Schematic representation of single walled nanotubes (A) and multiwalled nanotubes (B).

From one of the numerous experiments regarding the nanotubes in 2004 a new class of nanomaterials was discovered, the carbon dots (CDs). The authors found out that after the purification of the single walled nanotubes one fraction results to be very fluorescent. Analyzing the fraction, they were able to detect small nanoparticles with spherical shapes and ascribed to these nanoparticles the origin of the fluorescence. From this paper the research on the CDs gain an impressive attention and more details on their composition and characteristic were discovered and a great number of ways of synthesis were developed. In general, CDs are considered as nanoparticles with a diameter lower than 10 nm, a spherical shape and a highly functionalized surface. This nanomaterial, presents some unique properties that make it very attractive for the scientific community, such as tunable fluorescence with high quantum yield, high water solubility, excellent chemical stability, non-toxicity, good biocompatibility and ease of modification. These excellent properties could be employed in many applications including bioimaging^{29,30,31,32}, drug delivery^{33,34}, sensors^{35,36,37}, optoelectronics³⁸ and photocatalysis.³⁹ Moreover, researchers recently found out that CDs exhibit strong luminescence upon two-photon excitation in the NIR region, which further

expands their applications in bioimaging.⁴⁰ Along with these properties CDs could be prepared from a wide range of precursors, including cheap and abundant materials and with low cost techniques, making them very appealing for replacing other more expensive materials.

1.2. Methods of synthesis

In the last decade many synthetic pathways were developed in order to synthesize CDs from different substrates. The strategies for the synthesis of the CDs can be divided in two classes depending on the choice of precursors. The Top-Down approaches involve the use of techniques like arc-discharge, laser ablation and electrochemical oxidation to break large carbogenic structure such as graphite or graphene layers. On the contrary, with the bottom up approach, small organic molecules are carbonized in order to obtain the small nanoparticles employing solvothermal techniques or pyrolysis methods.

1.2.1. Top Down syntheses

Arc-Discharge

Historically the top-down methods were the first to be developed for the synthesis of the CDs. Indeed, when the laser ablation technique was employed to purify single walled nanotubes, the obtained suspension was then separated by gel-electrophoresis revealing the presence of a fluorescent fraction. That was investigated by TEM techniques revealing the presence of small spherical nanoparticles⁴¹. However, only few examples of CDs obtained from arc-discharge treatment were reported until now, as example Bottini et al. produce small nanoparticles with this technique employing as substrate pristine and acid oxide carbon nanotubes.⁴² This technique was then dismissed due to the high amount of impurity formed during the synthesis.

Laser Ablation

More widely used for the top-down synthesis of CDs is the laser ablation technique that can guarantee a more controllable morphology and size. Koshizaki *et al.* prepared CDs with tunable fluorescence starting from nanocarbon materials. In more details the precursor was dispersed in an organic solvent and then the mixture was irradiated with a laser, the supernatant, analyzed by TEM reveals the presence of smaller nanomaterials with a core displaying a graphitic structure. The PL behavior of the synthesized nanomaterial reveals an emission in the visible region that can be tuned varying the excitation wavelength.⁴³ The authors demonstrate also that the PL behavior was also correlated with the solvent used for the irradiation treatment, since the use of water in place of other organic solvent results in no appreciable PL. The ability of controlling the size of such nanoparticles

employing this approach was demonstrated by Hu *et al.* using graphite as precursor. The authors synthesized three types of CDs with different dimensions by treating the sample of graphite with different pulsed laser width.⁴⁴ The samples result to be highly fluorescent with an emission band centered at 430 nm, otherwise their dimensions is dependent on the width of the laser pulse, higher is the laser pulse width and greater is the average dimension of the CDs.

Electrochemical oxidation synthesis

The electrochemical oxidation synthesis of CDs is another widely used top-down approach that involves the treatments of large carbogenic structure supported on electrode to obtain small nanoparticles. This method has several advantages such as high purity, low cost, high yield, easy manipulation of size and good reproducibility, for these reasons is the most used top-down approach. The method was firstly reported by Zhou *et al.* that grew MWCNTs from scrolled graphene layers on carbon paper by chemical vapor deposition (CVD). These nanotubes were used as working electrode in an electrochemical cell consisting of a platinum (Pt) wire counter electrode and an Ag/AgClO₄ reference electrode in a degassed acetonitrile solution containing 0.1M tetrabutylammonium perchlorate (TBA⁺ClO₄⁻) as the electrolyte.⁴⁵ Applying a sufficiently high potential at the working electrode that the solution turned from colorless to yellow to dark brown, and also presents a blue fluorescence under UV-Light. The obtained nanoparticles present an average diameter of 3 nm and show an excitation dependent PL behavior. Another example in this context was reported by Liu *et al.*, were able to produce CDs with an average diameter of 4 nm by electrochemical oxidation of a graphite electrode in alkaline alcohols.⁴⁶ More in details the synthesis was carried out applying a potential of 5 V to the working electrode for 3 h under the nitrogen ambient obtaining a colorless CQDs dispersion. The nanoparticles present a high crystallinity structure and a bright blue fluorescence with an emission maximum centered at 436 nm and independent respect to the excitation wavelength. More recently, Ma *et al.* reported the synthesis of CDs through the electrochemical oxidation of two graphite electrode for 120 hours. The treatment results in a corrosion of the anode graphite rod and in a consequent yellow-black solution that was then filtered and centrifuged in order to recover the CDs fraction with a diameter <10 nm and with a graphitic structure. The as produced CDs result to be highly fluorescent and present hydroxyl group on the surface making them water soluble, furthermore their properties were exploited in developing a CDs doped semiconductor.

1.2.2. Bottom Up syntheses

The bottom-up approaches are the most used for the synthesis of the CDs since the procedures are very simple and it is possible to choose a wide range of precursors to tune the final properties of the nanomaterials. Furthermore, changing the reaction conditions it is also possible to obtain amorphous or graphitic materials, allowing to achieve different properties in terms of fluorescence and reactivity as will be discussed in the next chapter. With these methods the initial carbon precursor, in general small organic molecules, are treated at high temperature and for long time, and can undergo dehydration and decarboxylation reaction to generate an aromatic network.

Combustion/Acid oxidation method

Liu *et al.* first reported that fluorescent CDs can be obtained from the combustion soot of candles after refluxing with oxidating acid.⁴⁷ In more details, a glass plate was used to collect the hydrophobic soot produced by the candle, and by treatment with HNO₃ it could be turned to hydrophilic. After a purification with gel electrophoresis, the mixture was separated into three bands and the first one consisted of nine fast-moving fluorescent smaller bands, showing different emission spectra although they were excited at the same wavelength. This study indicated that the fluorescent emission of CDs is size-dependent and/or charge-dependent. Furthermore, different precursors were employed to obtain high luminescent CDs. As an example, very recently Zhang *et al.* compared CDs obtained by combustion of ethanol, n-butanol, domestic candle and benzene. The recovered soot was analyzed by TEM, IR, UV-Vis and fluorescence spectroscopy revealing in all the cases the presence of CDs with a graphitic structure. Interestingly the choice of precursors, does not affect the final results with these methods as their properties results to be very similar to each other. All the synthesized CDs presents an emission wavelength centered at 430 nm with an excitation dependent behavior and their fluorescence results to be very stable over time.⁴⁸

Another similar bottom up technique is the acid oxidation method, involving a strong acid treatment of carbon precursors conducted at high temperature. In this context, a recent example was provided by Bayda *et al.* synthesized CDs from black tea. This synthesis is simple and economical due to the inexpensive nature of the carbon source. The as synthesized nanoparticles present a narrow size distribution, tunable optical properties covering visible to deep red absorption and proved to be non-toxic. Furthermore, Wang *et al.* synthesized P-doped CDs using glacial acetic acid and P₂O₅ in a 5 minutes synthesis (Figure 4).⁴⁹ The nanoparticles were then characterized revealing a hollow structure and a green fluorescence with an excitation dependent fluorescence, furthermore the

study revealed the autocatalytic nature of this reaction that can self-generate enough heat to produce CDs from the selected precursors.

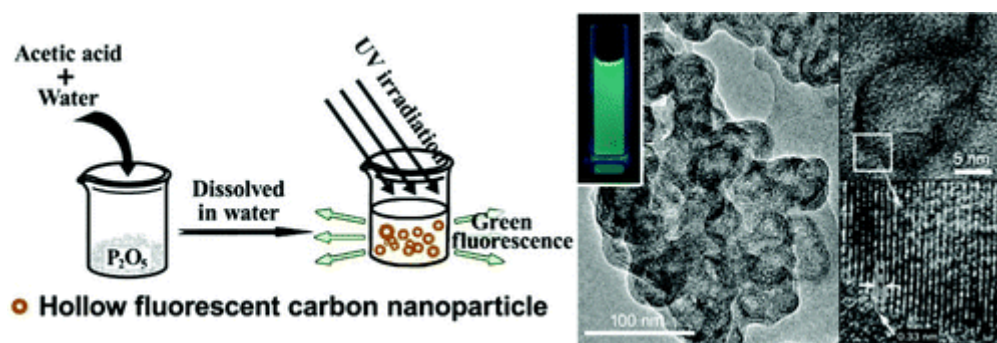


Figure 4. Schematic representation of acid oxidation synthesis of CDs.⁴⁹

Microwave

Another very common and affordable method to synthesis CDs is through the microwave synthesis. This approach simply implies the microwave irradiation of a solution of the precursor. The advantage of this method relies on the short reaction time, the uniform size of the as synthesized nanoparticles and also high yields. One of the mostly used carbon precursors in this processes is the citric acid, due to its cheap nature and to the three carboxylic groups that can easily undergo dehydration reaction and polymerization with other reagents. An example of the potentiality of the molecule was highlighted by Huang *et al.* that produces nitrogen CDs from the microwave treatment of citric acid and ethylenediamine.⁵⁰ Such nanoparticles exhibit a very high QY and also a good biocompatibility, the emission is centered at 450 nm. Furthermore, the nanoparticles were used for a bioimaging application demonstrating a good photostability and also could successfully been used to sensitively detect Fe(III), Hg(II), and chlorite ions with satisfying results. In the years innumerable amounts of CDs were produced with this technique employing a wide range of starting materials to dope the nanomaterials and induce new properties and characteristics.⁵¹ Another recent example of CDs produced from a microwave irradiation treatment was furnished by Wang *et al.* employing thiourea and citric acid as sulfur and carbon sources respectively.⁵² The study reveals that such nanomaterial was produced with high yields and exhibits a QY of 56% with a green emission that is affected by an excitation dependent PL phenomenon. The CDs present also an absorption peaks in the visible region that make them very promising in bioimaging application, in addition the toxicity test performed on these nanoparticles reveals that this nanomaterial is nontoxic and could be employed in biomedical application. Besides the use of simple organic molecules also polymers, like the polyethylene glycol⁵³ or ionic liquid⁵⁴ could be used in this approach to obtain high luminescent CDs. Very recently, Prato

and co-workers starting from commercially available quinones, arginine and ethylene diamine by means of the microwave irradiation technique prepared and characterized a redox library of amino doped CDs with tunable oxidation/reduction properties highlighting their potential applicability as photocatalysts (Figure 5).⁵⁵ In all cases, after the hydrothermal treatment, the colour of the reaction mixture turned dark brown as a result of the formation of CDs.

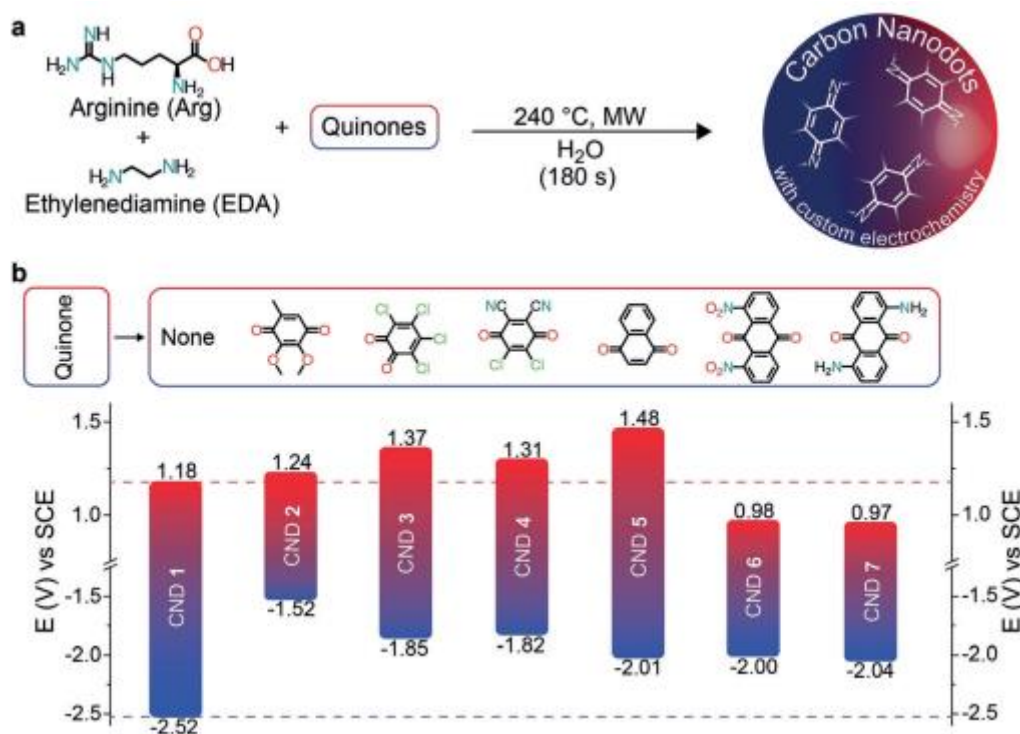


Figure 5. a) Bottom-up synthesis of quinones derived amino doped CDs. b) Redox potentials of the CDs.⁵⁵

By extending the as developed microwave assisted multi-component synthetic approach, the Prato group prepared the first example of chiral CDs (CNDs-R or CNDs-S) by using arginine, as the core precursor, and (R,R)- or (S,S)-1,2-cyclohexanediamine (CHDA) as the chiral surface precursor. The nanoparticles were completely soluble in water and by electronic and vibrational circular dichroism, a mirror image profile in both UV-Vis and IR region was detected. The origin of chirality has been ascribed to the presence of numerous cyclohexane diamine moieties around the carbon-based amorphous core. The authors used the as formed chiral nanodots as templates for the preparation of porphyrins based supramolecular assemblies thus opening the way for developing a variety of new chiral composite materials and applications.⁵⁶

Thermal/Hydrothermal/Solvothermal Methods

These approaches are most widely used to date for the synthesis of carbon dots, due to their low cost, easy feasibility, environmental friendliness and applicability with various renewables carbon sources. The thermal approach involves the direct carbonization of the selected precursors without the presence of a solvent, the reaction is normally carried out at high temperature (200-400 °C) and for long time (24-100 h). The resulting black viscous materials is normally treated with a basic solution and then dialyzed in order to recover the pure carbon nanomaterials. One of the first example of thermal synthesis of CDs was reported by Giannelis's group in 2008.⁵⁷ The authors demonstrate the applicability of the synthetic procedure by heating at 300 °C for 2 h in air different ammonium citrate salts or 4-aminoantipyrine leading to the formation of both hydrophilic or lipophilic surface-functionalized carbogenic nanoparticles. These nanoparticles possess an average size of less than 10 nm, are highly dispersible in organic or aqueous solvents (depending on their surface functionalization) and emit light in the visible when stimulated with different excitation wavelengths. When extending the procedure by using neat citric acid a completely insoluble carbogenic solid was obtained. Later on, Guo's groups successfully reported the synthesis of CDs from sole citric acid by a thermal treatment at 180 °C for 2,5 hours and subsequent basification of the carboxylic surface groups (Figure 6).⁵⁸ The latter steps result of be if fundamental importance for the water solubility of the nanoparticles. Reisner's group improved this synthesis in order to produce large scale CDs from solely citric acid by a pyrolysis treatment. The procedure involves the carbonization of the reagent at 200 °C for 48 hours followed by a basification with a solution of NaOH and a purification with dialysis.⁵⁹ The recovered materials results to be highly graphitic and demonstrate also good performance in photocatalytic water splitting reaction. Furthermore, the group extend the protocols to the nitrogen doped CDs replacing the citric acid with aspartic acid.⁶⁰ The synthesis affords the obtainment of a great amount of CDs with an enhanced light harvesting properties that results to be a crucial parameter in boosting the photocatalytic properties of such nanomaterial.



Figure 6. Thermal synthesis of CDs from citric acid.⁵⁸

Besides the use of citric acid or analogous molecules the pyrolysis treatment could be employed to produce CDs from a wide range of carbon precursors. Among the others also natural materials such as wool⁶¹, goose feathers⁶² and flour⁶³ were used for producing doped CDs.

The solvothermal/hydrothermal approach instead involves the carbonization of the carbon precursor dissolved in an organic solvent or water in an autoclave. Unlike the previous case, with this method the temperature cannot be very high (140-200°C) due the pressure restriction of the autoclave. In general, from an initial clear solution, after the treatment a yellow-dark brown solution is obtained and after the evaporation of the solvent the CDs can be recovered and used without any further purification. This procedure is very simple and allows to use a wider range of precursors, as long as they are soluble in the selected solvent. In particular this procedure permits to easily dope the CDs by employing a multicomponent approach or employing molecules containing the desired heteroatom. Also in this case the main carbon precursors employed is the citric acid, especially in combination with amine or poly amine⁶⁴. As an example, Zhu *et al.* produced nitrogen-doped citric acid derived CDs by a hydrothermal method employing ethylenediamine as co-reagent. The quantum yield of N-doped CDs reached up to 80.6 % at the excitation wavelength of 360 nm, nearly equal to most semiconductor QDs and fluorescent dyes.⁶⁵ In this context, Chandra *et al.* fabricated N,P doped CDs by employing citric acid and ammonium hydrogen phosphate as precursors. The reaction conducted at 180 °C for 4 hours afforded the synthesis of CDs with a QY of 59% with an emission at 420 nm. Such materials demonstrate to be a great tool for the selective detection of Fe(III) ions with a detection limits of 20 µM.⁶⁶ In recent years, more works have been carried out to find other bio-based precursors (glucose⁶⁷, sucrose⁶⁸, polyols⁶⁹, polymers⁷⁰, amino acids⁷¹, proteins⁷², natural products⁷³, and some wastes⁷⁴) to synthesize CDs. In this context, Yang *et al.* synthesized CDs from glucose and monopotassium phosphate by a hydrothermal treatment in autoclave at 200°C for 12 hours.⁷⁵ The authors found out that increasing the amount of KH₂PO₄ in the initial mixture results in different outcomes properties of the CDs. In more details, with a ratio glucose/ KH₂PO₄ of 1:26 blue emitting nanoparticles are produced, while increasing the ratio to 1:36 results in a green emission photoluminescence. The role of the phosphate is to act as dehydrating agent instead of the common diamine, furthermore this work highlighted the ease of tuning the properties of CDs by simply varying the ratio of the initial precursors. Besides the use of water, also organic solvent could be employed for the solvothermal treatment, in particular, ethanol is one of the most common used organic solvent. A clear example in this context was reported by Jiang *et al.*, who synthesized color-tunable CDs.⁷⁶ Phenyldiamines were chosen as carbon and nitrogen precursors and were solvothermally

heated in ethanol at 180 °C for 12 h (Figure 7). Interestingly, depending on the configuration of the relative substituent position in the precursor (from ortho, to meta and para) the emission color of the resulting CDs changed from green, to blue and red.

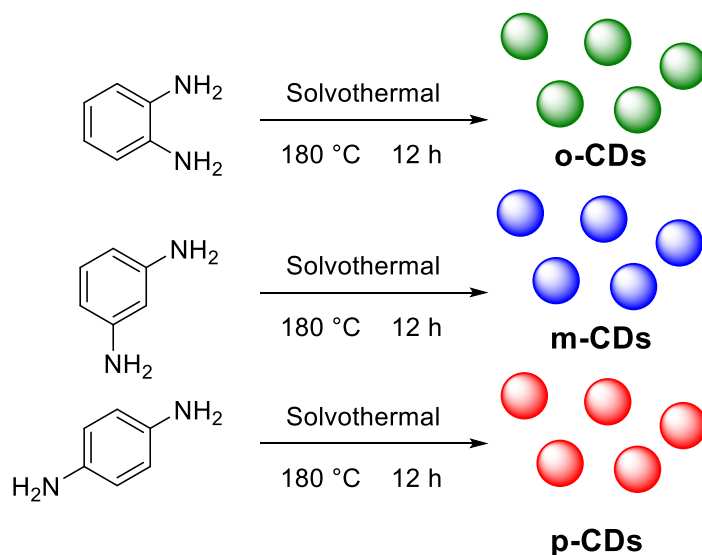


Figure 7. Preparation of the red, green and blue PL CDs from three different phenylenediamine isomers.⁷⁶

1.3. Structure of the CDs

The CDs are mainly composed by C, H and O in various ratio depending on the precursors employed and the synthetic method adopted. Other atoms could be incorporated inside the structure, conferring new properties to the nanomaterials, such as an enhanced fluorescence, tune the fluorescence emission band and more other. The main doping atom is the nitrogen, that is known to enhance the QY of the CDs^{77,78}, the presence of the sulfur atom instead has the effect of widen the band-gap between the valence and conduction band⁷⁹, while doping the CDs with phosphorous could results in a green fluorescence that is of crucial importance for the bioimaging applications⁸⁰. Besides the chemical composition, another important factor to take into account working with these nanomaterials is their morphology. It has been demonstrated that the CDs could possess a graphitic or amorphous core depending on the synthetic approach employed and also the reaction condition. Generally, the top-down synthesis, as expected, led to the obtainment of a highly crystalline material, with well-defined graphitic layer. Tian *et al.* were able to confirm the presence of sp^2 carbon with signals in the $\delta=90-180$ ppm range.⁸¹ Furthermore, FT-IR measurements also confirmed the presence of C=C aromatic ring stretches. Therefore, the authors concluded that these CDs consisted of a nanocrystalline core of graphitic sp^2 carbon atoms functionalized with carboxylic/carbonyl moieties (Figure 8).

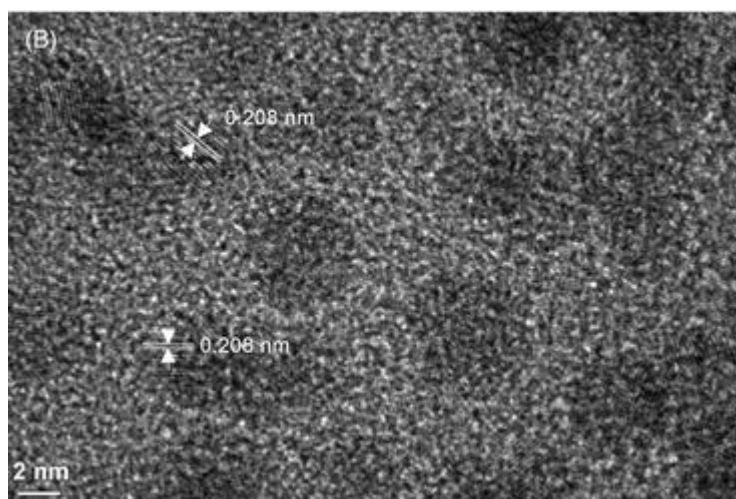


Figure 8. HR-TEM images of CDs obtained from natural gas soot.

While the morphology of the CDs obtained from the top-down methods, are of unquestionable nature, the ones of the CDs obtained from the bottom-up methods are still an open issue. Contextually, in the last year, several studies were conducted, in order to have a better comprehension of the morphology of this system and how this aspect is affected by the synthetic procedure employed. In general, CDs obtained with such method are constituted by a graphitic-like carbogenic core, amorphous polymeric-like compounds, and even of small molecular-like fluorophores. In order to distinguish between the different materials the term “degree of carbonization” that quantifies the efficiency in converting the molecular precursors in graphitic-like carbonaceous CDs was introduced. A study conducted by Wang et al. on the decomposition of citric acid explained how the synthetic conditions used affect the morphology.⁸² The authors carried out the pyrolysis treatment at different time and temperature and reveal the intrinsic differences between the obtained CDs. For those experiments conducted at relatively low temperatures (180 and 200 °C) and shorter reaction times, sufficient quantities of highly luminescent uniformly-sized CDs were formed exhibiting a strong excitation-independent photo-luminescence. The authors suggest that in first instance the reaction proceeds towards the nucleation of some molecules of citric acid producing high fluorescence materials which further evolve through crosslinking and stacking forming extended amorphous and crystalline carbon domains (**Figure 9**).

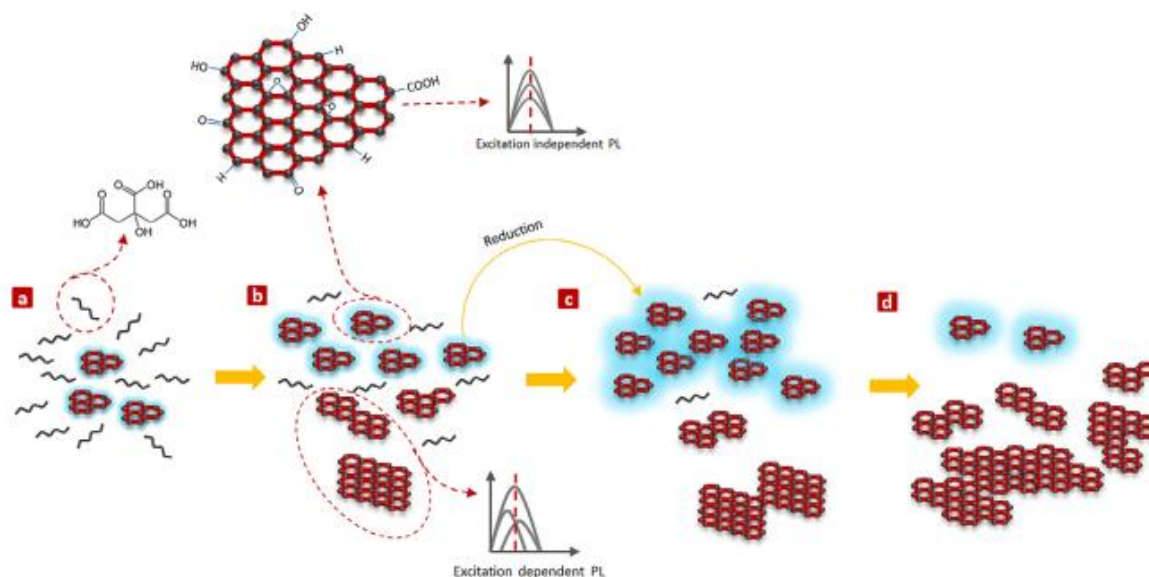


Figure 9. Schematic representation of the thermal decomposition process of CA. ⁸²

Furthermore, for the synthesis of heteroatom doped CDs a structural diversity was put in light depending on the conditions employed.⁸³ Specifically, the reaction between citric acid and ethanol amine was performed at different temperatures of 180, 230 300 and 400 °C. For the lower temperature no CDs were detected notwithstanding the highly fluorescence nature of the final solution. NMR and ESI-MS analyses reveal the presence of citric acid derived molecular fluorophores. Increasing the reaction temperature has as results the formation of small spherical nanoparticle and progressive decreasing of the QY (**Figure 10**). The data suggest that the fluorophores produced at low temperature are used as building blocks for the synthesis of the CDs at higher temperature.

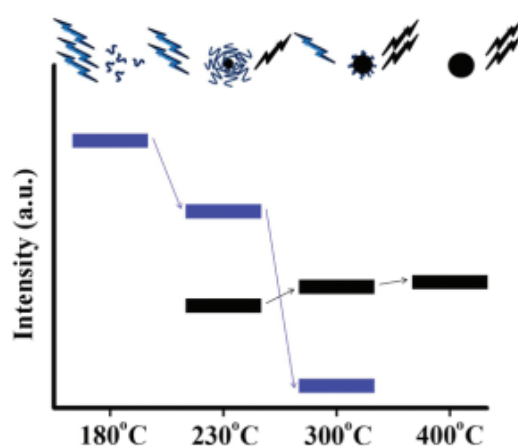


Figure 10. Schematic representation of the emission characteristics of three photoactive species produced from the thermal treatment of mixture of CA and EA. ⁸³

Also the hydrothermal procedures was employed to study the morphology of the CDs. As an example Song *et al.* investigated the properties of the CDs obtained from the hydrothermal treatment of citric acid and ethylenediamine at low temperature.⁸⁴ The authors identify a specific bright blue fluorophores named IPCA (imidazo[1,2-a]pyridine-7-carboxylicacid, 1,2,3,5-tetrahydro-5-oxo) fluorophore (Figure 10, a), which was found to exist individually or attached to the carbon core and thus to strongly affect the luminescence properties of the synthesized nanoparticles. At higher temperature higher degree of carbonization was observed in the obtained nanoparticles, while a lower amount of fluorophores was detected. From these experimental evidences, the authors hypothesised the presence of a chemical equilibrium between IPCA and carbon cores with polymer clusters acting as a transition state. According to that, the synthetic outcomes could be affected by many factors such as by reagents ratio, initial pH value and temperature. Since then, many fluorophore molecules have been detected in solution during the synthesis of CA-derived CDs. TPCA and TPDCA (**Figure 11**, b and c) were the organic fluorophores main obtained from the N,S-CDs synthesized by hydrothermal treatment of CA with L-cysteine or cysteamine at low temperatures (200 °C) for 3h.^{85,86}

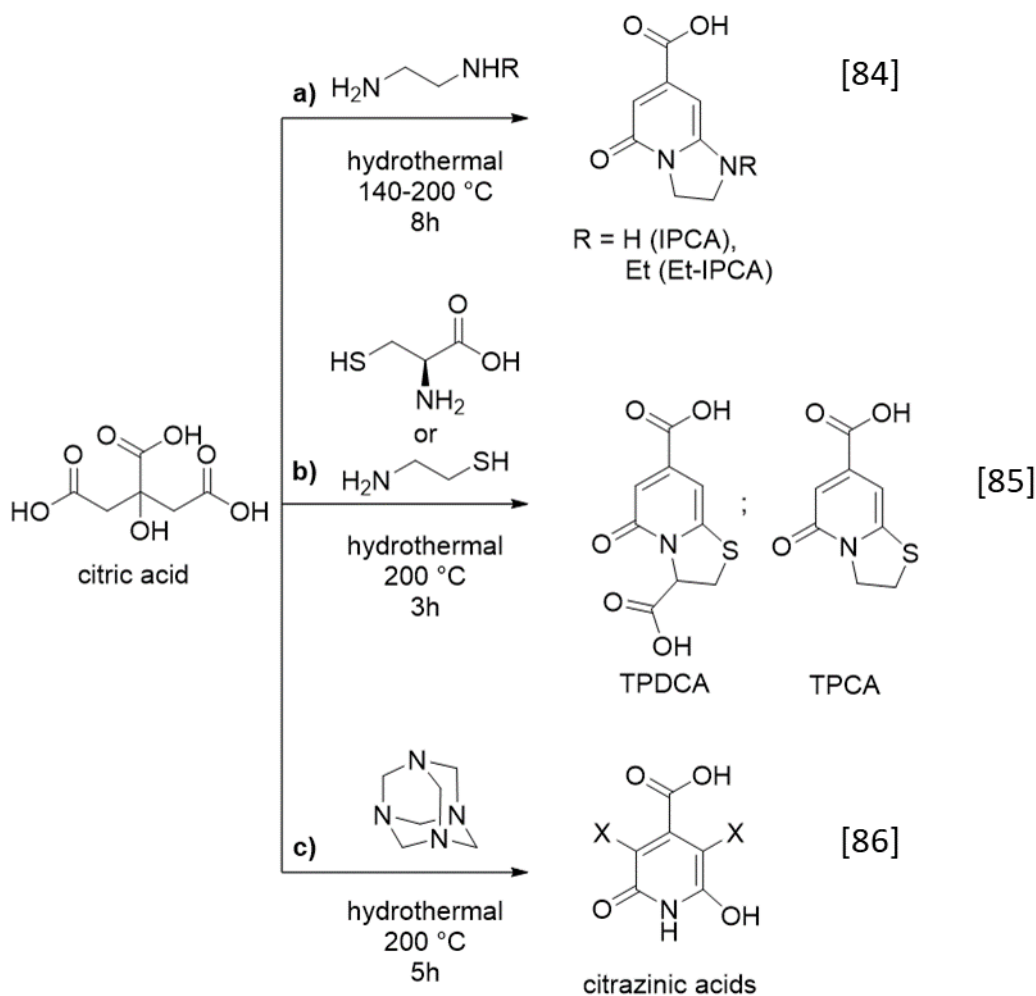


Figure 11. Molecular fluorophores identified in the synthesis of CA-based CDs using different amino-containing precursors.

From all this observation, it could be concluded that hydrothermal procedures produce a more amorphous material with also the formation of organic fluorophore, that guarantee a high QY and an easy tunable fluorescence. On the other hand, employing harsher conditions like in the pyrolysis method, the material obtained shows a more graphitic structure, with surface defects that can give rise to photoluminescent emission. Regarding the top-down methods, the materials produced presents always a graphitic structure, since the precursors are themselves graphitic-like.

1.4. Photoluminescence

One the most fascinating and intriguing properties of the CDs is their photoluminescence, but, notwithstanding the many effort made, its mechanism remains unclear. The most reasonable explanation of this phenomenon is to attribute the origin of the fluorescence to the different components of the CDs such as: the graphitic-like carbogenic core, the surface states and the molecular fluorophores. These three components can generate emission in three different ways:

- i)* The quantum confinement effect, which is determined by the degrees of π conjugation and so by the presence and the size of the graphitic core. This type of PL, which arises from a band-edge recombination process, commonly observed also in the homologous "metal based" Quantum Dots, confers to the here discussed carbon-based nanoparticles a size-dependent, excitation-independent, and a very narrow emission band.
- ii)* The second type of emission is generated by the surface states, which are determined by surface defects, functional groups, and surface passivation of the carbogenic core. In this case the superficial defects entrap the photoexcited electrons and/or holes in the bandgap thus generating PL with lower energy. The resulting PL exhibits a not well-defined behavior and strongly dependent on the synthetic procedure used.
- iii)* The third is the molecular state type which is associated to the presence of fluorophores on the CDs composition. In this case, neither quantum confinement or surface defect effects exist, and the luminescence is solely a consequence of the superposition of several "molecular" type emissions. PL is therefore size and excitation-dependent and exhibits a very broad emission band.

A great number of study was focused the origin of the fluorescence and what type of mechanism was involved. Li *et al.* investigated the quantum-confinement effects and size-dependent optical properties of CDs prepared by alkali-assisted electrochemical method starting from graphite honeycomb⁸⁷. Depending on the reaction time they obtained CDs with different dimensions that shows different emission behavior. The smaller CDs (1.2 nm, center) giving UV light emission, medium-sized CDs (1.5-3 nm) visible light emission (400–700 nm), and large CDs (3.8 nm, center) NIR emission (Figure 12a, b). The bright blue, green, yellow, and red PL of CDs is strong enough to be seen by the naked eye. A series of control experiments showed no obvious change in the PL spectra of CDs before and after hydrogen plasma treatment that remove the superficial adsorbed oxygen. Figure 12c and d show the dependence of HOMO–LUMO gap on the size of the graphene fragments. As the size of the fragment increases, the gap decreases gradually, and the gap energy in the visible spectral range is obtained from graphene fragments with a diameter of 14-22 Å, which is in agreement with the visible emission of CDs with diameters of <3 nm. Thus, they deduced that the strong emission of CDs comes from the quantum-sized graphite structure instead from the carbon–oxygen surface.

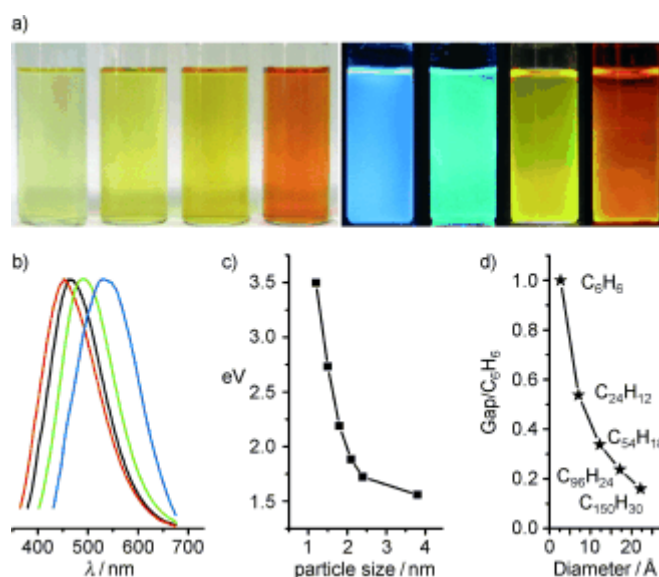


Figure 12. Emission properties of CDs with different size.⁸⁷

An additional extensive analysis of the contribution on the PL of the carbon core of the CDs was reported by Zhu *et al.* which demonstrated the role of the aromatic carbon domain in achieving the blue fluorescence of the carbon nanoparticles.⁸⁸ In more details, in a perfect graphene core and few surface groups, the bandgap between the conjugated π -domains is the intrinsic PL center. Another important contribution to the photoluminescence of the carbon nanoparticles may derive from their surface states. Concisely, the surface chemical groups and the hybridization structure of the edge groups. Carboxyl and amide groups are responsible for the green emission of the carbon nanoparticles, while the hydroxyl groups guarantee a blue photoluminescence. These results were proved by different factors; first of all, a long exposure to the UV light results in an enhanced PL due to the oxidation of the hydroxyl groups to carboxyl groups. Converting the carboxyl groups in amide groups results in an enhanced PL and if these CDs are reduced a strong blue luminescence. These results confirmed the great complexity of the photoluminescence origin of the CDs and that different factor may contribute to it.

Regarding the effect on the PL of the surface states of the CDs, many studies have appeared in the last years. Sun *et al.*, passivated CDs formed by laser ablation of graphite powder and cement with PEG1500N, this procedure produces nanoparticles with an emission spectrum spanning from purple to red which further spreads to the NIR region.⁸⁹ Interestingly, the multicolor fluorescence behavior was expressed only after the surface passivation with organic or polymeric materials since the unpassivated nanoparticles exhibits no observable fluorescence emission. It should be noted that the surface passivation agents used were not emissive in the visible and NIR regions, thus any

fluorescence emissions observed must have originated from the surface passivated CDs. Furthermore, the surface states PL emission could be detected by varying the pH of the CDs solution. A study on this topic was performed by Qu *et al.*⁹⁰ Functional groups such as N–H and O–H on the surface of CDs can form intramolecular and intermolecular hydrogen bonds, which endows the CDs with different surface states. When pH increases or decreases, deprotonation or protonation of functional groups can lead to the variation of surface states and fluorescence. The third and last mechanism envisaged for the PL of the CDs is the one correlated to the molecular fluorescence. This behavior is strictly correlated to the presence in the mixture of the CDs of molecular fluorophores, and so it is correlated to the bottom-up solvothermal procedure. This effect was first highlighted by the already mentioned work of Song *et al.* which was able to isolate and to characterize the molecular fluorophore IPCA demonstrating that its absorption and emission spectra were identical to the one of the synthesized CDs⁸⁴. The fluorophore resulted to be the main emitting species in the synthesized CDs. Depending on the precursor employed for the synthesis, a great number of molecular fluorophores were identified, in particular a study conducted by Schneider *et al.* on CDs derived from the soft hydrothermal treatment of citric acid in presence of three different amino compounds highlighted this concept.⁸⁶ In the solutions of CDs obtained from the reactions a and b schematized in **Figure 13**, molecular fluorophores were detected, and their PL and absorption spectra resemble the one of a pure solution of the fluorophore. In addition, the authors demonstrated that the structure of the precursors is a key factor in determining the formation of the fluorophores, since the reaction c in **Figure 13** did not produce any detectable fluorescent compounds, having a different PL spectrum with a redshifted emission peaks and significantly lower PL lifetime and QY. This is due to the tertiary amine in the reaction mixture that cannot undergo decomposition to ammonia and further react with citric acid to form citrazinic acid like compound. In the described case instead is more likely that the carboxylic functionalities from citric acid may react with the terminal alcohols from triethanolamine under hydrothermal conditions, resulting in the formation of networks linked by ester bonds.

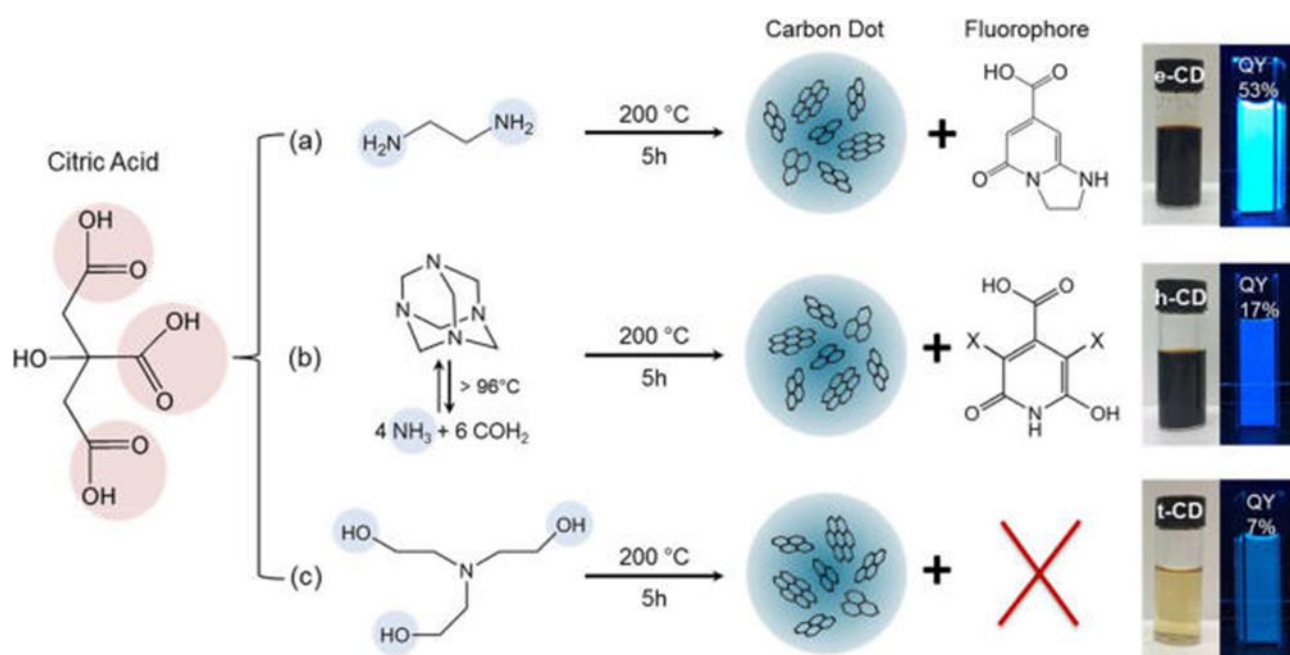


Figure 13. Synthesis conditions of citric acid-based CDs using three different nitrogen-containing precursors.

A very recent hypothesis on the origin of the PL behavior of the CDs and the specific role played by the different component was made by Fang *et al.*⁹¹ They suggested that the PL of CDs is the result of a cooperative effects between the graphitic carbon core, the defect states and the molecular fluorophore. For this aim, citric acid and amino group-containing molecules were employed as precursors to prepare CDs having luminescent pyridine-derivatives along with a carbogenic core that were separated by a dialysis treatment. The PL behavior of the molecules agree with the one of the original CDs solution with, however, a higher QY and a less evident excitation-dependent behavior. Combining these outcomes with an accurate optical study, the authors proposed a hypothetical PL mechanism in which fluorophores, defect states and carbon core play a different role. As illustrated in **Figure 14**, under the irradiation of UV light the fluorophores generate excited electrons from the π orbitals to the π^* orbitals (Process a). Some of the excited electrons in the π^* orbitals may recombine with the holes in the π orbitals directly, emitting the PL signal centred at 420-440 nm (Process b), which can be referred as the intrinsic emission like the band-edge emission observed in QDs. The other excited electrons in the π orbitals may be trapped by the defect states of energies lower than in the π^* orbitals (Process c) before they are finally recombining with the holes in the π orbitals. Meanwhile, some electrons may be excited and trapped directly by the defect states (Process d) and relax through either radiative (Process e) or non-radiative (Process f) ways. Therefore, when the excitation wavelength is in the range of 280-380 nm, the CD produces both intrinsic and defect PL signal. When the excitation wavelength is longer than 380 nm, the energy of which is less than that

needed for the π - π^* transition, the electrons can only be excited to the defect states. The graphitic core, in this hypothesis, acts as a quencher of the radiative relaxation pathway of both defect states and intrinsically through a fluorescence resonance energy transfer (FRET) effect thus lowering the QY. In conclusion, while the PL spectra depends on both molecular fluorophores and defect states, the magnitude of QY is mainly affected by the graphitic core of the CDs.

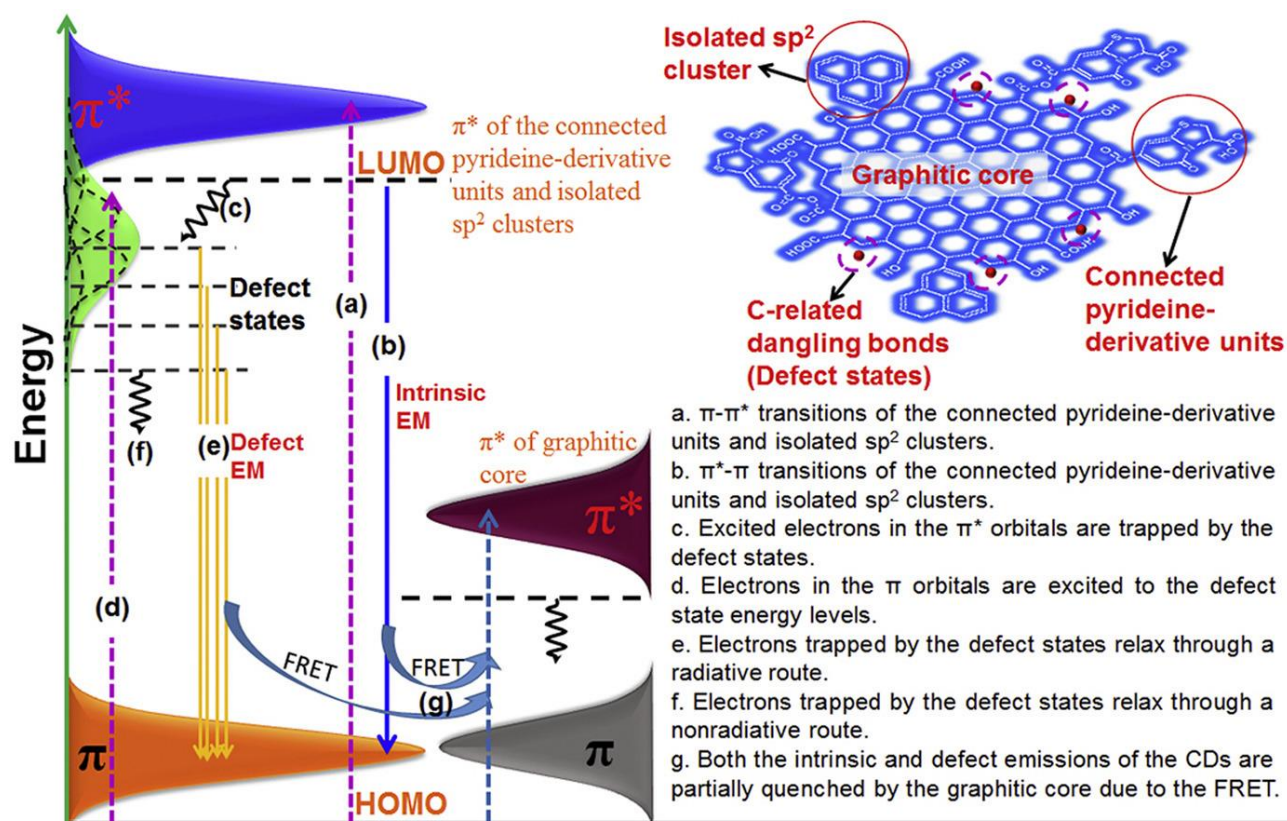


Figure 14. Proposed photoluminescence mechanism in CDs.⁹¹

Overall, even if this latter PL mechanism is satisfactory from an intuitive level, many other issues (such as role of the carbon core size and the structural morphologies of the CD, i.e. amorphous or crystalline) were not effectively addressed. Therefore, a real understanding on the mechanisms of fluorescence of these nano-systems remain unresolved to date.

1.5. Applications

In this last decade CDs were employed in many different applications exploiting their unique properties. They were used for a plethora of chemical, medicinal and optoelectronic applications,⁵¹ and for the fabrication of many CDs-incorporated nano-devices.⁹² One of the most studied and investigated field on this topic is biomedicine, due to the complete water solubility of the CDs and

also their biocompatibility. In this context, many efforts were made in order to synthesize CDs that could be used for applications like bioimaging and biosensing. Two of the most fascinating applications in which CDs could bring new perspectives are the drug delivery system (DDS) and the photocatalysis. In the next paragraph the more recent discoveries are reported and discussed.

1.5.1. Drug delivery

The field of the nanomedicine is an important topic, in particular the development of drug delivery system. This approach, could give the possibility to vehiculate the drug directly on the targeted cell, without attacking the normal ones. Correlated to this mechanism is the fact that a minor amount of drug could be employed due to the reduction of the unspecific contact of the drug with healthy cells and permit also to increase the local concentration, in the desired site, and consequentially the anticancer efficacy. CDs could be used as a carrier in the DDS since they can load the drug onto the surface and release it in particular condition. Sun *et al.* synthesized a theragnostic nanomedicine (CDs-Oxa) by condensation reaction between the amino groups on the surface of fluorescent CDs and the carboxyl group of the oxaliplatin derivative Oxa(IV)-COOH (Figure 15).⁹³ The CDs-Oxa were taken up by cancer cells through endocytosis and the drug was released upon the reduction of Oxa(IV)-COOH to oxaliplatin(II) because of the highly reducing environment in cancer cells. It was also demonstrated that the distribution of the CDs-Oxa can be closely tracked by monitoring the fluorescence signal of the CDs, thereby offering great help in the customization of the injection time and dosage of the medicine.

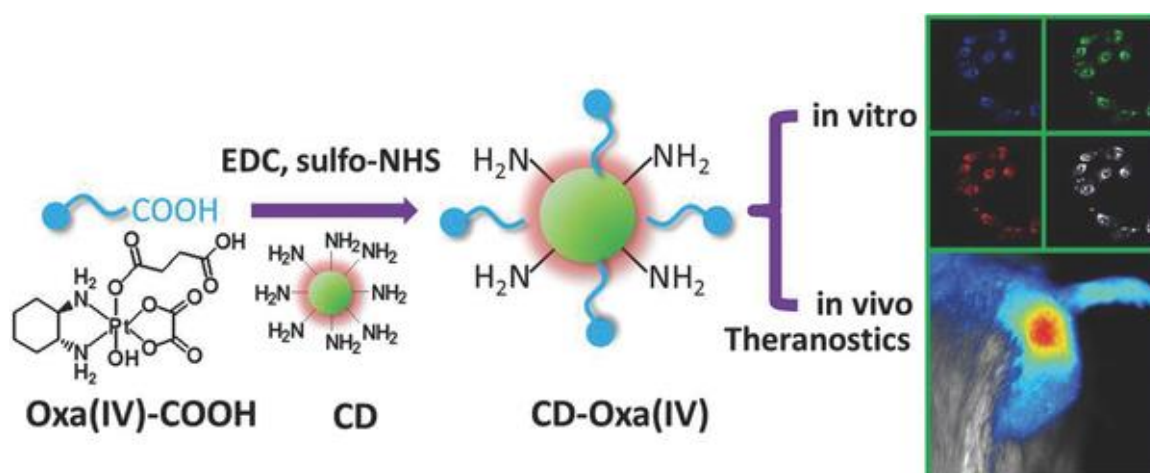


Figure 15. Synthetic scheme for CDs-Oxa (CD-Oxa) and its applications in bioimaging and theragnostic.⁹³

This approach was also employed for the control release of an ACE enzymes inhibitors such as the Lisinopril as highlighted by Vaibhavkumar *et al.* in a recent study.⁹⁴ The authors synthesized CDs from

milk and then after the purification with dialysis, they modified the surface by attaching the Lisinopril molecule. UV and FT-IR spectroscopic investigation confirmed the successful derivation of the nanoparticles. The as synthesized CDs were easily internalized into the cells and accumulated in the acidic endosomal/lysosomal compartments and could efficiently target HeLa cells. These results pointed out that Lis-loaded CDs could be used to develop novel targeted therapeutic modalities for either anticancer or antihypertensive drug delivery system.

A lot of attention was focused on developing DDSs employing the Doxorubicin (DOX) as drug due to its fluorescent behaviors that allows an easily detection and quantification. It has been demonstrated that many different CDs could be used for loading this drug, and, depending on the structure of the nanomaterials, various interactions could arise between the two-species guaranteeing a high loading capability.⁹⁵ One example was reported by Kim *et al.*, employing zwitterionic carbon dots for obtaining an efficient drug delivery system that attack the cell nucleus.⁹⁶ In more details the authors produce CDs starting from citric acid and β -alanine under microwave procedure (**Figure 16**). The obtained nanoparticles have a high QY (21%) and a lifetime of 4.3 ns. Furthermore, they exhibit an almost neutral ζ -potential, due to the zwitterionic nature of the β -alanine. The authors then demonstrate by Bio-TEM analysis that this type of CDs can be successfully internalized in the nuclei of HeLa cell after 24 hours of incubation. They proposed that the positive charge on the surface can interact with the negatively charged cell membranes to enter the cytoplasm and then the negative surface groups caused the expulsion from the endoplasm towards the nuclei that have a pH slightly above that of the cytosol. Finally, the DOX was loaded on the nanoparticles by exploiting the π - π staking interactions between the sp^2 -carbon network of CDs and the aromatic structure of DOX, with a loading of 14 %_w DOX in the CDs. The DOX-CDs conjugates considerably improve therapeutic efficacy by 9.7-fold in cancer cells by 4.2-fold enhanced nuclear transport of DOX and inhibit tumor growth by prolonging the accumulation of DOX/CDs in tumor tissues, as compared to free DOX.

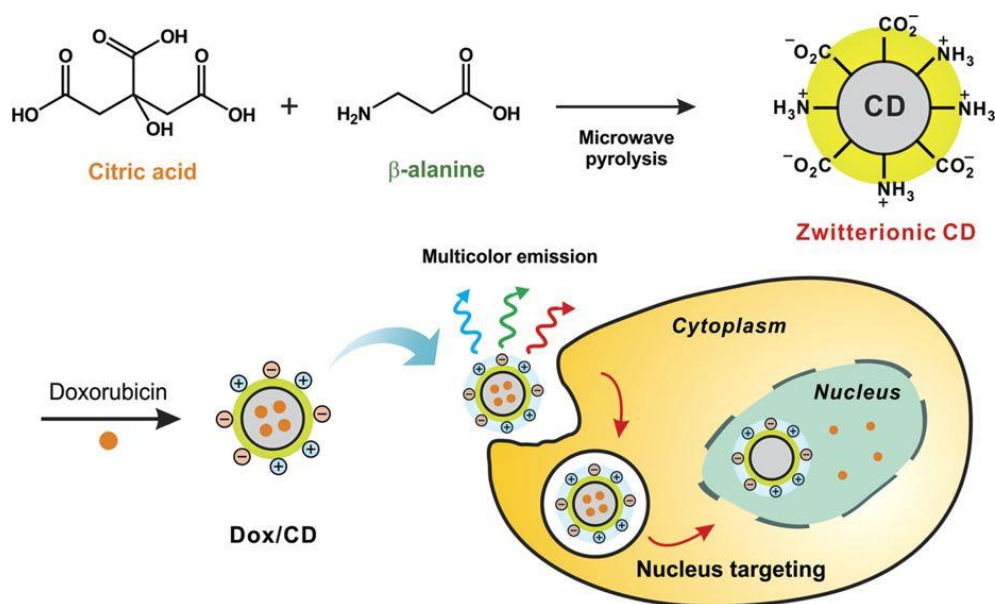


Figure 16. Schematic illustration of the synthesis of zwitterionic carbon dots and the fabrication of doxorubicin (DOX)-loaded CD (DOX-CDs) and simultaneous cell imaging and efficient DOX delivery.⁹⁶

The electrostatic interaction between the CDs and the drug was exploited to obtain high loading capability by Tan *et al.* by synthesizing CDs.⁹⁷ Through a solvothermal approach dissolving citric acid and o-phenylenediamine in dimethylformamide (DMF) and heating the mixture in an autoclave at 200 °C for 5 hours. After evaporation of the solvent and purification CDs were obtained in an amorphous structure and with a high QY (>40%). The negative surface charge of the nanoparticles was then exploited to attach the positively charged DOX and a loading capacity of 15 % was achieved. Interestingly the conjugation of the CDs and DOX results in an almost total quenching of the fluorescence of the system. The authors took advantage from this effect to measure the drug release inside the cells, since in the initial stage of the incubation no fluorescence is observed but after 8 hours a bright luminescence of both CDs and DOX was displayed. This turn “on” effect is due to the released of the DOX from the surface of the nanoparticles and allow to understand where the CDs and the DOX are located. In this specific case the DOX was successfully release inside the HeLa cell to induce the apoptosis. For all these reasons this DDS holds great promise for personal drug delivery with maximal pharmaceutical effects and minimal side effects during cancer therapy.

As all these studies, and more others, demonstrate that CDs are an effective tool in the biomedical fields, and exploiting their unique properties such as the biocompatibility, fluorescence and water solubility.

1.5.2. Photocatalysis

Due to their great light harvesting properties, the CDs could be exploited in photocatalytic applications. Sun *et al.* first proposed that photoexcited CQDs can be quenched efficiently by either electron acceptors or electron donors, and so it could be concluded that the CQDs are both excellent electron donors and electron acceptors.⁹⁸ Despite this consideration, only in the last few years this field was explored, and the first photocatalytic applications of CDs were reported. Most of the applications regard the use of the CDs as photosensitizer in combination with another species that could be a metal, enzymes or also organic dyes. One of the first application in this topic was reported again by Sun *et al.* which produced CDs from a carbon powder employing an acid oxidation methodology.³⁹ The as synthesized nanoparticles were then derivatized with oligomeric poly(ethylene glycol) diamine (PEG1500N) and then were coated with gold or platinum by simple solution-phase photolysis. The authors then tested this nanocomposite in the photoreduction of the CO₂ under solar light irradiation reporting the formation of formic acid along with other products. The same nanocomposite material demonstrates also to successfully generate H₂ under the same conditions. The photocatalytic H₂ evolution catalyzed by CDs were also studied by Yu *et al.* which prepared a CQDs/P25 composite with efficient activity *via* a facile one-step hydrothermal approach.⁹⁹ The CDs were produced by an electrochemical method starting from graphite rod. The nanomaterial was then treated with TiO₂ (P25) in autoclave at 140°C for 4 hours achieving the formation of the nanomaterial with a UV-Vis absorption. This material was used in the production of H₂ from methanol aqueous solution at room temperature under UV-Vis and visible light ($\lambda > 450$ nm) irradiation. Under UV-Vis light irradiation, the nanocomposite triggered the H₂ evolution with an optimized rate of 9.1 mmol h⁻¹ that is 4 times higher than that of pure P25. Furthermore, CQDs/P25 also exhibited efficient visible-light-driven photocatalytic H₂. The authors hypothesized that the system act as a photosensitizer, like organic dyes, in which the photoinduced electrons are transferred from the excited CQDs to P25 *via* electronic coupling between the LUMO orbitals of CQDs and the conduction band states of TiO₂, and then react with protons for H₂ production as represented in **Figure 17**.

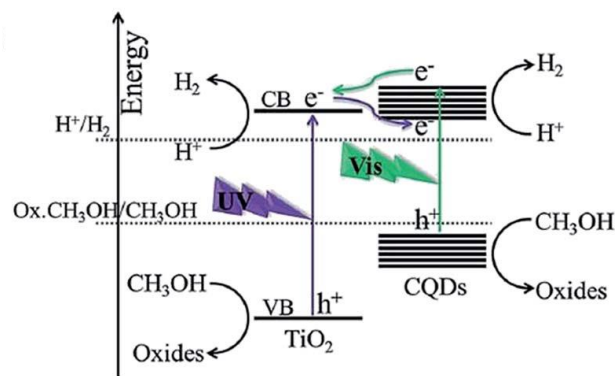


Figure 17. Hypothetical mechanism of electron transfer and photocatalytic H₂ production.⁹⁹

In the years many other metals were employed in order to achieve better results. Some examples regards the use of Cu₂O for the degradation of methyl blue under near-IR light irradiation¹⁰⁰ and also the photodegradation of benzene employing CQDs/Fe₂O₃¹⁰¹ or CQDs/ZnO¹⁰² composites and also many other applications.¹⁰³ Similar materials were also employed in performing organic reactions. An example is the oxidation of cyclohexane to cyclohexanone with Au-CDs composite together with H₂O₂ as oxidant and without any solvents under visible light irradiation at room temperature.¹⁰⁴ The authors were able to perform the reaction with a total selectivity towards the desired products, and they also demonstrated that the material could be recycled for more than 10 cycles without a loss in activity and selectivity. The use of metals in combination with CDs is an essential feature to perform this kind of reactions, as already stated the metal could be deposit on the surface of the CDs or, on the contrary, the CDs could be attached to a bigger particle of metals. A further improvement of this system based on the use of sole CDs, was implemented by Reisner's group which employed as co-catalyst along with CDs a Ni-organic complex for achieving high hydrogen production.⁵⁹ Employing the same methodologies but using a nitrogen doped CDs they were able to achieve even better results due to the higher light harvesting capabilities of the new nanomaterial.⁶⁰ Surprisingly only few works report the use of sole CDs as photosensitizer, one of these regards the oxidation of benzyl alcohol to the corresponding benzaldehyde.¹⁰⁵ The study employed CDs prepared from an alkali-assisted electrochemical method from graphite rods. The reactions with the benzyl alcohol were conduct on the grams scale employing H₂O₂ as oxidant and under NIR light irradiation. The reactions were accomplished with high conversion and an almost total selectivity. The authors speculate that the H₂O₂ molecules adsorbed on CDs could be decomposed into hydroxyl radicals which have strong oxidation ability and could oxidize benzyl alcohol to benzaldehyde or benzoic acid (**Figure 18**). Furthermore, they hypothesized that π - π interaction could exists between CDs and benzyl alcohol or

benzaldehyde, facilitating the electron transfer and also protecting the aldehyde from further oxidation.

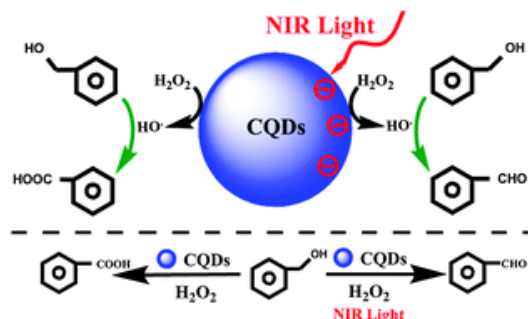


Figure 18. Schematic representation of the oxidation mechanism of benzyl alcohol to benzaldehyde triggered by CDs.¹⁰⁵

Few more examples could be found on this topic and are mainly related to the photodegradation of organic dyes like methyl orange¹⁰⁶ or to water-splitting reaction¹⁰⁷. Since to date, no example of sole CDs as photosensitizer in organic reactions are reported, leaving space for innovations and applications in this field. Furthermore, a clear and complete understanding on the properties and characteristics fundamental for achieving an efficient process is yet to be fulfilled, due to the high complexity of the CDs.

1.6. Aim and structure of the thesis

The aim of this thesis is to propose a new approach towards a rational design of CDs-based systems, tuning the synthetic procedure, the structure of the final material and its properties to achieve the desired results in medical and photocatalytic applications. In particular, it will be investigated how the choice of the initial precursors and the synthetic method employed could affect the morphology and the structure of the obtained nanomaterials. Furthermore, also the properties arising from the different structure such as fluorescence, surface charge, cytotoxicity, redox potential and many others were investigated. For this aim, a series of CDs were synthesized from low cost and commercially available precursors, such as monosaccharides and citric acid. The nanoparticles were synthesized employing two different approaches, the hydrothermal treatment, and a harsher one such as pyrolysis, to investigate the structural diversity arising from the different synthesis. Furthermore, the effect on the structural properties of the addition of a nitrogen doping compound was investigated by adding diethylenetriamine in the synthetic protocols. The nanoparticles were then

characterized and employed in two different fields, such as a drug delivery system and for photocatalytic applications. For the medical application, the nanoparticles obtained from monosaccharides are characterized and tested for the loading of a common anticancer drug. The major achievement of this study was the ability to properly tune the CDs morphologies to achieve biocompatible nanoparticles with efficient drug loading capabilities. Glucose derived CDs result to be the best one, demonstrating both a high biocompatibility and excellent drug loading capabilities, while the fructose derived CDs shows an unexpected high toxicity. In chapter 4 the CDs synthesized from citric acid by hydrothermal or pyrolytic treatments and with or without a doping agent were tested in the photoreduction of the methyl viologen. The study revealed that the photoreactivity of the nanoparticles depends on various parameters, in particular, an inversion in the reactivity trend was observed in the presence of the doping agent. For the non-doped CDs, the presence of a graphitic core is essential to achieve a high reactivity, while for the doped samples, the graphitic core acted as a quencher of the photoelectron transfer. One of the most interestingly results obtained by this study was the great reactivity of the amorphous doped CDs that had never been used before in this context. In the final chapter, taking advantage of the knowledge acquired on the photocatalytic performance of the CDs, the CDs catalyzed photodeprotection of the N-Methyl picolinium esters was investigated. The study demonstrates for the first time that CDs can successfully be used as the only sensitizer, without any addition of oxidant or metal complex, to perform an organic reaction. In particular, the deprotections were accomplished with a total selectivity towards the desired products and can also be done without the sacrificial donor. Furthermore, the photocatalytic performance of the different CDs and the reactivity trend of the substrates were explained by their redox potential, calculate by cyclovoltammetric measurements.

2. Synthesis of CDs

2.1. Monosaccharides and Ascorbic acid derived CDs

A first set of CDs was prepared by using fructose, glucose and ascorbic acid as carbon precursors, either by via a “single source” synthesis and or by combining a nitrogen doping agent such as diethylenetriamine (DETA). To achieve the formation of different types of CDs, two synthetic pathways were tested, a soft hydrothermal treatment (HTT) and a harsher pyrolytic (PYR) one. The nanoparticles obtained were characterized by ^1H -, ^{13}C -NMR, and DOSY-NMR techniques to monitor the progress of the reaction.

2.1.1. Hydrothermal syntheses

The hydrothermal syntheses of CDs from fructose, glucose and ascorbic acid were carried out in an autoclave using milliQ water as solvent. The precursor was first dissolved in 20 mL of milliQ water to form a clear solution. Next, the solution was transferred into a glass reactor and placed inside a stainless-steel autoclave. The latter was then heated at 200 °C with an aluminum heater for 24 h and then allowed to cool to room temperature. The solution inside the reactor turned from clear colorless to dark yellow, indicative of the formation of the carbon nanoparticles. The mixture was then filtered through a 0.22 µm filter, water was removed by rotary evaporation, and then freeze dried to recover the CDs as a dark brown–black powder. Glucose CDs (**G-CDs**), fructose CDs (**F-CDs**) and ascorbic acid CDs (**A-CDs**) were obtained in 34, 29 and 56 %_wt yield respectively. The reaction products were investigated by NMR and the nanoparticles were characterized by DOSY-NMR to determine size. With these techniques it is not possible to investigate directly the CDs because only the species present in solution could be analyzed. Nevertheless, this technique allows to acquire information about the formation of small organic molecules, polymeric cluster and other species from the carbonization reaction of the precursors.

The **G-CDs**, **F-CDs** and **A-CDs** were characterized chemically by NMR spectroscopy. In a first instance the ¹H-NMR and ¹³C{¹H} NMR of the three samples were recorded and compared to the spectrum of the original precursors (Figure 19). For all the three samples, furthermore, the signals of the initial precursors completely disappeared as shown in Figure 19 and Figure 20. The ¹H-NMR spectrum of the **G-CDs** and **A-CDs** reveals the presence of different groups of signals in the region from 2 to 4 ppm. The **F-CDs**, show the same set of signals of the other CDs also along with signals at higher ppm, tentatively assigned to the presence of small organic molecules or polymeric clusters formed during the synthesis of the nanoparticles.

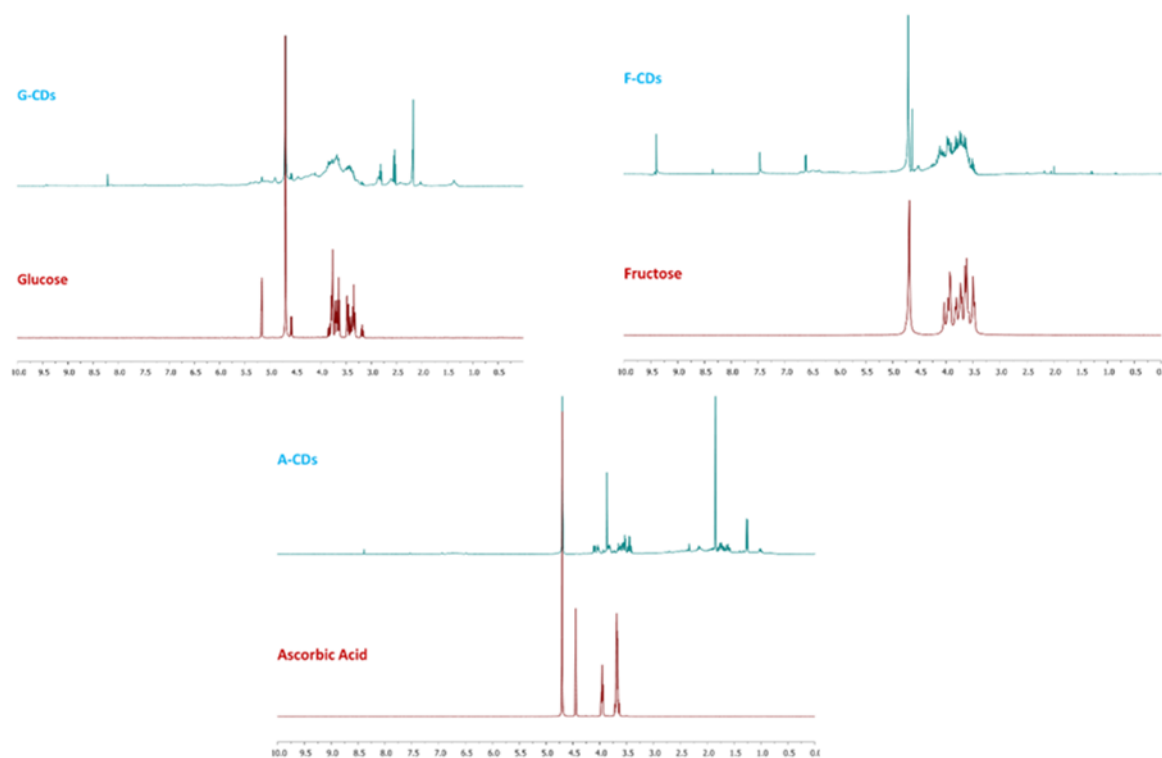


Figure 19. ^1H NMR spectra of **G-CDs**, **F-CDs** and **A-CDs** and their respective precursors in D_2O at $\text{pD}=7$.

The $^{13}\text{C}\{^1\text{H}\}$ NMR spectra of the CDs revealed differences: **G-CDs** show low intensity signals at low ppm. **F-CDs** and **A-CDs** revealed the presence of various signals at high ppm suggesting the presence of carbonyl/carboxylic carbon atoms that could be present on the surface of the nanoparticles or due to small organic molecules formed during the reaction.

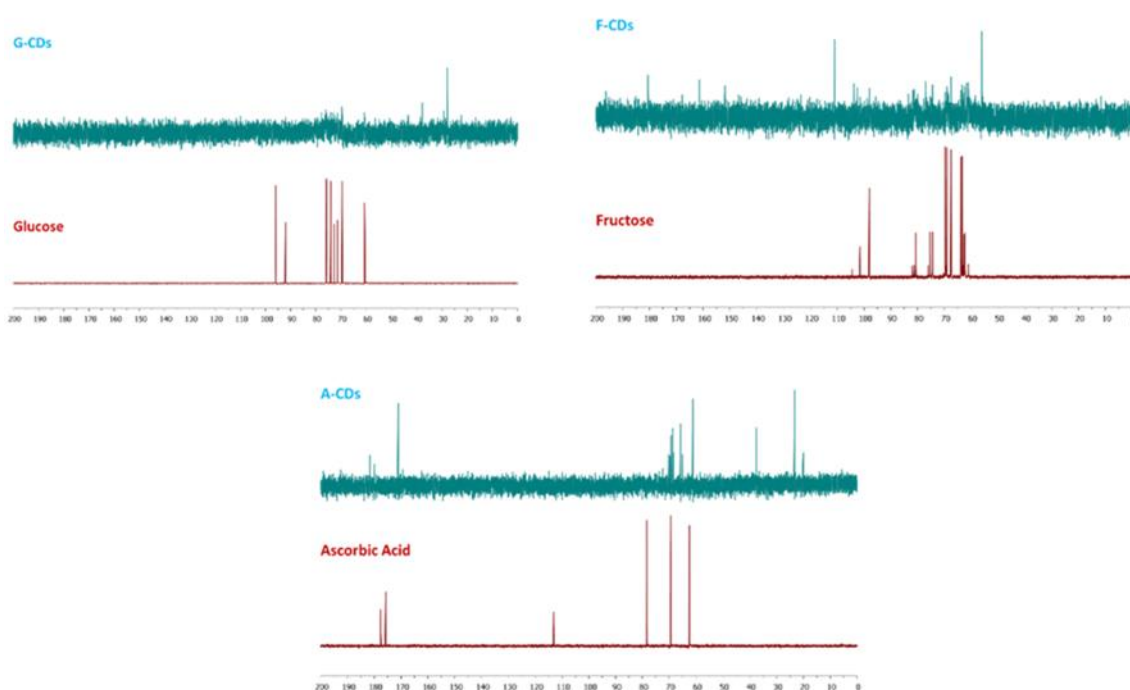
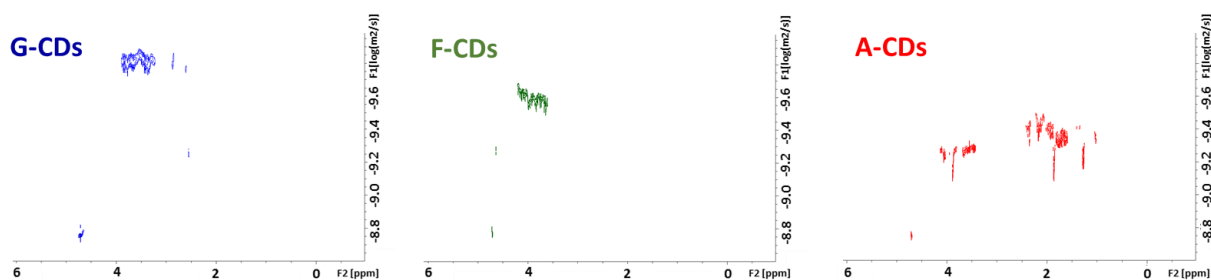


Figure 20. $^{13}\text{C}\{^1\text{H}\}$ NMR spectra of **G-CDs**, **F-CDs** and **A-CDs** and their respective precursors in D_2O at $\text{pD}=7$

Notwithstanding extensive NMR characterization, many signals remain unassigned. In order to understand whether they were correlated to the presence of other molecules in solution or to larger species, DOSY-NMR spectroscopy was used. This technique allows to measure the diffusion coefficients (δ) of the NMR-active species and it provides a weighted average of the mass of the ^1H -NMR active species, and thus it provides an indication on size. While it is usually employed to study well-defined molecular-like compounds,^{108,109,110} in the present case instead, the samples contain highly complex systems, therefore, the data obtained from such "non-ideal" samples must be considered indicative and used for an educated guess of the average molecular weight of the CDs. The three samples exhibit different behavior, specifically: the **G-CDs** have the lowest diffusion coefficient *i.e.* higher MW, the **F-CDs** demonstrate an intermediate value of δ , while the highest one was revealed for the **A-CDs** as shown in Figure 21.

**Figure 21.** DOSY-NMR of **G-CDs**, **F-CDs** and **A-CDs** in D_2O at $\text{pD}=7$.

By applying the Stoke-Einstein equation and the Graham's law as explained in the experimental section and by using the initial precursors as internal references, it was possible to determine the ratios between volume, mass and radius of the synthesized CDs, as summarized in Table 1. The **G-CDs** appear to be 60 times larger and 15 times heavier respect to the precursor glucose. **F-CDs** appear 25 times larger and 9 times heavier respect to the precursor fructose, in agreement with the presence of carbon nanoparticles in solution. Finally **A-CDs** showed smaller sizes indicative of a lower degree of carbonization. Furthermore, by using the precursors as references, an average MW of the compounds was estimated, and the results are reported in Table 1.

Table 1. Diffusion coefficient (δ), average volume ($\bar{\epsilon}$), mass ratios (\bar{M}), and estimated molecular mass (\overline{MW}) of the CDs

Entry	Sample	δ (*10 ¹⁰) (m ² /s)	$\bar{\epsilon}$	\bar{M}	\overline{MW} (Da)
1	G-CDs	1.51	55.7	14.6	2600±120
2	Glucose	5.37			
3	F-CDs	2.74	22.0	7.8	1400±160
4	Fructose	5.50			
5	A-CDs	5.37	13.4	5.6	990±70
6	Ascorbic Acid	5.62			

2.1.2. Pyrolytic synthesis

Four new CDs were synthesized starting from glucose and fructose by employing a harsher pyrolytic method aimed at obtaining more graphitic nanoparticles as well as to introduce a nitrogen doping atom. Pyrolysis involves thermal treatment of the neat precursors in air and in the absence of solvent. In detail, 20 g of glucose/fructose were heated at 200 °C in a conical flask: the solid slowly turned into a viscous material that changed from white to orange and finally black. Next, the mixture was neutralized with NaOH 5M in order to make the CDs water-soluble. **g-Glu-CDs** and **g-Fru-CDs** were obtained in 65 and 48 %_{wt} yield after removal of water by evaporation and freeze-drying. A similar procedure was adopted for the synthesis of nitrogen doped CDs. In this case, the precursors (glucose and fructose) were pyrolyzed in combination with diethylenetriamine (DETA) as doping agent. The **g-N-Glu-CDs** and **g-N-Fru-CDs** were recovered in 53 and 42%_{wt} yields with the same procedure described for the non-doped ones. Extensive characterization of their structure and chemical properties was carried out.

The evolution of all the four reactions was monitored by ¹HNMR and ¹³CNMR spectroscopy. For the non-doped CDs, after 48 hours of heating the signals attributed to the precursor almost disappeared. For the glucose-derived materials new signals appeared in the proton spectra in the region 1 - 3 ppm tentatively ascribed to protons of chemical groups on the surface of the carbon nanoparticles, along

with a singlet at 8.5 ppm. For the fructose derivatives a similar pattern revealed, with the same signal at 8.5 ppm and a group of three signals in the region 1 - 3 ppm.

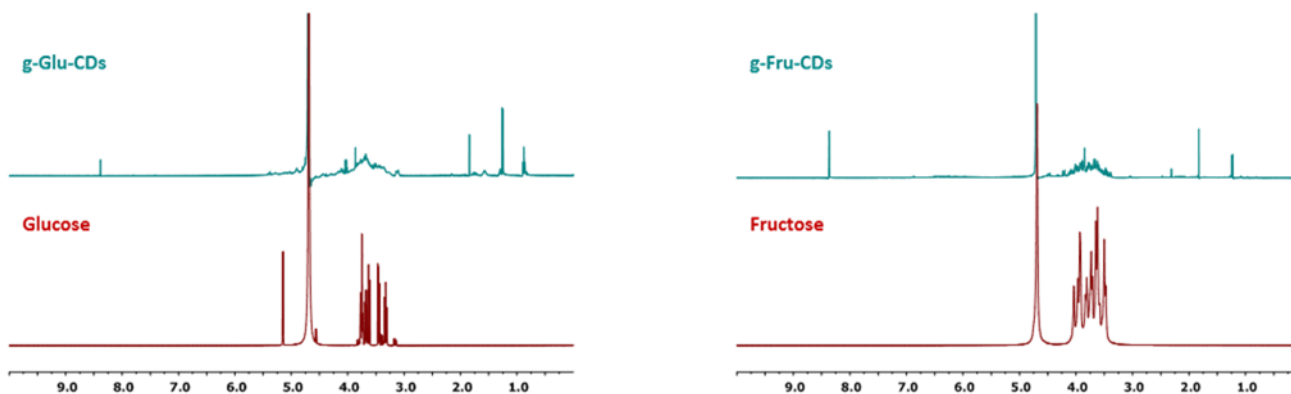


Figure 22. ^1H -NMR spectra of **g-Glu-CDs** and **g-Fru-CDs** and their precursors in D_2O at $\text{pD} = 7$.

The ^{13}C -NMR spectra of both samples showed hardly any resonances, implying a low concentration of organic molecules in the solutions (Figure 23). For the **g-Glu-CDs** only a signal at 70 ppm and two signals lower around 20 ppm were detected while for the fructose derivative only a signal a 170 ppm was noticed.

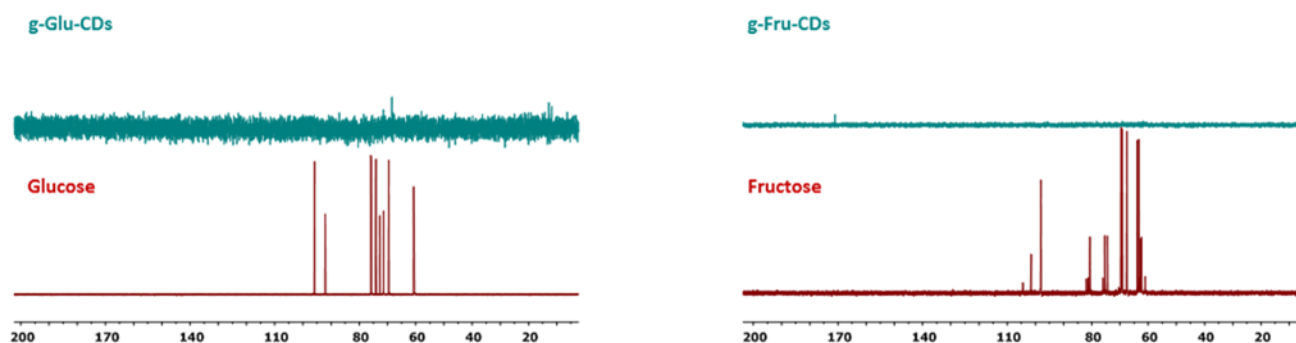


Figure 23. $^{13}\text{C}\{^1\text{H}\}$ NMR spectra of **g-CDs** and **g-Fru-CDs** and their precursors in D_2O at $\text{pD} = 7$.

DOSY-NMR was used to assess an approximate size, i.e. a hypothetical molecular weight of the CDs, and also to evaluate if species of different sizes were present in the mixture. The analyses revealed that the two samples showed different δ ($10^{-9.82}$ and $10^{-9.56} \text{ m}^2\text{s}^{-1}$, respectively), suggestive of nanoparticles with different sizes and MWs (Figure 24).

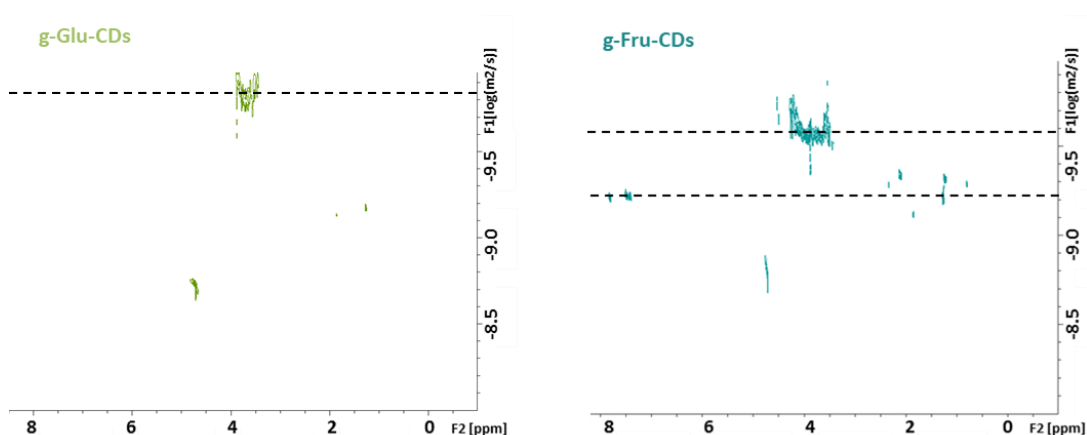


Figure 24. DOSY-NMR of **g-Glu-CDs** and **g-Fru-CDs** in D₂O at pD= 7

Using the DOSY signal of the starting material as internal reference for size and normalizing the δ values with that of the solvent, the average volume (V), mass ratio (M_{rel}) and a hypothetical MW were calculated, and the results are showed in Table 2. The **g-Glu-CDs** samples showed species with the highest MW (ca. 3000 Da) and a volume 70 times larger than glucose, indicative of the formation of large carbogenic structures. For **g-Fru-CDs** instead, the values were lower, suggesting a less extended graphitic structure. Furthermore, in this sample, a second series of signals was identified, and its δ value led to an estimated MW of 130 Da, confirming the presence of small organic molecules in the mixture.

Table 2. Diffusion coefficients (δ) and calculated average volume (V), mass ratio (M_{rel}) and MW for **g-Glu-CDs** and **g-Fru-CDs**.

Entry	Compounds	δ ($m^2 \cdot s^{-1}$) $\times 10^{10}$	V_{rel}	M_{rel}	Estimated MW (Da)
1	g-Glu-CDs	1.51	70	17	3000
2	Glucose	5.37			
3	g-Fru-CDs	2.74	7.5	3.8	690
4	Fructose	5.50			

The **g-N-Glu-CDs** and **g-N-Fru-CDs** were analyzed by NMR spectroscopy as well, and the resulting spectra were compared with those of the corresponding carbon precursor and of DETA. The ¹H-NMR spectra after the 48 hours of thermal treatment revealed **Figure 25** complete conversion of the starting materials and the formation of new signals similar to the ones obtained for the non-doped

CDs. In more detail, a signal at ~ 8.5 ppm was detected in both the spectra, and new proton signals were detected in the region 1 – 4 ppm. All these signals were attributed to protons of surface chemical groups of the carbon nanoparticles.

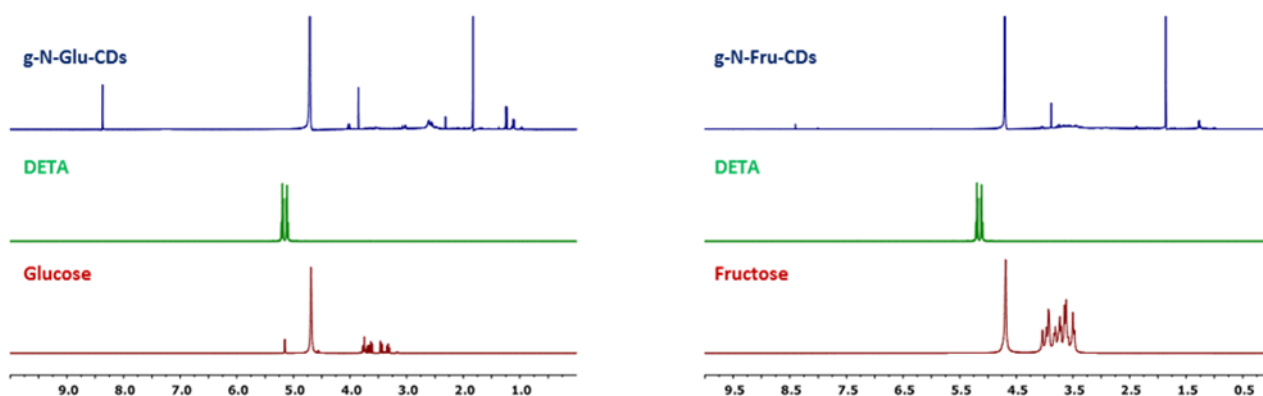


Figure 25. ^1H NMR spectra of **g-N-Glu-CDs** and **g-N-Fru-CDs** and their precursors in D_2O at pD = 7.

The $^{13}\text{C}\{^1\text{H}\}$ NMR spectra (Figure 26) of **g-N-Glu-CDs** and **g-N-Fru-CDs** exhibited showed hardly any resonances implying the presence of few organic molecules in solution and more carbonaceous materials that are NMR-inactive due to their colloidal nature.

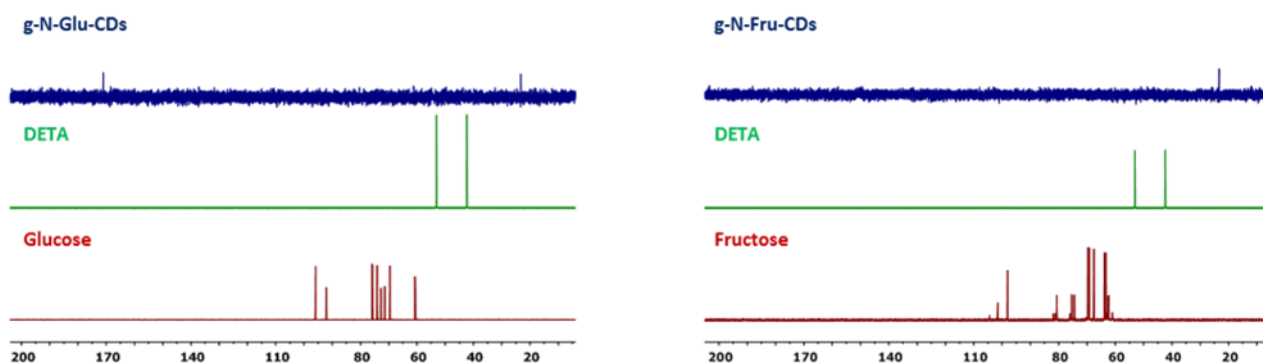


Figure 26. $^{13}\text{C}\{^1\text{H}\}$ NMR spectra of **g-N-Glu-CDs** and **g-N-Fru-CDs** and their precursors in D_2O at pD = 7.

More information on the **g-N-G-CDs** and **g-N-F-CDs** nanoparticles was gained by performing DOSY-NMR experiments. The diffusion coefficients of the nanoparticles were compared to the one of the molecular precursors in order to estimate an average MW. The DOSY-NMR experiments revealed different diffusion coefficients for the **g-N-G-CDs** and **g-N-F-CDs** ($\delta = 10^{-9.60}$ and $10^{-9.52} \text{ m}^2\text{s}^{-1}$, respectively), in particular, the fructose derived sample showed a lower diffusion coefficient as reported in Figure 27.

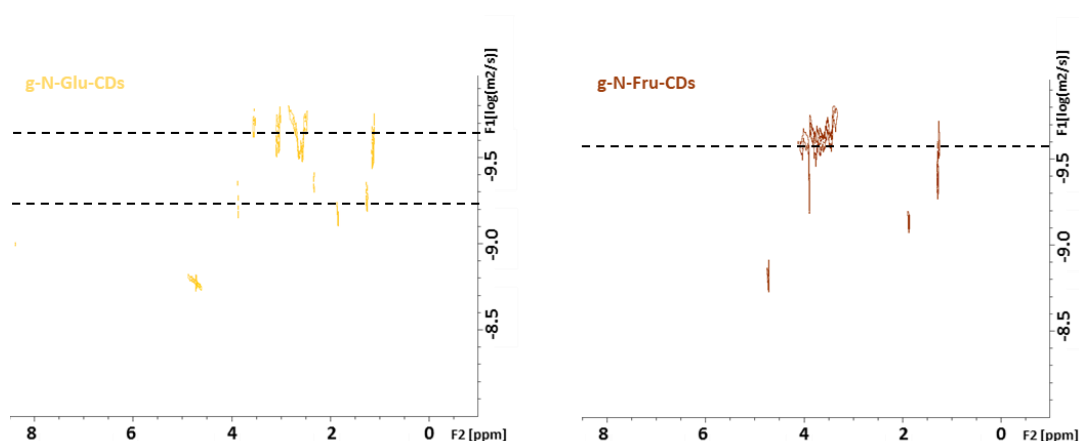


Figure 27. DOSY-NMR of **g-N-Glu-CDs** and **g-N-Fru-CDs** in D₂O at pD= 7

The calculation led to an estimated MW for the **g-Fru-CDs** of 830 Da, while lighter compounds with a MW of 580 Da were detected for **g-Glu-CDs** (Table 3).

Table 3. Diffusion coefficients and calculated parameter for **g-N-Glu-CDs** and **g-N-Fru-CDs**.

Entry	Compounds	δ (m ² *s ⁻¹) x 10 ¹⁰	V _{rel}	M _{rel}	Estimated MW (Da)
1	g-N-Glu-CDs	3.00	5.7	3.2	580
2	Glucose	5.37			
3	g-N-Fru-CDs	2.50	10	4.6	830
4	Fructose	5.50			

2.2. Citric Acid derived CDs

Another group of CDs was synthesized employing a different carbon precursor, citric acid (CA). Citric acid is a common substrate for the synthesis of CDs and is widely used in combination with other reagents and doping agents.^{82,83,84,85,86, 91, 111,112,113,114,115}. In the present case, four CDs were obtained using two sets of reagents: sole citric acid or citric acid in combination with DETA, and by two different synthetic pathways: HTT (**a-CDs** and **a-N-CDs**) and PYR (**g-CDs** and **g-N-CDs**).

2.2.1. Non-doped CDs

The **a-CDs** and the **g-CDs** were obtained by using citric acid as sole carbon precursor by HTT and PYR, respectively. The reactions were monitored, and the products characterized by NMR.

For the amorphous-like **a-CDs**, 2 g of CA were dissolved in 20 mL of MilliQ water in a glass vessel to form a clear solution, that was then inserted in an autoclave and heated at 180 °C. The reaction time was optimized by monitoring CA conversion over time by ^1H NMR (Figure 28).

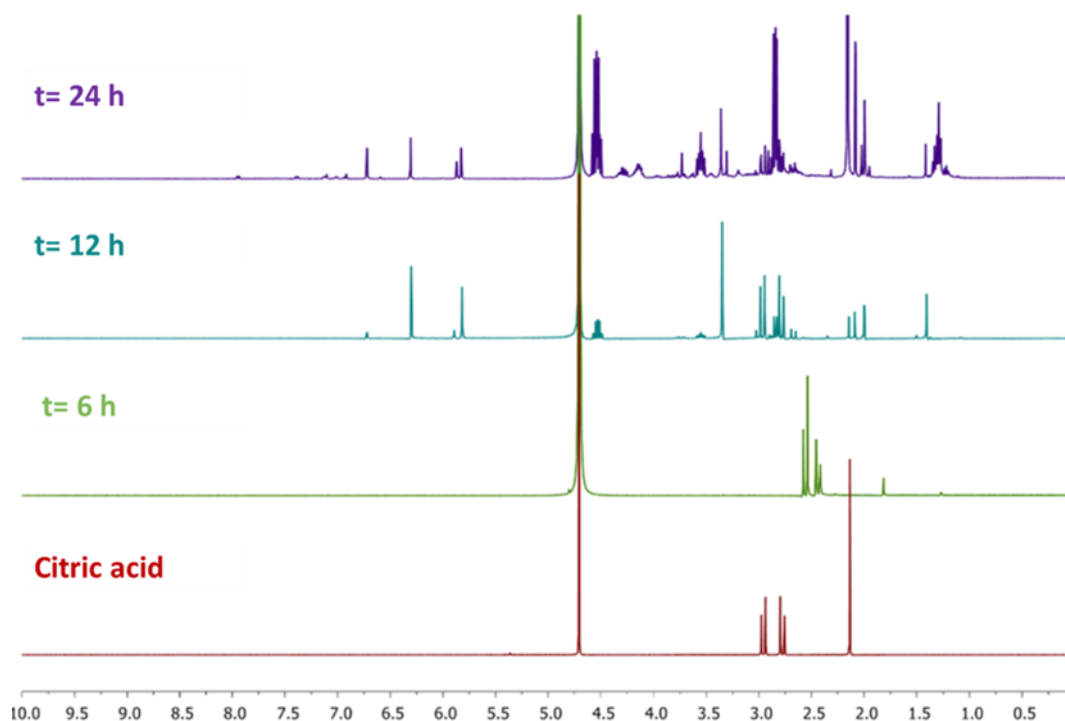


Figure 28. ^1H NMR spectra of the reaction at 6, 12 and 24 hours in D_2O at $\text{pD}=7$.

The crude products obtained at 6 and 12 hours still revealed the presence of the reagent while full conversion was observed after 24 hours, thereafter chosen as the optimal time for **a-CDs** synthesis. The crude mixture was neutralized to pH 7 with aqueous NaOH and evaporated to dryness leading to a dark yellow luminescent oil (0.4 g, 25 %_{wt} yield). The disappearance of CA was further confirmed by comparing the ^1H and $^{13}\text{C}\{^1\text{H}\}$ NMR of final **a-CDs** with the reagent at $\text{pD}=7$ (Figure 29). Dialysis of the mixture with a 1-kDa membrane to separate the large carbogenic structures from the lighter aggregates and volatile organic molecules, resulted unnecessary as the **a-CDs** freely permeated this membrane.

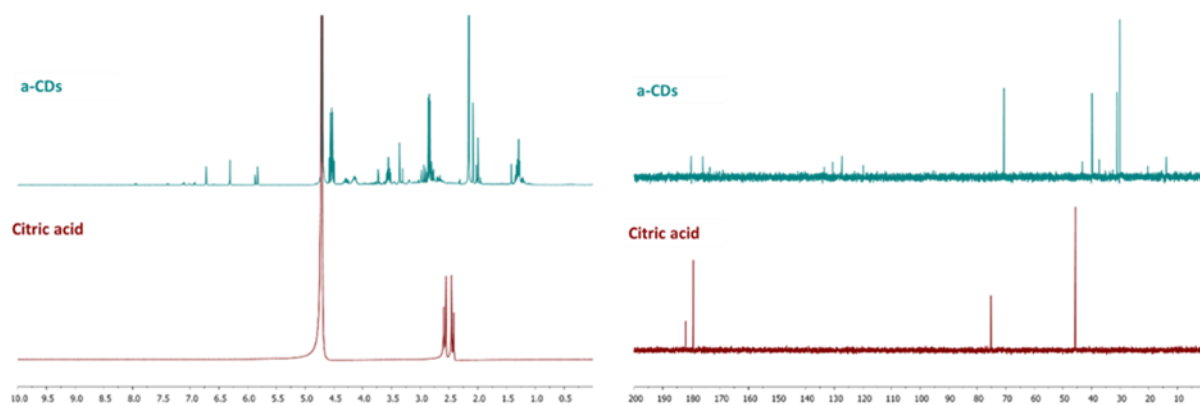


Figure 29. ^1H (left) and $^{13}\text{C}\{^1\text{H}\}$ NMR (right) spectra comparison of CA and a-CDs in D_2O at $\text{pD} = 7$.

The presence of light molecules and more extended structures was revealed by DOSY-NMR (Figure 30). Two groups of signals one at low diffusion coefficient ($10^{-9.52} \text{ m}^2\text{s}^{-1}$) and the other at higher δ ($10^{-9.18} \text{ m}^2\text{s}^{-1}$) allowed to calculate an approximate value of MW. The one with the higher diffusion coefficient resulted in a MW of 118 Da, compatible with small organic molecules, while a value of 710 Da was calculated for the other group of signals, highlighting the presence of oligomers and/or extend carbogenic structures.

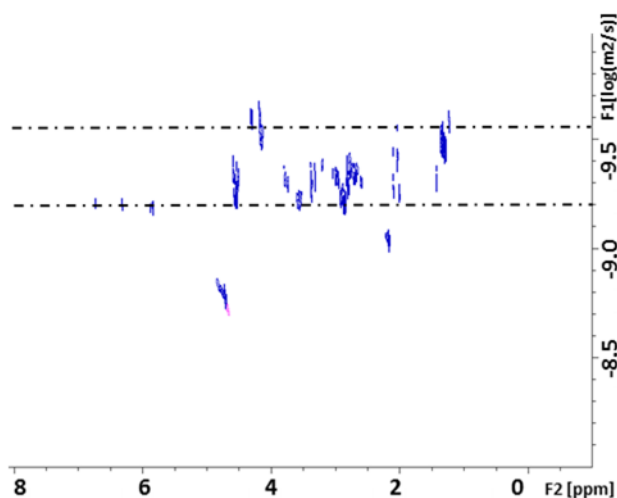


Figure 30. DOSY NMR of the a-CDs in D_2O at $\text{pD} = 7$.

For the PYR synthesis of the **g-CDs** a different approach was employed, the citric acid (100 g) was heated without solvent under air in a conical flask at 220°C for 48 hours. The white solid, as the reaction proceed, turned from a colorless liquid to yellow, brown, and finally a black viscous liquid. Sampling at time intervals and ^1H NMR analysis allowed to monitor the reaction and the formation of carbogenic structures. The evolution of the reaction is reported in Figure 31. After the first two hours almost all the signals of the precursors completely disappeared, and after 48 hours a silent

spectrum was obtained, a clear indication of the absence of small organic molecules and of the formation of extended carbogenic structures.

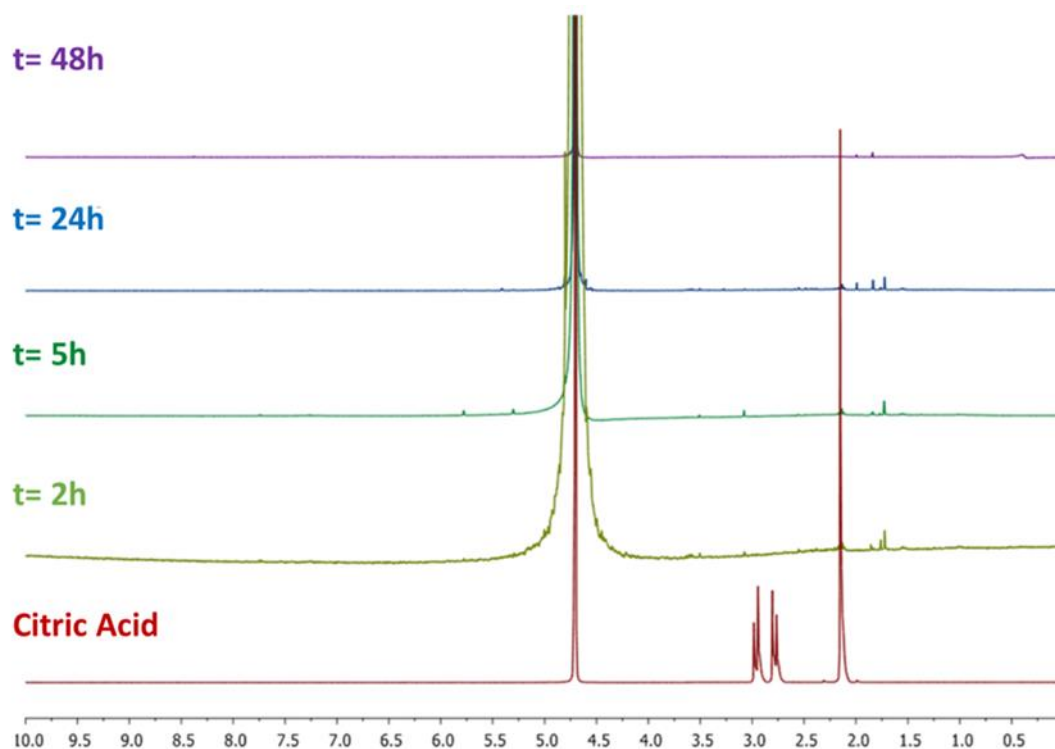


Figure 31. ^1H NMR spectra of the reaction of **g-CDs** at different time compared to the citric acid neutralized at $\text{pD}=7$ in D_2O

The final crude reaction mixture was neutralized with aqueous NaOH 5M in order to dissolve the black solid and then freeze dried in order to obtain the solid **g-CDs** in 40%_w yield. Dialysis with a 1-kDa membrane to purify the nanoparticles from the small molecules was carried out by suspending 600 mg of crude CDs in 10 mL of milliQ water for 24 hours and changing the external water every 12 hours. The pure **g-CDs** were obtained in 20%_w yield by evaporation of the water inside the membrane followed by freeze-drying. ^1H and $^{13}\text{C}\{^1\text{H}\}$ NMR spectroscopy of the **g-CDs** showed complete absence of resonances as seen in Figure 32.

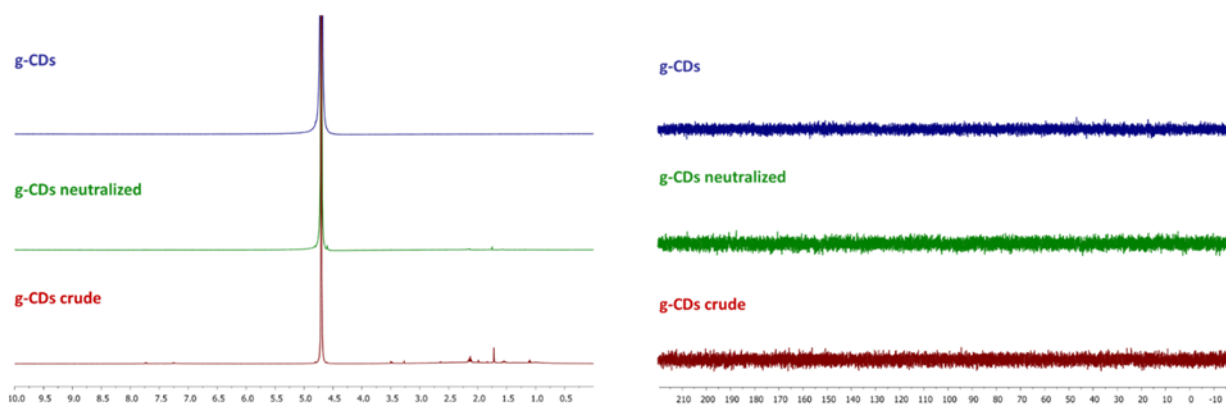


Figure 32. ^1H and $^{13}\text{C}\{^1\text{H}\}$ NMR of crude, neutralized, and purified g-CDs.

2.2.2. N-doped CDs

Applying the same HTT and PYR methodologies, two other different CDs were synthesized starting from CA and DETA as doping agent. For HTT, 2g of CA and 0.675 mL of DETA were dissolved in 20 mL of milliQ water to form a clear solution. The mixture was then transferred to a glass vessel and placed in a stainless-steel autoclave and heated at 180 °C for 6 hours. The solution was allowed to cool to room temperature, then the dark brown solution was analyzed by ^1H and $^{13}\text{C}\{^1\text{H}\}$ NMR revealing the complete conversion of the reagents and the appearance of new signals as reported in Figure 33. Dialysis of the mixture with a 1-kDa membrane to separate the large carbogenic structures from the lighter aggregates and volatile organic molecules, resulted unnecessary as the **a-N-CDs** freely permeated this membrane.

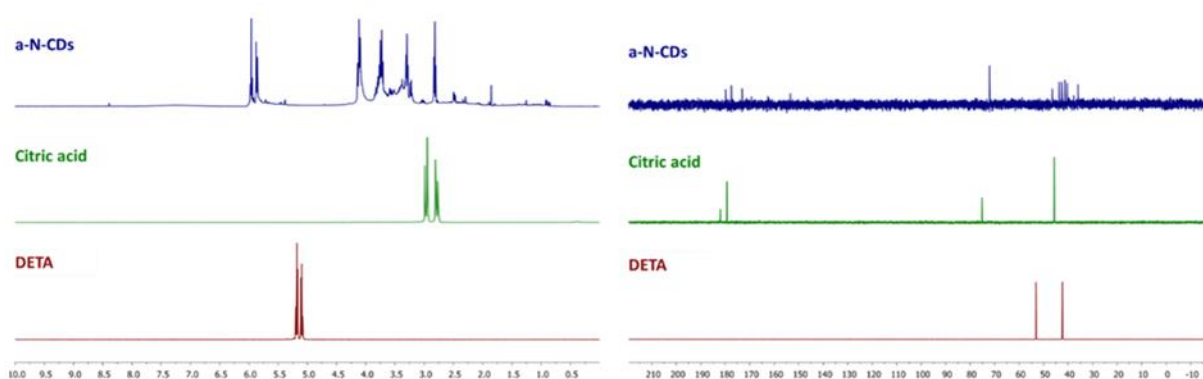


Figure 33. ^1H and $^{13}\text{C}\{^1\text{H}\}$ spectra of CA, DETA and crude products of the reaction in D_2O at $\text{pD}=7$

The presence of light molecules and more extended structures was revealed by DOSY-NMR. As shown in Figure 34 two different groups of peaks were identified in the 2D spectra, a lower line, corresponding to a δ of $0.25 \times 10^{10} \text{ (m}^2\text{s}^{-1}\text{)}$ and an upper one with a δ of $0.11 \times 10^{10} \text{ (m}^2\text{s}^{-1}\text{)}$. Applying Graham's law and the Stoke-Einstein equation, approximate MWs were calculated for both lines, a 40

value of 258 Da was obtained for the lower one, while the heavier compound results to have a MW of ca. 1200 Da.

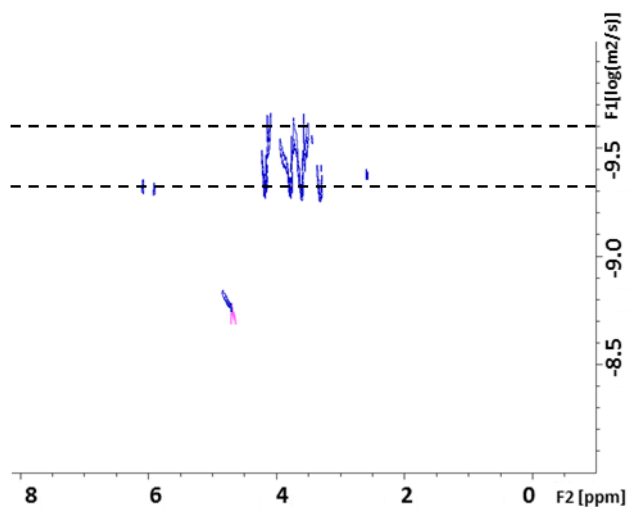


Figure 34. DOSY-NMR of **a-N-CDs** in D₂O at pH=7

The **g-N-CDs** were synthesized by PYR of CA and DETA in a conical flask equipped with a distillation setup: 100 g of CA and 25 mL of DETA were heated at 220 °C for 48 hours. The mixture turned from a colorless to a dark brown very viscous liquid. The reaction was monitored by ¹H NMR as shown in Figure 35: the signals of the reagents disappeared after 20 hours and new signal appeared in the region 2 - 4 ppm and around 6 ppm.

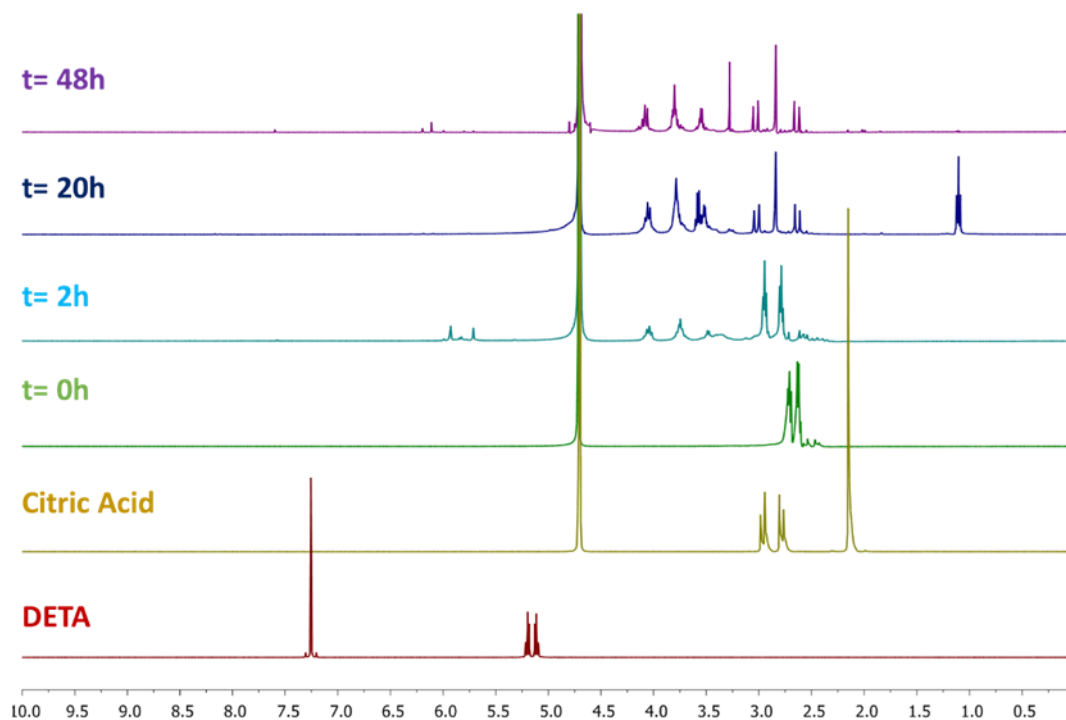


Figure 35. ^1H NMR spectra of CA, DETA and evolution of the reaction at different time in D_2O at $\text{pD}=7$.

The evolution of the reaction was monitored by DOSY NMR, revealing increasing MW of the compounds formed during the reaction, as indicated by the spot at lower δ (Figure 36).

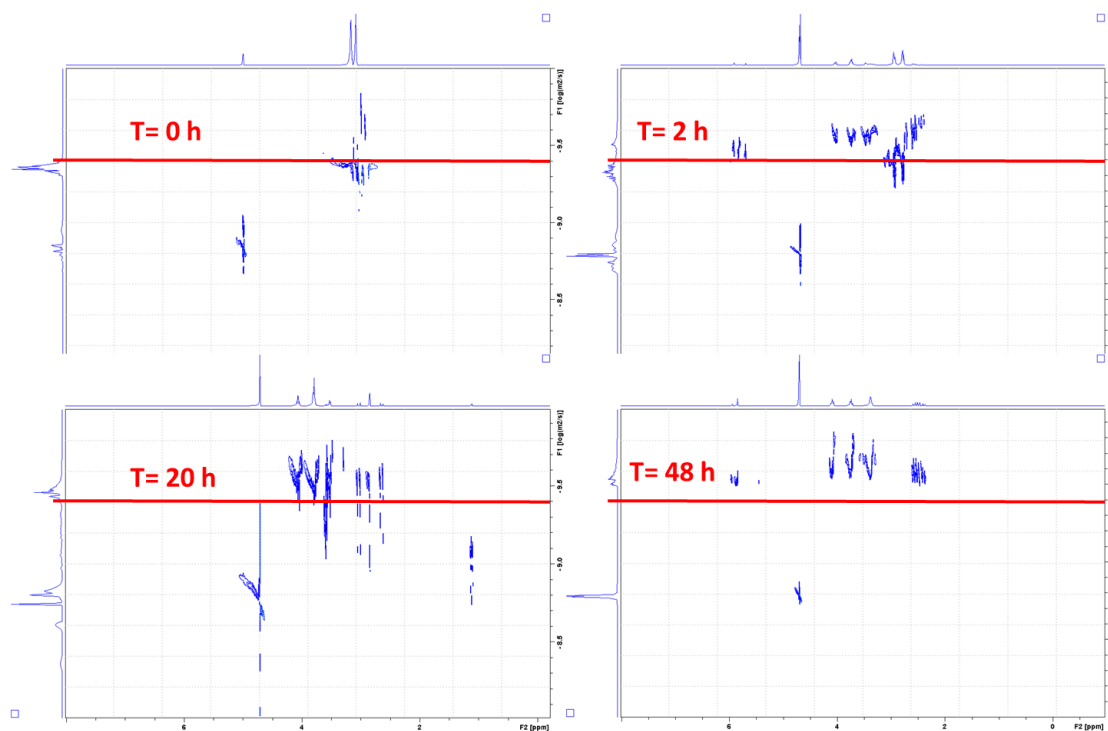


Figure 36. DOSY NMR evolution of the reaction in D_2O at $\text{pD}=7$

The crude mixture was then neutralized with NaOH 5M and then freeze-dried in order to obtain the crude **g-N-CDs** in 70%_{wt} yield. Dialysis with a 1k-Da MWCO membrane of 600 mg of CDs dissolved in 10 mL of milliQ water, followed by freeze-drying led to the recovery of pure **g-N-CDs** in 18%_{wt} yield. The sample was characterized by ¹H and ¹³C{¹H} NMR, as shown in Figure 37. The dialyzed materials afforded silent spectra confirming the successful separation of the small organic molecules from the carbonaceous nanoparticles.

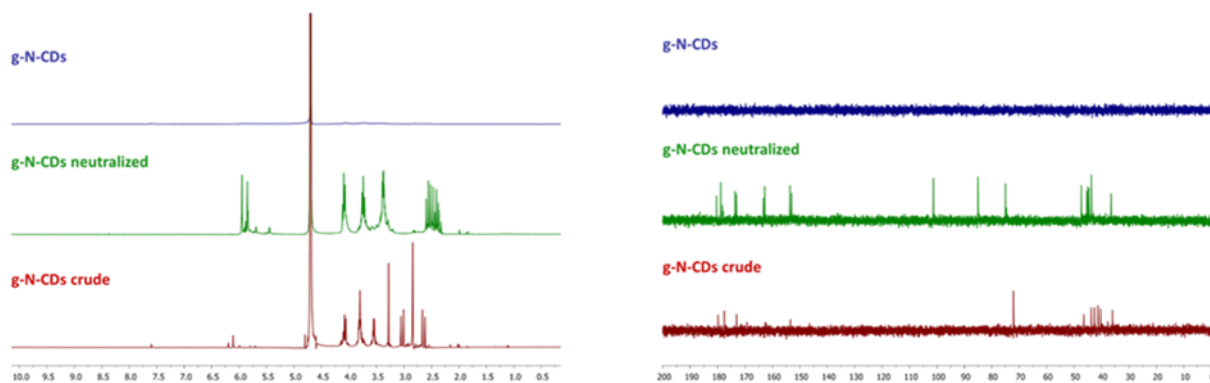


Figure 37. ¹H and ¹³C{¹H} NMR spectra of the crude, neutralized and purified g-N-CDs in D₂O at pH=7.

2.3. Experimental

2.3.1. Material and instrumentation

Fructose, glucose, ascorbic acid and diethylenetriamine were purchased from Sigma Aldrich and used as received. For the NMR study a Bruker Magnet System spectrometer 400'54 Ascend (¹H: 400 MHz; ¹³C: 100.6 MHz). The chemical shifts (δ) of the ¹H and ¹³C NMR spectra have been reported in parts per million (ppm).

2.3.2. DOSY-NMR

A DOSY NMR study was performed highlighting the presence of various signals in the ¹H NMR spectra of **a-CDs** and **a-N-CDs** related to the distinct compounds with different diffusion coefficients (Δ). By assuming ideal spherical structures for the CDs and by comparing with a known reference (the solvent), the Stokes-Einstein equation (1) allows to correlate the Diffusion coefficients of the compounds with their hydrodynamic radius.¹⁰⁸

$$1) \Delta = \frac{k_B * T}{6\pi\eta r_H}$$

Comparing the Δ values, normalized to the solvent, of the CDs and the one of a known reference (citric acid), it is possible to correlate the ratio of the diffusion coefficient to the ratio of the radius (R_{rel}) and consequently to calculate the relative volume ($V_{rel.}$) and mass ($M_{rel.}$)^{109,110}.

$$2) \frac{\Delta_c}{\Delta} = \frac{r}{r_p} \quad 3) \left(\frac{\Delta_c}{\Delta}\right)^3 = \left(\frac{V}{V_c}\right)$$

By applying the Graham's law (4), it is possible to correlate the diffusion coefficient to the mass of the analysed compound and their relative mass (M_{rel}) is given by 5

$$4) \Delta = k * \left(\frac{T}{m}\right)^{\frac{1}{2}} \quad 5) \left(\frac{\Delta_c}{\Delta}\right)^2 = \frac{m}{m_c}$$

Finally using the equation 6 it is possible to estimate their MW.^{116,117,118}:

$$6) m = m_c * \left(\frac{\Delta_c}{\Delta}\right)^2$$

Respect to the well-defined molecular compounds that are typically investigated with this technique, the present solutions are complex systems formed by a mixture of different carbogenic frameworks that are far from ideal and spherical. This fact and the fact that the diffusion coefficient measured by DOSY is a weighted average of all the contributions of the ¹H-NMR active species, prompts prudence in assigning the volumes, mass and MW of these CDs.

3. Results: Carbon dots for drug delivery

3.1. Introduction

The use of nanomaterials is currently one of the challenges in biomedical applications.¹¹⁹ The use of nanotechnology and in particular of fluorescent nanoparticles in this field introduce new approaches for fluorescence imaging and sensing as well as for in vitro and in vivo labeling in cells, tissues, and organisms.¹²⁰ The use of nanoparticles in the medical field offers new opportunities for detecting ions, protein and DNA and drug delivery applications. In the years several types of nanoparticles have been synthesized and used with this aim polymeric nanocomposites, magnetic nanomaterials¹²¹, semiconductor nanocrystals¹²² and noble metals nanomaterials (Au¹²³, Ag¹²⁴). In order to use these nanomaterials for medical applications, two main characteristics must be met: the first is biocompatibility, the second is the possibility of being functionalized for recognition of specific target

sites in the body after systemic administration. An additional unique characteristic that makes certain nanoparticles so attractive in these applications is photoluminescence. By exploiting these properties, many different applications can be envisaged such as the use of nanomaterials for bioimaging, or to create sensors for specific targets inside the body¹²⁵. However, the use of metal nanoparticles in medicine raises questions relating to their potential toxicity and issues over the lifecycle of inorganic nanoparticles¹²⁶. In order to avoid the use of metals in medicine, carbon-based nanoparticle have been proposed as an alternative.

Carbon dots in particular have elicited a lot of interest in the biomedical field since their discovery, due to their biological and chemical properties.^{51,127} Specifically, their high solubility in water, good cell permeability, low photobleaching, the absence of metals and their low toxicity make CDs very appealing substrates in this field. CDs were already proposed as nano-theragnostic agents for combined cancer therapy and diagnostics⁶⁵. One of the most promising applications is the use of CDs in bioimaging¹²⁸ to monitor drug release inside the cell. The first examples of CDs in bioimaging were described by Sun *et al.* who produced a series of CDs by laser ablation of graphite powder followed by surface passivation with different organic compounds like poly(propionylethyleneimine-co-ethyleneimine) and PEG₁₅₀₀. They were able to achieve nanoparticles with different color emissions and to label the cell membrane and the cytoplasm of MCF-7 cells.^{40,89}

The interest was then directed towards the use of CDs as nanocarriers for drug delivery systems (DDSs). DDSs are one of the most important and researched approaches in nanomedicine, where the aim is to design a nanosystem that can load a drug and release it under specific conditions in a precise spot^{129, 130}. The possibility to easily tune the chemical characteristics of the CDs and to change the surface chemical properties of the carbon nanoparticles, combined with the low toxicity and the cheap starting materials, make CDs very suitable for this application.¹³¹ Song *et al.* proposed a folic acid derivatized CDs obtained from the microwave treatment of glucose and trioxotridecadiamine for DDS. This nanosystem proved to be efficient for selective detection of cancer cells vs. normal cells, providing an effective route for cell screening and disease diagnosis.¹³² The ability of CDs to act as drug loading and delivery systems was also highlighted by Bayda *et al.* who produced biocompatible CDs starting from tea leaves. They also proved the ability of such nanoparticles in loading the drug Doxorubicin (DOX) and the possibility of controlled release at acidic pH typical of cancer cells¹³³ The *in vivo* tests on mice proved the effectiveness of this system and the low toxicity of the nanoparticles: during a 2-month clinical study, no symptoms of stress or clinical illness were observed.

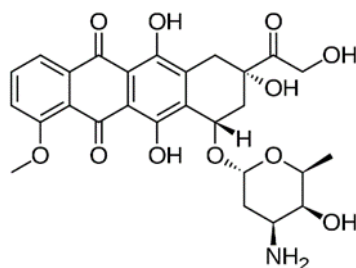


Figure 38. Chemical structure of Doxorubicin (DOX).

DOX, represented in Figure 38 and isolated for the first time from the fungus *Streptomyces peucetius*¹³⁴, is a chemotherapeutic agent with strong activity against a wide range of human malignant neoplasms including acute leukemia, non-Hodgkin lymphomas, breast cancer, Hodgkin's disease and sarcomas.¹³⁵ DOX is able to kill cancer cells by stabilizing a key enzyme (topoisomerase II complex) that prevents the DNA helix from resealing during the replication process.^{136, 137} The use of DOX in anticancer treatment suffers from a range of problems, such as a systemic toxicity, rapid drug resistance and congestive heart failure. These issues are correlated to the non-selective metabolism of DOX that can interact with healthy as well as cancerous cells. To overcome these problems, a series of CDs-based DDSs were developed to reduce the unnecessary contact of DOX with healthy cells and to permit controlled release of the drug in the desired site, increasing the local concentration, thereby promoting anticancer efficacy.⁹⁵ CDs obtained from a wide range of carbon precursors were tested for drug delivery. For example, Zeng *et al.* reported the synthesis of CDs from urea and citric acid, showing that they can function as trackable drug delivery agents with controlled drug release at pH 5.4. Another study conducted by Mewada *et al.* tested DOX-carrying and folic acid-mediated delivering capacity of highly fluorescent CDs.¹³⁸ Drug loading was estimated to be 86%_{wt} and the release of DOX from the system CDs-DOX followed first order release kinetics at physiological pH, an ideal drug release profile. Moreover, the combined drug-nanoparticles system showed a higher killing rate of cancer cells respect to the free DOX and also lower toxicity for healthy cells.

Notwithstanding the large number of publications and results obtained in this field there is the need for reproducible, simple, high-yielding synthetic protocols aimed at obtaining carbon dots with tunable fluorescence, photothermal and photochemical behavior, surface properties, biocompatibility, tumor targeting ability, drug absorption biodistribution, and tumor uptake. In order to achieve this aim in this study we investigated the synthesis three types of CDs starting from a single precursor. The synthetic methods adopted for this work involve bottom-up hydrothermal treatment.

Glucose, fructose and ascorbic acid were chosen as carbon precursors for their low toxicity and because they are cheap, abundant and biocompatible. Furthermore, the chemical structures of the selected starting materials ensure the presence of a high number of hydroxyl groups on the CDs surface, a feature that was found to be very important in the bonding of DOX. Non-covalent interactions such as electrostatic, hydrogen bonding, and π - π^* stacking, were found to be mainly responsible for the interaction of the DOX with the nanoparticles.¹³⁹

Monosaccharide-derived CDs were already published in the last decades, mainly in conjunction with passivating or doping agent. As an example, Yang et al. described the synthesis of CDs starting from glucose and using PEG-200 as passivating agent to obtain materials with high QYs of 6.3%.¹⁴⁰ Instead the addition of sulfuric acid¹⁴¹ or monopotassium phosphate⁷⁵ in the synthesis allowed to obtain CDs doped respectively with S or P that with good QY (10-12 %).

In this work CDs three types of CDs were synthesized from fructose, glucose and ascorbic acid without any addition of doping agent for avoid the presence of harmful elements that can affect the final toxicity of the system. The obtained nanoparticle was then deeply characterized in chemical, optical and toxicological point of view, revealing that despite the similarity of the starting precursors the final structures of the nanoparticles results to be very different and also their outcoming properties. Furthermore, the loading capability of such CDs with DOX were accomplished revealing that the affinity of these species is correlated to the structure of the nanoparticle more than their surface chemical composition. The results of this study were published in the paper "Carbon Dots from Sugars and Ascorbic Acid: Role of the Precursors on Morphology, Properties, Toxicity, and Drug Uptake."¹⁴²

3.2. Synthesis and Characterization

Fructose, glucose and ascorbic acid were the three precursors used to prepare the corresponding three CDs abbreviated respectively as: **F-CDs**, **G-CDs** and **A-CDs**. The synthetic method of choice involved hydrothermal treatment. The detailed conditions used, and the work-up procedure are described in the "Synthesis of CDs". The three different classes of CDs were characterized by ¹HNMR and ¹³C{¹H} NMR spectroscopy, revealing the complete conversion of the starting materials. Nevertheless, the spectra presented a series of new signals, especially in the region 2 - 4 ppm, reasonably ascribed to the olefinic protons in the graphitic domains of the carbon nanoparticles. The **F-CDs** samples showed also signals at higher ppm, both in the proton and carbon spectra (Figure 39).

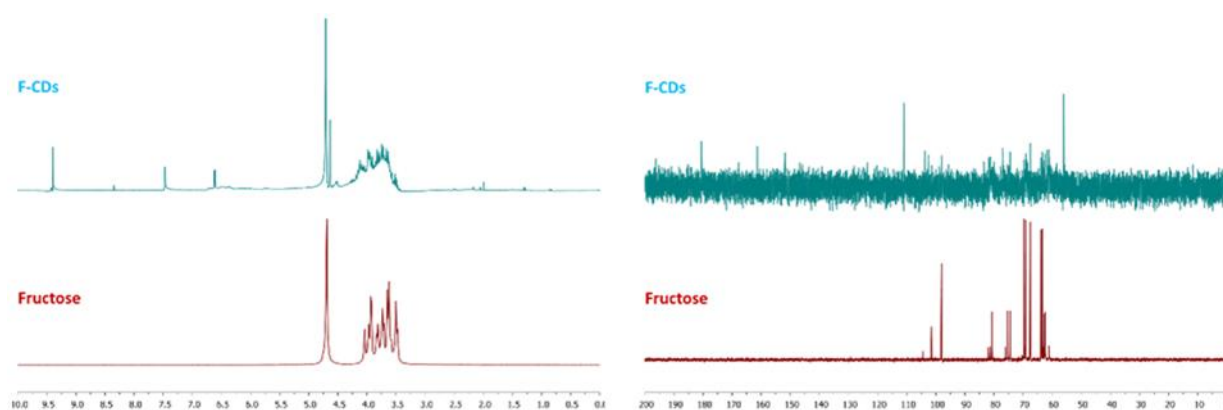


Figure 39. ^1H -NMR and $^{13}\text{C}\{^1\text{H}\}$ NMR of F-CDs in D_2O $\text{pD}=7$

In order to better understand the composition of the materials, a more detailed analysis of their chemical composition was performed by GC-MS. Solutions of the three CDs dissolved in water and acetonitrile were analysed. The **G-CDs** and **A-CDs** analysis reveal the absence of any molecular compounds, while for the **F-CDs** two molecules were detected, hydroxymethylfurfural (HMF) and 2,5-furandicarbaldehyde (FDCA), whose gas chromatogram and mass fragmentation patterns are shown in Figure 40.

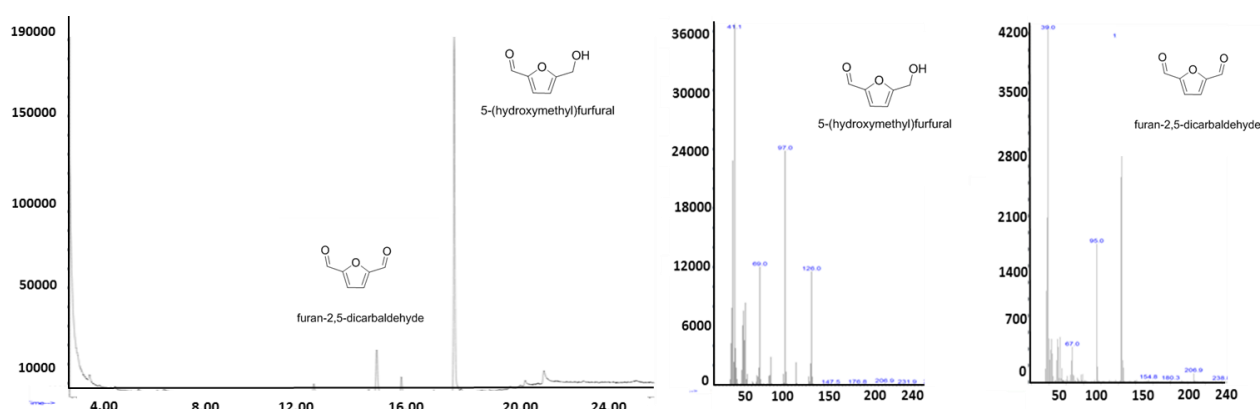


Figure 40. GC chromatogram of F-CDs and MS spectra of the identified compounds.

After detecting these molecules, the signals of HMF were identified and assigned in both the ^1H -NMR and $^{13}\text{C}\{^1\text{H}\}$ NMR spectra of the **F-CDs** as shown in Figure 41.

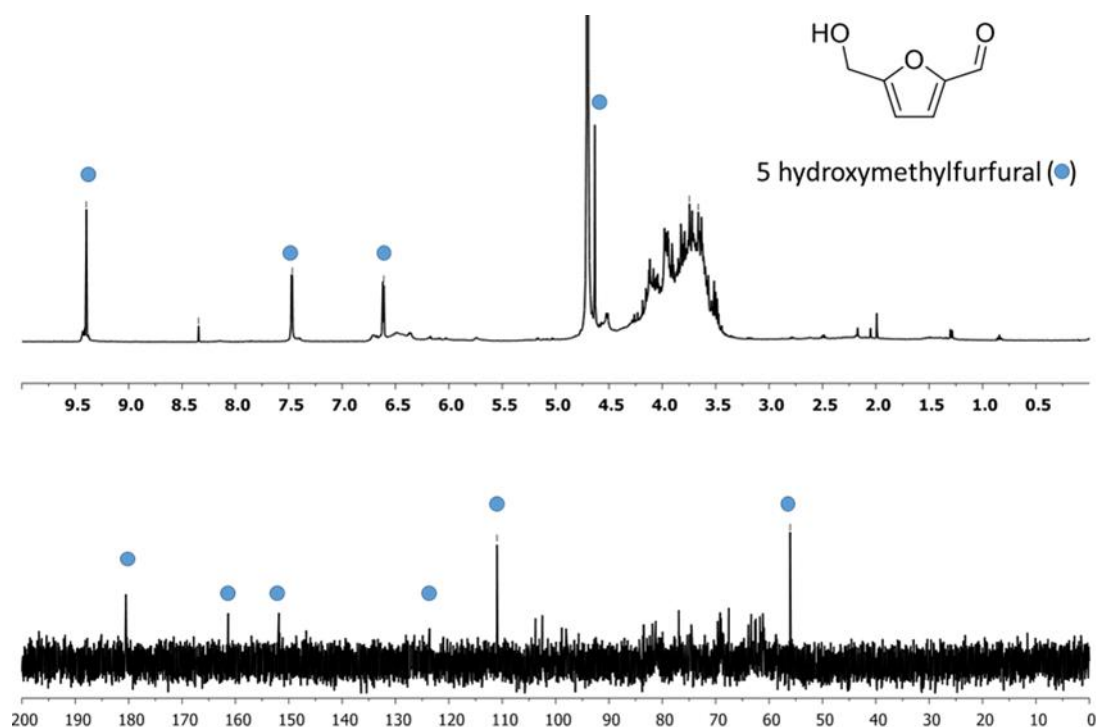


Figure 41. HMF signal assignment in ^1H NMR and $^{13}\text{C}\{^1\text{H}\}$ NMR spectra of F-CDs.

The formation of furan compounds such as HMF and FDCA by thermal dehydration of fructose is well known, and follows the mechanism shown in Figure 42. As reported by Fan *et al.* the pH and the temperature are key factors in the formation of furanics, in particular at acidic pH fructose and ascorbic acid produce a considerable amount of furans. While, at neutral pH furanics are detected only when starting from fructose. Furthermore, as expected, increasing the heating temperature promote extensive formation of furanics¹⁴³. A similar study conducted by the same author confirmed the pH effect on furanics formation starting from sugars and ascorbic acid. As expected based the different conformation of the ring structure and the more reducing properties of the fructose respect to the glucose the hydrothermal treatment of the latter in the same conditions yielded negligible amounts of furanics.¹⁴⁴ This behavior can be explained by the different conformation of the ring structure and the more reducing properties of the fructose respect to the glucose.¹⁴⁵

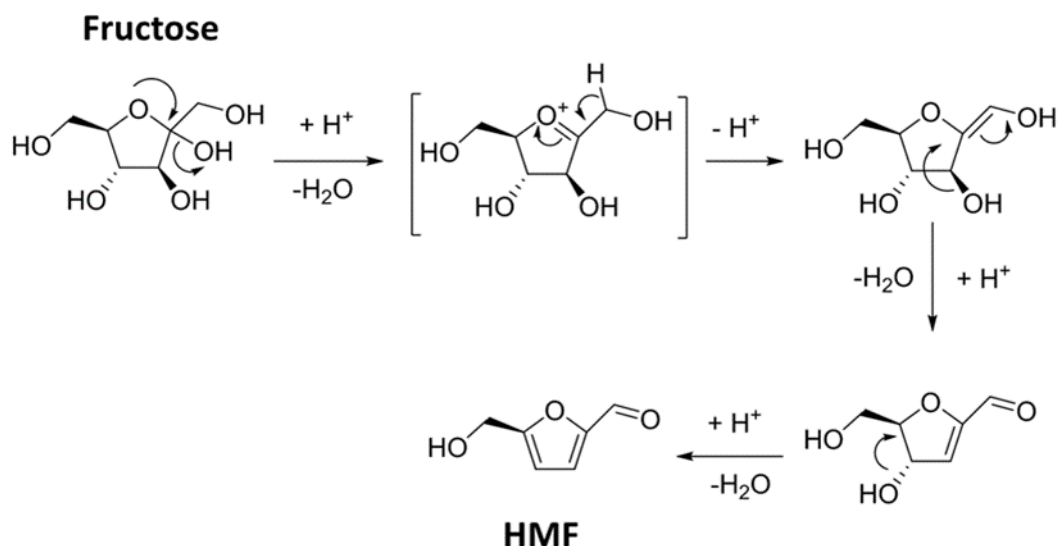


Figure 42. Formation mechanism of HMF from fructose.

Employing DOSY-NMR we attempted to estimate the dimensions and the MW of the nanoparticles. Figure 43 shows that the three samples have different size and masses. In particular, **G-CDs** have the lowest δ , and consequently the higher MW and volume. Intermediate values were observed for the **F-CDs**, with an average MW of 1200 Da, while for **A-CDs** the δ value was similar to the one of the initial ascorbic acid, suggesting a low degree of carbonization and a low MW.

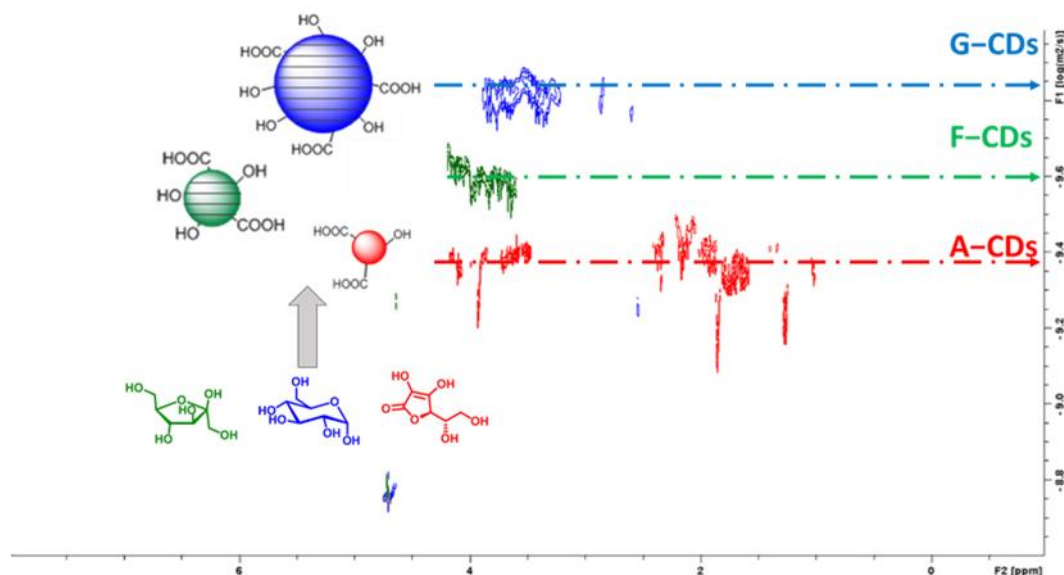


Figure 43. DOSY NMR of **G-CDs**, **F-CDs** and **A-CDs** in D₂O at pH=7.

In order to establish what kind of functional groups were present on the surface of the CDs, the FT-IR spectra in KBr were registered and are shown in Figure 44. The spectra revealed the presence of

hydroxyl groups in the region $3440\text{--}3375\text{ cm}^{-1}$ for all the three samples, as well as the band related to the presence of the C=C conjugated aromatic system centered at 1586 cm^{-1} , 1585 cm^{-1} and 1635 cm^{-1} for **G-CDs**, **F-CDs** and **A-CDs** respectively¹⁴⁶. The presence of C=O bonds was also apparent from the presence of the band at 1658 cm^{-1} for **G-CDs**, 1645 cm^{-1} for **F-CDs** and 1707 cm^{-1} for **A-CDs** respectively. Another moiety that was identified was the C-O-C bond highlighted by the presence of the band in the region $1200\text{--}1180\text{ cm}^{-1}$, and finally the absorption peak in the region from $2934\text{--}2920\text{ cm}^{-1}$ are indicative of the presence of C-H bonds¹⁴⁷.

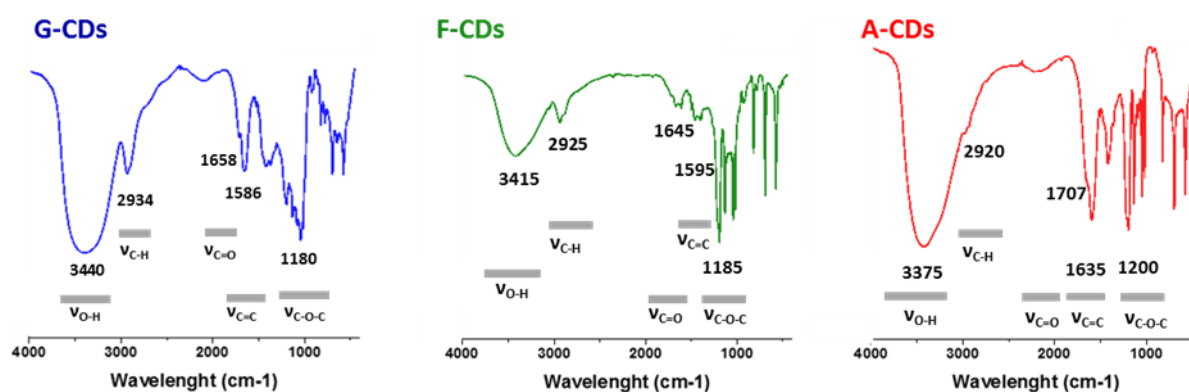


Figure 44. FT-IR spectra of **G-CDs**, **F-CDs** and **A-CDs**.

For a better knowledge on the surface chemical features of the carbon nanoparticles synthesized and of the possible interactions that can take place with the drug a quantification of the surface hydroxyl groups was accomplished. The methodology for the calculation of the hydroxyl value (HV) are explained in the experimental section. The titration results are summarized in Figure 45, revealing that **G-CDs** and **F-CDs** possess a comparable number of OH moieties on the surface ≈ 1500 corresponding to $26.8\text{ mol(OH)/g(CD)}$; this was not surprising since the two precursors are very similar and the resulting nanomaterials show similar characterization data. For the **A-CDs**, instead the values extrapolated from the analysis results to be almost three times higher respect to the other CDs. The lower HV obtained for the fructose and glucose derivatives can be explained by the observation that during hydrothermal synthesis, the thermolysis produced large amounts of CO_2 and H_2O along with the **F-CDs** and **G-CDs** in 34% and 29% yield, respectively, implying a large loss of oxygen and higher degree of carbonization. Instead, higher mass yields and less carbogenic structure were observed for **A-CDs** in the NMR characterization, explaining the higher residual hydroxyl groups in the sample.

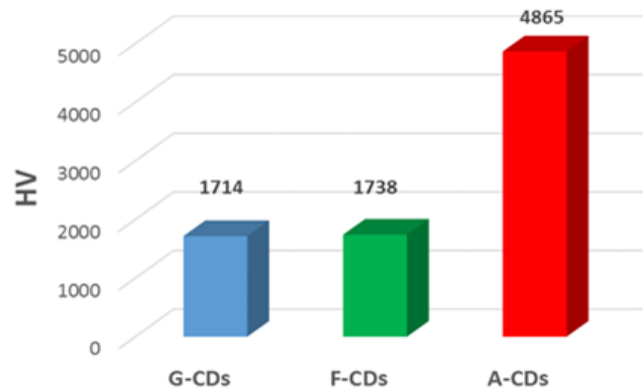


Figure 45. HV of G-CDs, F-CDs and A-CDs.

A picture of the physical structure of the CDs was obtained by collecting their TEM images. As shown in Figure 46, TEM revealed a graphitic structure for the G-CDs and F-CDs while the A-CDs appeared amorphous suggesting an incomplete carbonization of the material. The average dimensions were evaluated by measuring the diameter of 100 nanoparticles: for both G-CDs and F-CDs an average value of 10 nm was calculated while no clear size could be calculated for the A-CDs due to their amorphous nature. For the glucose and fructose derivatives the graphitic planes of the nanoparticles were also noticed with an interlayer spacing of 2.4 Å in the HR-TEM, corresponding to the d space of the graphene, confirming their highly crystalline graphene structure.¹⁴⁸

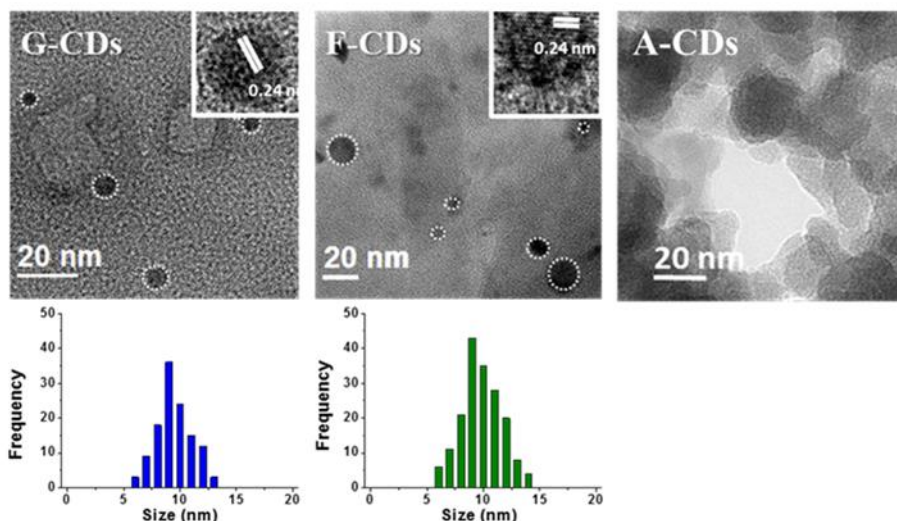


Figure 46. HR-TEM images of G-CDs, F-CDs (with a size distribution histogram), and A-CDs.

Another key parameter that was evaluated was the surface charge of the CDs, that is necessary in order to predict a good electrostatic interaction with the desired drug. The surface charge of the nanoparticles was investigated by electrophoresis. The specifics of this technique were described in chapter 1.7. In summary, the analyses were carried out using a running buffer at different pH (4, 6, 8 and 10). The resulting images, collected after a run of 30 minutes are shown in Figure 47. It is evident that all the three CDs migrate towards the positive pole, meaning an overall negative surface charge. These results are not surprising, since the nanoparticles contain a high number of hydroxyl group as shown by their HV and IR analysis. Interestingly the distances run by the samples seem to be related to the amount of hydroxyl groups on the surface of the nanoparticles. For example, the OH rich **A-CDs** show the longest electrophoresis run. **G-CDs** and **F-CDs** behave similarly in this analysis as well: fewer hydroxyl groups lead to a shorter run compared to the ascorbic acid derivatives.

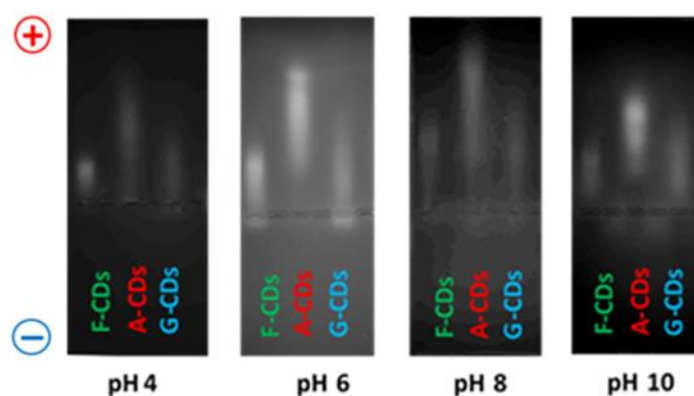


Figure 47. Electrophoresis experiment performed at different pH's on **G-CDs**, **F-CDs** and **A-CDs**.

The optical properties of the three nanomaterials were first investigated by UV-Vis spectroscopy. Figure 48 shows the UV-Vis spectra of the three samples and highlights the different behavior of the CDs. **G-CDs** show only one absorption peak centered at 265 nm, and reasonably ascribed to the $n-\pi^*$ transitions of the carbonyl groups on the surface of the nanoparticles¹⁴⁹. The same band is detected in the **F-CDs** sample. Moreover, all the CDs exhibit an absorption band in the region between 225-235 nm ascribed to the $\pi-\pi^*$ transition of the sp^2 C=C conjugated system. An additional band was also detected for the fructose derivatives at 360 nm correlated to the transition associated to trapping of the excited-state energy by the surface state.¹⁵⁰

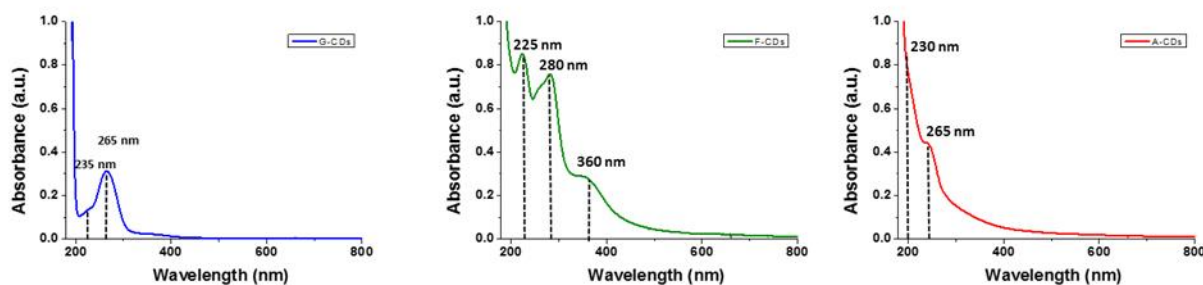


Figure 48. UV spectra of G-CDs, F-CDs, A-CDs.

The photoluminescence (PL) emission peaks registered at different excitation wavelengths (330–380 nm) revealed different behaviors of the CDs despite the similarity of the precursors. In particular, the G-CDs and A-CDs showed an excitation-dependent photoluminescence with the maximum of the emission peak red-shifted by 15 and 20 nm respectively. This phenomenon is very common in CDs, although its origin is still not clear. One possible explanation is related to the intrinsic defect states present on the nanoparticles as postulated by Pan *et al.* using a single-particle spectroscopy measurement.¹⁵¹ With the same technique, van Dam *et al.* demonstrated the presence of multiple active and independently excitable emission sites within a single-carbon dot.¹⁵² The PL emission peaks of the F-CDs instead, did not show any dependence on the excitation wavelength as shown in Figure 49.

The QYs of the CDs, calculated using quinine sulfate as standard, were 1.8%, 0.3%, and 1.5% for the G-CDs, F-CDs, and A-CDs, respectively. As expected, low QY were measured in all cases due to the absence of doping atoms (*e.g.* N or P) and of passivating agents, as well as to the presence of defects and conjugated carbon core domains, which favor nonradiative electron–hole recombination pathways.

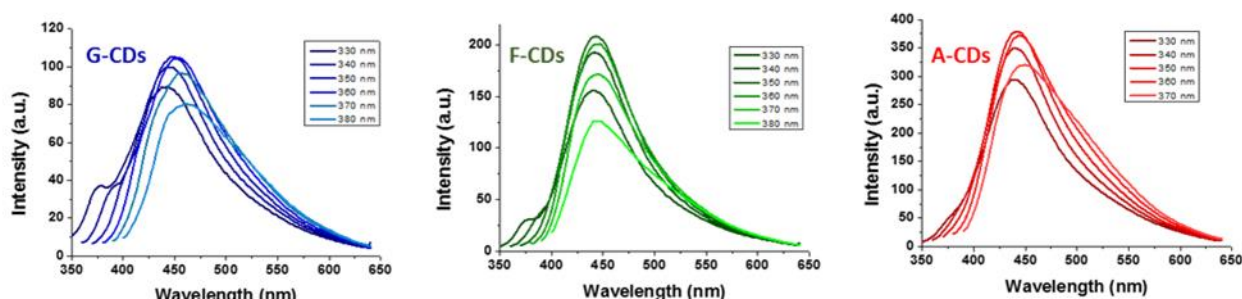


Figure 49. Emission spectra at different excitation wavelengths for G-CDs, F-CDs and A-CDs

3.3. Toxicity of the CDs

In order to create a biocompatible nanocarrier based on CDs, it is necessary to evaluate the toxicity of the sole nanoparticles. The toxicity measurement was carried out by the Experimental and Clinical Pharmacology Unit at C.R.O. National Cancer Institute of Aviano. All the experiments were performed in triplicate. The results obtained are shown in Figure 50. The **G-CDs** showed no evidence of toxicity up to a concentration of CDs of 1 mg/mL, as indicated by the viability which is similar to the one measured for the control solution. The ascorbic acid derived CDs demonstrated a measurable toxicity in high concentration (> 0.25 mg/mL) with the viability decreasing of 50% respect to the control experiment. Finally, the **F-CDs** showed significant toxicity even at low concentrations. Once more, the similarity of the precursors glucose and fructose still does not imply similar properties of the resulting CDs. The toxicity displayed by the **F-CDs** was explained by the presence of the furanics, such as HMF and furfural, detected by NMR and formed by dehydration of the carbohydrates.^{153,154}

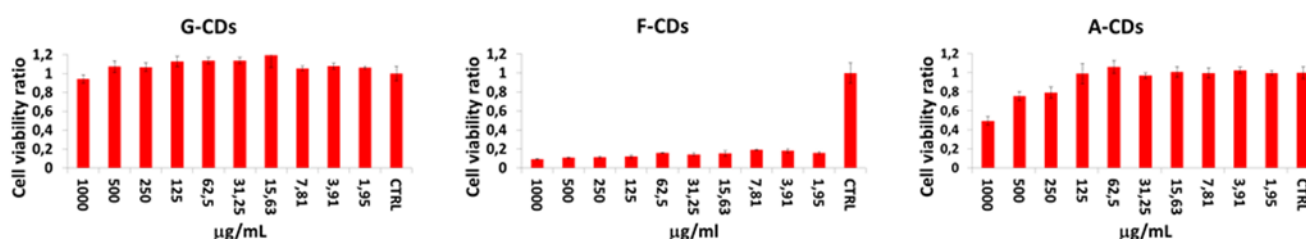


Figure 50. Cytotoxicity of G-CDs, F-CDs and A-CDs

An intriguing aspect revealed by this study is the possibility to synthesized toxic CDs starting from a fully biocompatible precursor. As herein demonstrated, the possible toxicity of the final CDs may arise from the formation of toxic molecules in the thermal degradation of the precursor. It is therefore of fundamental importance to have a complete knowledge of the possible degradation pathway that may take place for the chosen precursor. As consequence, the choice of the starting material is a key factor to successfully achieve the desired properties for the CDs.

3.4. Drug uptake experiments

After the investigation of the toxicity of the CDs, further study was focalized on the drug uptake properties of the CDs. For this aim, Doxorubicin (DOX) was chosen as a model drug. This compound is widely use as drug model for anticancer studies to evaluate its absorption and release in drug delivery systems. One of the main reasons why DOX is commonly used in this field is its photoluminescent and absorption properties. The molecule shows an absorption spectrum with a strong absorption peak at 500 nm and two emission peaks centered at 550 and 600 nm respectively. These features allow to employ simple spectrofluorometry technique to measure drug loading and

delivery, a technique used in this study as well. In more detail, the quenching of the emission peak of the CDs was evaluated at different concentrations of DOX. For this purpose, two 0.25 mg/mL water solutions of CDs were prepared, one without and one with 0.20 mg/mL of DOX. Next, the intensity of the emission peaks of the CDs solution was monitored at different addition of the DOX-containing solution, in a concentration range from 0 to 5.5×10^{-5} M. The CDs solutions were excited at 340 nm and the results are shown in Figure 51.

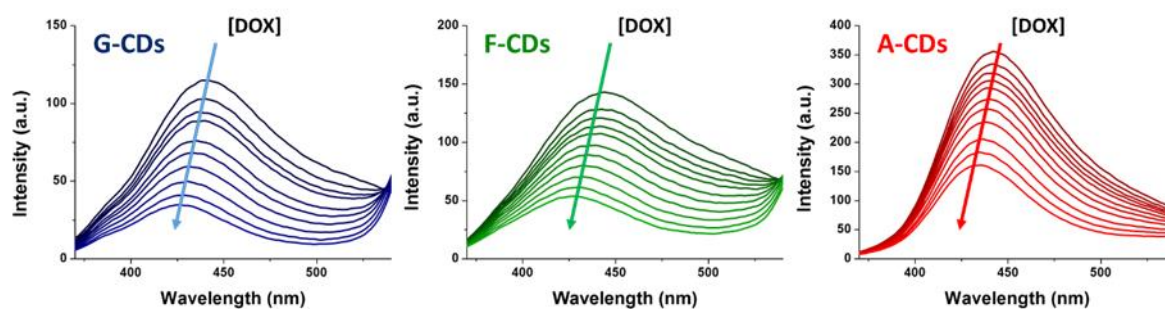


Figure 51. Emission spectra of CDs recorded at different addition of DOX.

For all the three CDs it is possible to notice that the gradual addition of DOX results in a progressive quenching of the luminescence and in a blue-shift of the emission maximum. The quenching of the luminescence takes place when the fluorophore (CDs) and the quencher (DOX) are in contact with each other either statically or dynamically.^{155, 156} In addition, the shift at lower wavelength of the emission peak, indicates a strong interaction between the drug and the nanoparticles. This phenomenon was previously observed by Sun *et al.* with CDs obtained from glucose and glutamic acid. After the titration of the DOX with CDs these authors noticed the quenching and the shift of the emission maximum and ascribed these effects to a strong electronical communication between the two species.¹⁵⁷

In order to evaluate the affinity constant between the CDs and the DOX, a Stern-Volmer plot was employed. The concentration of DOX was plotted versus the ratio between the intensity at that addition and the intensity without DOX measured at 441 nm. For the three CDs it was possible to obtain a linear trend as shown in Figure 52.

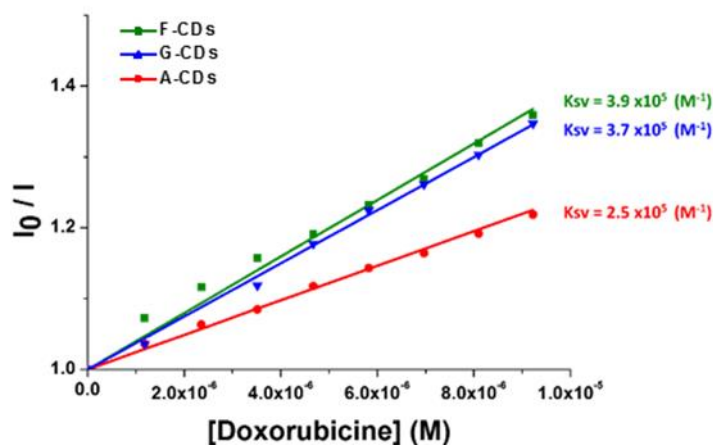


Figure 52. Stern-Volmer plots of the titration of G-CDs, F-CDs and A-CDs with DOX.

From the linear trend it is possible to extrapolate the Stern-Volmer constant. The Stern-Volmer constant is correlated to the association constant of the complex CDs-DOX. As reported in Figure 52 the association constants of F-CDs and G-CDs with DOX are very similar to each other, confirming once more the similarity of the two samples in terms of structural and chemical properties. Instead the A-CDs demonstrated a lower K_{sv} meaning a weaker interaction between the nanoparticles and the drug. From these results some deductions were made. First, the nanoparticles with fewer hydroxyl groups, have higher affinity with the drug. This suggests that the electrostatic interaction between the hydroxyl groups on the nanoparticles and the amino groups of DOX play a secondary role. Second, the interaction between the CDs and the drug are correlated to the morphology of the nanomaterial, with the amorphous materials like the A-CDs having a lower association constant respect to the graphitic F-CDs and G-CDs. These observations led to assume that the interactions between the two species are non-covalent rather than electrostatic. In particular, a crucial role may be played by non-covalent π - π interactions between the graphitic planes of the nanoparticles and the aromatic moieties of the drug. This hypothesis appears to be confirmed by other studies that report this type of interaction between the carbon nanoparticles and DOX, such as the one by Jung *et al.* on CDs derived from citric acid and β -alanine.⁹⁶

To estimate the amount of DOX that the CDs can load, another spectrofluorimetric approach was employed. A Job plot was used to determine the ratio of DOX and CDs in the complex as explained in the experimental section. The results are summarized in Figure 53. Two linear sections can be observed in the Job plot, indicating two different behaviors. In particular, the intersection of these two segments represents the stoichiometry of the CDs-DOX complex. This point corresponds to a

mass fraction of 0.72 that corresponds to a CDs-DOX binding-stoichiometry of 3.5:1. From this value it is also possible to calculate the mass percentage of DOX loaded on the CDs, that corresponds to a drug loading capability of the CDs, equal to 28%_{wt}. A comparison of the drug loading ability with other results for CDs obtained from similar precursors, was carried out. For example, by starting from glucose, ethylenediamine and phosphoric acid, Gong *et al.* synthesized hollow N,P-doped CDs. By a UV-Vis technique the authors calculated a DOX loading of 35 %_{wt} that is the highest reported to date for glucose-based CDs.¹⁵⁸ Another study on the drug loading capabilities of glucose-based CDs was conducted by Wang *et al.* employing glucose as the source for the synthesis of the nanoparticles and a PEG-chitosan polymer for the surface derivatization. DOX was used for the drug loading test, and the measurements were accomplished by a spectrofluorimetric approach. The results showed a drug loading efficacy of 3%_{wt} for the PEG-Chitosan@CDs hybrid system.¹⁵⁹ These results confirm that the system herein developed has a high efficiency in the loading of DOX, comparable to the best ones already published.

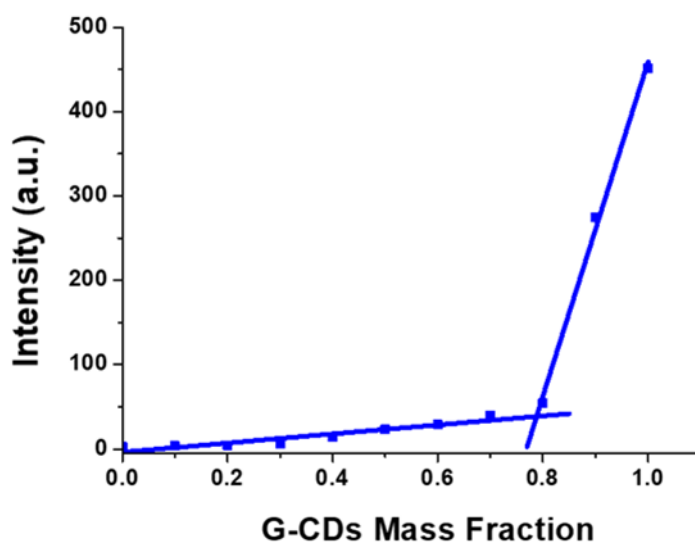


Figure 53. Job plot of the fluorescence decay of G-CDs with DOX.

The next step will be the investigation of controlled release of the drug under defined conditions, especially at acidic pH.

3.5. Conclusions

In conclusion, in this work three different CDs were synthesized from the biocompatible precursors glucose, fructose, and ascorbic acid. Hydrothermal treatment yielded CDs that were characterized from the structural, morphological, chemical, and optical standpoints. The analyses revealed that the

structure of the nanoparticles is related to the starting precursor, with glucose and fructose leading to graphitic CDs while ascorbic acid to amorphous materials. An extensive NMR characterization was performed, revealing the presence of furanics in the **F-CDs** sample. Furthermore, the surface chemical groups were demonstrated to depend on the precursor and its thermal degradation pathway. The amount of hydroxyl groups on the surface was quantified by a titration technique, revealing a similar content for **F-CDs** and **G-CDs** while a higher value was obtained for the **A-CDs**. The hydroxyl content determines also the surface charge of the nanoparticles, with the highly -OH rich sample having the more negative surface charge, as observed by electrophoresis. The optical properties were also investigated revealing an excitation dependent photoluminescence for **G-CDs** and **A-CDs** while for the **F-CDs** this effect was not noticed. The toxicity of the nanoparticles was evaluated on HeLa cells, and the experiments revealed that G-CDs are non-toxic, A-CDs are slightly toxic at high concentration, while **F-CDs** are more toxic due to the presence of furanics observed by NMR. The interactions with DOX, were studied by spectrofluorimetric techniques, revealing the importance of the graphitic core in achieving a good binding, and by showing that the π - π interactions with the drug are dominant. The capabilities of the CDs to bind the DOX was quantified for the **G-CDs** with a Job-plot revealing 28 %_{wt} of drug loading. These results highlight the importance of the starting materials and of control of the synthetic conditions in order to achieve CDs with the desired properties.

3.6. Experimental

Glucose, fructose, ascorbic acid, acetic anhydride and phenolphthalein were purchased from Sigma–Aldrich and used as received. Doxorubicin (2mg/mL in water) was purchased from Accord Healthcare Italia. The UV–VIS spectra were collected with an Agilent 8456 spectrophotometer and the PL & PLE spectra were obtained with a Perkin Elmer LS 55 fluorescence spectrophotometer. A BIO-RAD Sub-Cell GT agarose gel electrophoresis system was used for the electrophoresis experiment. The running buffer was composed by 1% of agarose gel and the run for 1 h at constant power (10 W). The ^1H , ^{13}C $\{^1\text{H}\}$ NMR and DOSY spectra were collected with a Bruker 400 MHz. (HR)–TEM images were obtained using a Jem2200fs instrument. The Quantum Yields (QY) were determined using an Infinite M1000Pro, Tecan; excitation wavelength 360nm; emission wavelength range 370–650nm, using Quinine Sulfate as reference. Cytotoxicity was measured by CellTiter-Glo[®] Luminescence assay (Promega, Madison, Wisconsin, US) after 96 hours with the Infinite 200 PRO instrument (Tecan).

3.6.1. Hydroxyl Value

The hydroxyl value (HV) is defined as the grams of KOH required to neutralize 1 g of CDs sample, and it is calculated using the following procedure. A small amount of CDs sample (50–100 mg) was placed in a flask and then 5 mL of acetic anhydride and 20 mL of pyridine were added. The mixture was heated at 95 °C for 1 h, 10 mL of water were added to hydrolyze the unreacted anhydride and then the mixture was reheated at 95 °C for 10 min. The resulting solution was titrated with KOH 0.1 N using phenolphthalein as indicator. As a reference, a blank test was carried out under the same condition but without CDs. The HV was calculated using the following equation.¹⁶⁰

$$HV = \frac{(mL\ blank - ml\ sample) * N(KOH) * PM(KOH)}{g\ sample}$$

3.6.2. Electrophoresis

A BIO-RAD Sub-Cell GT Agarose gel Electrophoresis system was used for the electrophoresis experiment. The running buffer was composed by 1% of agarose gel and the run for 1 h at constant power (10 W).

3.6.3. Cytotoxicity

The cytotoxicity tests were performed on HeLa cell lines and cytotoxicity were evaluated by the CellTiter-Glo[®] luminescence assay using an Infinite 200 PRO instrument. Cells were seeded in 96-well plates (Falcon BD, San Jose, CA, US) at a density of 103 cells/well and incubated for 24 h to allow for cell attachment. Apoptosis was evaluated after 24 hours by fluorescence-activated cell sorting, utilizing the PE Annexin V Apoptosis Detection Kit I. All the experiments were performed in triplicate.

3.6.4. Stern-Volmer method

CDs-DOX interaction was investigated by a steady-state absorption titration by simple mixing aqueous DOX (0.2 mg/mL) to a CDs (0.25 mg/mL) water solution at r.t. and pH 7. The fluorescent spectra of the resulting solutions were collected by exciting at 340 nm. The decrease of the CDs luminescence (at 440 nm) was correlated to the rise of the quencher concentration with the Stern-Volmer equation:

$$\frac{I_0}{I} = 1 + K_{sv} * [Q]$$

where I_0 and I are the respectively fluorescence intensity of the fluorophore before and after the addition of the quencher, and K_{sv} is the association constant of the fluorophore-quencher interaction.

3.6.5. Job's plot method

Different solutions with increasing mass fraction of DOX was prepared, keeping constant the sum of $m_{\text{CDs}}+m_{\text{DOX}}$ to 0.6 mg. The fluorescence emission intensity at 441 nm of the as prepared solutions was evaluated at by exciting the sample at 340 nm

4. Results: Carbon dots for photocatalytic applications

4.1. Introduction

In the last decade, a large amount of research has been carried out in the world of the CDs. By focusing attention on their unique properties, a great amount of applications has been developed: from the use in the biomedical field as nanocarriers or as biosensors, to the electronic field as supercapacitors or in photovoltaic cells. One of the emerging fields where CDs may have a strong impact is photocatalysis. The ability of CDs to act as photosensitizers for photochemical reactions has not yet been deeply investigated, despite having all the necessary characteristics. In fact, CDs are an optimal light harvesting material and can generate photoexcited photons if irradiated b at the appropriate wavelength. Furthermore, it was also recently demonstrated that CDs may also generate excited electrons with long life time, very useful for photoredox reactions.¹⁶¹ All these features make these nanoparticles very appealing for the development of a new photocatalytic system without the need for additional redox mediators, such as metal complexes for example. The first publication on the use of CDs in a photochemical reaction was conduct by Reisner's group. They proved that CDs can be used as photosensitizers to donate electrons to succinate reductase and perform the reduction of fumarate to succinate¹⁶². The CDs were prepared by pyrolysis of citric acid and the surface-derivatized with amino compounds. The nanoparticles, under solar light irradiation, demonstrated to behave as electron transfer agents towards the enzymes, and to efficiently catalyze the reduction of fumarate. The surface derivatization resulted to be an important characteristic in order to achieve a desirable conversion of the substrate due to the different surface charges, positive for amino derivatives and negative for the carboxylic ones, that influence the interactions between the enzymes and the nanoparticles. The study highlights how the surface functionalities and their effects on the CDs can modify the properties and reactivity of the CDs. The same group, analyzed also the effect of doping the carbon core of the CDs with nitrogen, on the photoreactivity of the system.⁶⁰ The authors compared three types of CDs, both amorphous and graphitic, obtained by the treatment of citric acid and an amino doped CDs synthesized from the pyrolysis of aspartic acid. The study demonstrated that all the tested CDs act, in combination with a molecular nickel catalyst, as photosensitizers *via* photo-induced electron transfer process for hydrogen evolution (Figure 54),

albeit with different reaction rates. The most promising class of CDs was found to be the graphitic doped nanoparticles, and the reason was ascribed to the enhanced light harvesting properties deriving from the presence of the nitrogen in the carbon core. Nonetheless, due to the different carbon sources employed for the CDs synthesis, and to the lack of comparison with amorphous nitrogen-doped nanoparticles, a clear and precise rationalization of the effect of the graphitization and nitrogen doping on the photocatalytic ability of the nanoparticles could not be drawn.

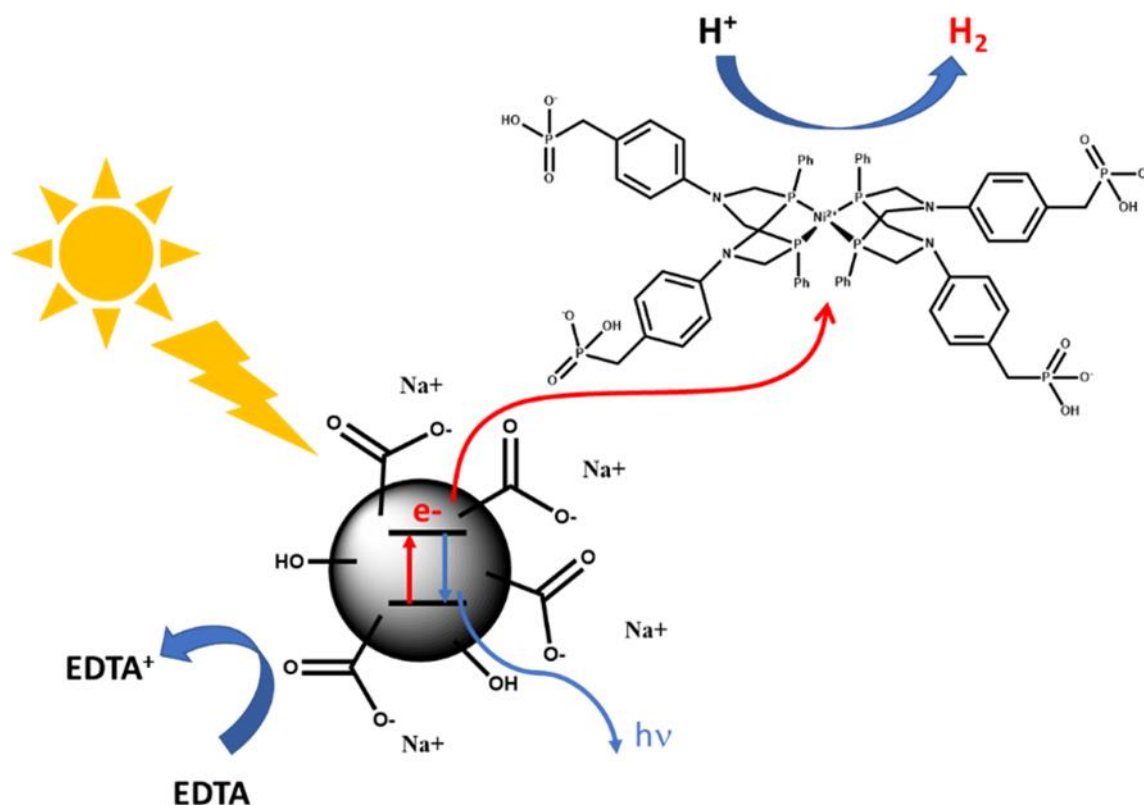


Figure 54. Solar hydrogen production using CDs-NiP hybrid system.

Another interesting study on the photocatalytic properties of the CDs was accomplished in Prato's group⁵⁵. The authors synthesized different CDs starting from ethylenediamine, arginine and different quinones. The authors explored the electrochemical properties of these nanomaterials employing cyclic voltammetry (CV). With this technique they were able to determine the anodic and cathodic potential for all the nanoparticles and correlate these values with the HOMO and LUMO energy and therefore ΔE . The data showed that all the CDs have an oxidation and reduction potential that is in a suitable range for many applications. In particular, the authors found that the oxidation potential of the nanomaterials was correlated to the presence of amino groups on the surface of the nanomaterials. Their investigation on the ability of their CDs to reduce methylviologen (MV) revealed

that the materials prepared starting from quinine and with the highest absorption in the visible region displayed the best activity, highlighting the importance of the quinone in increasing the photo-activity of the nanomaterials.

These studies revealed that CDs could be excellent photosensitizers for chemical reactions and that the surface properties, functional groups, and core composition play a crucial role on determining their reactivity. Nevertheless, a rationalization on how the synthetic methods and the precursors affect the reactivity of the resulting nanomaterials has not yet been accomplished.

In the present study, our work was focused on the synthesis and complete characterization of four type of CDs prepared from sole citric acid and in combination with diethylenetriamine (DETA) as nitrogen dopant. The CDs were then compared in their morphology, optical and chemical properties highlighting the difference arising from the diverse synthetic protocols employed. Next, the study on the reduction of MV) revealed that the morphological and optical properties of the CDs play a crucial role in determining the photoredox activity of the CDs. This study paves the road towards the rational design of carbon-nanoparticles for efficient photocatalytic organic transformations, as alternative to the currently used precious-metal inorganic dyes.

The results of this study were recently published in the paper “Design of Carbon Dots for Metal-free Photoredox Catalysis”.¹⁶⁴

4.2. Characterization

In order to understand and tune the photocatalytic potential of the CDs, control over the synthetic procedure, the morphology and the photophysical properties as a function of the carbonaceous precursors and of the reaction conditions is crucial. With this in mind, two synthetic methods were employed in this work: thermolysis and hydrothermal, expected to yield graphitic and amorphous CDs, respectively. Furthermore, nitrogen doping an important parameter that is known to affect the photocatalytic properties of the materials, was also considered. The carbon source employed for this work was the citric acid, one of most commonly used materials for the synthesis of carbon dots. As doping agent instead, diethylenetriamine was employed. By the combination of two different reaction conditions and the presence or absence of the N-doping agent, four different types of CDs were obtained:

- **a-CDs**, amorphous non-doped CDs,
- **g-CDs**, graphitic non-doped CDs,

- **a-N-CDs**, amorphous doped CDs,
- **g-N-CDs**, graphitic doped CDs.

A summary of the reaction conditions, and of the products obtained is shown in Figure 55 while the detailed reaction conditions and the workup procedure are described in the Chapter “Synthesis of CDs”.

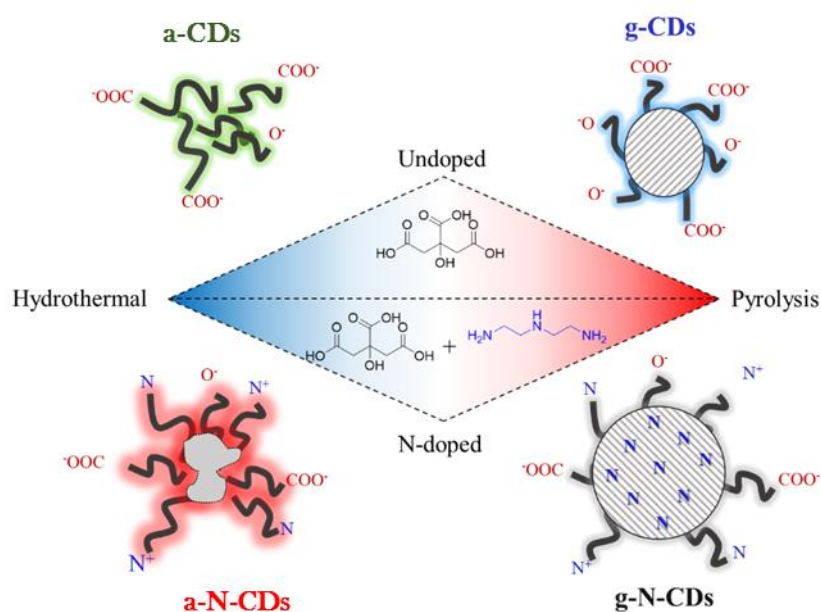


Figure 55. Schematic representations of the four CDs studied in this work: purely carbogenic (**a-CDs**, **g-CDs**) or N-doped (**a-N-CDs**, **g-N-CDs**) obtained by hydrothermal (180 °C, 24 hours, water) or thermolysis (220 °C, days, neat) of citric acid with or without diethylenetriamine as doping agent.

4.2.1. a-CDs and g-CDs

The **a-CDs** were obtained by hydrothermal treatment of citric acid for 24 h at 180 °C as a yellow solid in 25%_wt yield. The thermolysis of citric acid at 220 °C for 48 h followed by dialysis afforded **g-CDs** with an overall 20%_w yield.

The undoped CDs were first characterized by NMR spectroscopy. The **a-CDs**, after work-up, show ^1H -NMR and $^{13}\text{C}\{^1\text{H}\}$ NMR spectra with different signals, ascribed to the presence of small organic molecules in the mixture due to incomplete carbonization of the starting material. In order to have a more detailed understanding of the composition of this mixture, a dilute solution of the sample was further analyzed by GC-MS. The analysis shows the presence of at least two molecules in the mixture, citraconic anhydride and itaconic anhydride. The gas-chromatogram and the mass fragmentation of the two detected molecules are shown in Figure 56.

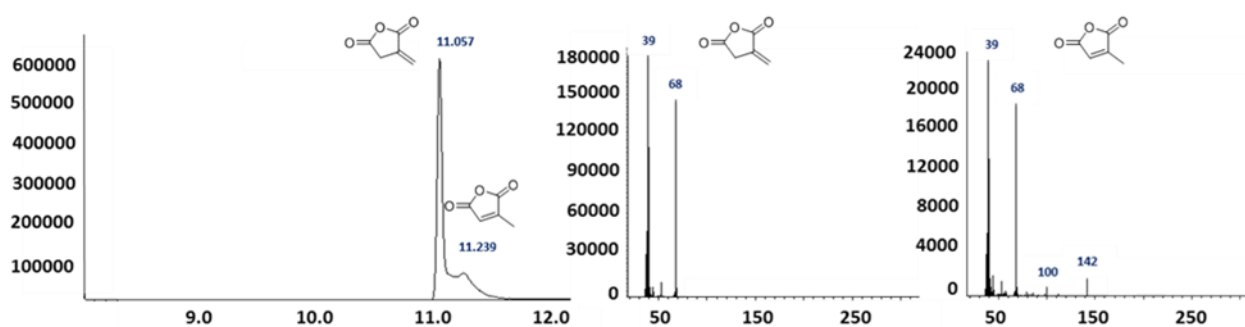


Figure 56. GC chromatogram of a-CDs and MS spectra of citraconic anhydride and itaconic anhydride

The presence of these molecules after the hydrothermal treatment of citric acid is not a complete surprise, since they are a common thermal degradation product of the precursor carbon source as already demonstrated in literature.¹⁶⁵ The proton and carbon resonances of citraconic and itaconic anhydride are highlighted in Figure 57.

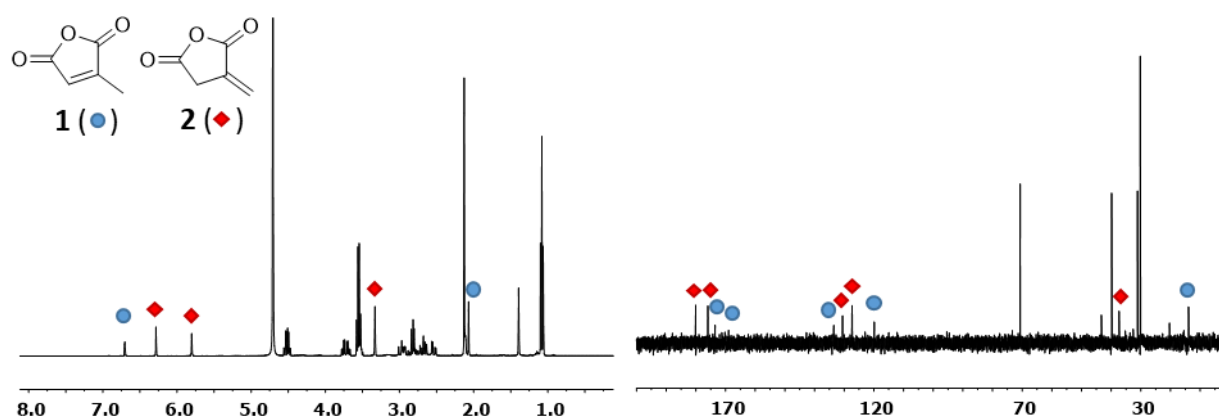


Figure 57. ¹H NMR and ¹³C{¹H} NMR interpretation.

DOSY NMR was employed to estimate the average sizes of the nanoparticles in the mixture. The analysis reveals a heterogeneous composition of the sample, with one set of signals with lower δ (green line), ascribable to heavier molecules, with an estimated MW of 600 – 700 Da. A second series of signals in correspondence to the one of the anhydrides was then identified with a higher δ , and with a calculated MW of 118 Da, very close to the effective MW of the anhydrides (112 Da). Support of the DOSY experiments was provided by the ESI analysis that reveal the presence of species with a MW of 800-900 Da for the sample as shown in Figure 58.

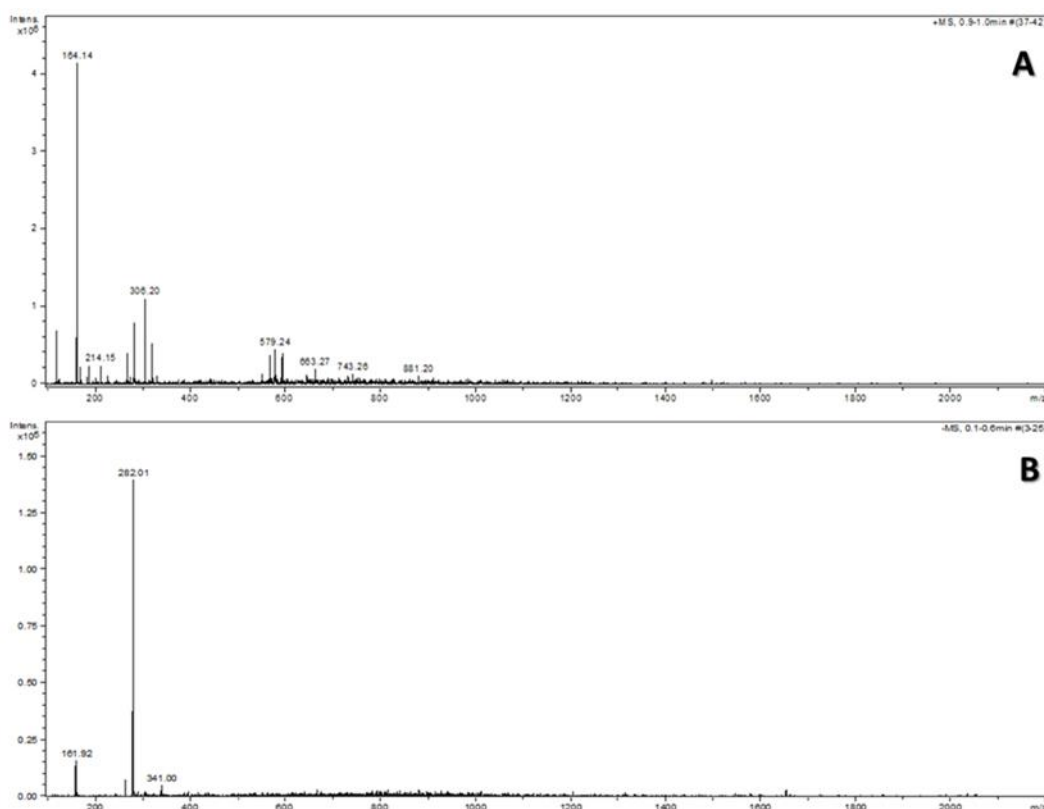


Figure 58. ESI(+/-)-MS spectra of **a-CDs** in H₂O. A) Positive mode. B) Negative mode.

The **g-CDs** obtained by thermolysis of citric acid at 220 °C for 48, after workup and dialysis, were recovered with an overall yield of 20%_{wt}. The nanoparticles were then characterized by ¹H-NMR and ¹³C{¹H} NMR spectroscopy revealing a blank spectrum, indicative of the complete absence of small organic molecules in the solution and a complete carbonization of the starting material.

The morphologies of **a-CDs** and **g-CDs** were investigated by HR-TEM and the images obtained are reported in Figure 59. A dependence of the structure on the synthetic methods employed was observed. The softer hydrothermal conditions led to the formation of an amorphous material with an ill-defined shape, while the harsher pyrolysis conditions yielded graphitic spherical structures.

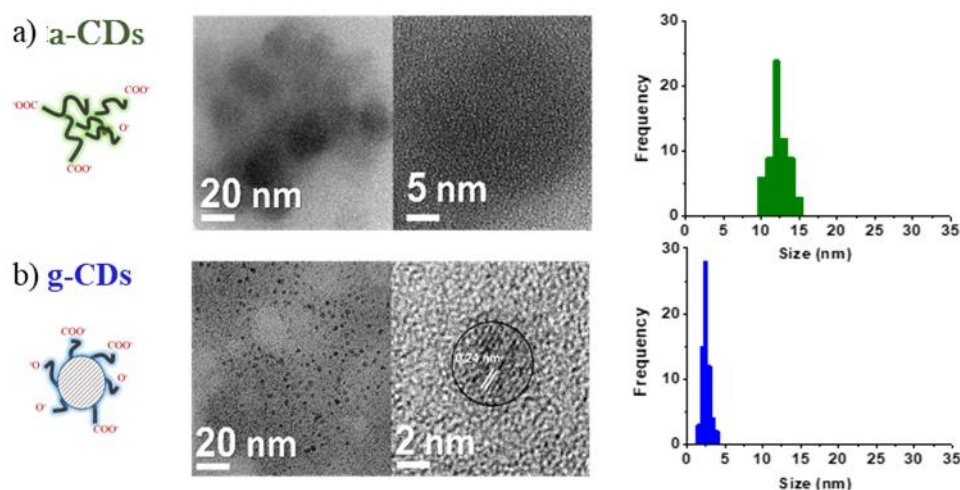


Figure 59. TEM images of **a-CDs** and **g-CDs**.

Another consideration that can be made looking at the TEM images, regards the average dimensions of the nanoparticles. Looking at the histogram, obtained by averaging the measurements of 100 particles, it is clear that the **g-CDs** have an average size (3 nm) that is far smaller than the **a-CDs** (12 nm). These results demonstrate that the synthetic method employed has a strong influence on the morphological structure of the CDs: the softer hydrothermal conditions and the closed environment of the autoclave does not allow complete graphitization of the carbon precursor. The high definition images also revealed that only for the **g-CDs**, it was possible to observe the lattice fringes with an interlayer spacing of 2.4 Å, confirming their crystallinity.¹⁴⁸ The surface chemical compositions of the CDs were evaluated employing FT-IR. The collected IR spectra of **a-CDs** and **g-CDs** are shown in Figure 60.

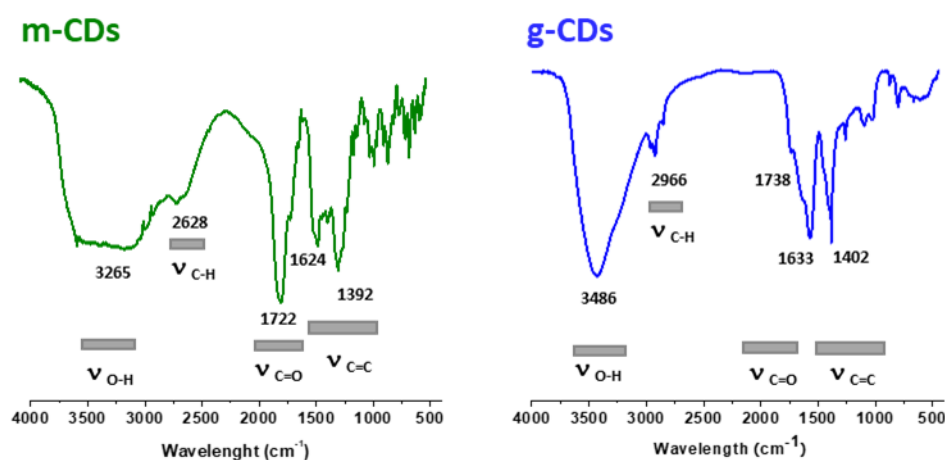


Figure 60. FT-IR of **a-CDs** and **g-CDs**.

As shown above both the samples presents similar features in their surface chemical composition.

Both the samples present a high content of hydroxyl groups, as revealed by the broad band at 3486-3265 cm^{-1} . The C-H bonds were also revealed by the band at 2966-2628 cm^{-1} , furthermore the CDs present also carbonyl groups at 1722-1738 cm^{-1} and the aromatic C=C bonds were detected at 1626-1633 cm^{-1} . To further investigate the chemical composition an XPS spectra of the CDs were registered and interpreted. XPS of the **a-CDs** and **g-CDs** showed that the CDs herein synthesized are composed by C and O in the ratios 45/55 and 65/35, respectively. The lower oxygen content of the **g-CDs** was attributed to the higher degree of carbonization reached by thermolysis. Analyzing the C1s band, the presence of C=C, C-O and C=O functional groups was revealed by the presence of three strong peaks centered around 284.6, 286.2 and 288.6 eV⁶⁰, respectively as shown in Figure 61.

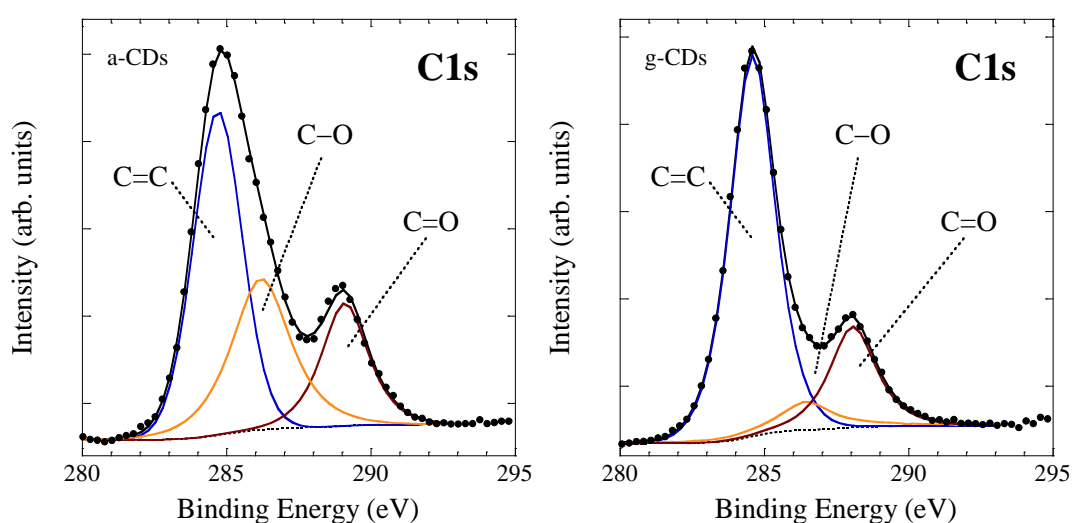


Figure 61. C1s XPS spectra of **a-CDs** (left) and **g-CDs** (right).

The optical properties of the nanomaterials were investigated by UV-Vis and fluorescence spectroscopy. The UV-Vis absorption spectra displayed in of **a-CDs** and **g-CDs** reveal a broad and largely featureless absorption across the near-UV tailing into the visible region as shown in Figure 62. This behavior is very common for CDs obtained without surface passivation or derivatization. This weak and asymmetric absorption band it is supposed to be generate by the various surface traps and defects states present on the surface which possess different energy levels below HOMO, which introduce multiple transition modes.

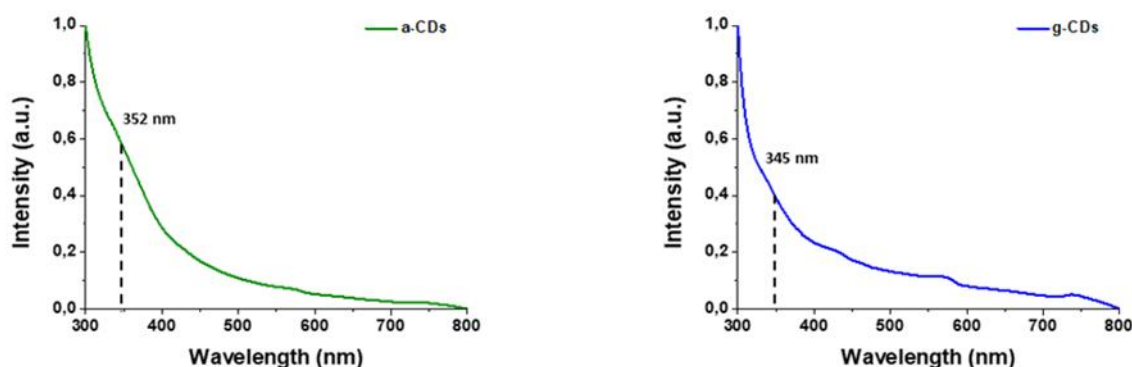


Figure 62. UV-Vis spectra of **a-CDs** (on the right) and **g-CDs** (on the left).

As shown in Figure 63 both the nanomaterials showed an excitation-dependent emission band whose maximum ranged between 420 and 500 nm. While no other contribution was visible for the **a-CDs**, a second sharp band was noticed for the **g-CDs**, whose intensity maximum at 385 nm seemed to be only slightly influenced by the excitation wavelength. The relatively simple emission spectrum of the **a-CDs** was tentatively attributed to the presence of multiple defects on the nanoparticle surface. The additional high energy transition of the emission spectra of the **g-CDs** could be instead ascribed to the crystalline core.¹⁶⁷

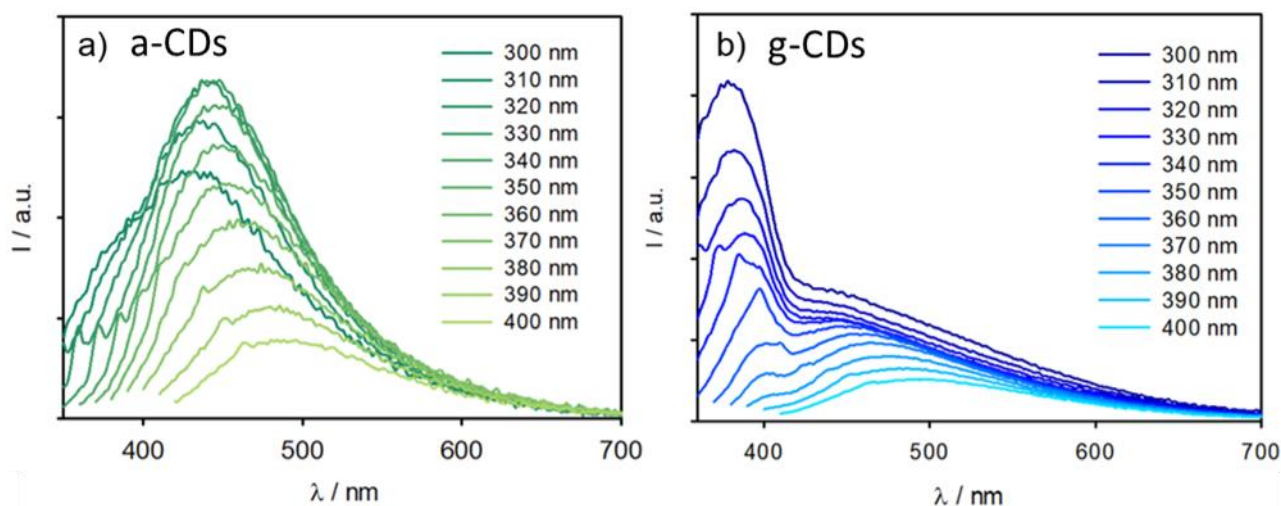


Figure 63. PL spectra of **a-CDs** (on the right) and **g-CDs** (on the left).

4.2.2. a-N-CDs and g-N-CDs

The nitrogen-doped **a-N-CDs** were synthesized by a procedure similar to the one described for the non-doped **a-CDs**. Hydrothermal treatment of citric acid in the presence of DETA at 180 °C for 6 h yielded the **a-N-CDs** as a brown solid in 72%_{wt} yield (See Chapter 2 for more details). Interestingly, the ¹H and ¹³C{¹H} NMR spectra (Figure 65) of the as-synthesized **a-N-CDs** showed a series of singlets and

triplets between 6 - 5 ppm and 4.8 - 2.8 ppm together with carbonyl (170-160 ppm), sp^2 (150-80 ppm) and aliphatic sp^3 (50-30 ppm) carbon environments that were assigned to molecular fluorophores with structures analogous to that of IPCA *e.g.* **3** (Figure 65) that is also responsible for the most abundant peak observed in the ESI(+/-)MS (Figure 64; $m/z = 224.1$ [**3** + H⁺]). In addition to the identified IPCA-like molecular compounds, the **a-N-CDs** samples contained also a series of un-defined oligomers with MW ranging from the signal at 270 Da assigned to **3**, up to 1000-1200 Da as revealed by both DOSY and ESI-MS.

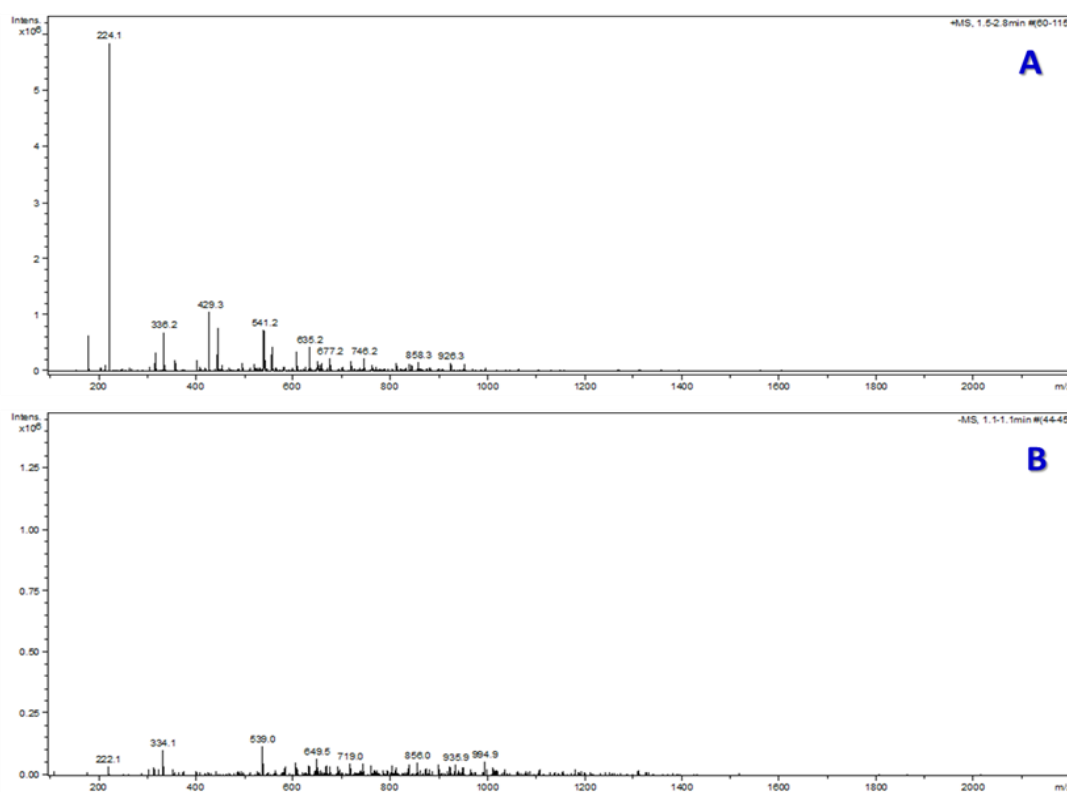


Figure 64. ESI(+/-)-MS spectra of **a-N-CDs** in H₂O. A) Positive mode. B) Negative mode.

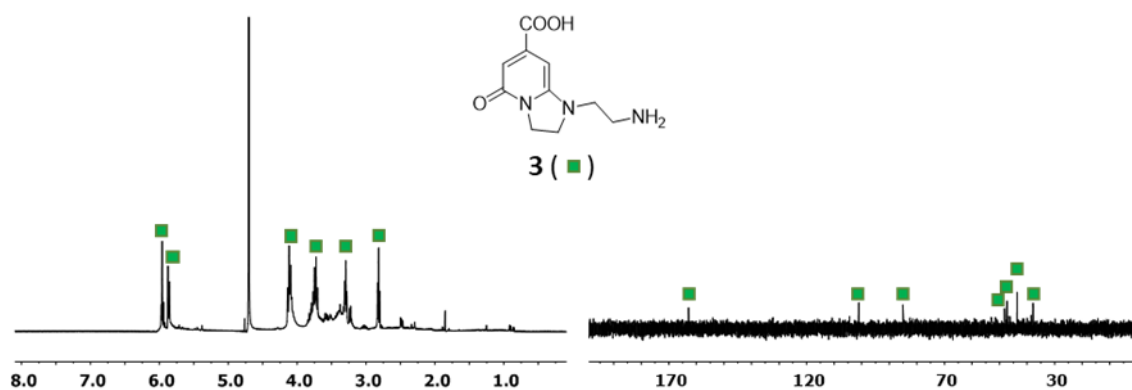


Figure 65. ¹H NMR and ¹³C{¹H} NMR interpretation.

The graphitic **g-N-CDs** were prepared by thermolysis followed by dialysis to selectively recover the doped carbogenic structures as a dark-brown solid in 18%_wt yield. The NMR analysis conducted on the **g-N-CDs** did not show significant resonances, while ESI-MS of the purified **g-N-CDs** led to detect the fluorophore **3** and a series of low-intensity signals spanning 200 - 2000 Da (upper instrumental detection limit). These data were consistent with the presence of complex mixtures formed by the coexistence of small fluorophores (probably non-covalently bonded to the dot), oligomers and/or extended carbonaceous cores.

HR-TEM of **a-N-CDs** yielded amorphous and poorly defined structures, while HR-TEM of the **g-N-CDs**, (Figure 66a) revealed the presence of a homogeneous and well-dispersed population of small nanoparticles with a quasi-spherical shape. Furthermore, as expected, only the **g-N-CDs** sample showed the presence of lattice fringes with an interlayer spacing of 2.4 Å, confirming their graphitic nature. In analogy to the above reported non-doped CDs, the size of the **a-N-CDs** and **g-N-CDs** was affected by the synthetic method: the harsher conditions led to the formation of smaller nanoparticles. However, N-doping increased their average dimensions from 3 to 17 nm **g-CDs/g-N-CDs**.

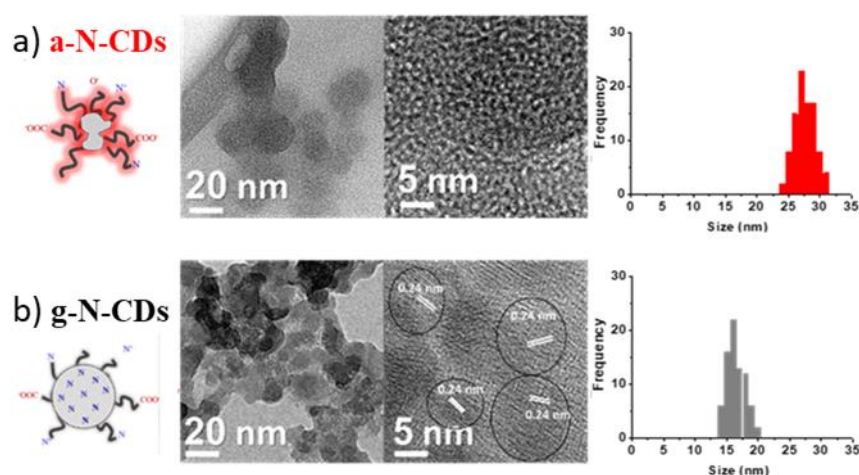


Figure 66. TEM and HR-TEM images of **a-N-CDs** and **g-N-CDs**.

The FT-IR spectra of the **a-N-CDs** and **g-N-CDs** in KBr are shown in Figure 67. along with the broad absorption bands around 3400 cm^{-1} corresponding to the O–H vibrations, new peaks due to the N-H stretching of amines/amide were detected around $3300\text{--}3000\text{ cm}^{-1}$. The presence of the doping reagent is also responsible for the additional very broad signals revealed around $3000\text{--}2800\text{ cm}^{-1}$ reasonably due to ammonium (RNH_3^+ ; R_2NH_2^+) groups. The strong absorption bands around $1773\text{--}1600\text{ cm}^{-1}$ reflected the presence of acids, ketones and amide groups. Furthermore, the multiple

signals at 1600-1400 cm^{-1} were assigned to both C-C stretching of aromatic or conjugated double bonds, and N-H bending of the above discussed N containing groups. Interestingly, only for the **a-N-CDs** sample uncommon signals were revealed at 2025 and 2015 cm^{-1} which were tentatively assigned to the presence of molecules containing $\text{-C}\equiv\text{N}$ or -C=N- groups.

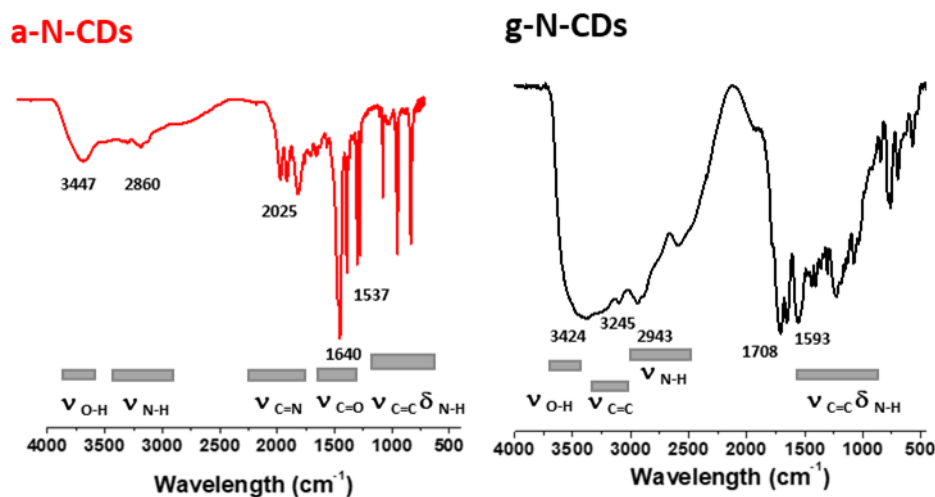


Figure 67. FT-IR spectra in KBr of **a-N-CDs** and **g-N-CDs**.

More specific details on the chemical composition of the as synthesized nitrogen doped CDs were extrapolated by the XPS spectra shown in Figure 68. The analysis reveal a composition dependent on the synthetic protocols employed, with a less amount of nitrogen detected for the pyrolysis (C,O,N ratio of 65/30/5 for **g-N-CDs**) respect to the hydrothermal (C,O,N ratio of 70/20/10 for **a-N-CDs**). The high resolution XPS spectra also confirmed the FTIR assignments, with a C1s region exhibiting C=C (around 284.7 eV), C-O and/or C-N (around 286.3 eV), C=O and/or C=N (around 288.6 eV) signals. The N1s peak shows two bands, related to both pyridinic environments or -NH_2 groups (around 399.1 eV),¹¹⁵ and to the C-N-C groups¹⁶⁸ (around 400.4 eV); this last band was absent in the **g-N-CDs**, consistent with the formation of an N-doped graphitic core, due to the harsh synthetic protocol.

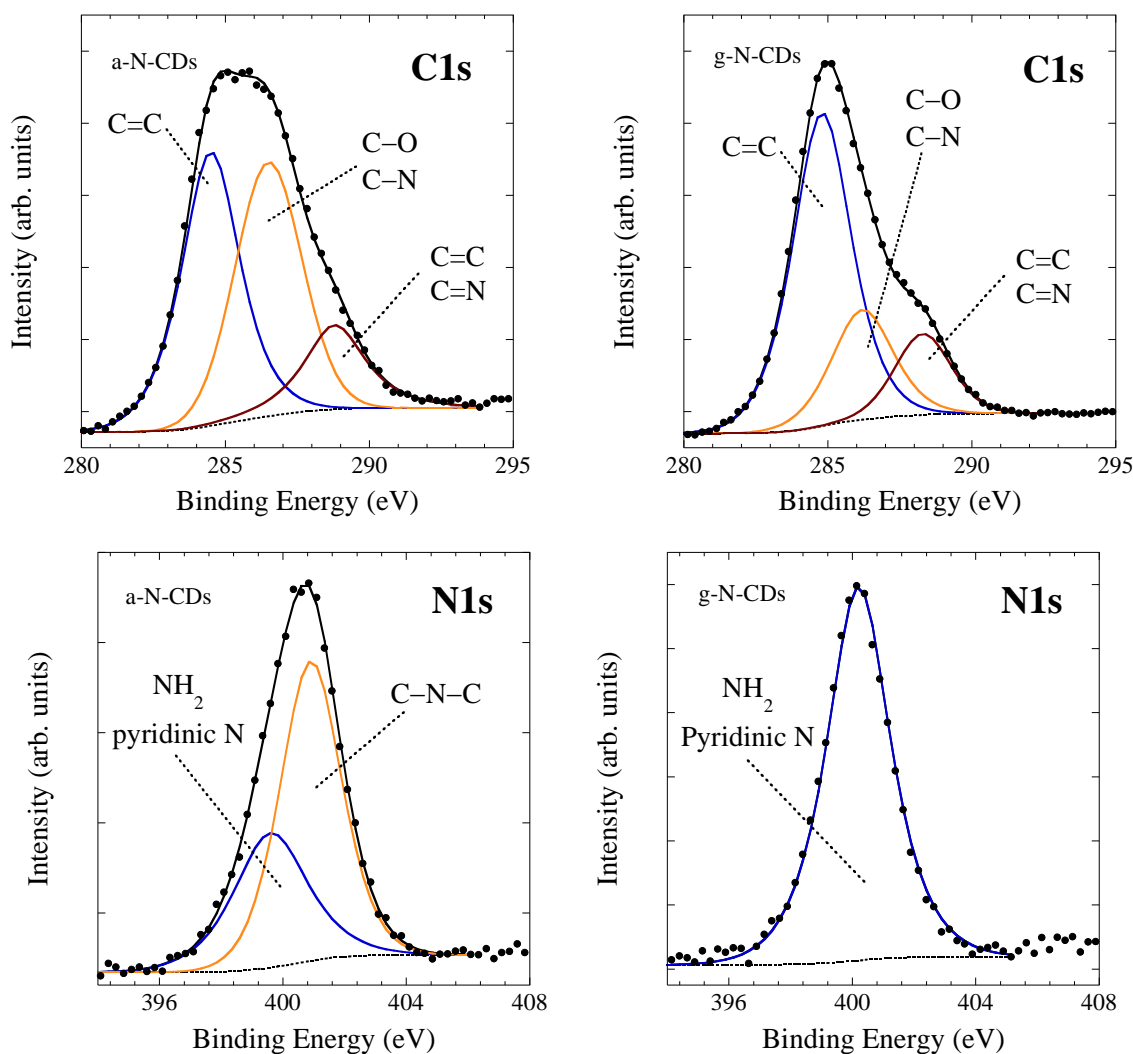


Figure 68. C1s (up) and Ns1 (down) XPS spectra of **a-N-CDs** (left panel) and **g-N-CDs** (right panel).

The optical characterization of the doped CDs was carried out with the UV-Vis and fluorescence spectroscopy. The absorption spectra of the two samples result to be very similar, showing two absorption bands centered at 240 and 350 nm. The presence of the detected fluorophore **3**, strictly affect the optical behavior of the **a-N-CDs**, since the transition observed could be easily ascribed to the π - π^* transition and to the n - π^* in the molecule as already demonstrate for similar compound. The absorption spectra of the graphitic sample confirm the presence of **3** in the mixture, reasonably absorbed or attached on the dots, as results the absorption spectra is dominate by the transition of the fluorophore molecule as illustrated in Figure 69.

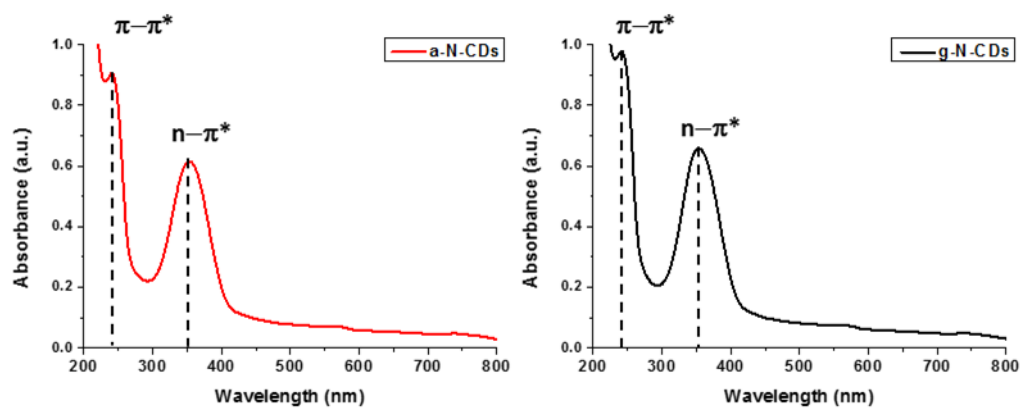


Figure 69. UV-Vis absorption spectra of **a-N-CDs** and **g-N-CDs**.

The molecular fluorophore affected also the PL spectrum of the **a-N-CDs** and **g-N-CDs** which resulted in a similar excitation independent wavelength behavior with an emission peak centered at 450 nm (Figure 70).⁸⁶ The results herein showed are consistent with other already published for similar fluorophore molecules.

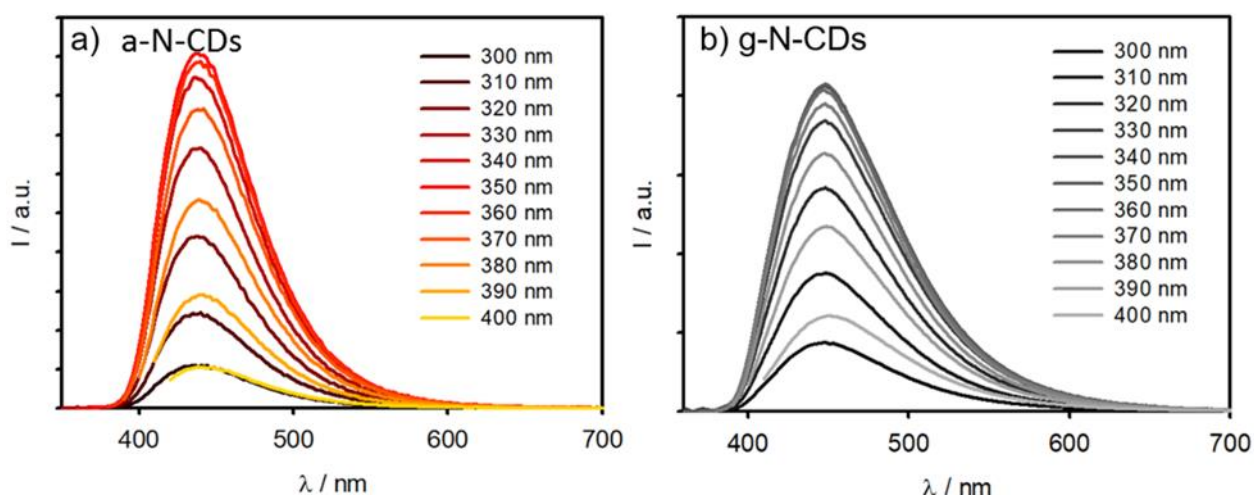


Figure 70. PL spectra of **a-N-CDs** and **g-N-CDs** at different excitation wavelength.

4.3. Quenching measurement

The as synthesized and characterized CDs were then employed as photosensitizer, and the photoreduction chosen as a model is the one of the MV^{2+} . This reaction due its simple and easy way of monitoring is often chosen as a model reaction to study the photocatalytic properties of various system. In order to correlate the photoinduced electron transfer process whereby an electron is transferred from the photoexcited state of the CDs to an acceptor molecule of the as synthesized CDs with their morphology, chemical structure and optical properties some preliminary tests were

conducts to evaluate other important parameters that could affect the photocatalytic behavior. In first instance the Quantum Yield (QY), the lifetime of the excited states (τ) and the mass absorption coefficient was evaluated. The QY was calculated based on the quinine sulfate, the results obtained were reported in **Table 4**. As reported the QY of the undoped CDs, results to be relatively low (Entry 1 and 2), these data are no surprising since the absence of any doping atom is known to led to the values of QY.⁵¹ The addition of a nitrogen compound in the synthesis has as consequence an enhancing of the QY as highlighted by the entry 3 of the **Table 4**, due to the formation of the fluorophore **3**. Interestingly, despite the addition of the doping agent the **g-N-CDs** shows a much lower QY compared to the amorphous counterpart. This observation confirms that the synthetic pathways employed combined with the dialysis purification led to the obtainment of a sample fluorophore-free. The atypical behavior of the graphitic nitrogen doped CDs could be explained by the mechanism of photoluminescence proposed by Fang *et al.* in which the graphitic core of the CDs could act as a quencher of the photoluminescence resulting in lower QY.⁴⁹

Table 4. QY, ϵ , and τ calculated for **a-CDs**, **g-CDs**, **a-N-CDs** and **g-N-CDs**.

Entry	CDs	QY	ϵ	τ
1	a-CDs	1.0 %	1.16	3.6
2	g-CDs	1.2 %	4.68	4.3
3	a-N-CDs	17.3%	13.93	13
4	g-N-CDs	2.4%	11.62	6

Another important parameter that has to been taken in account for deeper understand the characteristic of the nanomaterials and their photocatalytic ability, is the mass absorption coefficient (ϵ). This parameter allows to determine the light harvesting capability of the synthesized nanomaterials. The absorbance measured for different concentration at 365 nm for **a-CDs**, **g-CDs**, **a-N-CDs** and **g-N-CDs** along with the calculated linear regression are displayed in Figure 71 (See experimental section for more details).

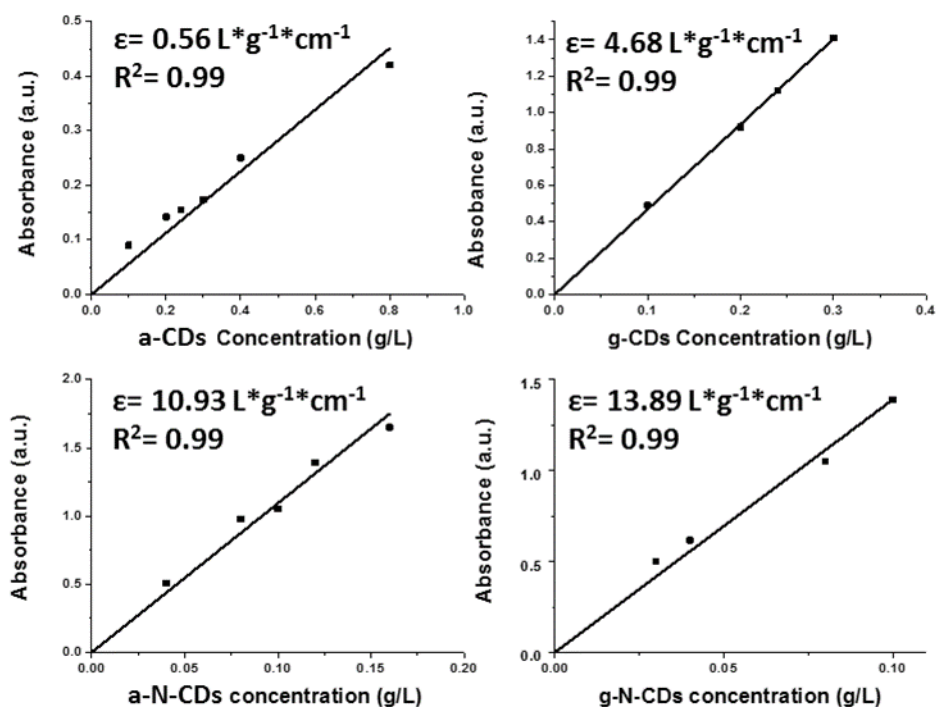


Figure 71. Calibration curve for mass absorbance coefficient (ϵ) of **a-CDs**, **g-CDs**, **a-N-CDs** and **g-N-CDs** at 365 nm.

The results obtained confirmed, once again, how the introduction of the nitrogen atom in the structure of the nanoparticles led to an enhancement of their optical properties. In this specific case, both **g-N-CDs** and **a-N-CDs** demonstrate an ϵ much higher respect to the similar undoped CDs. These results suggest that the nitrogen doped CDs could absorb a greater amount of photon and respect to the **a,g-CDs** consequently they could generate more exciton electron that could be used in the photocatalytic reaction.

Furthermore, in order to perform an efficient photo-reaction the excited electron generate upon irradiation should possess a sufficient lifetime to perform the PET. The lifetimes of the excited states for all the four CDs were calculated by time-resolved photoluminescence measurements and the PL decays are shown in Figure 72.

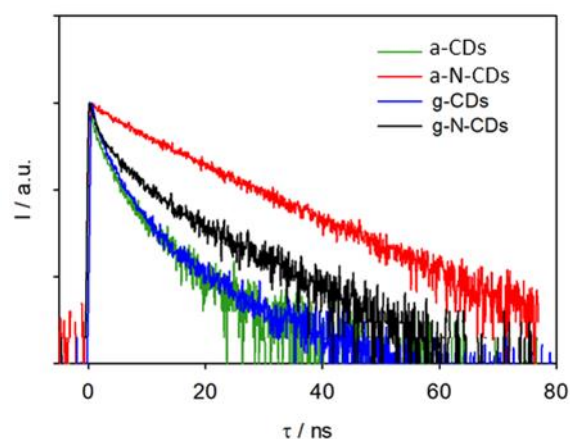


Figure 72. Time-resolved photoluminescent (PL) measurements of **a,g-CDs** and the **a,g-N-CDs**.

The decay showed in the figure is singly-exponential only for the **a-N-CDs**, while the other samples follow a multi exponential decay. Therefore, they were fitted by using a triple-exponential curve and the resulting parameters are reported in **Table 5**, the final lifetime was calculated as the weighted average of the lifetime of three contribution. The **a-N-CDs** results to possess the higher lifetime and its more linear character was consistent with a molecular-like emission,¹⁵⁵ explained by the presence in its structure of fluorophores such as **3** and other IPCA-like derivatives. Lower values were observed for the other CDs especially for the undoped CDs with a τ of 3.6 and 4.3 ns for **a-CDs** and **g-CDs** respectively.

Table 5. Fitting parameters of photoluminescence decays displayed in Figure 72.

Sample	τ_1 / ns	A1	τ_2 / ns	A2	τ_3 / ns	A3	$\langle \tau \rangle / \text{ns}$
a-CDs	0.35	311	2.06	496	6.69	153	3.6
g-CDs	0.64	1034	2.87	643	11.63	59	4.3
a-N-CDs	2.47	55	8.20	265	15.01	607	13.0
g-N-CDs	0.89	578	4.17	410	13.41	151	8.1

Finally, in order to evaluate the existence of a Photo Electron Transfer (PET) between the CDs and MV^{2+} a steady state fluorescence quenching approach was employed. In fact, in presence of an acceptor molecule in solution the CDs could donate their electron to such molecules, having as results a quenching of their luminescence. Measuring the fluorescence emission of a solutions with constant CDs concentration at a fixed wavelength with increasing amount of MV^{2+} led to understand the mutual interaction between the two species. In other words, more the two species are attracted to

each other, and more pronounced is the quenching of the fluorescence emission. The detailed procedure for measuring the quenching of the fluorescence is illustrated in the experimental section and the results of the as described studies for **a-CDs**, **g-CDs**, **a-N-CDs** and **g-N-CDs** are displayed in Figure 73. It is apparent that for all the CDs tested a quenching of the photoluminescence emission occur, confirming the feasibility of PET process between the species.

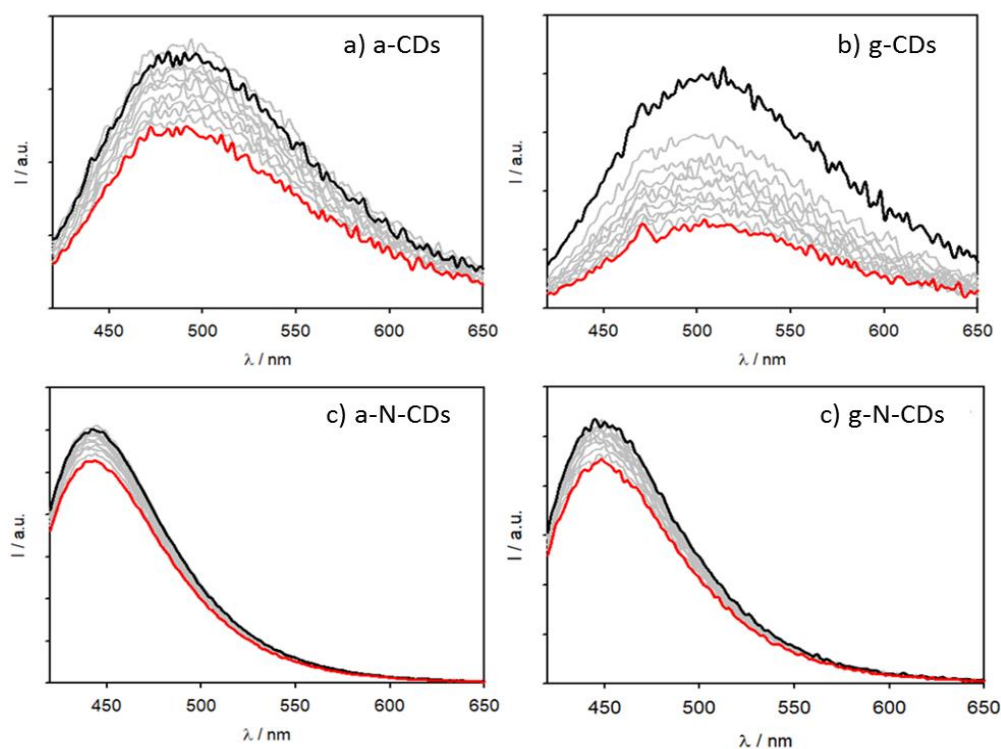


Figure 73. Emission spectra of CDs at different addition of MV^{2+} , starting from the black (no additions) to the red curve.

In order to evaluate the rate of the quenching, and consequently the strength of the interaction between the different CDs and the MV^{2+} , the Stern-Volmer plot of the above-mentioned emission spectra should be extrapolated. Furthermore, also the quenching of lifetimes of the excited states of the CDs in the same conditions was evaluate. The results obtained by the linearization are shown in Figure 74.

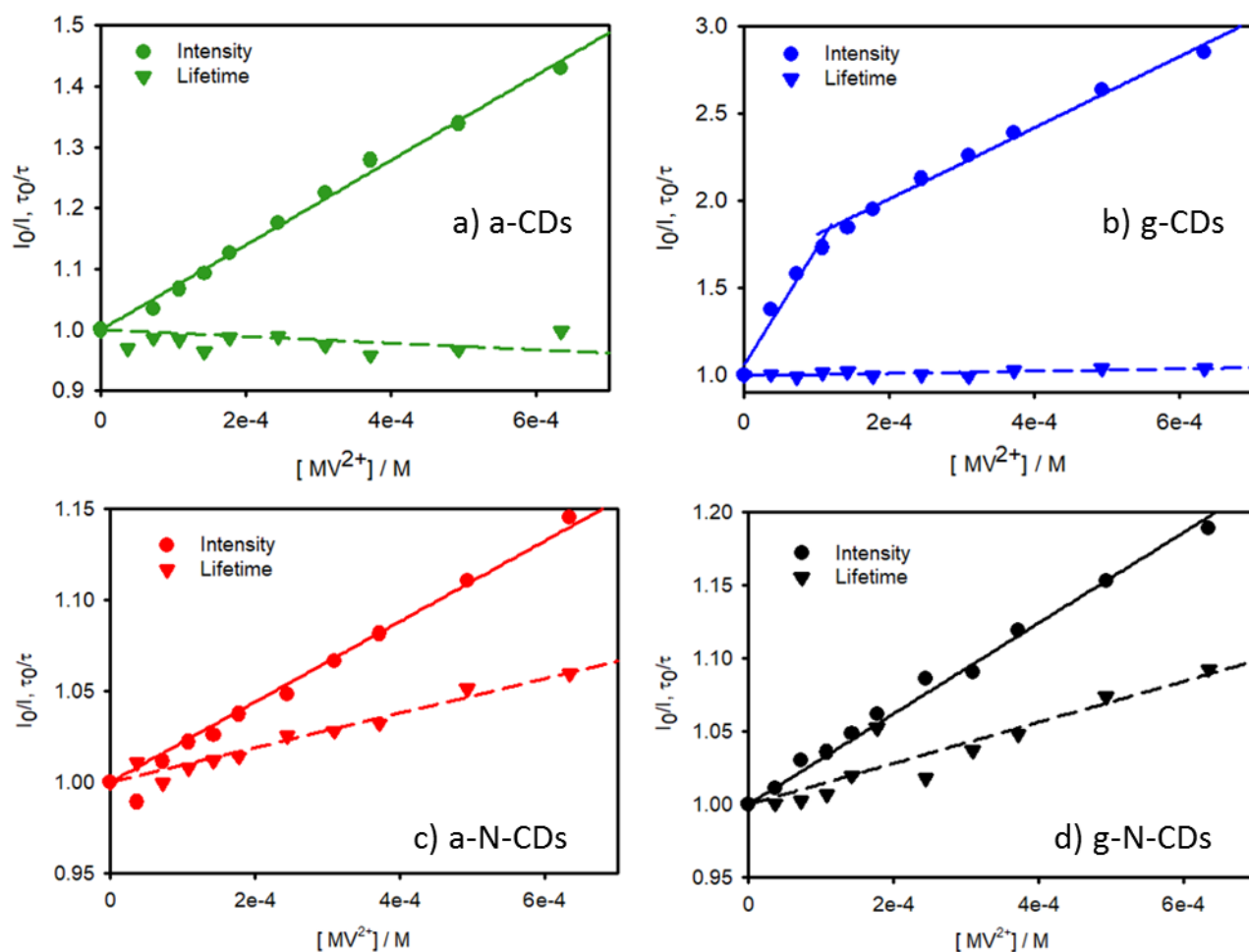


Figure 74. Variation of photoluminescence intensity and lifetime ($\lambda_{exc} = 405$ nm) for isoabsorbing CDs solutions upon addition of increasing concentration of MV^{2+} in solution up to 6×10^{-4} M.

For all the CDs synthesized except **g-CDs** a linear trend was observed for the quenching of the photoluminescence, and the Stern-Volmer constant $K_q(I)$ can be easily extrapolated from the plots, nevertheless for the graphitic undoped CDs two linear trends were noticed. This different behavior could be associated to the absorption of a first layer of MV^{2+} (for the first linear trend) and successive layer for the second trend. A similar procedure was employed for determine the constant of quenching of the lifetime of the excited states $K_q(\tau)$ and the results are summarized in Table 6.

The k_q values reveal high CDs- MV^{2+} interaction for both doped and non-doped CDs. The behavior of the N-doped **a-N-Cd** and **g-N-CD** was ascribed to a diffusion-limited dynamic quenching process,^{169, 170} since the k_q values obtained from the intensity and lifetime decay fittings are close to each other and to the diffusion limit.¹⁵⁵ On the contrary, for the non-doped samples the large discrepancy between the lifetime quenching rate and the photoluminescence quenching rate highlights a more complex situation. Indeed, the photoluminescence intensity quenching constant is far larger than the one obtained from the lifetime decay interpolation, whose value is close to 0 in the **a-CDs** sample. In

addition, the k_q (l) for these samples is larger than the expected diffusion limit, suggesting the occurrence of a static quenching process deriving from the ground-state interaction between CDs and MV^{2+} .

Table 6. Quenching constants of the CDs with MV, calculated on the fluorescence intensity and lifetime

Entry	k_q (l) ($\times 10^{10} \text{ M}^* \text{s}^{-1}$)	k_q (τ) ^a ($\times 10^{10} \text{ M}^* \text{s}^{-1}$)
a-CDs	19	0
g-CDs	59	1.6
a-N-CDs	1.6	0.78
g-N-CDs	4.1	1.8

^a Calculated on the average lifetime

The higher affinity revealed for the undoped CDs find a good explanation in the ζ -potential measurement (see experimental section for details and appendix). The analyses were carried out on the graphitic sample and highlighted the higher negative charge of -50 mV for the **g-CDs** respect to the **g-N-CDs** (ca. -15 mV). This difference can be easily explained by the different surface groups present on the nanoparticles, in particular the protonate amino groups of the doped sample could be the cause of the more positive potential. Furthermore, from these data it is intuitively that the CDs with the more negative ζ -potential can favors the ground state CDs-MV physical encounter, through strong coulombic interactions, while the less negative value of the N-doped g-N-CDs results in a more dynamic interaction between the **g-N-CDs** excited state and the MV quencher. Along with the rationalization of the nature of the MV-CDs supramolecular interactions, the luminescence quenching experiments pointed out a surface-dependent photoexcitation behavior of the CDs which is bound to affect also their photocatalytic behavior.

4.4. MV reduction

The photocatalytic activity of the prepared CDs was tested in the photoreduction of the MV^{2+} (-0.45V vs NHE). This reaction is widely use as model-reaction due to its easy way of monitoring, in fact the reduced species MV^{+} presents a characteristic blue coloration with an absorption maximum centered at 605 nm. Despite this great advantage the reaction presents some side effect, first of all the reduced specie could be instantly be quenched by the oxygen, consequently the reaction need to be performed under inert conditions. Furthermore, the radical cation specie formed after the irradiation can react with another to generate the diradical species the is colorless¹⁷¹. Due to these problematics

the photoreduction of MV^{2+} will be evaluated in term of initial rate more than its conversion. In order to compare the photoreactivity of the CDs towards the reduction of the MV isoabsorbing solution at 365 nm of the four CDs were prepared using different CDs concentrations. The reaction was performed in water solutions of CDs, using EDTA as sacrificial electron donor with a MV concentration of 60 μM and under LED irradiation (365 nm). The reaction profile obtained are shown in Figure 75 and in Table 7 and clearly highlight that the morphology and the composition of the CDs influence the PET reactivity.

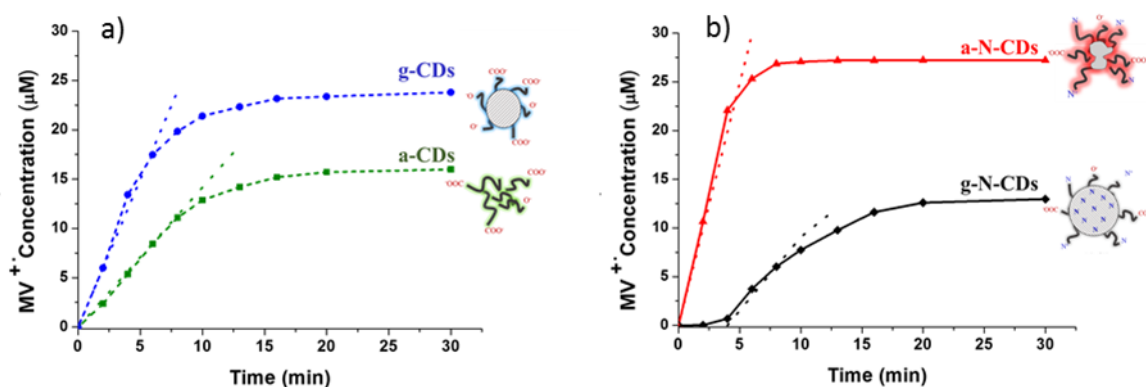


Figure 75. Reaction kinetics of formation of $MV^{\bullet+}$ using a,g-CDs (a) and a,g-N-CDs (b).

In detail, the **a-N-CDs** (red points) exhibited high initial photoreduction rate ($v_0 = 7.83 \times 10^{-8} \text{ Ms}^{-1}$), high TOF ($195 \text{ g} \cdot \text{CDs}^{-1} \cdot \text{s}^{-1}$) and the highest MV^{2+} conversion (27%), this results are comparable to the initial rate *ca.* $8 \times 10^{-8} \text{ Ms}^{-1}$ measured by Reisner and Prato.^{60, 55} The second-best performance was shown by the **g-CDs** ($v_0 = 5.06 \times 10^{-8} \text{ Ms}^{-1}$; TOF = $72 \text{ g} \cdot \text{CDs}^{-1} \cdot \text{s}^{-1}$), while poorer initial rates were instead observed for the **a-CDs** and **g-N-CDs**, the latter exhibiting also an induction time of 6 min. The latter was deeply investigated in order to evaluate if some chemical transformation occur and could affect the photoreaction. For this aim 3 repeated runs with the same CDs were carried out and the results shows that the induction time persist and that it is an intrinsic property of **g-N-CDs** not associated to an “irreversible” structural/morphological/chemical transformations (Figure 76).

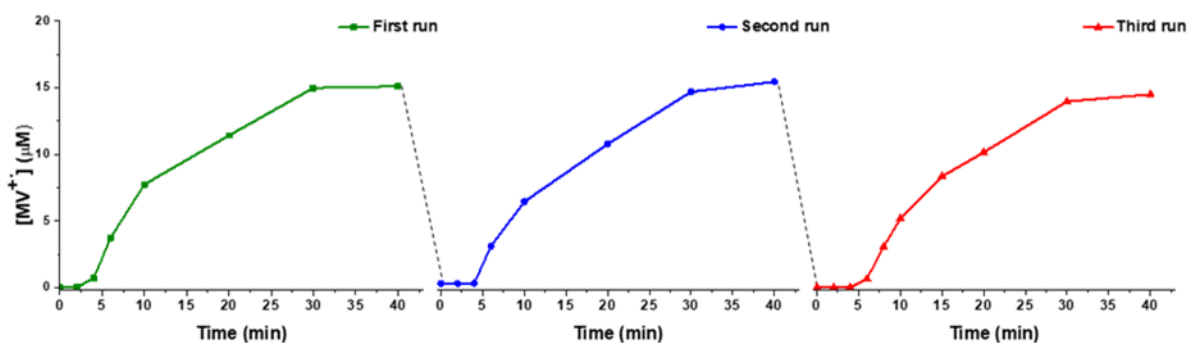


Figure 76. Subsequent MV photoreduction runs with **g-N-CDs**.

Looking at the MV photoreduction results an opposite structure/reactivity trends for the two families of CDs was noticed, specifically: the graphitic domains proved to be essential when using non-N doped systems (**g-CDs** > **a-CDs**); instead, for the N-doped nanostructures (**a-N-CDs** > **g-N-CDs**) the presence of molecular-like fluorophores, rather than the carbogenic core, is of crucial importance. As a control, all the experiments performed without CDs and without light gave no conversion of MV confirming that both a light source and the sensitizers were needed for the evolution of the reaction. These results help to understand the structure-activity relationship of CDs for photocatalysis, in particular the amorphous **a-N-CDs** for the first time were tested in this context and results to be the more active respect to both the non-doped **a-CDs** and **g-CDs** as well as the N-doped graphitic-like homologues (**g-N-CDs**), the latter considered the most promising class of nanoparticles for solar hydrogen production⁶⁰

Furthermore, for a deeper understanding of the structure-reactivity relationships the data obtained from the photocatalytic test were compared to the one obtained by the Stern-Volmer plots. The trend observed in the reaction of the non-doped samples (**g-CDs** > **a-CDs**) could be explained by the higher ground interaction observed for graphitic sample compared to the amorphous. This deduction, however cannot explain the photocatalytic result because the **a-N-CDs** showed higher performance notwithstanding their K_q values are more than one order of magnitude lower. An explanation on the higher reactivity exhibited by the **a-N-CDs** could be extrapolated comparing all the data obtained from the characterization previously performed which results are summarized in Table 7.

Table 7. Photocatalytic performance, average lifetime (τ), quantum yield (QY) and mass absorption coefficients (ϵ) of the synthesized CDs.

Entry	$\nu_0 \cdot 10^{-8}$ ($M \cdot s^{-1}$)	TOF mol MV \cdot g CDs $^{-1}$ s $^{-1}$	QY (%)	ϵ ($L \cdot g^{-1} \cdot cm^{-1}$)	τ (ns)
a-CDs	3.45	9	1.0	1.16	3.6
g-CDs	5.06	72	1.2	4.68	4.3
a-N-CDs	7.83	195	17.3	13.93	13
g-N-CDs	1.95	65	2.4	11.62	6

One of the main requirements to perform a photocatalytic reactivity is that the photosensitizer absorbs a great amount of energy and this can be evaluated by the ϵ . Furthermore, the excited electron should possess a sufficient lifetime to perform the reaction. From these considerations it is possible to understand why the a-N-CDs results to be the best choice for photocatalysis. The values of ϵ and τ are the responsible for the higher TOF calculated for this sample that is more than 3 time higher than that of the **g-N-CDs**, demonstrating that the presence of free molecular-like fluorophores and the absence of N-doped graphitic domains are among the key morphological features needed to ensure a high PET efficiency of the carbon dots in a fully dynamic MV-CDs interaction system.

4.5. Conclusion

In this work four new CDs were synthesized and characterized from either chemical, morphology and optical point of view, revealing how the different synthetic condition such as, pyrolysis or hydrothermal, and doped and non-doped, could affect the final properties of the nanomaterials. The softer condition employed in the hydrothermal synthesis led to the obtainment of amorphous materials, while the harsher condition of the pyrolysis afford the synthesis of graphitic materials. The presence of the nitrogen results in an enhancement of the optical properties of the nanomaterials with the formation of molecular-like fluorophores. All these effects result also to affect the photocatalytic properties of the materials towards the single-electron reduction of methyl viologen. First, the structure and morphology of the CDs act in opposite way with or without the doping agent, in promoting photoredox activity of the CDs. The sample obtained from the solely citric work best in the photoreduction of methyl viologen when their structure is graphitic rather than amorphous; while for nitrogen-doped CDs it is clear that graphitic particles are far less active compared to their amorphous counterpart. From these data emerged that the presence of molecular-like fluorophores

promotes the photoreduction of MV as showed by the **a-N-CDs**, but the presence at the same time of graphitic domains results in a poor reactivity due to the internal FRET that quench the excited electrons. Conversely, the non-doped graphitic particles are more photoredox-active of their amorphous analogous due to the lack in the latter of any photoactive molecules as well as to the absence of graphitic defect-states able to promote the excitation of an electron.

The results obtained are also supported by the electrostatic interactions between the surface of the CDs and the reactant methyl viologen that can determine whether the supramolecular attraction is static or dynamic. ζ -potential for the non-doped CDs results to be very negative and determines a static quenching favored by strong ground state interactions; while the behavior of the nitrogen-doped CDs was ascribed to a diffusion-limited fully dynamic quenching process between the excited state of the g-N-CDs* and methyl viologen.

Overall, the results herein reported highlight the complex nature of the photochemistry of CDs and demonstrate that full understanding of the role of the precursors and of the degree of carbonization are key parameters to achieve the desired photocatalytic properties.

4.6. Experimental

4.6.1. XPS measurement

X-ray photoelectron spectroscopy (XPS) was performed using a Perkin Elmer Φ 5600ci spectrometer using nonmonochromatic Al K_{α} radiation (1486.6 eV) in the 10^{-7} Pa pressure range. All the binding energy (BE) values are referred to the Fermi level. The correct calibration of the BE scale was verified by checking the position of both Au4f_{7/2} and Cu2p_{3/2} bands (from pure metal targets), falling at 84.0 and 932.6 eV, respectively. After a Shirley-type background subtraction, the raw spectra were fitted using a nonlinear least-squares fitting program adopting Gaussian–Lorentzian peak shapes for all the peaks. Because of surface charging, samples presented limited but different shifts of all bands toward higher BEs. The charging effect was then carefully determined and corrected in two steps: i) by using an internal reference (the C1s position of the band related to C=C bonds); ii) by checking, after the charging correction, the consistency of the BE positions of all the components evidenced in all the different XPS peaks. The uncertainty of the determined BEs was lower than 0.2 eV. The atomic composition was evaluated using sensitivity factors as provided by Φ V5.4A software. The relative uncertainty of the reported atomic fraction of the different elements is lower than 0.1.

4.6.2. Mass absorption coefficient

The measurements were performed by measuring the absorption of solutions with different concentration of CDs at a fixed wavelength, the values obtained were then plotted in function of the concentration. The calculated linear regression for these points reflect the Lambert Beer law (1) from which it is possible to extrapolate the mass absorption coefficient.⁶⁰

$$A = \varepsilon * b * C \quad (1)$$

Where:

A = Absorbance

ε = Mass absorption coefficient ($L \cdot g^{-1} \cdot cm^{-1}$)

b = path length (1 cm)

C = Concentrations (g/L)

4.6.3. CDs-Viologen quenching measurements

To measure the quenching efficacy of the CDs with the MV, a steady state fluorescence quenching approach was adopted. Briefly, to 2mL of isoabsorbing solutions of CDs ($\lambda_{exc}=405$ nm) 0.5mL of PBS buffer solution (pH 7.00) were added. After checking the pH with a pH-meter, the initial photoluminescence spectrum and time decay were collected. The solution was then titrated with increasing amount of a water solution of MV registering the variation of CDs luminescence properties. Despite the negligible volume variation, a volume correction has been applied to the registered spectra. The Stern-Volmer plots were obtained by plotting the concentration of the quencher added vs the ratio of the I/I_0 where I_0 and I are respectively the fluorescence intensity of the solution of CDs with and without the addition of MV, it is possible to correlate the result with the stern Volmer equation (2 and 3).

$$\frac{I}{I_0} = K_{sv} * [Q] \quad (2)$$

$$\frac{\tau}{\tau_0} = K_{sv} * [Q] \quad (3)$$

Where:

[Q]= Concentration of quencher (MV) added

I, τ = fluorescence intensity and lifetime of the solution of CDs with addition of MV

I_0, τ_0 = fluorescence intensity and lifetime of the solution of CDs without addition of MV

K_{sv} = Stern-Volmer constant

The initial lifetime τ_0 and the one measured at each MV^{2+} concentration were determined by averaging the multiple contributions to the multi-exponential photoluminescence decay while the intensity values are obtained by integrating the emission spectrum over the 400-650 nm wavelength range.

4.6.4. Photocatalytic experiments

A solution composed by 0.1M of EDTA, 60 μ M of MV with an absorbance normalized amount of CDs (a.b.s. = 0.5; 1.2 mg **a-CDs**, 0.21 mg **g-CDs**, 0.12 mg **a-N-CDs**, 0.09 mg **g-N-CDs**) were placed under inert atmosphere in a quartz cuvette. The solutions were then irradiated at 365 nm fixed wavelength emission (Hangar s.r.l.; ATON LED-UV 365; 80 W/m² of irradiance in the UVA spectral range 315-400 nm⁻¹). The progress of the reactions was monitored using an UV spectrophotometer following the formation of the typical absorption band of the reduced MV^+ radical cation form centered at 605nm and its concentration was estimated using $\epsilon = 13700 \text{ M}^{-1} \text{ cm}^{-1}$.

4.6.5. ζ -potential

The samples are dispersed in 0.1M NaCl solution and the pH adjusted to 7.00 by means of HCl or NaOH addition. NaCl was used as electrolyte to ensure sufficient charge mobility.

5. Results: Photoreductive cleavage of C-O bond

5.1. Introduction

The CDs ability in performing simple photocatalytic reactivity was previously described, demonstrating how the synthetic condition employed and the differences in chemical, structural and optical properties deriving from it affect the photoreduction. Assuming this concept and understanding the factors that could promote or quench the reactivity, the next step is to extend the reactivity towards more functional reactions and use the CDs as only photosensitizer in organic photoreaction. Up to date the use of CDs for performing organic reaction is limited by the use of co-catalyst such as metal complexes or enzymes. A case in point is the work published by Reisner's group on the reduction of the fumarate to succinate using the CDs as photocatalyst along with the fumarate reductase.¹⁶² They proved that employing CDs properly derivatized could act as electron donor if irradiated by a solar light simulator, demonstrating for the first time the possibility to use CDs for performing organic reaction. The strictly conditions in term of pH range activity and buffer solution required for the use of enzymes limits their application in the photochemical panorama. Up to date CDs were never employed as sole sensitizer to perform organic photoreactions. For this aim

the photodeprotection of N-Methyl-4-picolinium (NMP) esters was investigated. The N-Methyl-4-picolinium moiety is a well-known photoremovable protecting group (PRPG) that are already use for protecting the carboxylic groups in the peptide synthesis^{172,173}. The groups can be removed from the carboxylic acid via photochemical reaction employing a organic photocatalyst as demonstrated by Sundararajan *et al.*¹⁷⁴ In this chapter the use of CDs as cheaper, safe and sustainable alternative for performing photodeprotection of NMP esters was investigated. In this context, three carboxylic acids such as: octanoic acid, benzoic acid and p-nitro benzoic acid were protected with the NAP moiety through a four-step synthetic procedure. The photodeprotection reactions of such ester was investigated by using a library of CDs under irradiation with UV light. Different behaviors were observed for the CDs, confirming the results already discuss in the previous chapter. Furthermore, cyclovoltammetry study were conduct on both the CDs and the esters to rationalize the results of the photo-catalytic cleavage reaction. This study led to calculate the energy of the HOMO and LUMO orbitals in the CDs, along with the relative band gap, and also the propensity of the NMP esters to undergo the cleavage. All the consideration herein obtained led finally to the proposal of a new mechanism for the photocleavage of the NMP esters with CDs as sensitizer.

5.2. Synthesis of CDs

Along with the CDs already described and characterized in this thesis, four new CDs were synthesized from glucose and fructose in both a single precursor synthesis or in combination with DETA as doping agent with a pyrolysis synthesis as described in Chapter 2. The pyrolysis of glucose or fructose led to the obtainment of **g-Glu-CDs** and **g-Fru-CDs** respectively, while the addition of DETA in the pyrolysis of the carbohydrates afford the synthesis of **g-N-Glu-CDs** and **g-N-Fru-CDs**. The new nanomaterials were then characterized with a plethora of techniques in their structural and chemical properties.

The surface chemical groups were studied by the FT-IR techniques, the spectra of all the four sample were registered using a KBr pellet and are shown in Figure 77. It is possible to notice that the spectra of the non-doped CDs present only few absorption bands, the one at 3400 cm^{-1} attributed to the stretching of the hydroxyl groups and the two bands at 1660 and 1390 cm^{-1} respectively assigned to the stretching of the carbonyl and C=C double bonds. When the nitrogen dopant is added a new absorption band correlated to the bending of the N-H groups appear at $1580\text{-}1590\text{ cm}^{-1}$ confirming the addition of the nitrogen inside the nanostructure.

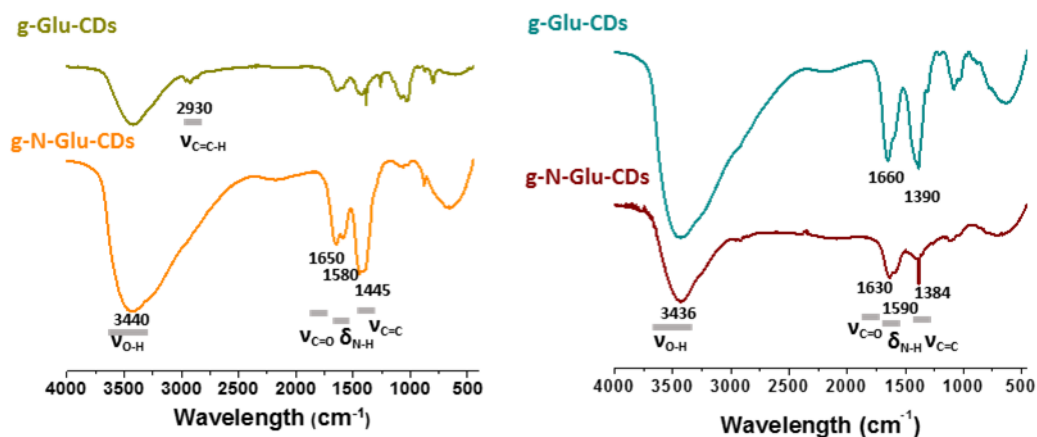


Figure 77. FT-IR spectra of g-Glu-CDs, g-Fru-CDs, g-N-Glu-CDs and g-N-Fru-CDs.

The four monosaccharides derived CDs obtained through the pyrolysis synthesis, were characterized in an optical point of view, with the already known techniques like UV-Visible and fluorescence spectroscopy. The UV spectra of the synthesized CDs were collected by preparing an aqueous solution of 0.25 mg/mL of nanoparticles. The resulting spectra are shown in Figure 78.

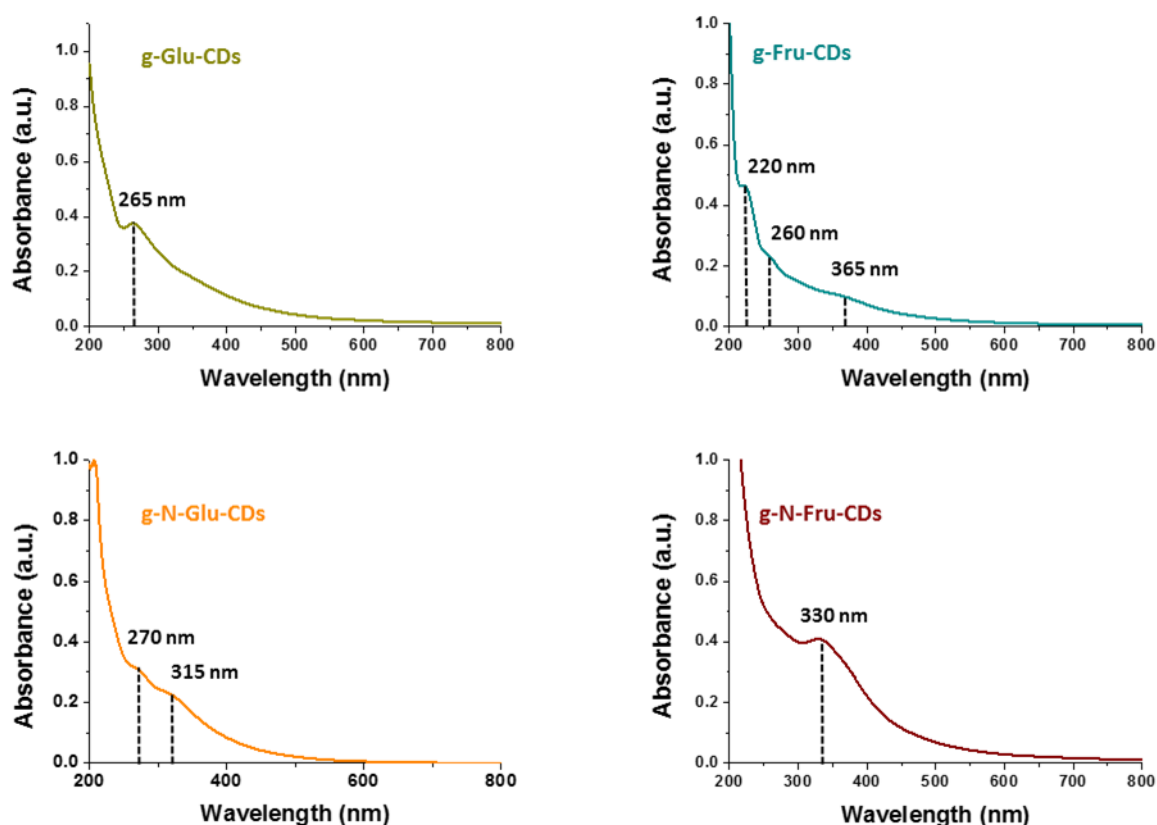


Figure 78. UV-Vis spectra of g-Glu-CDs, g-Fru-CDs, g-N-Glu-CDs and g-N-Fru-CDs.

For the glucose derivatives it is possible to see that the addition of the doping agent leads to the formation of a new absorption peak at 315 nm due to the $n-\pi^*$ transitions from nonbonding orbitals, while the transition at 270 nm is ascribed to the transition of the $n-\pi^*$ from surface carbonyl groups.¹⁷⁵ The fructose derivative instead show a more complex spectra for the undoped sample, with three absorption band at 220, 260 and 365 nm. The first two can be ascribed to the $\pi-\pi^*$ transition of the sp^2 C=C conjugated system and the C=O $n-\pi^*$ transitions respectively while the trapping of the excited-state energy by the surface state is correlated to the third one. The addition of the doping agent in the structure of the carbon nanoparticles, results in a simplification of the absorption spectrum, with a major band centered at 330 nm originated from the $n-\pi^*$ transitions from nonbonding orbitals. The photoluminescence properties of the as synthesized CDs were investigated by analyzing the emission at different excitation wavelength, in the range from 350 to 600 nm. The results are shown in Figure 79. The shift in the excitation wavelength produce a negligible or almost no changes in the emission peaks of all the four CDs. In more details for **g-Glu-CDs** and **g-Fru-CDs** the shift of maximum of emission is of 5 and 9 nm respectively, moving from 300 to 400 nm the excitation wavelength. For the doped analogous the instead a shift of 5 and 11 nm were observed for the **g-N-Glu-CDs** and **g-N-Fru-CDs** in the same conditions.

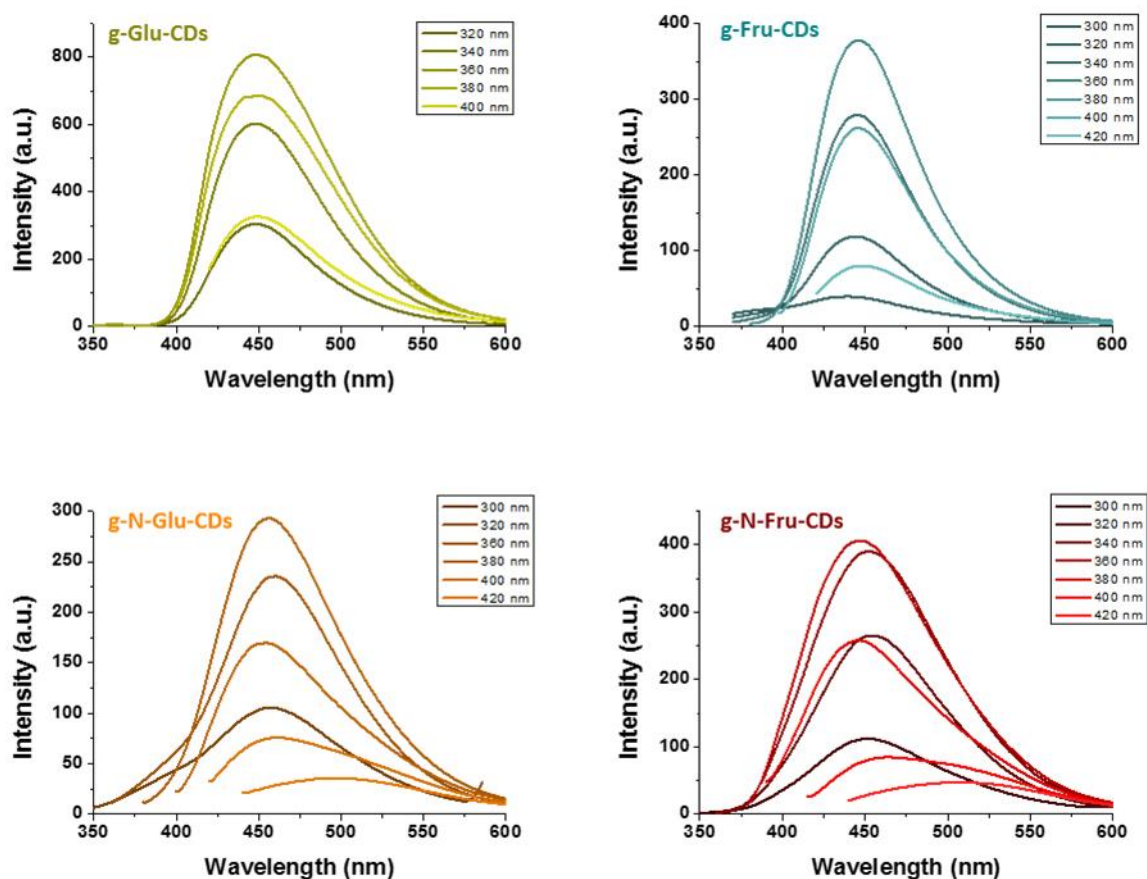


Figure 79. PL spectra at different excitation wavelength of **g-Glu-CDs**, **g-Fru-CDs**, **g-N-Glu-CDs** and **g-N-Fru-CDs**.

5.3. Synthesis of esters

The synthesis of the N-Methyl-picolinium esters was carried out starting from the carboxylic acids of interest following a modified procedure as shown in Figure 80.¹⁷⁶

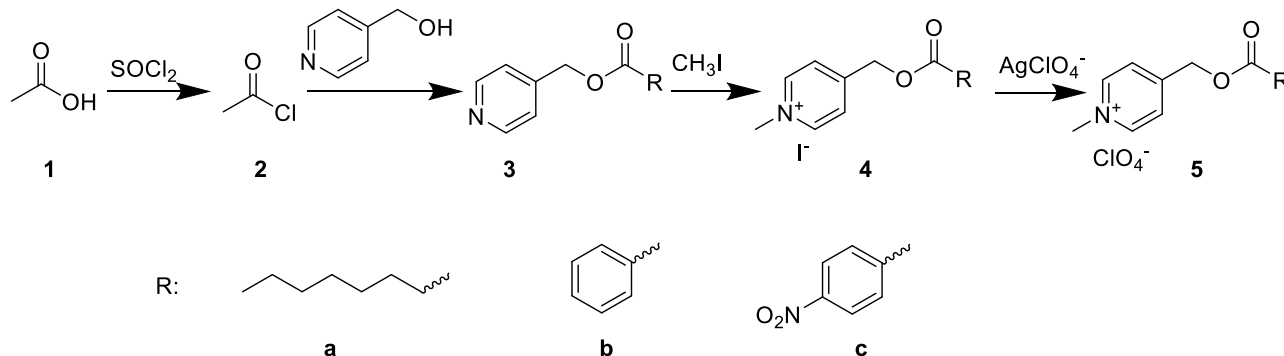


Figure 80. General scheme for the synthesis of NMP esters.

The reaction consists of four synthetic steps. Briefly, in the first step the selected carboxylic acid **1** is converted to the correspondent chloride **2** by reaction with thionyl chloride. In the second step the acyl chloride was reacted with 4-(Hydroxymethyl) pyridine to form the corresponding ester **3**. Then the pyridine was methylated with methyl iodide to form the corresponding iodate salt **4**. Finally, the iodide counterion was exchanged with silver perchlorate to form the corresponding perchlorate salt **5**. The product **5a**, **5b** and **5c** were obtained in 18 %, 7%, and 31% yields respectively and fully characterized, the detailed synthetic procedure and NMR characterization are described in the experimental section.

5.4. Reactivity

The photodeprotection reaction of the synthesized N-Methyl-picolinium esters was then evaluated employing CDs as the sole photosensitizer in the first synthetic organic reaction performed by CDs. The reaction in case involve the PET from the CDs to the esters and then the C-O cleavage of the molecules generating the methyl pyridinium (**6**) and the starting carboxylic acid (**8**) as shown in Figure 81.

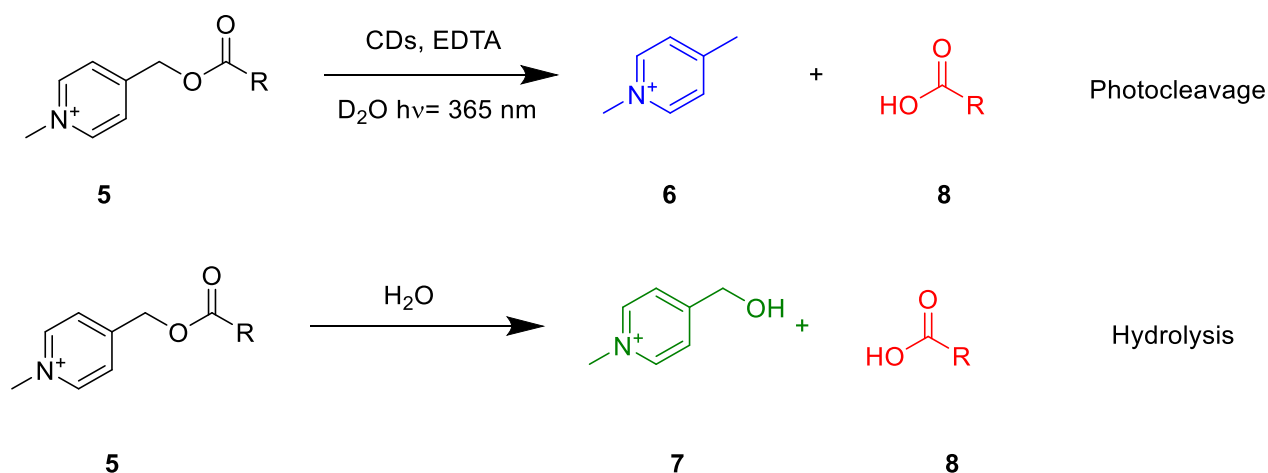


Figure 81. General photodeprotection reaction of the N-Methyl picolinium esters.

The reaction was carried out in NMR tubes under inert condition and employing EDTA as sacrificial donor and irradiating the sample with UV light at 365 nm for 48 hours. The reaction was monitored by 1H NMR spectroscopy, investigating the characteristic signals of the products. Beside the main reaction of C-O photocleavage, also the hydrolysis of the ester may occur, in the latter case the products of the reaction are the methylated pyridine carbinol and the starting carboxylic acid. The products of the photocleavage reaction and of the hydrolysis was synthesized with a dedicated synthesis (Figure 82) in order to evaluate their NMR signals and to perform an accurate evaluation of the NMR spectra of the reaction mixtures.

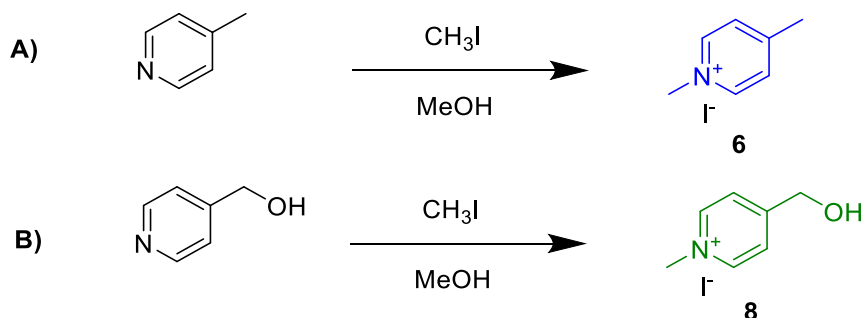


Figure 82. Synthesis of the products of cleavage **6** and hydrolysis **8**.

The cleavage products 1,4-dimethylpyridin-1-ium iodide (**6**) was obtained by the methylation with methyl iodide of the 4-Methyl pyridine (reaction **A**) while the 4-(hydroxymethyl)-1-methylpyridin-1-ium iodide (**7**) produced from the hydrolysis was synthesized applying the same procedure to the 4-(Hydroxymethyl)pyridine (reaction **B**).

5.4.1. Photodeprotection of the octanoic ester

The photodeprotection reaction mediated by the CDs was first investigated on the octanoic esters (**5a**) to yield the products **6** and **8a** for the C-O cleavage and **7** and **8a** if the hydrolysis occurs as shown in Figure 83.

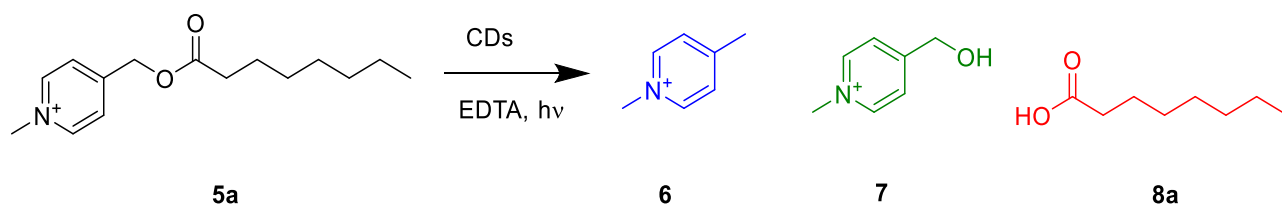


Figure 83. Reaction of octanoic ester and its possible products.

The reaction was carried out preparing a solution of 60 mM of the ester, 20 mg/mL of CDs, 0.1M of EDTA in D_2O/CD_3CN (60/40) and at $pD=7$ defined as the standard condition for the reaction. The mixture was placed in a NMR tube under inert conditions and irradiated with a UV lamp at 365nm for 48 hours, the evolution of the reaction was monitored by 1H NMR spectra at different exposition time and the typical results obtained are displayed in Figure 84.

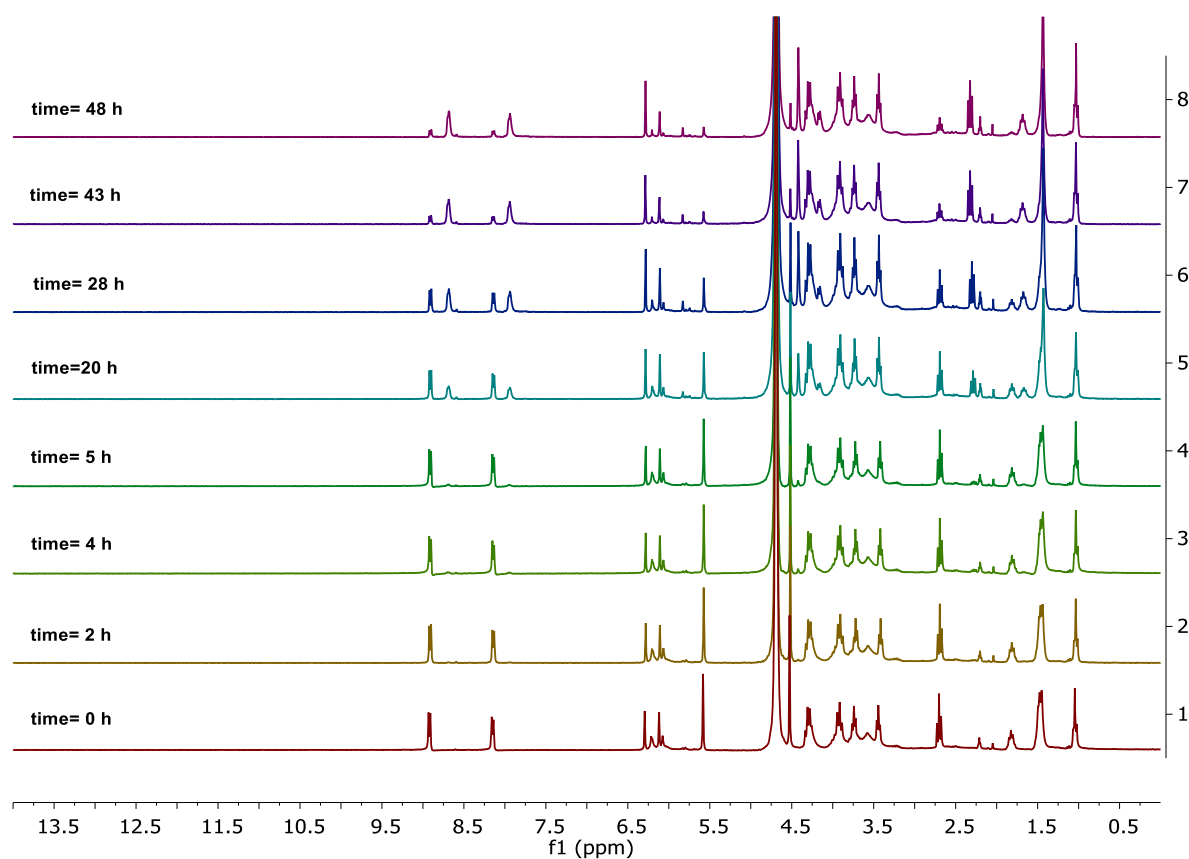


Figure 84. 1H NMR spectra of the evolution of a typical photodeprotection reaction of compounds **5a**.

As observed in the figure the ^1H NMR spectra of the reaction presents a great number of signals due to the simultaneous presence of products, reagents and the EDTA in the mixture. Despite the complexity of the system some variation could be noticed, and the formation of new signals were observed. To further assign the new signals to the one of the expected products, a comparison of the NMR spectra of the reaction at $t=0$ and 48 h along with the spectra of the three possible products were accomplished as shown in Figure 85.

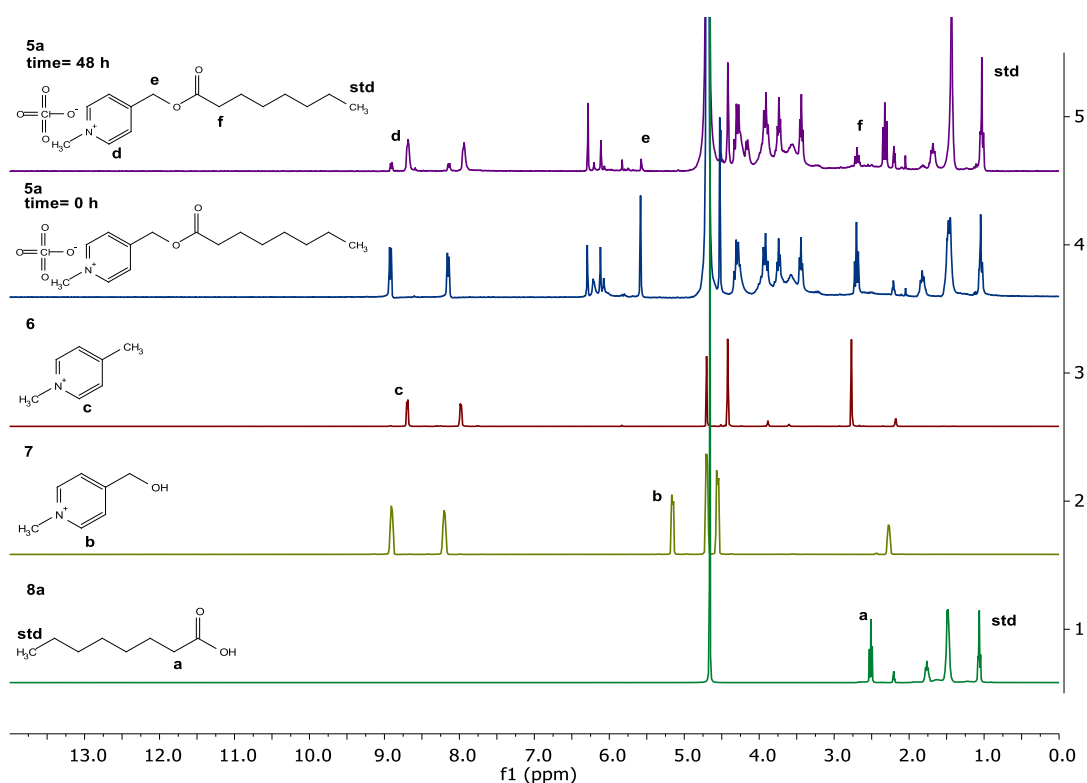


Figure 85. ^1H NMR spectra of the reaction at $t=0$ and 24h, and its expected products in $\text{D}_2\text{O}/\text{CD}_3\text{CN}$ at $\text{pD}=7$.

As highlighted in the figure specific signals for the three expected products was chosen as indicative to evaluate the selectivity of the reaction, namely the signal **c** of the product **6** was used for quantifying the photodeprotection reaction, while for evaluate the degree of hydrolysis the signal **b** of the product **7** was used. The signal **a** of the octanoic acid was employed for evaluate the total yield of the acid. Furthermore, the signals **d**, **e**, and **f** were employed to estimate the conversion of the reagent. All the CDs synthesized and characterized in this thesis were employed in the photodeprotection reaction of octanoic esters and the results in terms of conversion and selectivity are summarized in Table 8.

Table 8. Results of the photodeprotection reaction on the substrate **5a** in standard condition.

CDs	Conversion 5a	Selectivity C-O Cleavage
g-CDs	53	93
a-CDs	15	100
g-N-CDs	43	100
a-N-CDs	63	100
G-CDs	66	100
g-Glu-CDs	53	100
g-N-Glu-CDs	52	86
F-CDs	43	89
g-N-Fru-CDs	45	88
g-N-Fru-CDs	30	100

The CDs investigated demonstrate different behaviors towards the photodeprotection of the **5a**, the best performance was displayed by the **a-N-CDs** and the **G-CDs**, with a conversion up to 60 % and a total selectivity towards the C-O photocleavage. Instead, poor conversions were observed for the **a-CDs** with only a 15% of substrate reacted. Interestingly in all the test performed, the reaction demonstrates a total selectivity towards the photodeprotection, with only a small amount of hydrolysis detected for the **g-N-Glu-CDs**, **g-N-Fru-CDs** and **F-CDs**. Focusing the attention only on the first four lines of the table, the reactivity of the CDs employed follow the order **a-N-CDs**>**g-CDs**>**g-N-CDs**>**a-CDs**, the same already observed in the reduction of the MV. This observation could be in first instance explained by the structure similarity of the ester with MV in the pyridinium moiety, that can give raise to similar electrostatic interactions favoring the PET. Deeply studies on the CDs and substrates potentials and a more detailed discussion on the reactivity will be presented in the next chapter.

Due to its high activity and the already performed deep characterization the **a-N-CDs** was chosen as model to investigate the effect of different parameters in affecting the reaction. The effect of the presence of EDTA, light and CDs were first investigated.

Table 9. Effect of EDTA, CDs and light source on the photodeprotection of **5a** mediated by **a-N-CDs** for 48 h in D₂O/CD₃CN.

Entry	CDs (mg/mL)	Light source	EDTA (M)	Conversion (%)	Selectivity (%)
1	20	UV-light	0.1	63	100
2	20	UV-light	X	52	98
3	X	UV-light	0.1	0	0
4	20	X	0.1	0	0
5	20	Vis	0.1	0	0

From the results obtained it is clear that the presence of the UV-light source and of the CDs are of fundamental importance in triggering the reaction, however the absence of EDTA slightly affect the overall conversion but the selectivity remains almost complete towards the products of C-O cleavage. This result suggest that the CDs have the capability to donate the electron also in absence of a sacrificial donor and that the reaction could be conduct without the addition of EDTA. The possibility to remove the EDTA, could be very important since it simplify the subsequent purification steps, in case of scaled reaction, and also imply a less amount of reagent in the mixture. From this conclusion a study on the effect of the concentration of CDs on the photodeprotection reaction was carried out and the results are shown in Table 10.

Table 10. Results of photodeprotection of **5a** results with different concentration of CDs in standard conditions.

Entry	Concentration (mg/mL)	Conversion (%)	Selectivity (%)
1	0	0	0
2	1	35	93
3	5	36	96
4	10	58	99
5	20	63	100

The results reported in the table shows that increasing the amount of CDs in the solution led to an increasing of the conversion keeping constant the selectivity of the reaction. Since all this reaction

need the presence of the EDTA to reach a considerable conversion, the reaction performed with 20 mg/mL of CDs was defined as “catalytic”. For further explore the effect of the concentration other reaction were carried out with higher amount of CDs but in absence of the sacrificial donor. A range from 20 to 100 mg/mL was investigated and the results obtained are shown in Table 11.

Table 11. Results of photodeprotection of **5a** results with different concentration of CDs and without EDTA in standard conditions.

Entry	Concentration (mg/mL)	Conversion (%)	Selectivity (%)
1	20	52	98
2	50	73	100
3	100	90	100

Interestingly increasing the concentration of CDs up to 100 mg/mL results in an improvement of the conversion of **5a**. The reaction with 100 mg/mL allow to reach an almost complete conversion of the substrate, meaning that the amount of CDs present in solution could convert all the mol of substrates, in a sort of stoichiometric reaction. For this reason, this condition was named as “stoichiometric”. Furthermore, the advantage of working in stoichiometric condition rely on the fact it is possible to avoid the use of a considerable amount of EDTA, that could give problem in a hypothetical next step of purification to isolate the product and use only cheap and easily synthesizable nanoparticles. The reactivity of the CDs was then compared to the Ru(bpy)₂, one of the best sensitizer used up to date. The reactions should be taken as indicative since the two sensitizers need different light-source to work in the best condition: a UV-lamp for the CDs and a solar lamp (λ_{max} =540 nm) for the ruthenium complex. Furthermore, the light source employed in this test have different power and a fully comparison cannot be accomplished.

Table 12. Results of the comparison of the photodeprotection reaction of **5a** between CDs and Ru(bpy)₂³⁺

Entry	Sensitizer	Concentration	Light	EDTA	Conversion	Selectivity
1	a-N-CDs	20 mg/mL	UV (365 nm)	0.1 M	63	100
2	a-N-CDs	100 mg/mL	UV (365 nm)	X	90	100
3	Ru(bpy) ₃ ²⁺	2 mg/mL	Vis	0.1 M	100	97

The results shown in Table 13 highlight that the stoichiometric reaction and the one catalyzed by the ruthenium complex exhibit a similar reactivity. Also considering the not comparable conditions employed for the two types of catalysts, this result is very significant since demonstrate that a highly costly material such as the ruthenium complex could be ideally substituted with a new one, more cheaper and more stable guaranteeing a similar reactivity.

In conclusion from this screening of catalyst and reactivity conditions, it was possible to demonstrate for the first time that the CDs could be a good photosensitizer for performing organic reaction, opening a new scenario in this field. Furthermore, in this case of study the photodeprotection reaction could be carried out with good conversion and an almost complete selectivity. The use of EDTA could be avoided by increasing the amount of catalyst ensuring a similar or increased reactivity while working in simple conditions.

5.4.2. Scope of the substrate

After having investigate the best conditions and the catalyst to perform the reaction with the ester deriving from the protection of the octanoic acid, the same reaction was extended to other two similar substrate, such as the ester deriving from the protection of the benzoic acid and the p-nitro benzoic acid with the N-Methyl-picolinium moiety. The reaction studied, and their relative products, analyzed and quantified are shown in Figure 86.

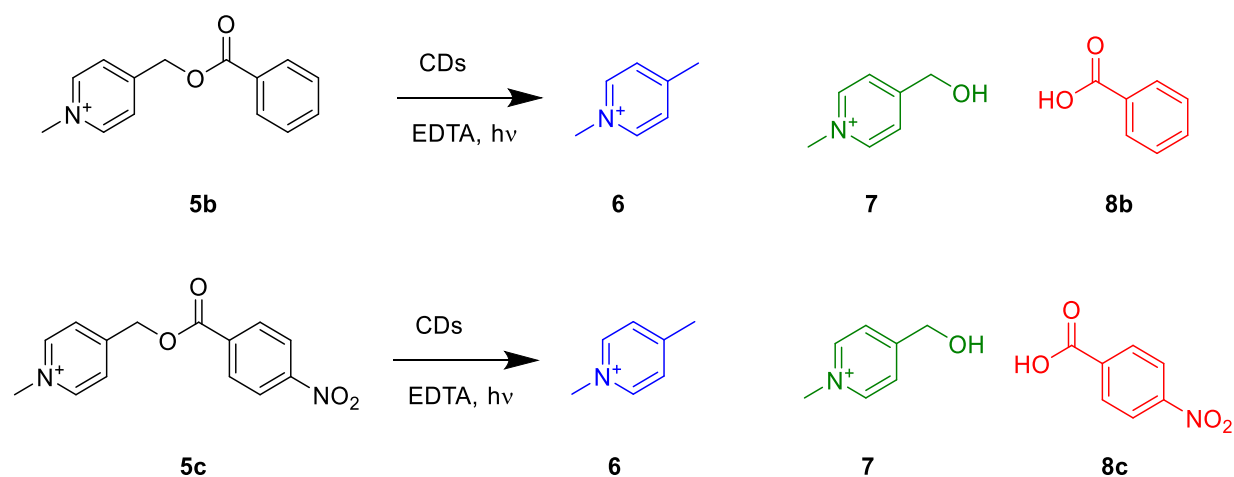


Figure 86. Photodeprotection reaction of substrate **5b** and **5c** with CDs in standard conditions.

The resulting products as stated in the figure above are the **6b/c** and **7b/c** for the C-O cleavage reaction while the formation of the products **8b** and **8c** are ascribed to the presence of the competing hydrolysis reaction. For these reactions, only the results obtained with the best CDs, the **a-N-CDs** and in the so called “catalytic” and “stoichiometric” condition will be discussed. Both the reactions were

monitored, as already performed in the previous case, by ^1H NMR spectroscopy. For calculate the conversion of the reagents and to determine the selectivity of the reaction specific signals on the spectra were chosen. In particular, in Figure 87 the spectra regarding the reaction with the benzoic ester along with the ones of its relative products are shown. For the benzoic ester the decreasing of the intensity of the signal **c** was exploited for calculate the conversion, while the signal **b** and **a** was respectively taken into consideration for evaluate the amount of C-O cleavage and hydrolysis respectively. In conclusion the quantification of the acid cannot be accomplished employing the ^1H NMR spectroscopy due to the great number of signal present in the aromatic region, for this reason the quantification was performed by a GC analysis (see Experimental for further details).

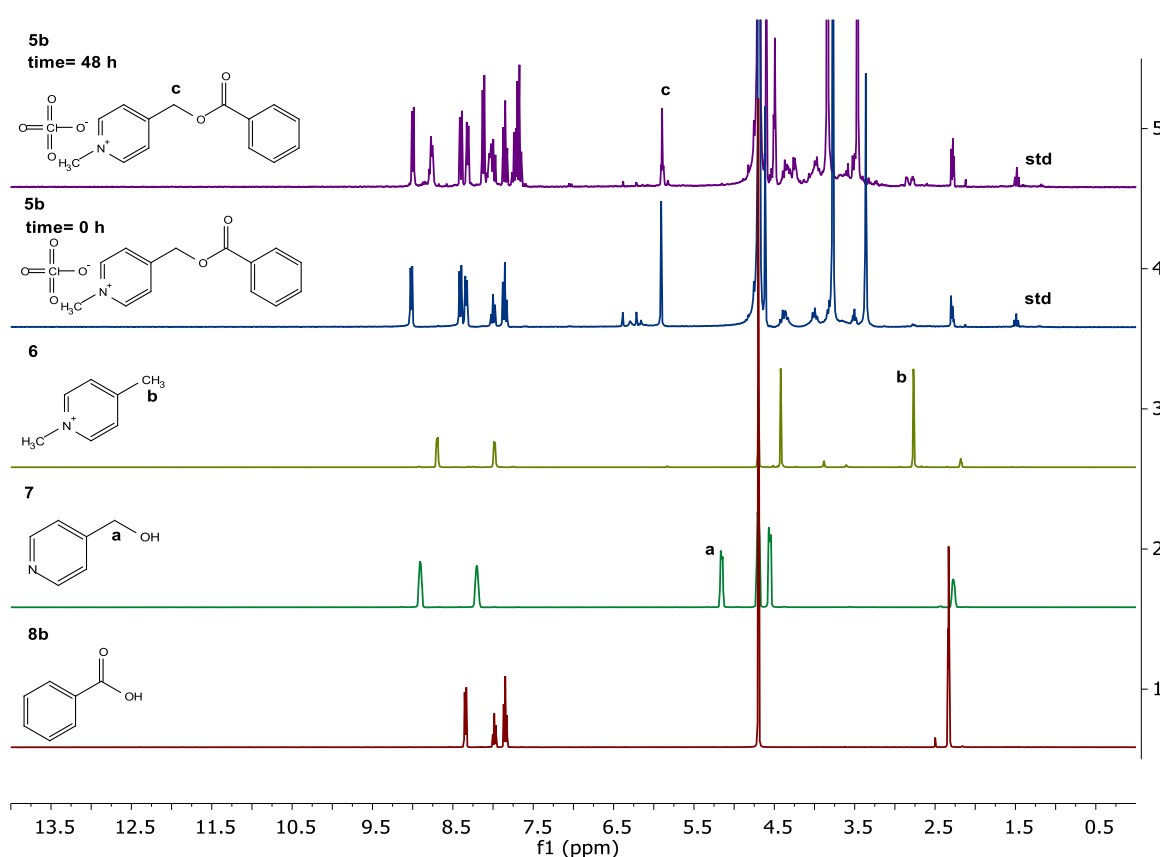


Figure 87. ^1H NMR spectra of the photodeprotection of **5b** at $t=0$ and 24h, and its expected products in $\text{D}_2\text{O}/\text{CD}_3\text{CN}$ at $\text{pD}=7$.

With the same methodology the spectra obtained from the photodeprotection of the substrate **5c** were analyzed. Also in this case the quantification of the obtained carboxylic acid was performed with a GC analysis (see experimental section). From these elaborations was possible to extrapolate the kinetics profile relative to the formation of the products, and the disappearing of the reagent, in Figure 88 are reported the kinetics profiles of the catalytic reaction on the substrate **5b** and **5c**.

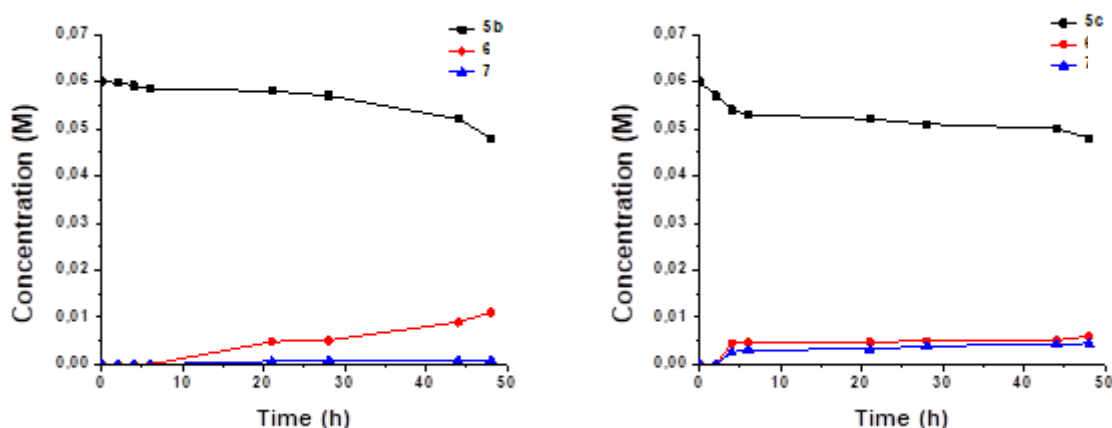


Figure 88. Kinetics profiles of the photodeprotection reaction performed on substrate **5b** (right) and **5c** (left). The results obtained for the photodeprotection reaction of **5b** and **5c** in both the stoichiometric and catalytic condition are summarized in Table 13.

Table 13. Results of the photodeprotection of **5b** and **5c** with a-N-CDs in stoichiometric and catalytic condition.

Entry	Substrate	CDs concentration	EDTA	Conversion	Selectivity
1	5b	20 mg/mL	0.1 M	20	33
2		100mg/mL	/	61	0
3	5c	20 mg/mL	0.1 M	20	57
4		100mg/mL	/	28	0

It could be noted that both the substrates exhibit a significant lower conversion respect to the **5a**, demonstrating that the nature of the substrate plays an important role in the reaction. Furthermore, the stoichiometric conditions in both cases results in an increasing of the conversion, but in much less selective reactivity. Significant, in this context, is the case of the substrate **5b** in which the conversion raised from 20 to 61 but the reaction did not produce any photocleavage products, not only, the signals obtained cannot be ascribed to both the cleavage or hydrolysis products and are more likely due to other side reactions. The addition of EDTA to the solution was found to be necessary in order to have a good selectivity towards the photocleavage reduction.

5.5. Cyclic voltammetry study

In order to better understand the reactivity behavior of either the CDs and the substrates herein employed, an electrochemical study was performed. In more details, a cyclic voltammetry approach was employed in order to determine the HOMO-LUMO energetic levels of the CDs and also the LUMO orbitals of the substrates. The detailed condition in which the measurement was performed are described in the experimental section. Briefly, a three-electrode cell, composed by a glassy carbon disc working electrode, a Ag/AgCl/KCl saturated as reference electrode and a platinum spiral was employed as counter electrode and tetrabutylammonium perchlorate (TBAP) was used as support electrolyte.

5.5.1. Cyclic voltammetry measurements on CDs

In first instance the **a-CDs**, **g-CDs**, **a-N-CDs**, and **g-N-CDs** were investigated, the nanoparticles were first dissolved in the less amount possible of milliQ water and then added to fresh distilled DMF. Preliminarily, cyclic voltammetric measurements were performed in the background electrolyte, *i.e.*, DMF + 0.1 M tetrabutylammonium perchlorate (TBAP), in order to establish the potential window in which CDs can be investigated. The obtained cyclic voltammograms reported in Figure 89, demonstrate that only small features, due to impurities, are evident before the background discharge, which occurs at about -2.7 V and 1.8 V in the cathodic and anodic regions, respectively. The only significant peak, the one at about -2.3 V is related to trace of water present in the solvent. These observations indicate that the potential window available to evaluate the CDs redox properties ranges from about -2.3 V to 1.7 V.

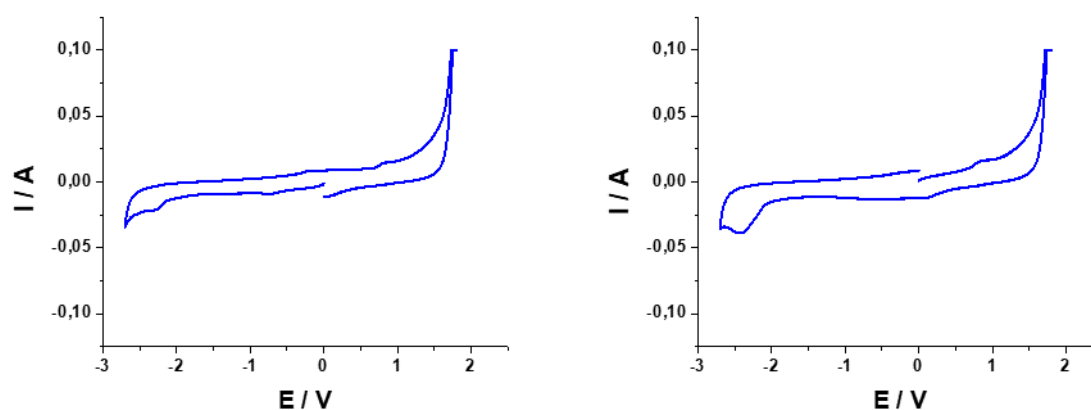


Figure 89. Cyclic voltammetry, scan rate 100mV/s, cathodic direction (left), anodic direction (right).

When the CDs are added to the mixture the voltammetric pictures changes and new waves appears both in reduction and oxidation. The CVs obtained for the four CDs taken into consideration scanning in both the cathodic and anodic region are shown in Figure 90.

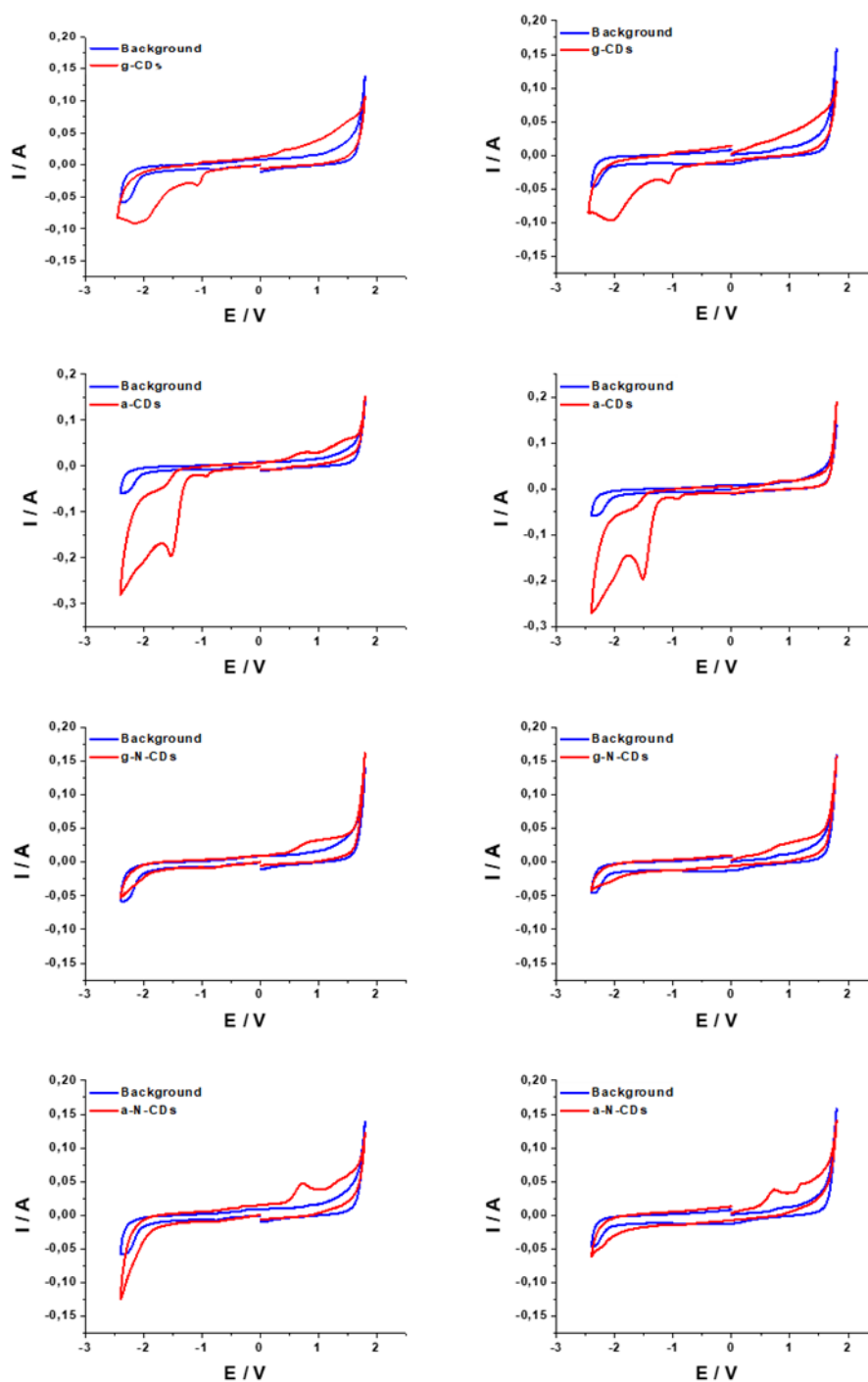


Figure 90. CVs of g-CDs, a-CDs, g-N-CDs, a-N-CDs scanning in both cathodic (left images) and anodic (right images) directions.

The CDs examined reveal different behavior in the CV study, exhibiting several waves in both the anodic and cathodic region. For a correct interpretation of the result obtained and for extrapolate the potential of the HOMO and LUMO orbitals the onset potentials of the different waves were obtained. Employing the mathematics described in the experimental section, it was possible to refer

the values of the onset potentials to the energy of the HOMO and LUMO of the CDs. The results obtained for both the cathodic and anodic CVs are shown in Table 14 and Table 15.

Table 14. Onset potentials and LUMO energy levels calculated for the four CDs.

CDs	$E_{\text{onset red}}$ (V) ^a	$E_{\text{onset red}}$ (V) ^b	E_{LUMO} (eV)
g-CDs	-0.97	-1.46	-3.6
	-1.60	-2.09	-3.0
a-CDs	-0.85	-1.34	-3.8
	-1.30	-1.79	-3.3
g-N-CDs	-1.83	-2.33	-2.8
	-1.87	-2.36	-2.7
a-N-CDs	-1.94	-2.43	-2.7

^a measured vs Ag/AgCl, ^b measured vs Fc/Fc⁺.

Table 15. Onset potentials and HOMO energy levels calculated for the four CDs.

CDs	$E_{\text{onset ox}}$ (V) ^a	$E_{\text{onset ox}}$ (V) ^b	E_{HOMO} (eV)
g-CDs	0.35	-0.14	-5.0
	0.69	0.20	-5.3
	1.27	0.77	-5.9
a-CDs	0.52	0.03	-5.1
g-N-CDs	0.56	0.06	-5.2
	0.53	0.03	-5.1
a-N-CDs	1.12	0.62	-5.7

^a measured vs Ag/AgCl, ^b measured vs Fc/Fc⁺.

With the same techniques also the three substrates investigated in this work were characterized in order to detect and calculate the corresponding onset potential of reduction and the LUMO energy levels. The CVs registered for a 10 mM solution of the esters are shown in Figure 91.

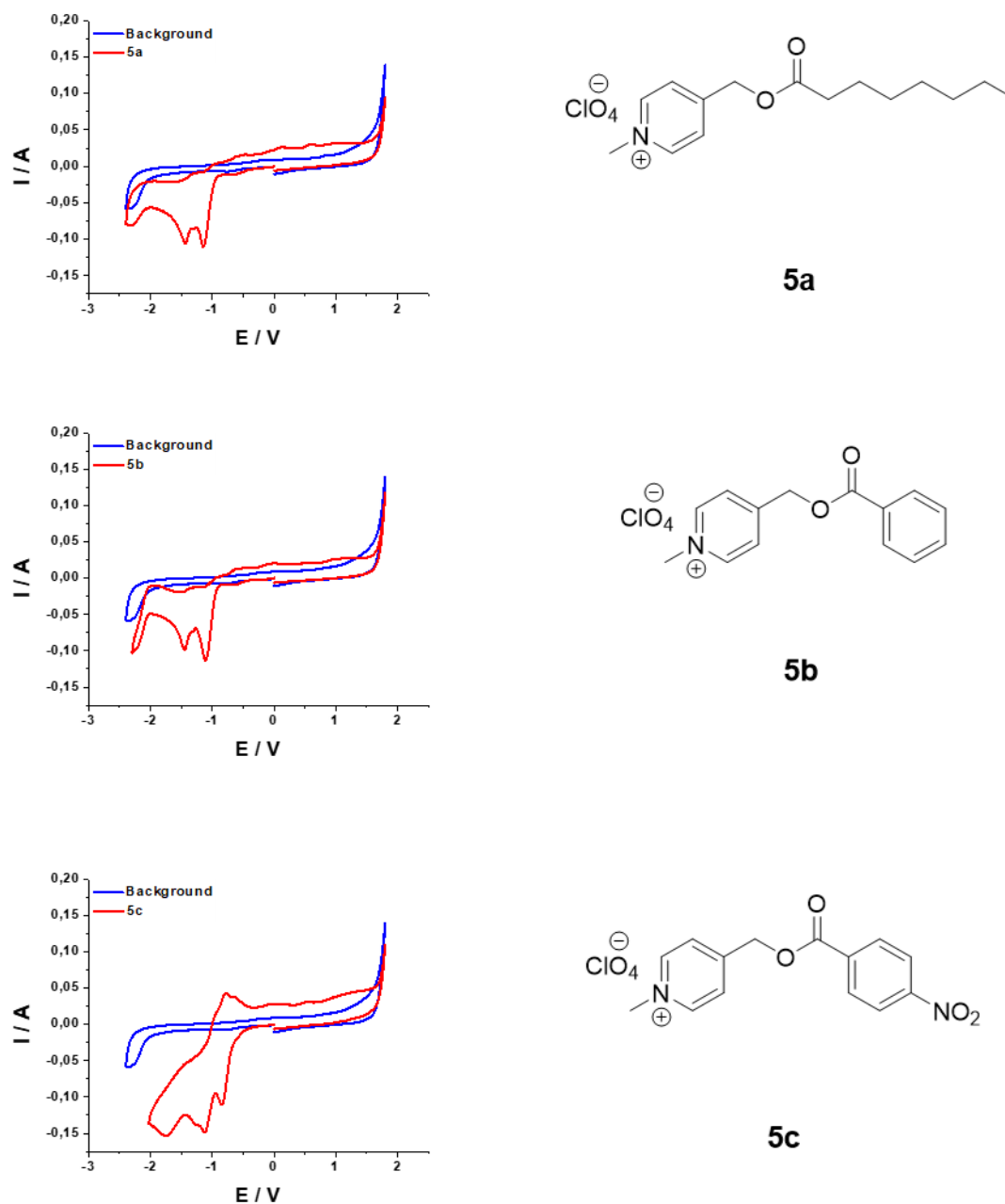


Figure 91. CVs of the N-Methyl-Picolinium esters synthesized registered in the cathodic direction.

The CVs registered for these organic substrates are much more complex respect to the one of the nanoparticles; in all cases, at least two main peaks were observed. As for the first peak, it is likely (also from literature data^{177,178}) that it belongs to the reduction of the C=O moiety of the ester group. This hypothesis is supported also by the values of this peak observed for the three compounds, as the order from the less to the more negative, follows the order **5b**, **5c**, **5a** consistent with the expected stability of the radical anion formed. For the substrate **5c** the high stability expected for the

radical anion is also the reason of the appearance, upon scan reversal, of a peak at -0.9 V due to the oxidation of the radical anion.^{179, 180}

Considering the onset potential of the first reduction peak associated to the reduction of the carboxyl group and applying the same formula as in the previous case it was possible to calculate the LUMO energy levels of the substrates. The results of these calculation are summarized in Table 16.

Table 16. Onset potentials and LUMO energy levels calculated for the substrates.

Substrate	$E_{\text{onset red}}$ (V) ^a	$E_{\text{onset red}}$ (V) ^b	E_{LUMO} (eV)
5a	-0.97	-1.46	-3.6
5b	-0.94	-1.43	-3.7
5c	-0.65	-1.14	-4.0

^a measured vs Ag/AgCl, ^b measured vs Fc/Fc⁺.

In order to compare all information gathered in the electrochemical experiments for CDs and esters, the correspondent HOMO and LUMO orbitals were summarized in the Figure 92.

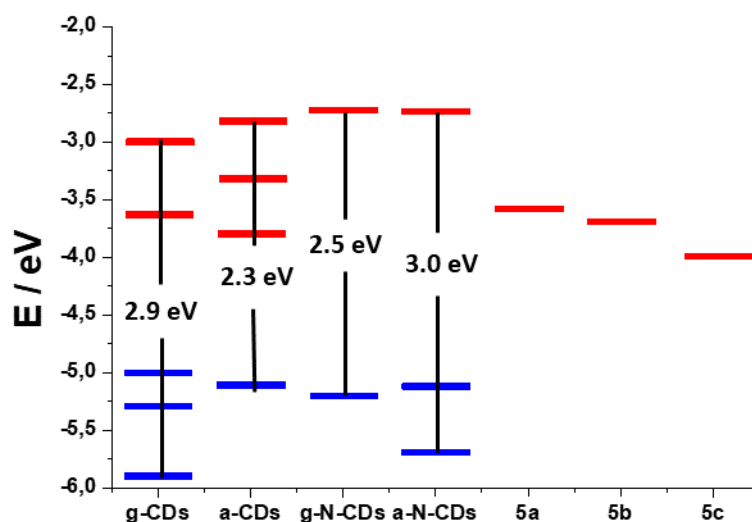


Figure 92. Schematization of the HOMO and LUMO energy levels of CDs and esters.

Interestingly some correlations between the HOMO-LUMO energies and the reactivity observed in the photodeprotection reactions could be deduced. It was found that the CDs with the higher gap HOMO-LUMO is also the best in triggering the photocleavage of the C-O bonds in the esters. A possible explanation to this behaviour rely on the fact that a higher energy gap imply also that the

excited electron possesses a higher energy that can be used to perform the reaction. In this context looking at the energy gap shown in Figure 92, the CDs energy gaps follow the order **a-N-CDs**> **g-CDs**> **g-N-CDs**> **a-CDs**, the same order already observed for the reactivity towards the photodeprotection of the octanoic acid. A similar consideration could also be done for explain the different reactivity observed for the **a-N-CDs** towards the substrates **5a**, **5b**, and **5c**. In this case the energy of the LUMO it is related to the stability of the radical formed after the reduction, and so to the intermediate of the photodeprotection reduction. A higher LUMO energy levels means that the specie is difficult to reduce and so a higher energy is required for the reduction and therefore the intermediate is less stable and so can easily undergo to a cleavage reaction.

The results obtained by the CV studies reveals that besides the already highlighted difference in structure/luminescence/reactivity for the CDs obtained by different synthesis with or without doping agent they present also different in their electrochemical properties, with different reduction and oxidation site. Furthermore, these analyses permit also to explain the different reactivity of the CDs towards the photodeprotection reaction of the N-Methyl-Picolinium esters.

5.6. Conclusion

In conclusion in this work for the first time it was proved that the CDs can act as only photosensitizer for performing synthetic reaction as the photodeprotection of esters. First the esters were synthesized from the corresponding carboxylic acid by reaction with the carbinol. The deprotection reaction was carried out in a NMR tube with a sacrificial donor and monitoring the reaction by ¹HNMR spectroscopy. The study reveal that all the CDs can promote this reaction on the octanoic ester with an almost total selectivity, and conversion ranged from 15 to 66 %. Different tests were performed, highlighting also the possibility to perform the reaction without the EDTA by only increasing the concentration of the CDs in the mixture. Furthermore, the reactivity was also compared to the one of the ruthenium bipyridyl, revealing that this cheap material possesses a similar reactivity respect to the highly costly metal complex. The investigation of the other synthesized esters reveals lower conversion and that the presence of the EDTA was essential in order to guarantee a high selectivity. The cyclovoltammetric study performed on either the nanomaterials and the organic substrates reveals important differences in the electrochemical properties of the nanomaterials resulting in different HOMO-LUMO energy gap. A correlation was also found between the energy gaps and the reactivity manifested by the nanomaterials, with the CDs with higher energy gaps exhibiting the better reactivity. In addition, the CVs allow also to understand the different reactivity of the ester by

studying their LUMO energies. Overall, the results herein reported demonstrate for the first time that the CDs can act as the sole photosensitizer without the addition of any metal complex or enzymes. This result could open a new series of application regarding the utilization of the CDs in organic synthesis, since their easy way of synthesis and the cheap value of the precursor makes them very attractive respect to the conventional photocatalyst. In this context, among the others, the cyclovoltammetry results to be a very useful technique in order to gain an exhaustive knowledge on the redox properties of these nanomaterials and consequently their reactivity.

5.7. Experimental

5.7.1. Reagents and instrumentation

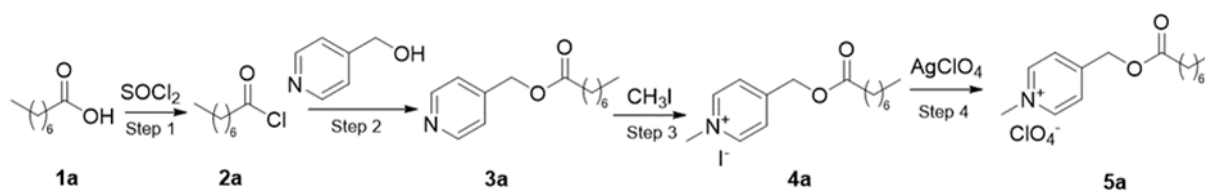
Acetonitrile, methanol, toluene, ethyl acetate, hexane, were supplied by Sigma-Aldrich and were used as received. All the reagents used in the synthesis were purchased by Sigma-Aldrich and used as received. Deuterated solvents such as chloroform, water and acetonitrile and methanol were supplied by Sigma-Aldrich. The GC-MS spectra were registered with an Agilent Technologies 6890N Network GC System interfaced with an Agilent Technologies 5975 Inert Mass Selective Detector. He Carrier gas (1.2 mL / min), phase SPB-5, capillary column 30 m, I.D. 0.32 mm, film 0.25 μm . Calibration curves for quantification were recorded with a GC Hp 5890 equipped with a capillary column Elite-624 (30 m x 0.32 mm, film width: 0.18 μm) coupled with FID detector. For the acquisition of ^1H , ^{13}C NMR spectra, a Bruker UltraShield 300'54 spectrometer was used (^1H : 300 MHz; ^{13}C : 75.5 MHz;) and a Bruker Magnet System spectrometer 400'54 Ascend (^1H : 400 MHz; ^{13}C : 100.6 MHz). The chemical shifts (δ) of the ^1H and ^{13}C NMR spectra have been reported in parts per million (ppm). For the photocatalysis reactions, a LED UV lamp with a fixed wavelength of 370 nm, 400 mA, 25 mV was used.

5.7.2. Synthesis of esters and cleavage products

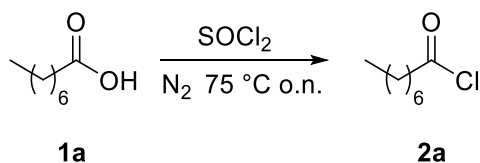
All the spectra regarding the synthesis of the esters could be find in the appendix section.

5.7.2.1. Octanoic acid protection

The synthesis of the protected octanoic acid consists of four synthetic steps as illustrated in the following scheme

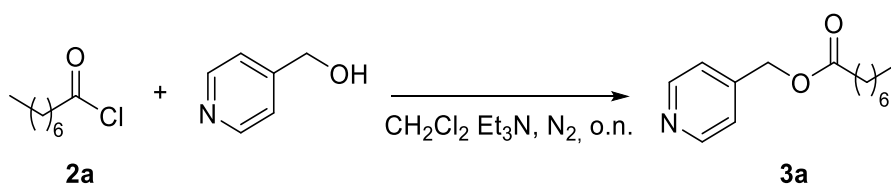


Step 1



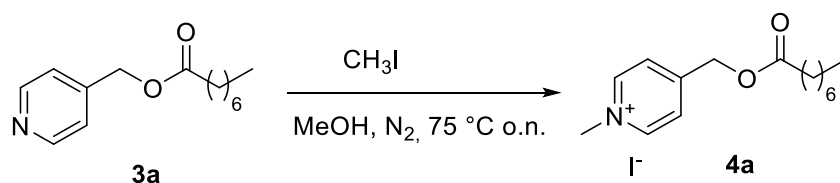
Octanoic acid **1a** (30.99 mmol) and toluene (20 ml) was introduced into a three-necked flask equipped with a condenser, sodium bicarbonate and calcium chloride trap, rubber septum and tail. Then thionyl chloride (137.84 mmol) was added and the mixture was refluxed overnight at 75°C. Then the unreacted thionyl chloride and toluene were removed from the system by vacuum evaporation. The acyl chloride product **2a** was obtained in 89% yield. ¹H NMR (400 MHz, Chloroform-*d*) δ= 2.91 (t, *J* = 6.7 Hz, 2H), 1.88 – 1.63 (m, 2H), 1.39 – 1.29 (m, 8H), 0.92 (t, *J* = 8.6 Hz, 3H). ¹³C NMR (101 MHz, Chloroform-*d*) δ= 173.77, 47.10, 31.51, 28.72, 28.38, 25.06, 22.52, 13.99.

Step 2



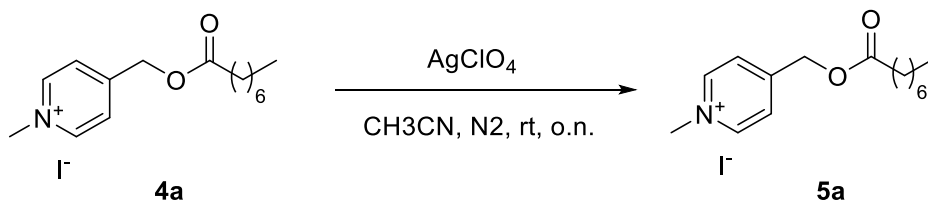
4-(Hydroxymethyl)pyridine (18.97 mmol), dichloromethane (20 ml) and triethylamine (32.92 mmol) were introduced into a three-necked flask equipped with a condenser, dropping funnel and gas inlet. A solution of the corresponding acyl chloride **2a** (27,37 mmol) in dichloromethane was then added dropwise and the reaction mixture was left under stirring overnight at room temperature and under nitrogen. Subsequently, the ester product **3a** was put into a separating funnel and washed with a solution of water and sodium bicarbonate (20ml), recovering the lower organic phase and repeating the operation three times. The organic phase was then dehydrated with sodium sulphate, filtered and the solvent was removed by rotary evaporation. The purified product **3a** was purified by column chromatography employing gradient elution with a mixture of hexane / ethyl acetate. The product **3a** was obtained in 53% yield. ¹H NMR (400 MHz, Chloroform-*d*) δ= 8.61 (d, 1H), 7.26 (d, 1H), 5.14 (s, 1H), 2.41 (t, 1H), 1.72 – 1.63 (m, 1H), 1.41 – 1.21 (m, 5H), 0.89 (t, 2H). ¹³C NMR (101 MHz, Chloroform-*d*) δ 173.29, 149.85, 145.24, 121.91, 64.01, 34.13, 31.62, 29.06, 24.90, 22.56, 14.03.

Step 3



The corresponding ester **3a** (7.38 mmol) and methanol (10 ml) were introduced into a three-necked darkened flask equipped with a condenser, rubber septum and tail. The system was put under nitrogen. The methyl iodide (11.29 mmol) was then added with a syringe and the reaction mixture was refluxed and left under stirring at 75 °C overnight. Subsequently, the unreacted methyl iodide and methanol were removed by vacuum evaporation leading to a solid. The product was recrystallized in hot methanol. The solid was filtered and stored in the dark. The product **4a** has been obtained in 53% yield. ^1H NMR (400 MHz, Chloroform- d) δ 9.25 (d, 2H), 8.01 (d, 2H), 5.40 (s, 2H), 4.71 (s, 3H), 2.50 (t, 2H), 1.76 – 1.59 (m, 3H), 1.39 – 1.25 (m, 6H), 0.91 (d, 4H). ^{13}C NMR (101 MHz, Acetonitrile- d_3) δ = 175.03, 156.48, 145.43, 125.48, 63.68, 49.23, 33.87, 31.57, 28.74, 24.71, 22.53, 13.80.

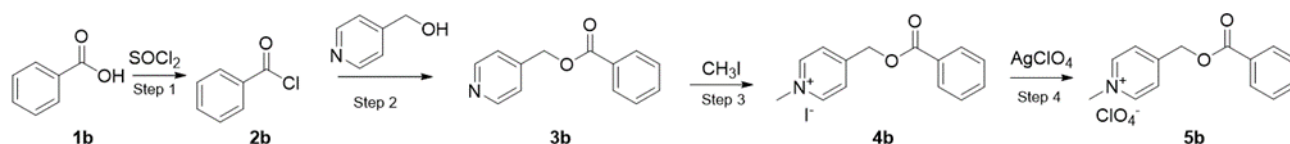
Step 4



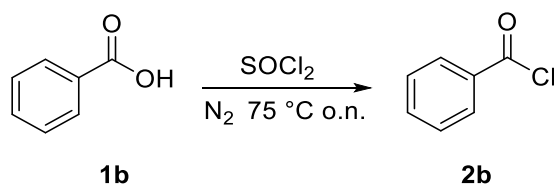
A solution of the corresponding ester **4a** (3.19 mmol) in acetonitrile was added in a three-necked darkened flask with a tail and a plug. The silver perchlorate was then added in a stoichiometric amount. The system was placed under nitrogen and left under stirring at room temperature overnight. The reaction mixture was then filtered to remove the precipitated silver iodide and the filtrate was dried. The product was then recrystallized with hot methanol. The product **5a** was obtained in 72% yield. ^1H NMR (400 MHz, Acetonitrile- d_3) δ = 8.59 (d, 2H), 7.94 (d, 2H), 5.37 (s, 2H), 4.29 (s, 3H), 2.50 (t, J = 7.5 Hz, 2H), 1.74 – 1.61 (m, 2H), 1.40 – 1.29 (m, 4H), 0.92 (t, J = 7.0, 5.1 Hz, 3H). ^{13}C NMR (101 MHz, Acetonitrile- d_3) δ = 174.70, 155.32, 145.05, 125.11, 62.87, 47.92, 33.38, 31.41, 28.70, 24.50, 22.32, 13.34.

5.7.2.2. Benzoic acid protection

The synthesis of the protected benzoic acid consists of four synthetic steps as illustrated in the following scheme

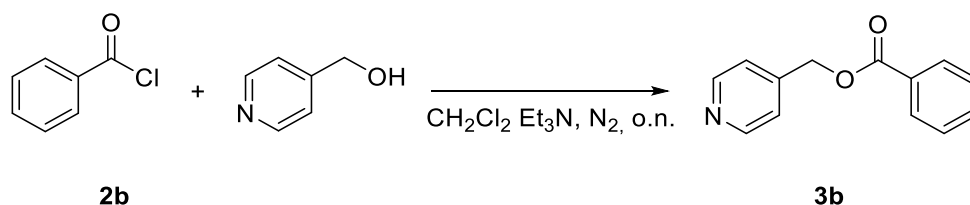


Step 1



Benzoic acid **1b** (30.85 mmol) and toluene (20 ml) was introduced into a three-necked flask equipped with a condenser, sodium bicarbonate and calcium chloride trap, rubber septum and tail. Then thionyl chloride (137.67 mmol) was added and the mixture was refluxed overnight at 75°C. Then the unreacted thionyl chloride and toluene was removed from the system by vacuum evaporation. The acyl chloride product **2b** was obtained in 85% yield. ^1H NMR (300 MHz, Chloroform-*d*) δ = 8.43 – 8.26 (m, 9H). ^{13}C NMR (75 MHz, Chloroform-*d*) δ = 167.41, 151.98, 138.38, 132.62, 124.43.

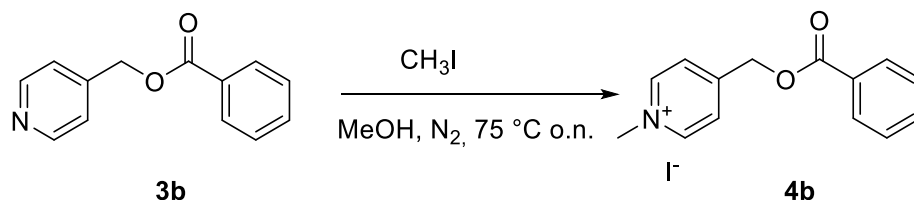
Step 2



4-(Hydroxymethyl)pyridine (23,26 mmol), dichloromethane (35 ml) and triethylamine (41.99 mmol) were introduced into a three-necked flask equipped with a condenser, dropping funnel and gas inlet. A solution of the corresponding acyl chloride **2b** (27,97 mmol) in dichloromethane was then added dropwise and the reaction mixture was left under stirring overnight at room temperature and under nitrogen. Subsequently, the ester product **3b** was put into a separating funnel and washed with a solution of water and sodium bicarbonate (20ml), recovering the lower organic phase and repeating the operation three times. The organic phase was then dehydrated with sodium sulphate, filtered and the solvent was removed by rotary evaporation. The purified product **3b** was purified by column chromatography employing gradient elution with a mixture of hexane / ethyl acetate. The product **3b** was obtained in 54% yield. ^1H NMR (400 MHz, Acetonitrile-*d*₃) δ = 8.62 (d, 1H), 8.39 – 8.25 (m, 2H),

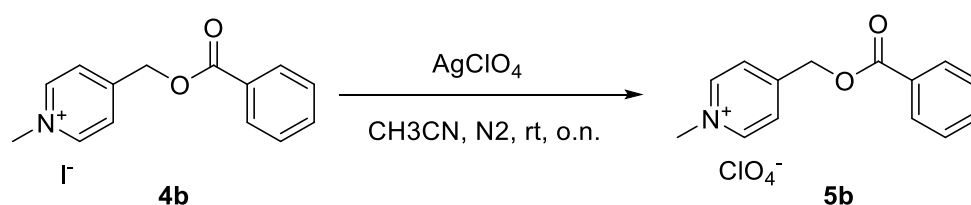
7.45 (d, $J = 4.4, 1.6, 0.7$ Hz, 1H), 5.44 (s, 1H). ^{13}C NMR (101 MHz, Acetonitrile- d_3) $\delta = 164.36, 150.90, 150.00, 144.81, 135.25, 130.77, 123.75, 121.92, 65.37$.

Step 3



The corresponding ester **3b** (11.72 mmol) and methanol (10 ml) were introduced into a three-necked darkened flask equipped with a condenser, rubber septum and tail. The system was put under nitrogen. The methyl iodide (19.44 mmol) was then added with a syringe and the reaction mixture was refluxed and left under stirring at 75°C overnight. Subsequently, the unreacted methyl iodide and methanol were removed by vacuum evaporation leading to a solid. The product was recrystallized in hot methanol. The solid was filtered and stored in the dark. The product **4b** has been obtained in 72% yield. ^1H NMR (400 MHz, Acetonitrile- d_3) $\delta = 8.72$ (d, 1H), 8.42 – 8.31 (m, 2H), 8.11 (d, $J = 6.3$ Hz, 1H), 5.69 (s, 1H), 4.35 (s, 1H). ^{13}C NMR (101 MHz, Acetonitrile- d_3) $\delta = 164.07, 155.87, 151.12, 147.17 - 143.86$ (m), 134.55, 130.99, 125.36, 123.85, 64.31, 48.05.

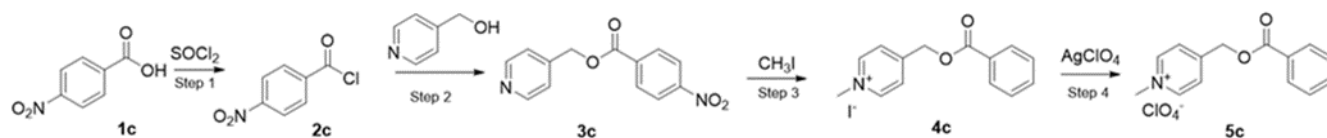
Step 4



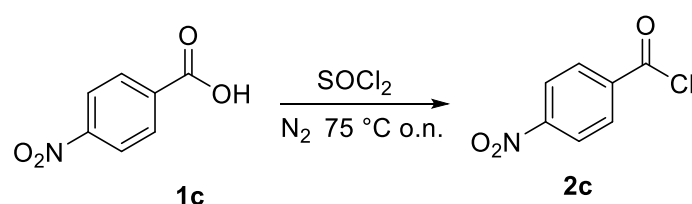
A solution of the corresponding ester **4b** (8.01 mmol) in acetonitrile was added in a three-necked darkened flask with a tail and a plug. The silver perchlorate was then added in a stoichiometric amount. The system was placed under nitrogen and left under stirring at room temperature overnight. The reaction mixture was then filtered to remove the precipitated silver iodide and the filtrate was dried. The product was then recrystallized with hot methanol. The product **5b** was obtained in 72% yield. ^1H NMR (400 MHz, Acetonitrile- d_3) $\delta = 8.69 - 8.62$ (m, 2H), 8.42 – 8.30 (m, 4H), 8.09 (d, $J = 6.3$ Hz, 2H), 5.68 (d, $J = 1.1$ Hz, 2H), 4.33 (s, 3H). ^{13}C NMR (101 MHz, Acetonitrile- d_3) $\delta = 164.07, 155.85, 151.10, 146.27 - 144.53$ (m), 134.58, 130.99, 125.36, 123.84, 64.32, 48.78 – 47.05 (m).

5.7.2.3. p-nitrobenzoic acid protection

The synthesis of the protected p-nitrobenzoic acid consists of four synthetic steps as illustrated in the following scheme.

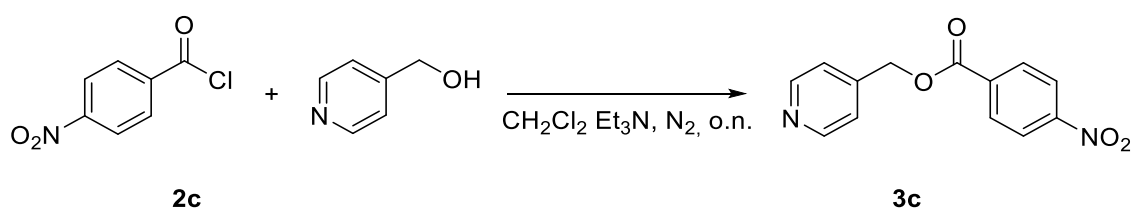


Step 1



p-nitrobenzoic acid **1c** (50.80 mmol) and toluene (20 ml) were introduced into a three-necked flask equipped with a condenser, sodium bicarbonate and calcium chloride trap, rubber septum and tail. Then thionyl chloride (344.65 mmol) was added and the mixture was refluxed overnight at 75°C. Then the unreacted thionyl chloride and toluene was removed from the system by vacuum evaporation. The acyl chloride product **2c** was obtained in 86% yield. ¹H NMR (300 MHz, Chloroform-*d*) δ= 8.43 – 8.26 (m, 9H). ¹³C NMR (75 MHz, Chloroform-*d*) δ= 167.41, 151.98, 138.38, 132.62, 124.43.

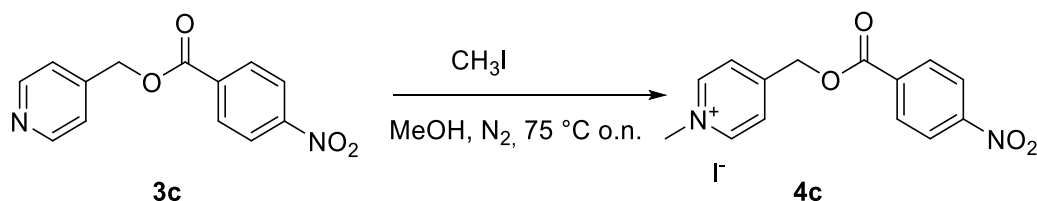
Step 2



4-(Hydroxymethyl)pyridine (23,24 mmol), dichloromethane (50 ml) and triethylamine (71,94 mmol) were introduced into a three-necked flask equipped with a condenser, dropping funnel and gas inlet. A solution of the corresponding acyl chloride **2c** (27,37 mmol) in dichloromethane was then added dropwise and the reaction mixture was left under stirring overnight at room temperature and under nitrogen. Subsequently, the ester product **3c** was put into a separating funnel and washed with a solution of water and sodium bicarbonate (20ml), recovering the lower organic phase and repeating the operation three times. The organic phase was then dehydrated with sodium sulphate, filtered

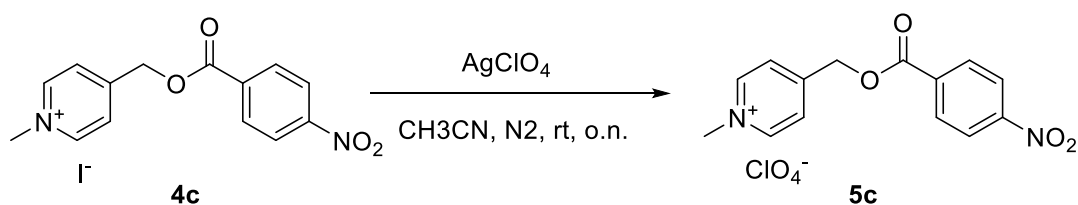
and the solvent was removed by rotary evaporation. The purified product **3c** was purified by column chromatography employing gradient elution with a mixture of hexane / ethyl acetate. The product **3c** was obtained in 35% yield. ^1H NMR (400 MHz, Acetonitrile- d_3) δ = 8.62 (d, 1H), 8.39 – 8.25 (m, 2H), 7.45 (d, J = 4.4, 1.6, 0.7 Hz, 1H), 5.44 (s, 1H). ^{13}C NMR (101 MHz, Acetonitrile- d_3) δ = 164.36, 150.90, 150.00, 144.81, 135.25, 130.77, 123.75, 121.92, 65.37.

Step 3



The corresponding ester **3c** (5,03 mmol) and methanol (50 ml) are introduced into a three-necked darkened flask equipped with a coolant connected to a nitrogen ball, pierceable septum and tail. The system is put under nitrogen. The methyl iodide (8,03 mmol) is then added with a syringe and the reaction mixture is refluxed and left under stirring at 75 °C overnight. Subsequently, the system is connected to the vacuum pump through a system of special traps to eliminate all the unreacted methyl iodide and methanol to obtain a solid. The product is then solubilized by adding the minimum amount of methanol and heating enough to solubilize. The solution is then left to rest overnight to allow crystallization. The solid was then filtered and stored in the dark. The product **4c** has been obtained with a yield of 40%. ^1H NMR (400 MHz, Acetonitrile- d_3) δ = 8.72 (d, 1H), 8.42 – 8.31 (m, 2H), 8.11 (d, J = 6.3 Hz, 1H), 5.69 (s, 1H), 4.35 (s, 1H). ^{13}C NMR (101 MHz, Acetonitrile- d_3) δ = 164.07, 155.87, 151.12, 147.17 – 143.86 (m), 134.55, 130.99, 125.36, 123.85, 64.31, 48.05.

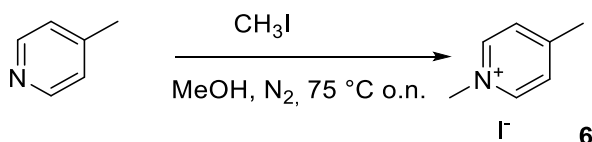
Step 4



A solution of the corresponding ester **4c** (1.89 mmol) in acetonitrile was added in a three-necked darkened flask with a tail and a plug. The silver perchlorate was then added in a stoichiometric amount. The system was placed under nitrogen and left under stirring at room temperature overnight. The reaction mixture was then filtered to remove the precipitated silver iodide and the

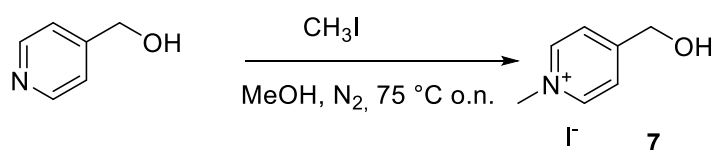
filtrate was dried. The product was then recrystallized with hot methanol. The product **5c** was obtained in 53% yield. ^1H NMR (400 MHz, Acetonitrile- d_3) δ = 8.69 – 8.62 (m, 2H), 8.42 – 8.30 (m, 4H), 8.09 (d, J = 6.3 Hz, 2H), 5.68 (d, J = 1.1 Hz, 2H), 4.33 (s, 3H). ^{13}C NMR (101 MHz, Acetonitrile- d_3) δ 164.07, 155.85, 151.10, 146.27 – 144.53 (m), 134.58, 130.99, 125.36, 123.84, 64.32, 48.78 – 47.05 (m).

5.7.2.4. Synthesis of 1,4-dimethylpyridin-1-ium iodide



The corresponding 4-methylpyridine (9.52 mmol) and methanol (10 ml) were introduced into a three-necked darkened flask equipped with a condenser, rubber septum and tail. The system was put under nitrogen. The methyl iodide (23.80 mmol) was then added with a syringe and the reaction mixture was refluxed and left under stirring at 75 °C overnight. Subsequently, the unreacted methyl iodide and methanol were removed by vacuum evaporation leading to a yellow solid. The product was recrystallized in hot methanol. The solid was filtered and stored in the dark. The product **6** has been obtained in 89% yield. ^1H NMR (400 MHz, Chloroform- d) δ 9.17 (d, 2H), 7.89 (d, J = 6.2 Hz, 2H), 4.64 (s, 2H), 2.70 (s, 3H). ^{13}C NMR (101 MHz, Chloroform- d) δ 159.00, 146.27 – 143.18 (m), 128.76, 48.87, 22.47.

5.7.2.5. Synthesis of 4-(hydroxymethyl)-1-methylpyridin-1-ium iodide



4-(Hydroxymethyl)pyridine (9.52 mmol) and methanol (10 ml) were introduced into a three-necked darkened flask equipped with a condenser, rubber septum and tail. The system was put under nitrogen. The methyl iodide (23.80 mmol) was then added with a syringe and the reaction mixture was refluxed and left under stirring at 75 °C overnight. Subsequently, the unreacted methyl iodide and methanol were removed by vacuum evaporation leading to a yellow solid. The product was recrystallized in hot methanol. The solid was filtered and stored in the dark. The product **7** has been obtained in 92% yield. ^1H NMR (300 MHz, Methanol- d_4) δ = 8.83 (d, 2H), 8.04 (d, J = 6.2 Hz, 2H), 4.83

(s, 2H), 4.40 (s, 3H). ^{13}C NMR (101 MHz, Methanol- d_4) δ = 164.11 – 161.70 (m), 144.66, 124.13, 61.38, 48.18.

5.7.1. Photocatalytic study

Photodeprotection reactions were conducted within an NMR tube. For each test an NMR tube was prepared containing the corresponding protected acid dissolved in a 60% water, 40% acetonitrile mixture. Depending on the test the CDs were added in variable quantities and the sacrificial donor EDTA in 0.1M concentration when present. The pH of the solution in this case because in a deuterated environment pD was corrected to 7 using hydrochloric acid. The mixture thus prepared was then degassed with nitrogen using a suitable system. The NMR tube was then exposed to the light of a UV lamp and NMR spectra were then recorded with different exposure times.

5.7.1.1. Quantification of acid formed by the reaction

As the formation of benzoic and p-nitro benzoic acid cannot be followed by NMR they have been quantified by gas chromatography. The quantifications were made by constructing calibration curves at different concentrations of acid using biphenyl as internal standard in 0.006M concentration. GC injection of the unknown sample was made at the end of photocatalysis without treatment. In Figure 93 the calibration curves are shown with the respective equations.

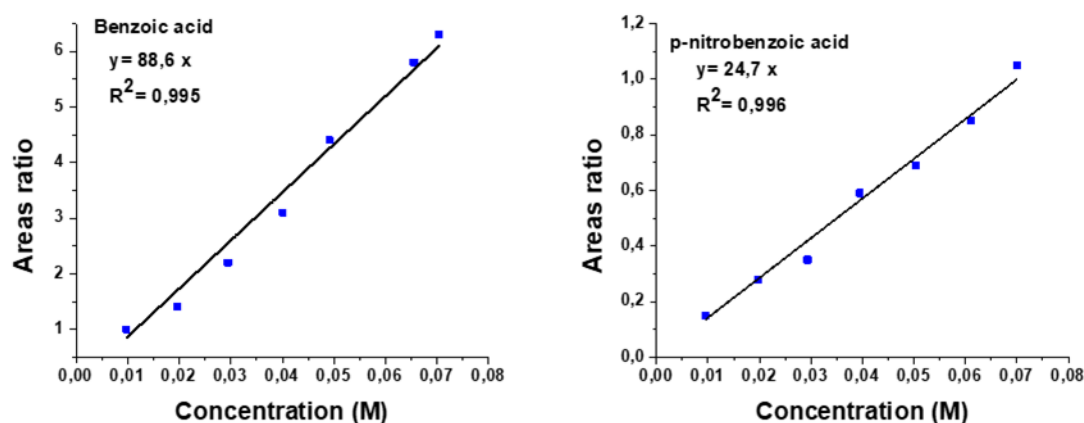


Figure 93. Calibration curves for benzoic and p-nitrobenzoic acid.

5.7.2. Cyclovoltammetry

5.7.2.1. Reagents

All reagents were analytical grade and supplied by Sigma Aldrich, and unless otherwise stated, they used as received. DMF was freshly distilled and for electrochemical measurements,

tetrabutylammonium perchlorate (TBAP), was employed as supporting electrolyte. Milli-Q water was used when necessary. Ferrocene (Fc) was employed as internal reference system.

5.7.2.2. Instrumentations and electrodes for electrochemical experiments

All voltammetric measurement were performed using a CHI 820 potentiostat (CH instrument, USA), along with the CHI instrument software version 8.15. A the three-electrode cell was prepared to carry out voltammetric experiments. The working electrode was glassy carbon disc electrode (GSE), $\phi=3\text{mm}$, A Platinum spiral was employed as counter electrode and a Ag/AgCl/KCl saturated as reference electrode. The latter was separated from the main solution by a porous septum in order to avoid contamination of DMF solutions with chloride ions leaching from the reference electrode.

5.7.2.3. Sample preparation

The DMF solutions containing CDs were prepared by adding the solvent (5ml) in 200 microliters of(L) water containing a weighted amount of CDs (typically 25mg). This procedure ensured the fully dispersion of CDs in the medium. All measurements were performed under nitrogen atmosphere.

6. Conclusion

In this thesis work, the versatility of the CDs was exploited in biomedical and photocatalytic applications, the properties of the nanomaterials were opportunely tuned focusing on the specific application by changing the carbon precursors and the synthetic methods. This work proposed also a rationalization of the outcoming morphological, optical, chemical, and electrochemical properties, with the choice of the precursors and synthetic procedures. The knowledge acquired in this study will permit the rational design of the CDs for a specific application.

In the first case of study the nanoparticles were tested in their drug loading capabilities with the view of creating a new drug delivery system. Monosaccharides-based CDs were chosen as the nanomaterials for this study for their high number of hydroxyl groups and for the intrinsic biocompatibility of precursors. The study highlighted the importance of the choice of the right to achieve the desired results. A key role in determining the biocompatibility of the CDs is played by the thermal degradation pathways of the precursors, since the fructose results to be highly toxic due to the formation of furans compounds. Glucose based CDs, shows the better biocompatibility, and also drug loading capabilities, that results to arise more from the π - π interaction than to electrostatic ones. In addition, the glucose CDs demonstrate a drug loading efficiency comparable to the best reported up to date for similar systems.

For study the photocatalytic properties of CDs, four citric acid derived CDs were employed in the photoreduction of the methylviologen. In order to investigate how the effect of the structure, and chemical composition affect the photocatalytic performance the CDs were produced by two different synthetic protocols and with or without the presence of a nitrogen doping agent. The amorphous materials produced with the hydrothermal treatment were found to present also some small organic molecule or molecular fluorophores while the pyrolysis yields graphitic materials. The photoreduction results revealed that the CDs have different reactivities that could be ascribe to their optical and physical properties. For the undoped sample due to the low luminescent properties the only species that could promote the reaction is the graphitic core, while in the doped samples the molecular fluorophore is the source of the high reactivity while the contemporaneous presence of the graphitic planes quenches the reaction due to an internal FRET process. In conclusion the salient result of this study is the incredible high reactivity pf the amorphous doped CDs, a species that was never taken into consideration for this application, opening up new perspective in this topic.

Finally, the knowledge acquired on the photocatalytic behavior of this nanoparticles was applied in the photodeprotection of N-Methyl-picolinium esters. The major achievement of the study was to prove that the carbon dots can act as photosensitizer for performing organic reaction without the addition of metal complexes or enzymes. The reaction was accomplished with high conversion and an almost total selectivity towards the desired products. Furthermore, as in the previous case the reactivity is affected by the optical and physical characteristics of the nanoparticles, revealing the same reactivity trend as before. The electrochemical studies carried out on both the nanoparticles and esters revealed that the reactivity depends on the HOMO-LUMO gap of the CDs, with the higher value having the best conversion, and also on the LUMO energy of the esters, higher is the value, and easily is its cleavage. The demonstrated ability of the CDs to perform this reaction without any additive open a new scenario in the field of the photochemistry, since these materials could be produce with low starting materials and with easy synthetic procedures.

The work herein presented demonstrated how the thorough knowledge on the structure, optical and chemical properties of the CDs could lead to the development of efficient biomedical or photochemical applications. The rationalization of the properties of the CDs with the synthetic procedure and the precursors is a crucial step to undertake in order to design the more suitable nanomaterials for a specific application.

7. References

1. Huaizhi, Z.; Yuantao, N. Techniques used for the preparation and application of gold powder in ancient China. *Gold Bull* 2000, 33, 103-105.
2. Faraday, M. X. The Bakerian Lecture. —Experimental relations of gold (and other metals) to light. *Philosophical Transactions of the Royal Society of London* 1857, 147, 145-181.
3. P. Feynman, R., There's plenty of room at the bottom: an invitation to enter a new field of physics. 2012, Vol. 23.
4. Moore, G. E. Cramming more components onto integrated circuits. *Proceedings of the IEEE* 1998, 86, 82-85.
5. Christian, P.; Von der Kammer, F.; Baalousha, M.; Hofmann, T. Nanoparticles: structure, properties, preparation and behaviour in environmental media. *Ecotoxicology* 2008, 17, 326-343.
6. Dutta, S., Applications and development of nanomaterials and nanotechnology: role of chemical engineers. 2013, Vol. 5, p 197-205.
7. Gleiter, H. Nanostructured materials: basic concepts and microstructure. *Acta Mater.* 2000, 48, 1-29.
8. Rao, C. N. R.; Müller, A.; Cheetham, A. K., *The chemistry of nanomaterials: synthesis, properties and applications.* John Wiley & Sons: 2006.
9. Iqbal, M.; Ahmad, Z., Electrical and dielectric properties of lithium manganate nanomaterials doped with rare-earth elements. 2008; Vol. 179, p 763-769.
10. Introduction. In *Nanostructures and Nanomaterials*, 2nd ed.; WORLD SCIENTIFIC: 2012; pp 1-17.
11. Zeng, S.; Yong, K.-T.; Roy, I.; Dinh, X.-Q.; Yu, X.; Luan, F. A Review on functionalized gold nanoparticles for biosensing applications. *Plasmonics* 2011, 6, 491.
12. Ghosh, P.; Han, G.; De, M.; Kim, C. K.; Rotello, V. M. Gold nanoparticles in delivery applications. *Adv. Drug Delivery Rev.* 2008, 60, 1307-1315.
13. Weir, A.; Westerhoff, P.; Fabricius, L.; Hristovski, K.; von Goetz, N. Titanium dioxide nanoparticles in food and personal care products. *Environ. Sci. Technol.* 2012, 46, 2242-2250.
14. Chen, X.; Mao, S. S. Titanium dioxide nanomaterials: synthesis, properties, modifications, and applications. *Chem. Rev.* 2007, 107, 2891-2959.
15. Bai, Y.; Mora-Seró, I.; De Angelis, F.; Bisquert, J.; Wang, P. Titanium dioxide nanomaterials for photovoltaic applications. *Chem. Rev.* 2014, 114, 10095-10130.
16. Djurišić Aleksandra, B.; Leung Yu, H.; Ng Alan, M. C.; Xu Xiao, Y.; Lee Patrick, K. H.; Degger, N.; Wu, R. S. S. Toxicity of metal oxide nanoparticles: mechanisms, characterization, and avoiding experimental artefacts. *Small* 2014, 11, 26-44.
17. P., B. H.; A., C.; O., F. G.; U., H. Das Adsorptionsverhalten sehr dünner Kohlenstoff-Folien. *Z. Anorg. Allg. Chem.* 1962, 316, 119-127.
18. Kroto, H. W.; Heath, J. R.; O'Brien, S. C.; Curl, R. F.; Smalley, R. E. C60: Buckminsterfullerene. *Nature* 1985, 318, 162.

19. E, G. K.; S, S. Syntheses and properties of macromolecular fullerenes, a review. *Polym. Int.* 1999, 48, 743-757.
20. Kausar, A., Advances in Polymer/Fullerene Nanocomposite: A Review on Essential Features and Applications. *Polym.-Plast. Technol. Eng.* 2017, 56, 594-605.
21. Coro, J.; Suárez, M.; Silva, L. S. R.; Eguiluz, K. I. B.; Salazar-Banda, G. R., Fullerene Applications in Fuel Cells: A Review. *Int. J. Hydrogen Energy* 2016, 41, 17944-17959.
22. Muñoz, A.; Sigwalt, D.; Illescas, B. M.; Luczkowiak, J.; Rodríguez-Pérez, L.; Nierengarten, I.; Holler, M.; Remy, J.-S.; Buffet, K.; Vincent, S. P.; Rojo, J.; Delgado, R.; Nierengarten, J.-F.; Martín, N., Synthesis of Giant Globular Multivalent Glycofullerenes as Potent Inhibitors in a Model of Ebola Virus Infection. *Nature Chem.* 2015, 8, 50.
23. Berber, S.; Kwon, Y.-K.; Tománek, D., Unusually High Thermal Conductivity of Carbon Nanotubes. *Phys. Rev. Lett.* 2000, 84, 4613-4616.
24. Shenogin, S.; Xue, L.; Ozisik, R.; Keblinski, P.; Cahill, D. G., Role of Thermal Boundary Resistance on the Heat Flow in Carbon-Nanotube Composites. *J. Appl. Phys.* 2004, 95, 8136-8144.
25. Salvétat, J. P.; Bonard, J. M.; Thomson, N. H.; Kulik, A. J.; Forró, L.; Benoit, W.; Zuppiroli, L., Mechanical Properties of Carbon Nanotubes. *Appl. Phys. A* 1999, 69, 255-260.
26. Habisreutinger, S. N.; Leijtens, T.; Eperon, G. E.; Stranks, S. D.; Nicholas, R. J.; Snaith, H. J., Carbon Nanotube/Polymer Composites as a Highly Stable Hole Collection Layer in Perovskite Solar Cells. *Nano Lett.* 2014, 14, 5561-5568.
27. Terrones, M., Carbon Nanotubes: Synthesis and Properties, Electronic Devices and Other Emerging Applications. *Int. Mater. Rev.* 2004, 49, 325-377.
28. Lefebvre, J.; Ding, J.; Li, Z.; Finnie, P.; Lopinski, G.; Malenfant, P. R. L., High-Purity Semiconducting Single-Walled Carbon Nanotubes: A Key Enabling Material in Emerging Electronics. *Acc. Chem. Res.* 2017, 50, 2479-2486.
29. Yang, S.-T.; Cao, L.; Luo, P. G.; Lu, F.; Wang, X.; Wang, H.; Meziani, M. J.; Liu, Y.; Qi, G.; Sun, Y.-P., Carbon Dots for Optical Imaging in Vivo. *J. Am. Chem. Soc.* 2009, 131, 11308-11309.
30. Yang, Y.; Cui, J.; Zheng, M.; Hu, C.; Tan, S.; Xiao, Y.; Yang, Q.; Liu, Y., One-Step Synthesis of Amino-Functionalized Fluorescent Carbon Nanoparticles by Hydrothermal Carbonization of Chitosan. *Chem. Commun. (Cambridge, U. K.)* 2012, 48, 380-382.
31. Bhunia, S. K.; Saha, A.; Maity, A. R.; Ray, S. C.; Jana, N. R., Carbon Nanoparticle-Based Fluorescent Bioimaging Probes. *Sci. Rep.* 2013, 3, 1473.
32. Chen, B.; Li, F.; Li, S.; Weng, W.; Guo, H.; Guo, T.; Zhang, X.; Chen, Y.; Huang, T.; Hong, X.; You, S.; Lin, Y.; Zeng, K.; Chen, S., Large Scale Synthesis of Photoluminescent Carbon Nanodots and Their Application for Bioimaging. *Nanoscale* 2013, 5, 1967-1971.

33. Skrabalak, S. E., Ultrasound-Assisted Synthesis of Carbon Materials. *Phys. Chem. Chem. Phys.* 2009, 11, 4930-4942.
34. Lee, H. U.; Park, S. Y.; Park, E. S.; Son, B.; Lee, S. C.; Lee, J. W.; Lee, Y.-C.; Kang, K. S.; Kim, M. I.; Park, H. G.; Choi, S.; Huh, Y. S.; Lee, S.-Y.; Lee, K.-B.; Oh, Y.-K.; Lee, J., Photoluminescent Carbon Nanotags from Harmful Cyanobacteria for Drug Delivery and Imaging in Cancer Cells. *Sci. Rep.* 2014, 4, 4665.
35. Zhang, Z.; Shi, Y.; Pan, Y.; Cheng, X.; Zhang, L.; Chen, J.; Li, M.-J.; Yi, C., Quinoline Derivative-Functionalized Carbon Dots as a Fluorescent Nanosensor for Sensing and Intracellular Imaging of Zn²⁺. *J. Mater. Chem. B* 2014, 2, 5020-5027.
36. Zhou, L.; Lin, Y.; Huang, Z.; Ren, J.; Qu, X., Carbon Nanodots as Fluorescence Probes for Rapid, Sensitive, and Label-Free Detection of Hg²⁺ and Biothiols in Complex Matrices. *Chem. Commun. (Cambridge, U. K.)* 2012, 48, 1147-1149.
37. Qu, Q.; Zhu, A.; Shao, X.; Shi, G.; Tian, Y., Development of a Carbon Quantum Dots-Based Fluorescent Cu²⁺ Probe Suitable for Living Cell Imaging. *Chem. Commun. (Cambridge, U. K.)* 2012, 48, 5473-5475.
38. Tang, L.; Ji, R.; Cao, X.; Lin, J.; Jiang, H.; Li, X.; Teng, K. S.; Luk, C. M.; Zeng, S.; Hao, J.; Lau, S. P., Deep Ultraviolet Photoluminescence of Water-Soluble Self-Passivated Graphene Quantum Dots. *ACS Nano* 2012, 6, 5102-5110.
39. Cao, L.; Sahu, S.; Anilkumar, P.; Bunker, C. E.; Xu, J.; Fernando, K. A. S.; Wang, P.; Gulians, E. A.; Tackett, K. N.; Sun, Y.-P., Carbon Nanoparticles as Visible-Light Photocatalysts for Efficient Co₂ Conversion and Beyond. *J. Am. Chem. Soc.* 2011, 133, 4754-4757.
40. Cao, L.; Wang, X.; Mezziani, M. J.; Lu, F.; Wang, H.; Luo, P. G.; Lin, Y.; Harruff, B. A.; Veca, L. M.; Murray, D.; Xie, S.-Y.; Sun, Y.-P., Carbon Dots for Multiphoton Bioimaging. *J. Am. Chem. Soc.* 2007, 129, 11318-11319.
41. Xu, X.; Ray, R.; Gu, Y.; Ploehn, H. J.; Gearheart, L.; Raker, K.; Scrivens, W. A., Electrophoretic Analysis and Purification of Fluorescent Single-Walled Carbon Nanotube Fragments. *J. Am. Chem. Soc.* 2004, 126, 12736-12737.
42. Bottini, M.; Balasubramanian, C.; Dawson, M. I.; Bergamaschi, A.; Bellucci, S.; Mustelin, T., Isolation and Characterization of Fluorescent Nanoparticles from Pristine and Oxidized Electric Arc-Produced Single-Walled Carbon Nanotubes. *J. Phys. Chem. B* 2006, 110, 831-836.
43. Li, X.; Wang, H.; Shimizu, Y.; Pyatenko, A.; Kawaguchi, K.; Koshizaki, N., Preparation of Carbon Quantum Dots with Tunable Photoluminescence by Rapid Laser Passivation in Ordinary Organic Solvents. *Chem. Commun.* 2011, 47, 932-934.
44. Hu, S.; Liu, J.; Yang, J.; Wang, Y.; Cao, S., Laser Synthesis and Size Tailor of Carbon Quantum Dots. *Journal of Nanoparticle Research* 2011, 13, 7247-7252.

-
45. Zhou, J.; Booker, C.; Li, R.; Zhou, X.; Sham, T.-K.; Sun, X.; Ding, Z., An Electrochemical Avenue to Blue Luminescent Nanocrystals from Multiwalled Carbon Nanotubes (Mwcnts). *J. Am. Chem. Soc.* 2007, 129, 744-745.
 46. Liu, M.; Xu, Y.; Niu, F.; Gooding, J. J.; Liu, J., Carbon Quantum Dots Directly Generated from Electrochemical Oxidation of Graphite Electrodes in Alkaline Alcohols and the Applications for Specific Ferric Ion Detection and Cell Imaging. *Analyst* **2016**, 141, 2657-2664.
 47. Liu, H.; Ye, T.; Mao, C. Fluorescent carbon nanoparticles derived from candle soot. *Angew. Chem. Int. Ed. Engl.*, 2007, 46(34), 6473-5.
 48. Zhang, S.; Zhang, L.; Huang, L.; Zheng, G.; Zhang, P.; Jin, Y.; Jiao, Z.; Sun, X., Study on the Fluorescence Properties of Carbon Dots Prepared Via Combustion Process. *J. Lumin.* 2018.
 49. Fang, Y.; Guo, S.; Li, D.; Zhu, C.; Ren, W.; Dong, S.; Wang, E., Easy Synthesis and Imaging Applications of Cross-Linked Green Fluorescent Hollow Carbon Nanoparticles. *ACS Nano* 2012, 6, 400-409.
 50. Xiao, Q.; Liang, Y.; Zhu, F.; Lu, S.; Huang, S., Microwave-Assisted One-Pot Synthesis of Highly Luminescent N-Doped Carbon Dots for Cellular Imaging and Multi-Ion Probing. *Microchim. Acta* 2017, 184, 2429-2438.
 51. Lim, S. Y.; Shen, W.; Gao, Z., Carbon Quantum Dots and Their Applications. *Chem. Soc. Rev.* 2015, 44, 362-381.
 52. Li, H.; Shao, F.-Q.; Huang, H.; Feng, J.-J.; Wang, A.-J., Eco-Friendly and Rapid Microwave Synthesis of Green Fluorescent Graphitic Carbon Nitride Quantum Dots for Vitro Bioimaging. *Sensors and Actuators B: Chemical* 2016, 226, 506-511.
 53. Jaiswal, A.; Ghosh, S.S.; Chattopadhyay, A. One step synthesis of CDs by microwave mediated caramelization of poly(ethylene glycol). *Chem. Commun.*, 2012, 48(3), 407-409.
 54. Pham-Truong, T.-N.; Petenzi, T.; Ranjan, C.; Randriamahazaka, H.; Ghilane, J., Microwave Assisted Synthesis of Carbon Dots in Ionic Liquid as Metal Free Catalyst for Highly Selective Production of Hydrogen Peroxide. *Carbon* 2018, 130, 544-552.
 55. Francesco, R.; Luka, Đ.; Francesca, A.; Maurizio, P., Customizing the Electrochemical Properties of Carbon Nanodots by Using Quinones in Bottom-up Synthesis. *Angew. Chem., Int. Ed.* 2018, 57, 5062-5067.
 56. Đorđević, L.; Arcudi, F.; D'Urso, A.; Cacioppo, M.; Micali, N.; Bürgi, T.; Purrello, R.; Prato, M., Design Principles of Chiral Carbon Nanodots Help Convey Chirality from Molecular to Nanoscale Level. *Nature Communications* 2018, 9, 3442.
 57. Bourlinos, A. B.; Stassinopoulos, A.; Angelos, D.; Zboril, R.; Karakassides, M.; Giannelis, E. P., Surface Functionalized Carbogenic Quantum Dots. *Small* 2008, 4, 455-458.

58. Guo, C. X.; Zhao, D.; Zhao, Q.; Wang, P.; Lu, X., Na⁺-Functionalized Carbon Quantum Dots: A New Draw Solute in Forward Osmosis for Seawater Desalination. *Chem. Commun. (Cambridge, U. K.)* 2014, 50, 7318-7321.
59. Martindale, B. C. M.; Hutton, G. A. M.; Caputo, C. A.; Reisner, E., Solar Hydrogen Production Using Carbon Quantum Dots and a Molecular Nickel Catalyst. *J. Am. Chem. Soc.* 2015, 137, 6018-6025.
60. Martindale, B. C. M.; Hutton, G. A. M.; Caputo, C. A.; Prantl, S.; Godin, R.; Durrant, J. R.; Reisner, E., Enhancing Light Absorption and Charge Transfer Efficiency in Carbon Dots through Graphitization and Core Nitrogen Doping. *Angew. Chem., Int. Ed.* 2017, 56, 6459-6463.
61. Wang, L.; Bi, Y.; Hou, J.; Li, H.; Xu, Y.; Wang, B.; Ding, H.; Ding, L., Facile, Green and Clean One-Step Synthesis of Carbon Dots from Wool: Application as a Sensor for Glyphosate Detection Based on the Inner Filter Effect. *Talanta* 2016, 160, 268-275.
62. Liu, R.; Zhang, J.; Gao, M.; Li, Z.; Chen, J.; Wu, D.; Liu, P., A Facile Microwave-Hydrothermal Approach Towards Highly Photoluminescent Carbon Dots from Goose Feathers. *RSC Advances* 2015, 5, 4428-4433.
63. Qin, X.; Lu, W.; Asiri, A. M.; Al-Youbi, A. O.; Sun, X., Microwave-Assisted Rapid Green Synthesis of Photoluminescent Carbon Nanodots from Flour and Their Applications for Sensitive and Selective Detection of Mercury(II) Ions. *Sensors and Actuators B: Chemical* 2013, 184, 156-162.
64. Dong, Y.; Wang, R.; Li, H.; Shao, J.; Chi, Y.; Lin, X.; Chen, G., Polyamine-Functionalized Carbon Quantum Dots for Chemical Sensing. *Carbon* 2012, 50, 2810-2815.
65. Zhu, S.; Meng, Q.; Wang, L.; Zhang, J.; Song, Y.; Jin, H.; Zhang, K.; Sun, H.; Wang, H.; Yang, B. Highly Photoluminescent Carbon Dots for Multicolor Patterning, Sensors, and Bioimaging. *Angew. Chemie*, 2013, 125(14), 4045–4049.
66. Chandra, S.; Laha, D.; Pramanik, A.; Ray Chowdhuri, A.; Karmakar, P.; Sahu, S. K., Synthesis of Highly Fluorescent Nitrogen and Phosphorus Doped Carbon Dots for the Detection of Fe³⁺ Ions in Cancer Cells. *Luminescence* 2015, 31, 81-87.
67. Wang, L.; Ruan, F.; Lv, T.; Liu, Y.; Deng, D.; Zhao, S.; Wang, H.; Xu, S. One step synthesis of Al/N co-doped carbon nanoparticles with enhanced photoluminescence. *J. Lumin.*, 2015, 158, 1–5.
68. Sadhanala, H.K.; Khatei, J.; Nanda, K.K. Facile hydrothermal synthesis of carbon nanoparticles and possible application as white light phosphors and catalysts for the reduction of nitrophenol. *RSC Adv.*, 2014, 4(22), 11481.
69. Gao, X.; Lu, Y.; Zhang, R.; He, S.; Ju, J.; Liu, M.; Li, L.; Chen, W. One-pot synthesis of carbon nanodots for fluorescence turn-on detection of Ag⁺ based on the Ag⁺-induced enhancement of fluorescence. *J. Mater. Chem. C*, 2015, 3(10), 2302–2309.

70. Tong, G.; Wang, J.; Wang, R.; Guo, X.; He, L.; Qiu, F.; Wang, G.; Zhu, B.; Zhu, X.; Liu, T. Amorphous carbon dots with high two-photon fluorescence for cellular imaging passivated by hyperbranched poly(amino amine). *J. Mater. Chem. B*, 2015, 3(4), 700–706.
71. Li, C.-L.; Huang, C.-C.; Periasamy, A.P.; Roy, P.; Wu, W.-C.; Hsu, C.-L.; Chang, H.-T. Synthesis of photoluminescent carbon dots for the detection of cobalt ions. *RSC Adv.*, 2015, 5(3), 2285–2291.
72. Wu, Z.L.; Zhang, P.; Gao, M.X.; Liu, C.F.; Wang, W.; Leng, F.; Huang, C.Z. One-pot hydrothermal synthesis of highly luminescent nitrogen-doped amphoteric carbon dots for bioimaging from *Bombyx mori* silk – natural proteins. *J. Mater. Chem. B*, 2013, 1(22), 2868.
73. Das, R.; Bandyopadhyay, R.; Pramanik, P., Carbon Quantum Dots from Natural Resource: A Review. *Materials Today Chemistry* 2018, 8, 96-109.
74. Park, S.Y.; Lee, H.U.; Park, E.S.; Lee, S.C.; Lee, J.-W.; Jeong, S.W.; Kim, C.H.; Lee, Y.-C.; Huh, Y.S.; Lee, J. Photoluminescent green carbon nanodots from food-waste-derived sources: large-scale synthesis, properties, and biomedical applications. *ACS Appl. Mater. Interfaces*, 2014, 6(5), 3365–3370.
75. Yang, Z.-C.; Wang, M.; Yong, A. M.; Wong, S. Y.; Zhang, X.-H.; Tan, H.; Chang, A. Y.; Li, X.; Wang, J., Intrinsically Fluorescent Carbon Dots with Tunable Emission Derived from Hydrothermal Treatment of Glucose in the Presence of Monopotassium Phosphate. *Chem. Commun. (Cambridge, U. K.)* 2011, 47, 11615-11617.
76. Jiang, K.; Sun, S.; Zhang, L.; Lu, Y.; Wu, A.; Cai, C.; Lin, H. Red, Green, and Blue Luminescence by Carbon Dots: Full-Color Emission Tuning and Multicolor Cellular Imaging. *Angew. Chemie Int. Ed.*, 2015, 54(18), 5360–5363
77. Li, Y.; Zhao, Y.; Cheng, H.; Hu, Y.; Shi, G.; Dai, L.; Qu, L., Nitrogen-Doped Graphene Quantum Dots with Oxygen-Rich Functional Groups. *J. Am. Chem. Soc.* 2012, 134, 15-18.
78. Dong, Y.; Pang, H.; Yang, H. B.; Guo, C.; Shao, J.; Chi, Y.; Li, C. M.; Yu, T., Carbon-Based Dots Co-Doped with Nitrogen and Sulfur for High Quantum Yield and Excitation-Independent Emission. *Angew. Chem.* 2013, 125, 7954-7958.
79. Chandra, S.; Patra, P.; Pathan, S. H.; Roy, S.; Mitra, S.; Layek, A.; Bhar, R.; Pramanik, P.; Goswami, A., Luminescent S-Doped Carbon Dots: An Emergent Architecture for Multimodal Applications. *J. Mater. Chem. B* 2013, 1, 2375-2382.
80. Wang, W.; Li, Y.; Cheng, L.; Cao, Z.; Liu, W., Water-Soluble and Phosphorus-Containing Carbon Dots with Strong Green Fluorescence for Cell Labeling. *J. Mater. Chem. B* 2014, 2, 46-48.
81. Tian, L.; Ghosh, D.; Chen, W.; Pradhan, S.; Chang, X.; Chen, S., Nanosized Carbon Particles from Natural Gas Soot. *Chem. Mater.* 2009, 21, 2803-2809.
82. Wang, S.; Chen, Z.-G.; Cole, I.; Li, Q., Structural Evolution of Graphene Quantum Dots During Thermal Decomposition of Citric Acid and the Corresponding Photoluminescence. *Carbon* 2015, 82, 304-313.

83. Krysmann, M. J.; Kelarakis, A.; Dallas, P.; Giannelis, E. P., Formation Mechanism of Carbogenic Nanoparticles with Dual Photoluminescence Emission. *J. Am. Chem. Soc.* 2012, 134, 747-750.
84. Song, Y.; Zhu, S.; Zhang, S.; Fu, Y.; Wang, L.; Zhao, X.; Yang, B., Investigation from Chemical Structure to Photoluminescent Mechanism: A Type of Carbon Dots from the Pyrolysis of Citric Acid and an Amine. *J. Mater. Chem. C* 2015, 3, 5976-5984.
85. Shi, L.; Yang, J. H.; Zeng, H. B.; Chen, Y. M.; Yang, S. C.; Wu, C.; Zeng, H.; Yoshihito, O.; Zhang, Q., Carbon Dots with High Fluorescence Quantum Yield: The Fluorescence Originates from Organic Fluorophores. *Nanoscale* 2016, 8, 14374-14378.
86. Schneider, J.; Reckmeier, C. J.; Xiong, Y.; von Seckendorff, M.; Susa, A. S.; Kasák, P.; Rogach, A. L., Molecular Fluorescence in Citric Acid-Based Carbon Dots. *The Journal of Physical Chemistry C* 2017, 121, 2014-2022.
87. Li, H.; He, X.; Kang, Z.; Huang, H.; Liu, Y.; Liu, J.; Lian, S.; Tsang, C.H.A.; Yang, X.; Lee, S.T. Water-soluble fluorescent carbon quantum dots and photocatalyst design. *Angew. Chemie - Int. Ed.*, 2010, 49(26), 4430-4434.
88. Zhu, S.; Song, Y.; Wang, J.; Wan, H.; Zhang, Y.; Ning, Y.; Yang, B., Photoluminescence mechanism in graphene quantum dots: Quantum confinement effect and surface/edge state. *Nano Today* 2017, 13, 10-14.
89. Sun, Y.-P.; Zhou, B.; Lin, Y.; Wang, W.; Fernando, K. A. S.; Pathak, P.; Mezziani, M. J.; Harruff, B. A.; Wang, X.; Wang, H.; Luo, P. G.; Yang, H.; Kose, M. E.; Chen, B.; Veca, L. M.; Xie, S.-Y., Quantum-Sized Carbon Dots for Bright and Colorful Photoluminescence. *J. Am. Chem. Soc.* 2006, 128, 7756-7757.
90. Qu, S.; Chen, H.; Zheng, X.; Cao, J.; Liu, X. Ratiometric fluorescent nanosensor based on water soluble carbon nanodots with multiple sensing capacities. *Nanoscale*, 2013, 5(12), 5514.
91. Fang, Q.; Dong, Y.; Chen, Y.; Lu, C.-H.; Chi, Y.; Yang, H.-H.; Yu, T., Luminescence Origin of Carbon Based Dots Obtained from Citric Acid and Amino Group-Containing Molecules. *Carbon* 2017, 118, 319-326.
92. Essner, J. B.; Baker, G. A., The Emerging Roles of Carbon Dots in Solar Photovoltaics: A Critical Review. *Environmental Science: Nano* 2017, 4, 1216-1263.
93. Zheng, M.; Liu, S.; Li, J.; Qu, D.; Zhao, H.; Guan, X.; Hu, X.; Xie, Z.; Jing, X.; Sun, Z., Integrating Oxaliplatin with Highly Luminescent Carbon Dots: An Unprecedented Theranostic Agent for Personalized Medicine. *Adv. Mater.* 2014, 26, 3554-3560.
94. Mehta, V. N.; Chettiar, S. S.; Bhamore, J. R.; Kailasa, S. K.; Patel, R. M., Green Synthetic Approach for Synthesis of Fluorescent Carbon Dots for Lisinopril Drug Delivery System and Their Confirmations in the Cells. *J. Fluoresc.* 2017, 27, 111-124.

- ⁹⁵ Peng, Z.; Han, X.; Li, S.; Al-Youbi, A. O.; Bashammakh, A. S.; El-Shahawi, M. S.; Leblanc, R. M., Carbon Dots: Biomacromolecule Interaction, Bioimaging and Nanomedicine. *Coord. Chem. Rev.* 2017, 343, 256-277.
- ⁹⁶ Jung, Y. K.; Shin, E.; Kim, B.-S., Cell Nucleus-Targeting Zwitterionic Carbon Dots. *Sci. Rep.* 2015, 5, 18807.
- ⁹⁷ Wang, B.; Wang, S.; Wang, Y.; Lv, Y.; Wu, H.; Ma, X.; Tan, M., Highly Fluorescent Carbon Dots for Visible Sensing of Doxorubicin Release Based on Efficient Nanosurface Energy Transfer. *Biotechnol. Lett.* 2016, 38, 191-201.
- ⁹⁸ Wang, X.; Cao, L.; Lu, F.; Meziani, M. J.; Li, H.; Qi, G.; Zhou, B.; Harruff, B. A.; Kermarrec, F.; Sun, Y.-P., Photoinduced Electron Transfers with Carbon Dots. *Chem. Commun. (Cambridge, U. K.)* 2009, 3774-3776.
- ⁹⁹ Yu, H.; Zhao, Y.; Zhou, C.; Shang, L.; Peng, Y.; Cao, Y.; Wu, L.-Z.; Tung, C.-H.; Zhang, T., Carbon Quantum Dots/TiO₂ Composites for Efficient Photocatalytic Hydrogen Evolution. *J. Mater. Chem. A* 2014, 2, 3344-3351.
- ¹⁰⁰ Li, H.; Liu, R.; Liu, Y.; Huang, H.; Yu, H.; Ming, H.; Lian, S.; Lee, S.-T.; Kang, Z., Carbon Quantum Dots/Cu₂O Composites with Protruding Nanostructures and Their Highly Efficient (near) Infrared Photocatalytic Behavior. *Journal of Materials Chemistry* 2012, 22, 17470-17475.
- ¹⁰¹ Zhang, H.; Ming, H.; Lian, S.; Huang, H.; Li, H.; Zhang, L.; Liu, Y.; Kang, Z.; Lee, S.-T., Fe₂O₃/Carbon Quantum Dots Complex Photocatalysts and Their Enhanced Photocatalytic Activity under Visible Light. *Dalton Trans.* 2011, 40, 10822-10825.
- ¹⁰² Yu, H.; Zhang, H.; Huang, H.; Liu, Y.; Li, H.; Ming, H.; Kang, Z., ZnO/Carbon Quantum Dots Nanocomposites: One-Step Fabrication and Superior Photocatalytic Ability for Toxic Gas Degradation under Visible Light at Room Temperature. *New J. Chem.* 2012, 36, 1031-1035.
- ¹⁰³ Han, M.; Zhu, S.; Lu, S.; Song, Y.; Feng, T.; Tao, S.; Liu, J.; Yang, B., Recent Progress on the Photocatalysis of Carbon Dots: Classification, Mechanism and Applications. *Nano Today* 2018.
- ¹⁰⁴ Liu, R.; Huang, H.; Li, H.; Liu, Y.; Zhong, J.; Li, Y.; Zhang, S.; Kang, Z., Metal Nanoparticle/Carbon Quantum Dot Composite as a Photocatalyst for High-Efficiency Cyclohexane Oxidation. *ACS Catalysis* 2014, 4, 328-336.
- ¹⁰⁵ Li, H.; Liu, R.; Lian, S.; Liu, Y.; Huang, H.; Kang, Z., Near-Infrared Light Controlled Photocatalytic Activity of Carbon Quantum Dots for Highly Selective Oxidation Reaction. *Nanoscale* 2013, 5, 3289-3297.
- ¹⁰⁶ Ma, Z.; Ming, H.; Huang, H.; Liu, Y.; Kang, Z., One-Step Ultrasonic Synthesis of Fluorescent N-Doped Carbon Dots from Glucose and Their Visible-Light Sensitive Photocatalytic Ability. *New J. Chem.* 2012, 36, 861-864.

- ¹⁰⁷. Yang, P.; Zhao, J.; Wang, J.; Cui, H.; Li, L.; Zhu, Z., Pure Carbon Nanodots for Excellent Photocatalytic Hydrogen Generation. *RSC Advances* 2015, 5, 21332-21335.
- ¹⁰⁸. Consiglio, G.; Failla, S.; Finocchiaro, P.; Oliveri, I. P.; Purrello, R.; Di Bella, S. Supramolecular aggregation/deaggregation in amphiphilic dipolar schiff-base zinc(II) complexes. *Inorg. Chem.* 2010, 49, 5134-5142.
- ¹⁰⁹. Consiglio, G.; Failla, S.; Finocchiaro, P.; Oliveri, I. P.; Bella, S. D. Aggregation properties of bis(salicylaldiminato)zinc(ii) Schiff-base complexes and their Lewis acidic character. *Dalton Trans.* 2012, 41, 387-395.
- ¹¹⁰. Pilone, A.; Lamberti, M.; Mazzeo, M.; Milione, S.; Pellicchia, C. Ring-opening polymerization of cyclic esters by phenoxy-thioether complexes derived from biocompatible metals. *Dalton Trans.* 2013, 42, 13036-13047.
- ¹¹¹. Zhu, S.; Zhao, X.; Song, Y.; Lu, S.; Yang, B., Beyond bottom-up carbon nanodots: Citric-acid derived organic molecules. *Nano Today* 2016, 11 (2), 128-132.
- ¹¹². Bagheri, Z.; Ehtesabi, H.; Rahmandoust, M.; Ahadian, M. M.; Hallaji, Z.; Eskandari, F.; Jokar, E., New insight into the concept of carbonization degree in synthesis of carbon dots to achieve facile smartphone based sensing platform. *Sc. Rep.* 2017, 7 (1), 11013.
- ¹¹³. Zhou, J.; Zhou, H.; Tang, J.; Deng, S.; Yan, F.; Li, W.; Qu, M., Carbon dots doped with heteroatoms for fluorescent bioimaging: a review. *Microchim. Acta* 2017, 184 (2), 343-368.
- ¹¹⁴. Dong, Y.; Shao, J.; Chen, C.; Li, H.; Wang, R.; Chi, Y.; Lin, X.; Chen, G., Blue luminescent graphene quantum dots and graphene oxide prepared by tuning the carbonization degree of citric acid. *Carbon* 2012, 50 (12), 4738-4743.
- ¹¹⁵. Hutton, G. A. M.; Martindale, B. C. M.; Reisner, E., Carbon dots as photosensitizers for solar-driven catalysis. *Chem. Soc. Rev.* 2017, 46 (20), 6111-6123.
- ¹¹⁶. Cohen, Y.; Avram, L.; Frish, L., Diffusion Nmr Spectroscopy in Supramolecular and Combinatorial Chemistry: An Old Parameter—New Insights. *Angew. Chem., Int. Ed.* 2005, 44, 520-554.
- ¹¹⁷. Fielden, J.; Long, D.-I.; Slawin, A. M. Z.; Kögerler, P.; Cronin, L., Ligand and Counterion Control of Ag(I) Architectures: Assembly of a {Ag₈} Ring Cluster Mediated by Hydrophobic and Ag...Ag Interactions. *Inorg. Chem.* 2007, 46, 9090-9097.
- ¹¹⁸. Macchioni, A.; Ciancaleoni, G.; Zuccaccia, C.; Zuccaccia, D., Determining Accurate Molecular Sizes in Solution through Nmr Diffusion Spectroscopy. *Chem. Soc. Rev.* 2008, 37, 479-489.
- ¹¹⁹. Bae, K. H.; Chung, H. J.; Park, T. G., Nanomaterials for cancer therapy and imaging. *Mol. Cells* 2011, 31 (4), 295-302.
- ¹²⁰. Yao, J.; Yang, M.; Duan, Y., Chemistry, biology, and medicine of fluorescent nanomaterials and related systems: new insights into biosensing, bioimaging, genomics, diagnostics, and therapy. *Chem. Rev.* 2014, 114 (12), 6130-6178

121. Baldi, G.; Bonacchi, D.; Innocenti, C.; Lorenzi, G.; Sangregorio, C., Cobalt ferrite nanoparticles: The control of the particle size and surface state and their effects on magnetic properties. *J. Magn. Mater.* 2007, 311 (1), 10-16.
122. Rogach, A. L.; Eychmüller, A.; Hickey, S. G.; Kershaw, S. V., Infrared-emitting colloidal nanocrystals: synthesis, assembly, spectroscopy, and applications. *Small* 2007, 3 (4), 536-557.
123. Boisselier, E.; Astruc, D., Gold nanoparticles in nanomedicine: preparations, imaging, diagnostics, therapies and toxicity. *Chem. Soc. Rev.* 2009, 38 (6), 1759-1782
124. Podsiadlo, P.; Paternel, S.; Rouillard, J.-M.; Zhang, Z.; Lee, J.; Lee, J.-W.; Gulari, E.; Kotov, N., Layer-by-Layer Assembly of Nacre-Like Nanostructured Composites with Antimicrobial Properties. 2006; Vol. 21, p 11915-21.
125. Chinen, A. B.; Guan, C. M.; Ferrer, J. R.; Barnaby, S. N.; Merkel, T. J.; Mirkin, C. A., Nanoparticle probes for the detection of cancer biomarkers, cells, and tissues by fluorescence. *Chem. Rev. (Washington, DC, U. S.)* 2015, 115 (19), 10530-10574.
126. Hofmann-Antenbrink, M.; Grainger, D. W.; Hofmann, H., Nanoparticles in medicine: Current challenges facing inorganic nanoparticle toxicity assessments and standardizations. *Nanomedicine: Nanotechnology, Biology and Medicine* 2015, 11 (7), 1689-1694.
127. Wang, J. L.; Qiu, J. J., A review of carbon dots in biological applications. *J. Mater. Sci.* 2016, 51 (10), 4728-4738.
128. Sharma, P.; Brown, S.; Walter, G.; Santra, S.; Moudgil, B., Nanoparticles for bioimaging. *Adv. Colloid Interface Sci.* 2006, 123-126, 471-485.
129. Yuan, Y.; Guo, B.; Hao, L.; Liu, N.; Lin, Y.; Guo, W.; Li, X.; Gu, B., Doxorubicin-loaded environmentally friendly carbon dots as a novel drug delivery system for nucleus targeted cancer therapy. *Colloids and Surfaces B: Biointerfaces* 2017, 159, 349-359.
130. Zhang, M.; Yuan, P.; Zhou, N.; Su, Y.; Shao, M.; Chi, C., pH-Sensitive N-doped carbon dots–heparin and doxorubicin drug delivery system: preparation and anticancer research. *RSC Advances* 2017, 7 (15), 9347-9356.
131. Kumar, V.; Toffoli, G.; Rizzolio, F., Fluorescent carbon nanoparticles in medicine for cancer therapy. *ACS Medicinal Chemistry Letters* 2013, 4 (11), 1012-1013.
132. Song, Y.; Shi, W.; Chen, W.; Li, X.; Ma, H., Fluorescent carbon nanodots conjugated with folic acid for distinguishing folate-receptor-positive cancer cells from normal cells. *J. Mater. Chem.* 2012, 22 (25), 12568-12573
133. Bayda, S.; Hadla, M.; Palazzolo, S.; Kumar, V.; Caligiuri, I.; Ambrosi, E.; Pontoglio, E.; Agostini, M.; Tuccinardi, T.; Benedetti, A.; Riello, P.; Canzonieri, V.; Corona, G.; Toffoli, G.; Rizzolio, F., Bottom-up synthesis of carbon nanoparticles with higher doxorubicin efficacy. *J. Controlled Release* 2017, 248 (Supplement C), 144-152

134. Arcamone, F.; Cassinelli, G.; Franceschi, G.; Penco, S.; Pol, C.; Redaelli, S.; Selva, A. In *Structure and Physicochemical Properties of Adriamycin (Doxorubicin)*, Berlin, Heidelberg, Springer Berlin Heidelberg: Berlin, Heidelberg, 1972, pp 9-22.
135. Young, R. C.; Ozols, R. F.; Myers, C. E., *The Anthracycline Antineoplastic Drugs*. 1981, 305 (3), 139-153
136. Hurley, L. H., DNA and its associated processes as targets for cancer therapy. *Nature Reviews Cancer* 2002, 2, 188.
137. Tacar, O.; Sriamornsak, P.; Dass, C. R., Doxorubicin: an update on anticancer molecular action, toxicity and novel drug delivery systems. 2013, 65 (2), 157-170
138. Mewada, A.; Pandey, S.; Thakur, M.; Jadhav, D.; Sharon, M., Swarming carbon dots for folic acid mediated delivery of doxorubicin and biological imaging. *J. Mat. Chem. B* 2014, 2 (6), 698-705
139. Zeng, Q.; Shao, D.; He, X.; Ren, Z.; Ji, W.; Shan, C.; Qu, S.; Li, J.; Chen, L.; Li, Q., Carbon dots as a trackable drug delivery carrier for localized cancer therapy in vivo. *J. Mat. Chem. B* 2016, 4 (30), 5119-5126.
140. Zhu, H.; Wang, X.; Li, Y.; Wang, Z.; Yang, F.; Yang, X., Microwave synthesis of fluorescent carbon nanoparticles with electrochemiluminescence properties. *Chem Commun* 2009, 34.
141. Peng, H.; Travas-Sejdic, J., Simple aqueous solution route to luminescent carbogenic dots from carbohydrates. *Chem. Mater.* 2009, 21 (23), 5563-5565.
142. Cailotto, S.; Amadio, E.; Facchin, M.; Selva, M.; Pontoglio, E.; Rizzolio, F.; Riello, P.; Toffoli, G.; Benedetti, A.; Perosa, A., Carbon Dots from Sugars and Ascorbic Acid: Role of the Precursors on Morphology, Properties, Toxicity, and Drug Uptake. *ACS Medicinal Chemistry Letters* 2018, 9, 832-837.
143. Fan, X.; Huang, L.; Sokorai, K. J. B., Factors affecting thermally induced furan formation. *J. Agric. Food Chem.* 2008, 56 (20), 9490-9494.
144. Fan, X., Formation of furan from carbohydrates and ascorbic acid following exposure to ionizing radiation and thermal processing. *J. Agric. Food Chem.* 2005, 53 (20), 7826-7831.
145. Tong, X.; Ma, Y.; Li, Y., Biomass into chemicals: conversion of sugars to furan derivatives by catalytic processes. *Applied Catalysis A: General* 2010, 385 (1), 1-13.
146. Loo, A. H.; Sofer, Z.; Bouša, D.; Ulbrich, P.; Bonanni, A.; Pumera, M. Carboxylic carbon quantum dots as a fluorescent sensing platform for DNA detection. *ACS Appl. Mater. Interfaces* 2016, 8, 1951-1957.
147. Wang, H.; Lu, Q.; Hou, Y.; Liu, Y.; Zhang, Y. High fluorescence S, N co-doped carbon dots as an ultra-sensitive fluorescent probe for the determination of uric acid. *Talanta* 2016, 155, 62-69.
148. Baker, S. N.; Baker, G. A., Luminescent carbon nanodots: emergent nanolights. *Angew. Chem., Int. Ed.* 2010, 49 (38), 6726-6744.
149. Xue, M.; Zhang, L.; Zhan, Z.; Zou, M.; Huang, Y.; Zhao, S. Sulfur and nitrogen binary doped carbon dots derived from ammonium thiocyanate for selective probing doxycycline in living cells and multicolor cell imaging. *Talanta* 2016, 150, 324-330.

150. Gong, Y.; Yu, B.; Yang, W.; Zhang, X. Phosphorus, and nitrogen co-doped carbon dots as a fluorescent probe for real-time measurement of reactive oxygen and nitrogen species inside macrophages. *Biosensors and Bioelectronics* 2016, 79, 822-828.
151. Xu, Q.; Zhou, Q.; Hua, Z.; Xue, Q.; Zhang, C.; Wang, X.; Pan, D.; Xiao, M., Single-particle spectroscopic measurements of fluorescent graphene quantum dots. *ACS Nano* 2013, 7 (12), 10654-10661.
152. van Dam, B.; Nie, H.; Ju, B.; Marino, E.; Paulusse, J. M. J.; Schall, P.; Li, M.; Dohnalová, K., Excitation-Dependent Photoluminescence from Single-Carbon Dots. *Small* 2017, 13 (48), 1702098
153. Krainer, S.; Brodschneider, R.; Vollmann, J.; Crailsheim, K.; Riessberger-Gallé, U., Effect of hydroxymethylfurfural (HMF) on mortality of artificially reared honey bee larvae (*Apis mellifera carnica*). *Ecotoxicology* 2016, 25 (2), 320-328.
154. Bauer-Marinovic, M.; Taugner, F.; Florian, S.; Glatt, H., Toxicity studies with 5-hydroxymethylfurfural and its metabolite 5-sulphoxymethylfurfural in wild-type mice and transgenic mice expressing human sulphotransferases 1A1 and 1A2. *Arch. Toxicol.* 2012, 86 (5), 701-711.
155. Principles of Steady-State and Time-Resolved Fluorometric Techniques. In *Molecular Fluorescence*, 2001; pp 155-199.
156. Quenching of Fluorescence. In *Principles of Fluorescence Spectroscopy*, Lakowicz, J. R., Ed. Springer US: Boston, MA, 2006; pp 277-330.
157. Sun, T.; Zheng, M.; Xie, Z.; Jing, X., Supramolecular hybrids of carbon dots with doxorubicin: synthesis, stability and cellular trafficking. *Materials Chemistry Frontiers* 2017, 1 (2), 354-360
158. Gong, X.; Zhang, Q.; Gao, Y.; Shuang, S.; Choi, M. M. F.; Dong, C., Phosphorus and Nitrogen Dual-Doped Hollow Carbon Dot as a Nanocarrier for Doxorubicin Delivery and Biological Imaging. *ACS Applied Materials & Interfaces* 2016, 8 (18), 11288-11297.
159. Wang, H.; Di, J.; Sun, Y.; Fu, J.; Wei, Z.; Matsui, H.; Alonso, A. d. C.; Zhou, S., Biocompatible PEG-Chitosan@Carbon Dots Hybrid Nanogels for Two-Photon Fluorescence Imaging, Near-Infrared Light/pH Dual-Responsive Drug Carrier, and Synergistic Therapy. *Advanced Functional Materials* 2015, 25 (34), 5537-5547.
160. Paquot, C., 2.241 - Determination of the Hydroxyl Value (OH. V.). In *Standard Methods for the Analysis of Oils, Fats and Derivatives (Sixth Edition)*, Pergamon: 1979; pp 89-91.
161. Jiang, K.; Wang, Y.; Cai, C.; Lin, H., Conversion of Carbon Dots from Fluorescence to Ultralong Room-Temperature Phosphorescence by Heating for Security Applications. 2018, 30, 1800783.
162. Hutton, G. A. M.; Reuillard, B.; Martindale, B. C. M.; Caputo, C. A.; Lockwood, C. W. J.; Butt, J. N.; Reisner, E., Carbon Dots as Versatile Photosensitizers for Solar-Driven Catalysis with Redox Enzymes. *J. Am. Chem. Soc.* 2016, 138, 16722-16730.

163. Martindale, B. C. M.; Hutton, G. A. M.; Caputo, C. A.; Prantl, S.; Godin, R.; Durrant, J. R.; Reisner, E., Enhancing Light Absorption and Charge Transfer Efficiency in Carbon Dots through Graphitization and Core Nitrogen Doping. *Angew. Chem., Int. Ed.* 2017, 56, 6459-6463.
164. Cailotto, S.; Mazzaro, R.; Enrichi, F.; Vomiero, A.; Selva, M.; Cattaruzza, E.; Cristofori, D.; Amadio, E.; Perosa, A., Design of Carbon Dots for Metal-Free Photoredox Catalysis. *ACS Appl. Mater. Interfaces* 2018.
165. Wyrzykowski, D.; Hebanowska, E.; Nowak-Wicz, G.; Makowski, M.; Chmurzyński, L., Thermal Behaviour of Citric Acid and Isomeric Aconitic Acids. *J. Therm. Anal. Calorim.* 2011, 104, 731-735.
166. Li, X.; Zhang, S.; Kulinich, S. A.; Liu, Y.; Zeng, H., Engineering Surface States of Carbon Dots to Achieve Controllable Luminescence for Solid-Luminescent Composites and Sensitive Be(2+) Detection. *Scientific Reports* 2014, 4, 4976.
167. Sciortino, A.; Marino, E.; Dam, B. v.; Schall, P.; Cannas, M.; Messina, F., Solvatochromism Unravels the Emission Mechanism of Carbon Nanodots. *J. Phys. Chem. Lett.* 2016, 7, 3419-3423.
168. Francesca, A.; Luka, Đ.; Maurizio, P., Synthesis, Separation, and Characterization of Small and Highly Fluorescent Nitrogen-Doped Carbon Nanodots. *Angew. Chem. Int. Ed.* 2016, 55, 2107-2112.
169. Arrigo, A.; Mazzaro, R.; Romano, F.; Bergamini, G.; Ceroni, P., Photoinduced Electron-Transfer Quenching of Luminescent Silicon Nanocrystals as a Way to Estimate the Position of the Conduction and Valence Bands by Marcus Theory. *Chem. Mater.* 2016, 28, 6664-6671.
170. Mazzaro, R.; Locritani, M.; Molloy, J. K.; Montalti, M.; Yu, Y.; Korgel, B. A.; Bergamini, G.; Morandi, V.; Ceroni, P., Photoinduced Processes between Pyrene-Functionalized Silicon Nanocrystals and Carbon Allotropes. *Chem. Mater.* 2015, 27, 4390-4397.
171. Michaelis, L.; Hill, E. S., The Viologen Indicators. *The Journal of General Physiology* 1933, 16, 859-873.
172. Garner, R.; Young, G. T., Amino-Acids and Peptides. Part Xxxiii. Synthesis of Val⁵-Angiotensin-II by the Picolyl Ester Method. *Journal of the Chemical Society C: Organic* 1971, 50-53.
173. Camble, R.; Garner, R.; Young, G. T., Novel Facilitation of Peptide Synthesis. *Nature* 1968, 217, 247.
174. Sundararajan, C.; Falvey, D. E., Photorelease of Carboxylic and Amino Acids from N-Methyl-4-Picolinium Esters by Mediated Electron Transfer. *Photochem. Photobiol. Sci.* 2006, 5, 116-121.
175. Das, R. K.; Mohapatra, S., Highly luminescent, heteroatom-doped carbon quantum dots for ultrasensitive sensing of glucosamine and targeted imaging of liver cancer cells. *J. Mat. Chem. B* 2017, 5 (11), 2190-2197.
176. Sundararajan, C.; Falvey, D. E., C-O Bond Fragmentation of 4-Picolyl- and N-Methyl-4-Picolinium Esters Triggered by Photochemical Electron Transfer. *The Journal of Organic Chemistry* 2004, 69, 5547-5554.
177. Webster, R. D.; Bond, A. M.; Compton, R. G., Voltammetric and Epr Spectroscopic Studies Associated with the Reduction of Pyridine- and Benzene-Substituted N-Alkyl Esters and Thioic S-Esters in Aprotic Solvents. *The Journal of Physical Chemistry* 1996, 100, 10288-10297.

-
- ^{178.} Mattiello, L.; Rampazzo, L., Electrochemistry of a Spirolactone. *J. Electroanal. Chem.* 2001, 507, 118-123.
- ^{179.} Sundararajan, C.; Falvey, D. E., Photorelease of Carboxylic Acids, Amino Acids, and Phosphates from N-Alkylpicolinium Esters Using Photosensitization by High Wavelength Laser Dyes. *J. Am. Chem. Soc.* 2005, 127, 8000-8001.
- ^{180.} Bonazza, G.; Tartaglia, S.; Toffoli, G.; Polo, F.; Daniele, S., Voltammetric Behaviour of the Anticancer Drug Irinotecan and Its Metabolites in Acetonitrile. Implications for Electrochemical Therapeutic Drug Monitoring. *Electrochim. Acta* 2018, 289, 483-493.

8. Appendix

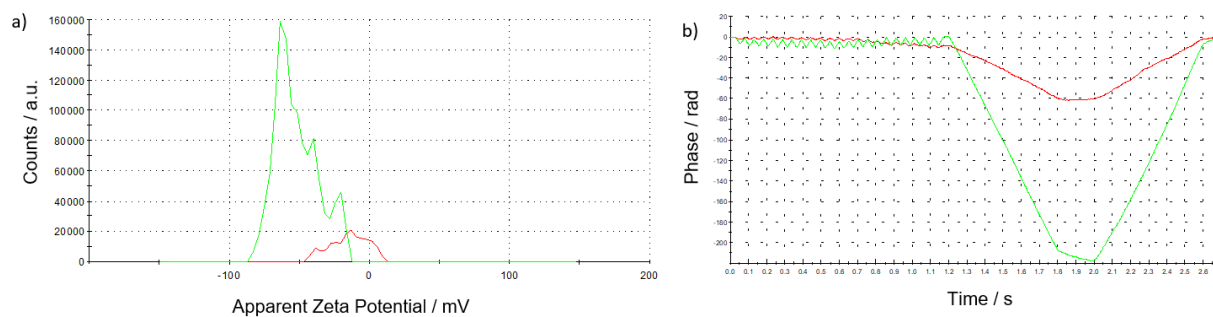


Figure A1. ζ -potential distribution and phase plot for **g-CDs** (green) and **g-N-CDs** (red). The samples are dispersed in 0.1M NaCl solution and the pH adjusted to 7.00 by means of HCl or NaOH addition.

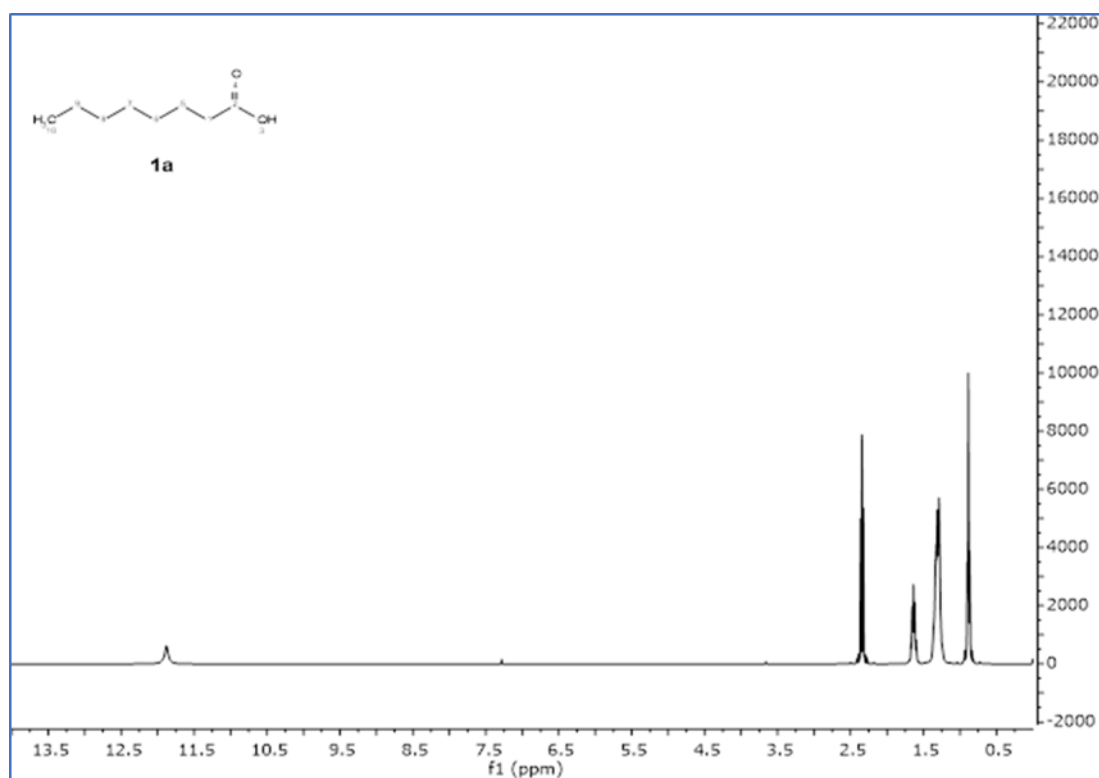


Figure A2. ^1H NMR spectra of **1a**.

^1H NMR (400 MHz, Chloroform-*d*) δ = 2.91 (t, J = 6.7 Hz, 2H), 1.88 – 1.63 (m, 2H), 1.39 – 1.29 (m, 8H), 0.92 (t, J = 8.6 Hz, 3H).

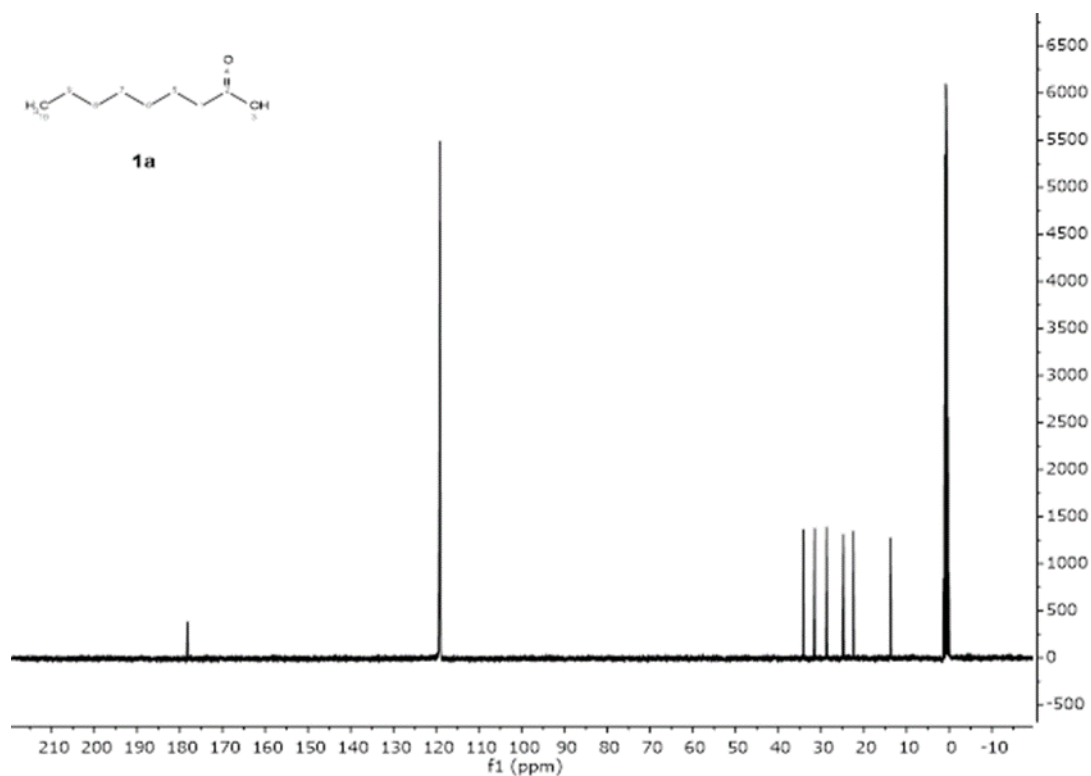


Figure A3. ¹³C NMR spectra of **1a**.

¹³C NMR (101 MHz, Chloroform-*d*) δ = 173.77, 47.10, 31.51, 28.72, 28.38, 25.06, 22.52, 13.99.

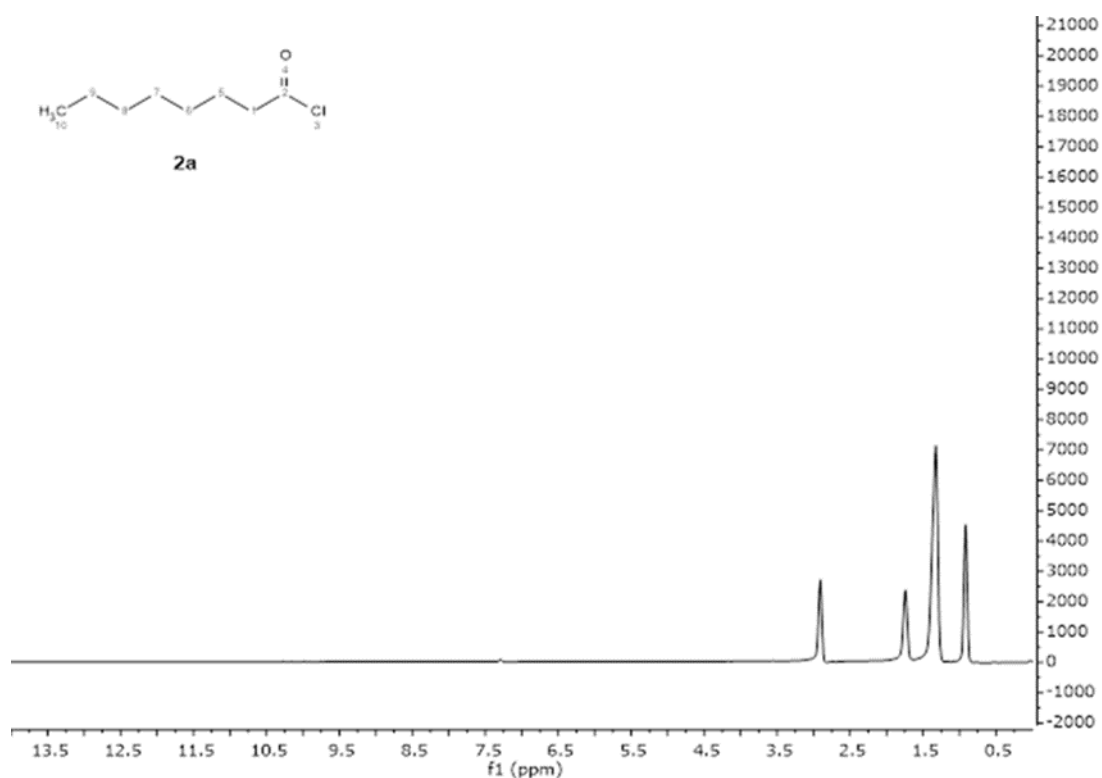
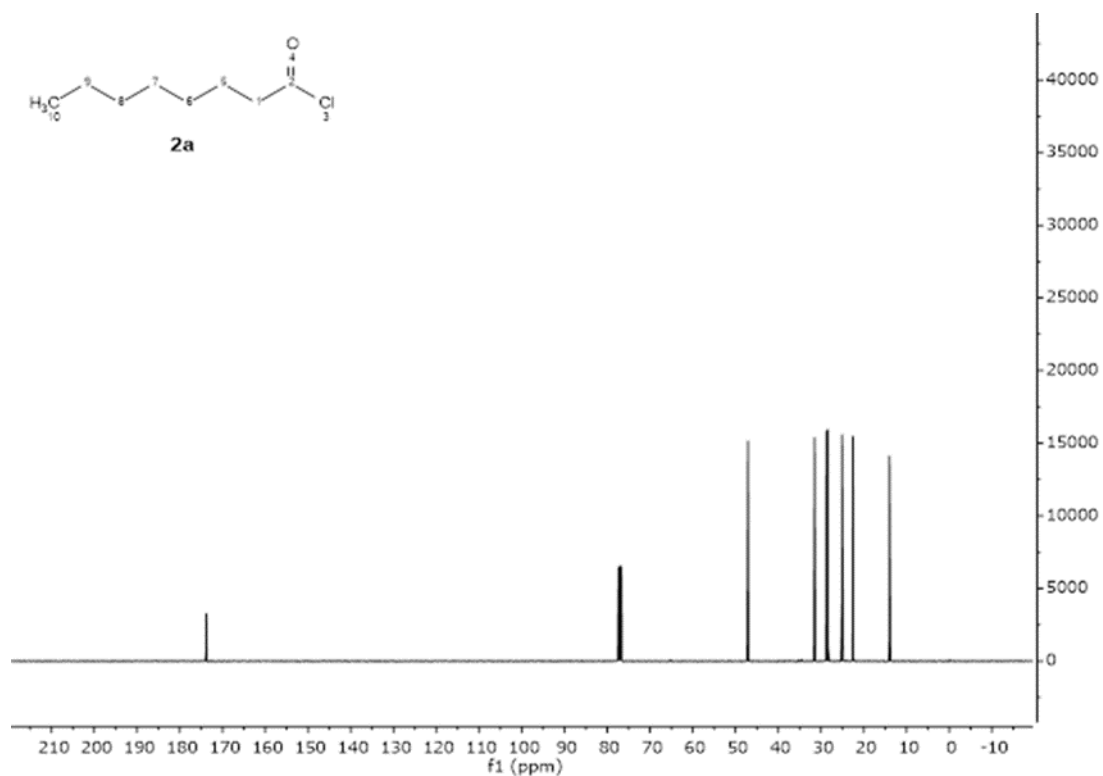
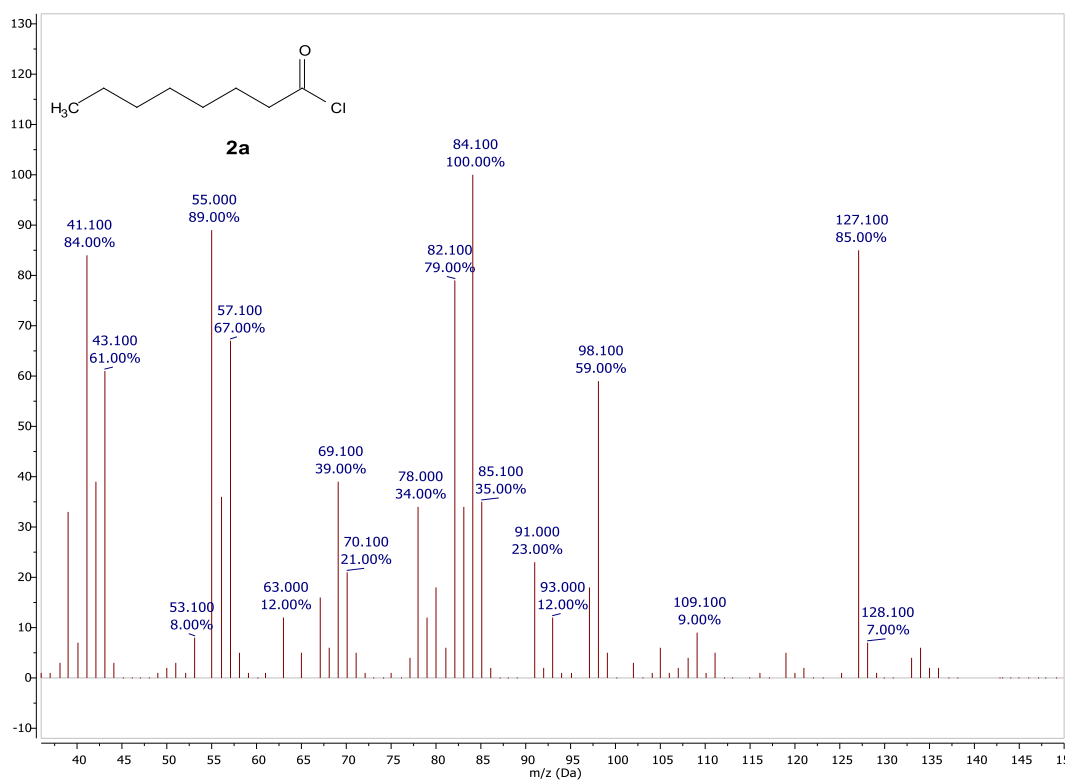


Figure A4. ¹H NMR spectra of **2a**.

¹H NMR (400 MHz, Chloroform-*d*) δ = 8.61 (d, 1H), 7.26 (d, 1H), 5.14 (s, 1H), 2.41 (t, 1H), 1.72 – 1.63 (m, 1H), 1.41 – 1.21 (m, 5H), 0.89 (t, 2H).

Figure A5. ¹³C NMR spectra of **2a**.

¹³C NMR (101 MHz, Chloroform-*d*) δ = 173.77, 47.10, 31.51, 28.72, 28.38, 25.06, 22.52, 13.99.

Figure A6. MS spectra of **2a**

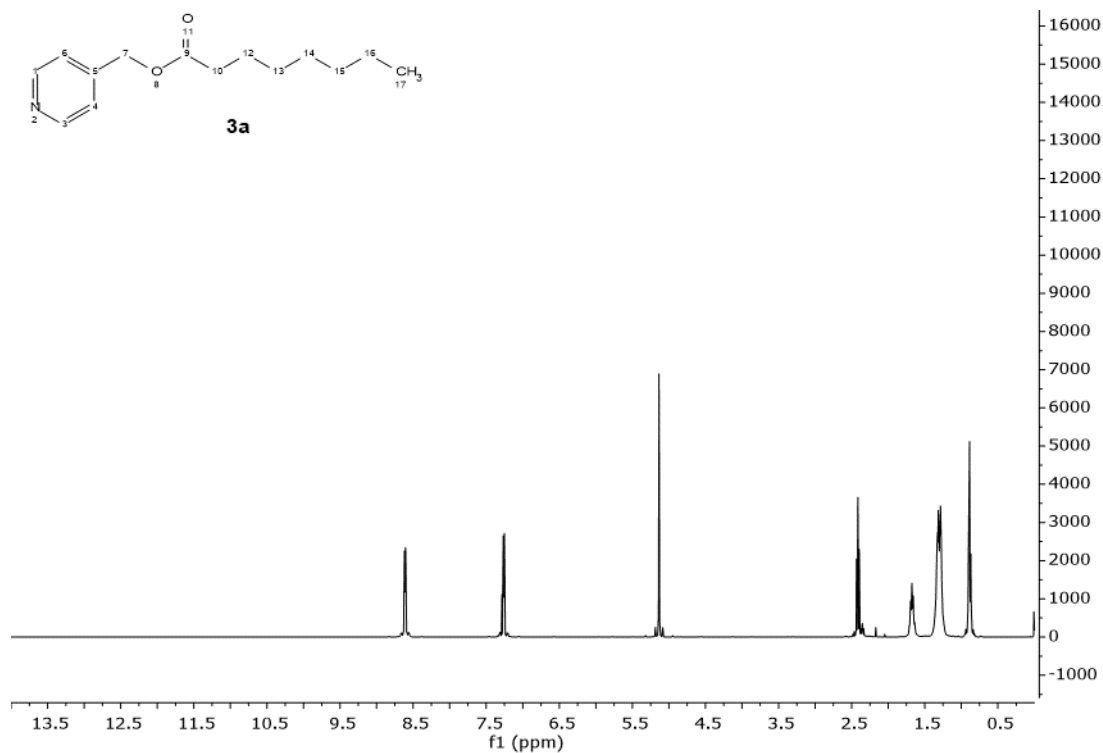


Figure A7. ¹H NMR spectra of **3a**.

¹H NMR (400 MHz, Chloroform-*d*) δ 8.61 (d, 1H), 7.26 (d, 1H), 5.14 (s, 1H), 2.41 (t, 1H), 1.72 – 1.63 (m, 1H), 1.41 – 1.21 (m, 5H), 0.89 (t, 2H).

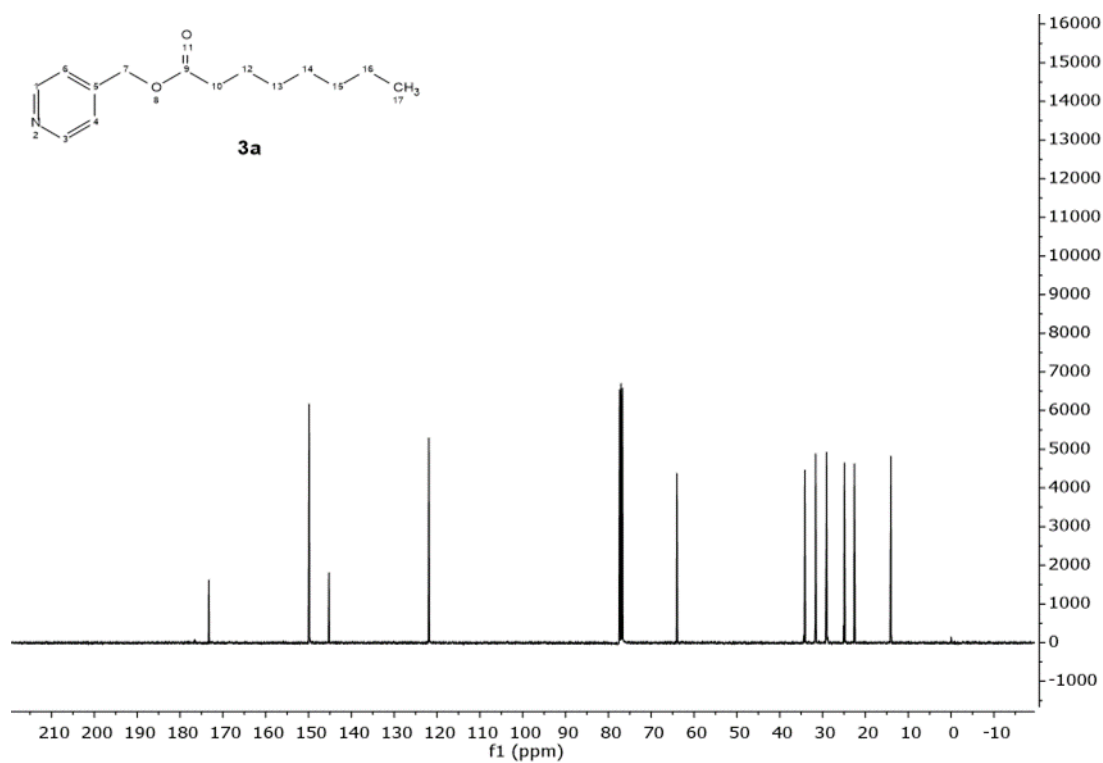


Figure A8. ¹³C NMR spectra of **3a**.

^{13}C NMR (101 MHz, Chloroform-*d*) δ 173.29, 149.85, 145.24, 121.91, 64.01, 34.13, 31.62, 29.06, 24.90, 22.56, 14.03.

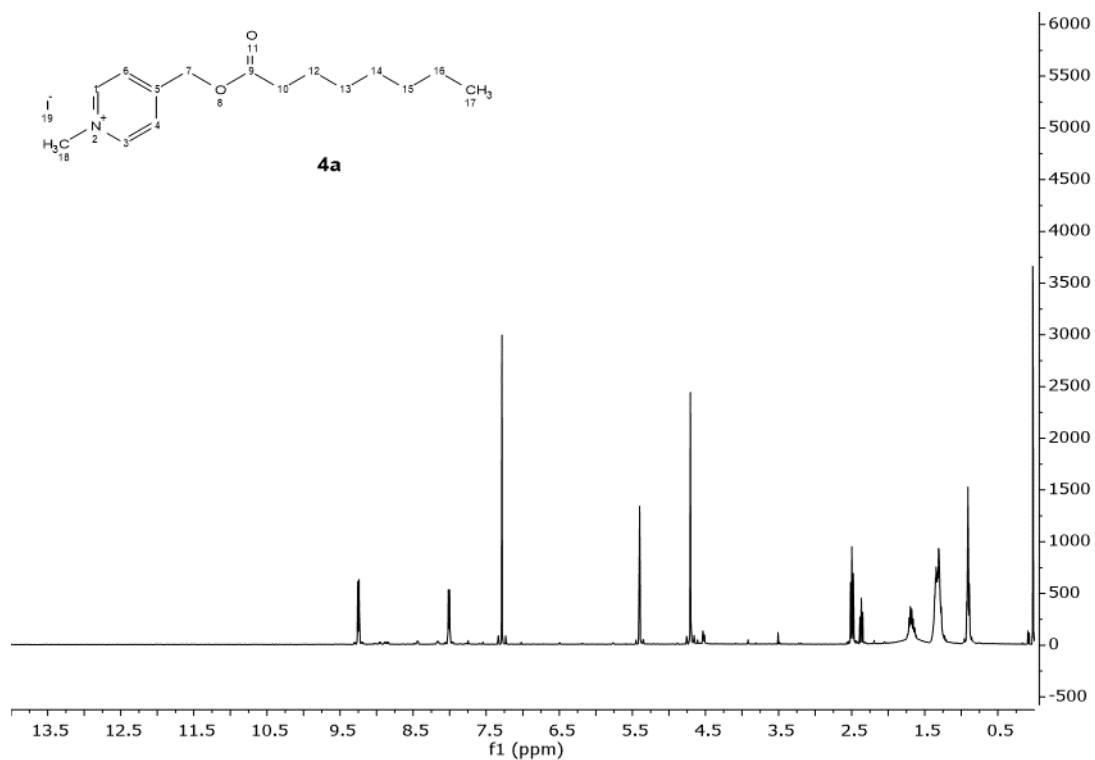


Figure A9. ^1H NMR spectra of **4a**.

^1H NMR (400 MHz, Chloroform-*d*) δ 9.25 (d, 2H), 8.01 (d, 2H), 5.40 (s, 2H), 4.71 (s, 3H), 2.50 (t, 2H), 1.76 – 1.59 (m, 3H), 1.39 – 1.25 (m, 6H), 0.91 (d, 4H).

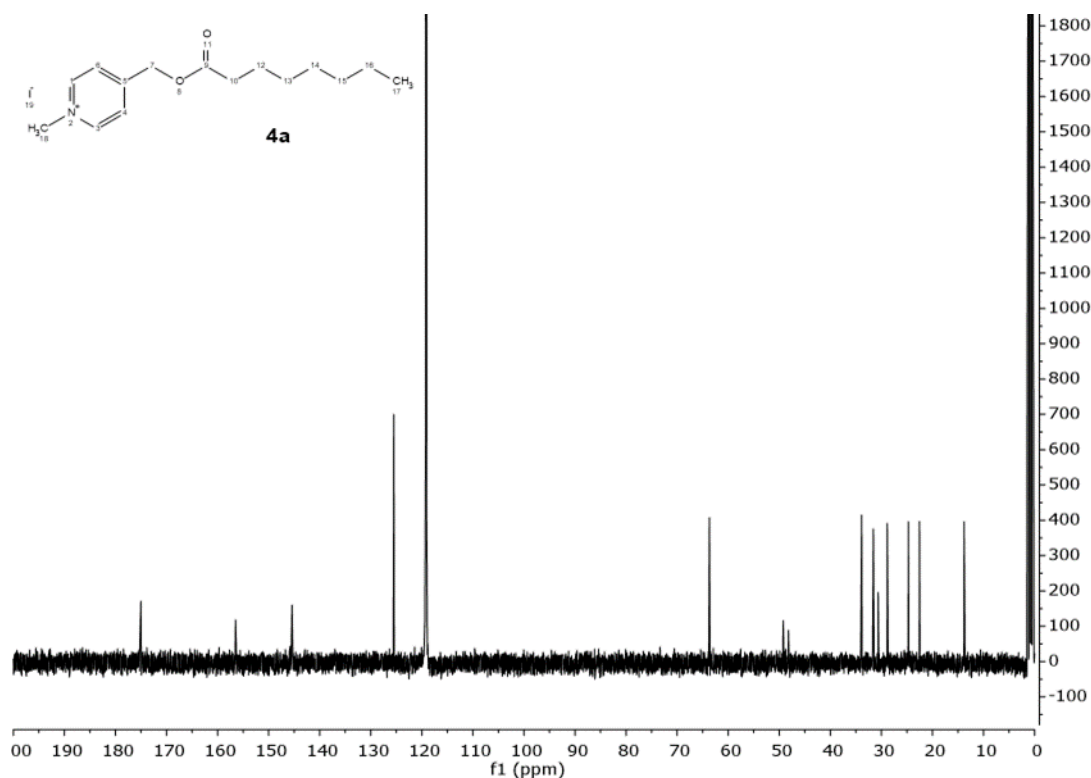


Figure A10. ^{13}C NMR spectra of **4a**.

^{13}C NMR (101 MHz, Acetonitrile- d_3) δ 175.03, 156.48, 145.43, 125.48, 63.68, 49.23, 33.87, 31.57, 28.74, 24.71, 22.53, 13.80.

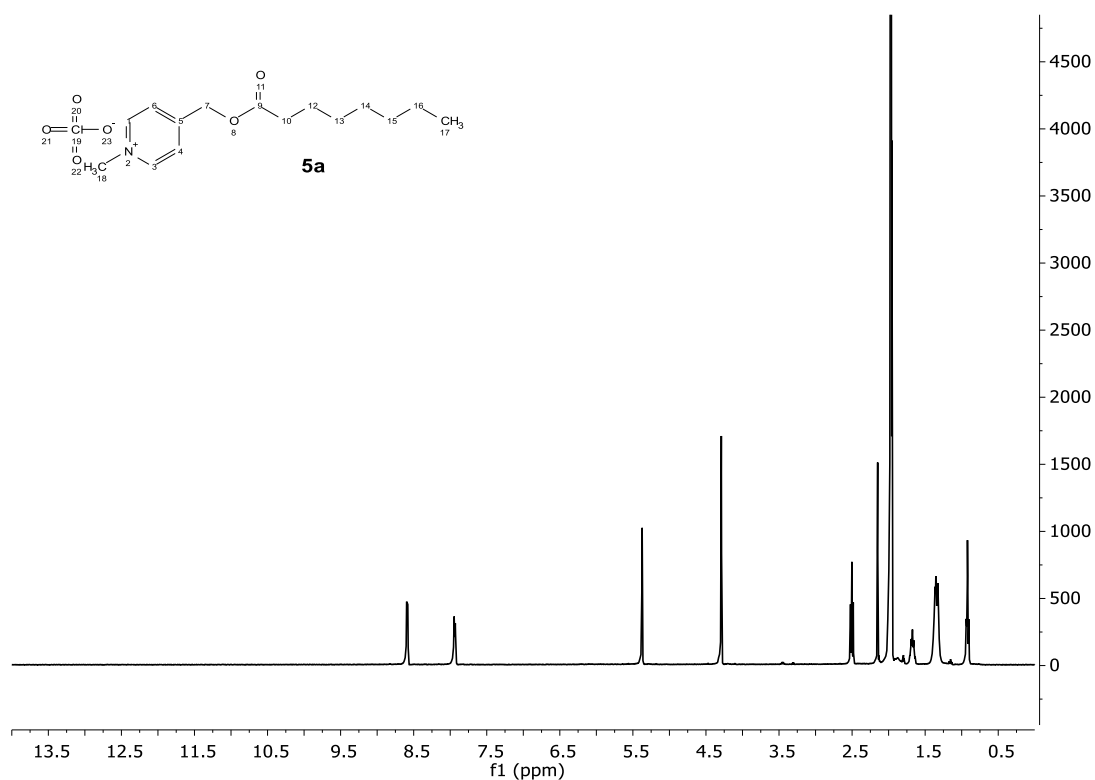


Figure A11. ^1H NMR spectra of **5a**.

^1H NMR (400 MHz, Acetonitrile- d_3) δ 8.59 (d, 2H), 7.94 (d, 2H), 5.37 (s, 2H), 4.29 (s, 3H), 2.50 (t, $J = 7.5$ Hz, 2H), 1.74 – 1.61 (m, 2H), 1.40 – 1.29 (m, 4H), 0.92 (t, $J = 7.0, 5.1$ Hz, 3H).

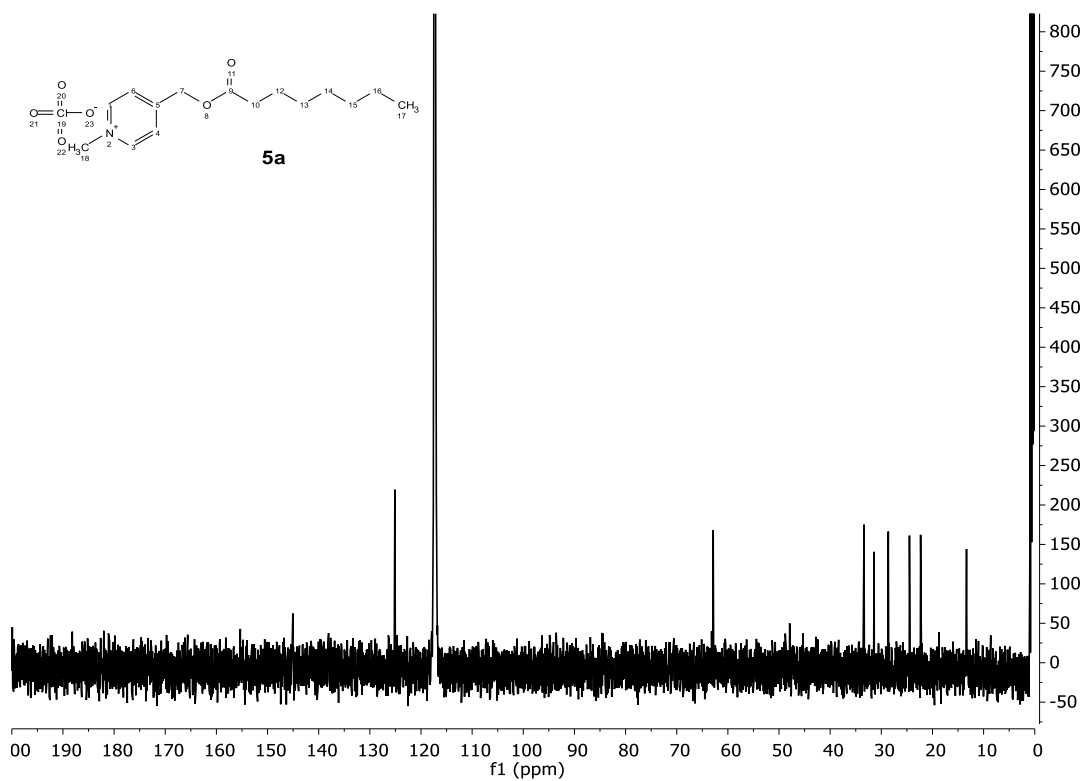
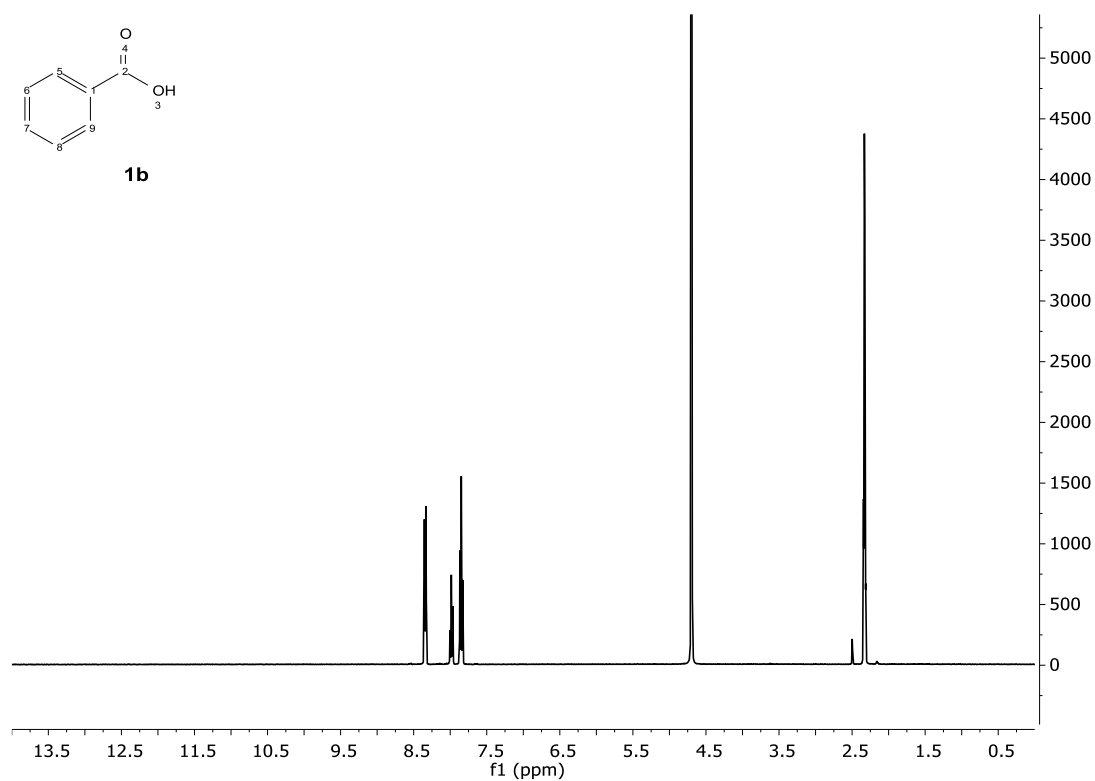


Figure A12. ^{13}C NMR spectra of **5a**.

^{13}C NMR (101 MHz, Acetonitrile- d_3) δ 174.70, 155.32, 145.05, 125.11, 62.87, 47.92, 33.38, 31.41, 28.70, 24.50, 22.32, 13.34.

Figure A13. ^1H NMR spectra of **1b**.

^1H NMR (400 MHz,) δ 8.34 (d, $J = 8.5, 2.5, 1.3$ Hz, 2H), 7.98 (dd, 1H), 7.89 – 7.80 (m, 2H).

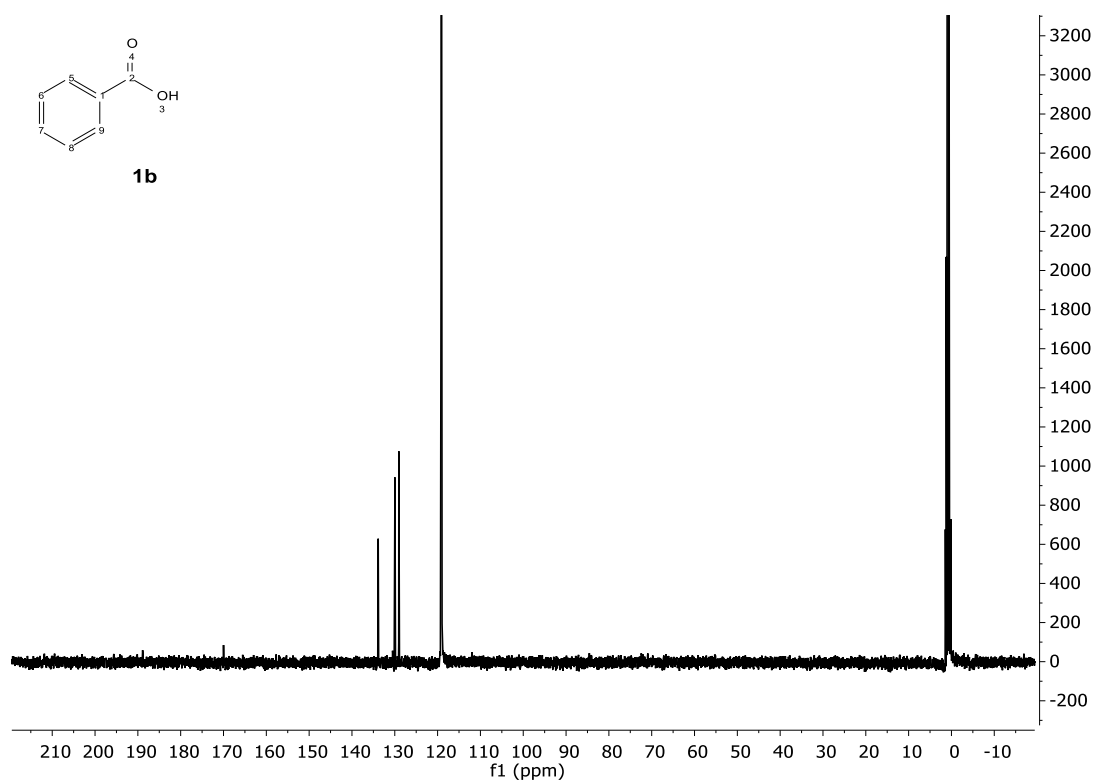


Figure A14. ^{13}C NMR spectra of **1b**.

^{13}C NMR (101 MHz,) δ 170.96 – 169.23 (m), 133.87, 130.51, 129.96, 129.05.

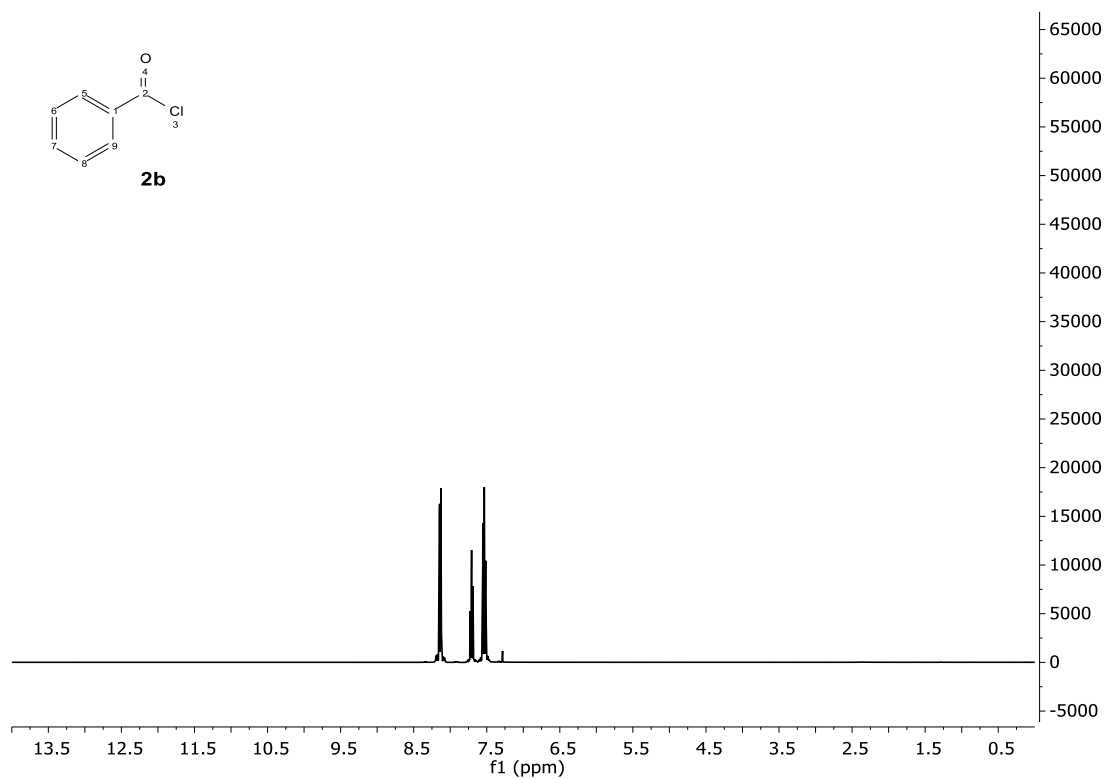
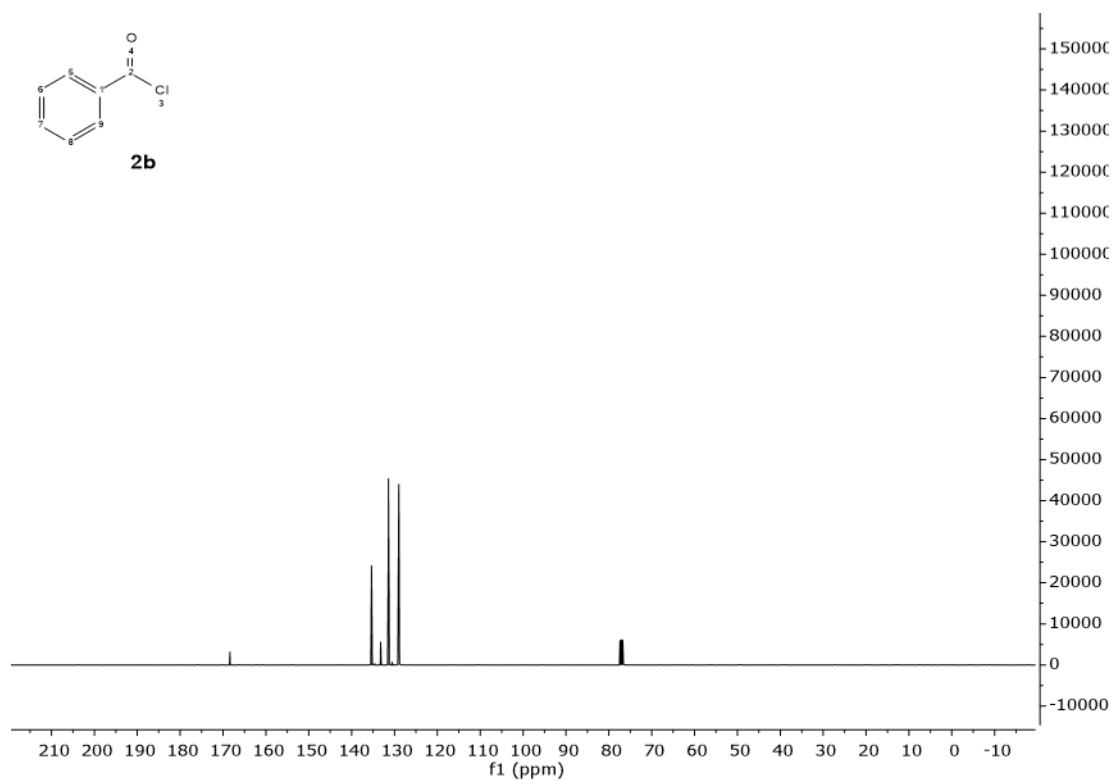
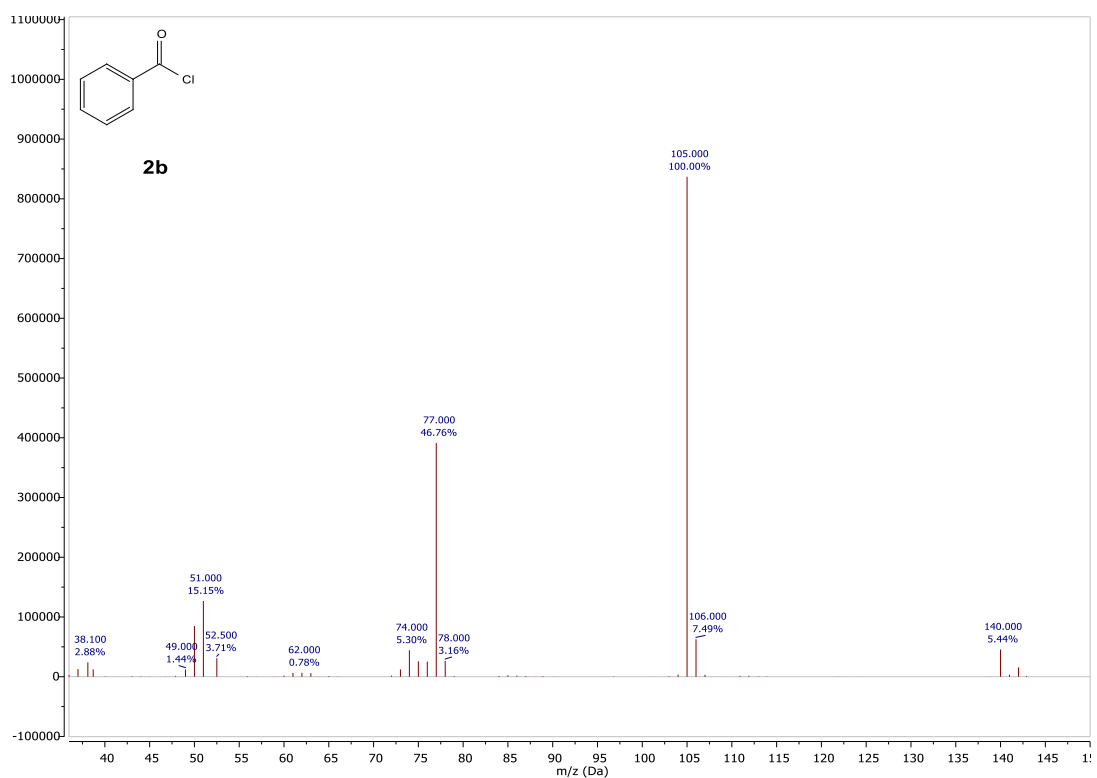


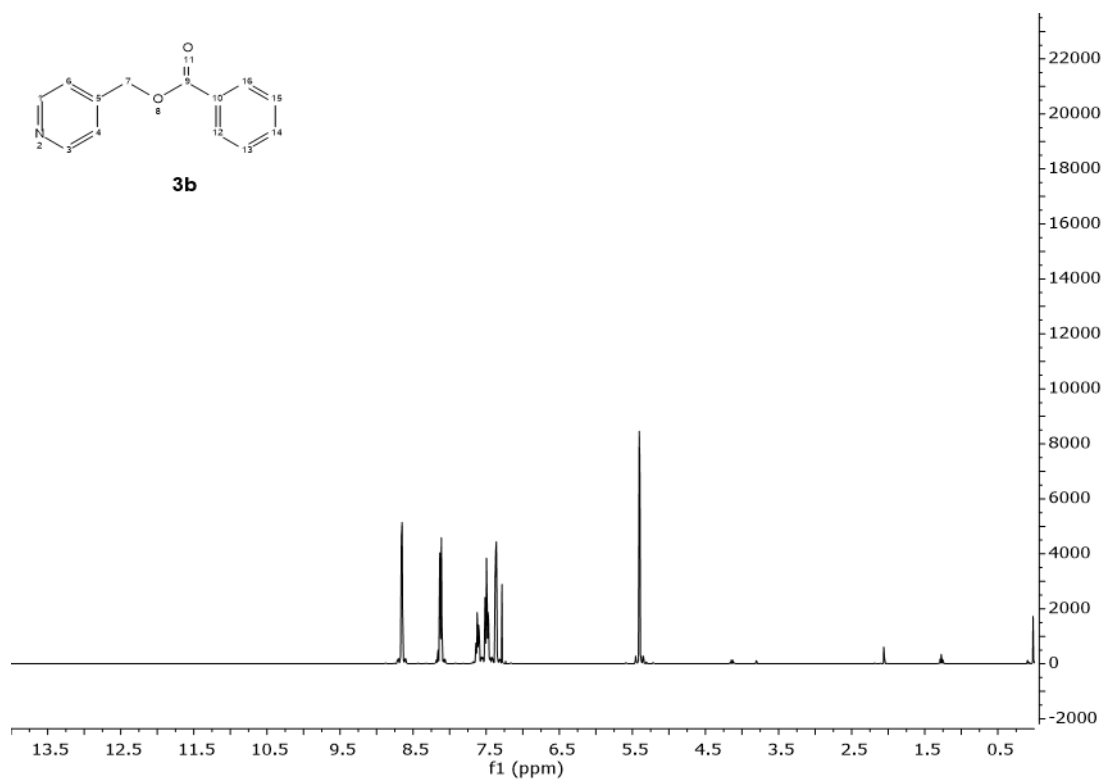
Figure A15. ^1H NMR spectra of **2b**.

^1H NMR (400 MHz, Chloroform-*d*) δ 8.14 (d, 2H), 7.71 (d, 2H), 7.63 – 7.44 (m, 1H).

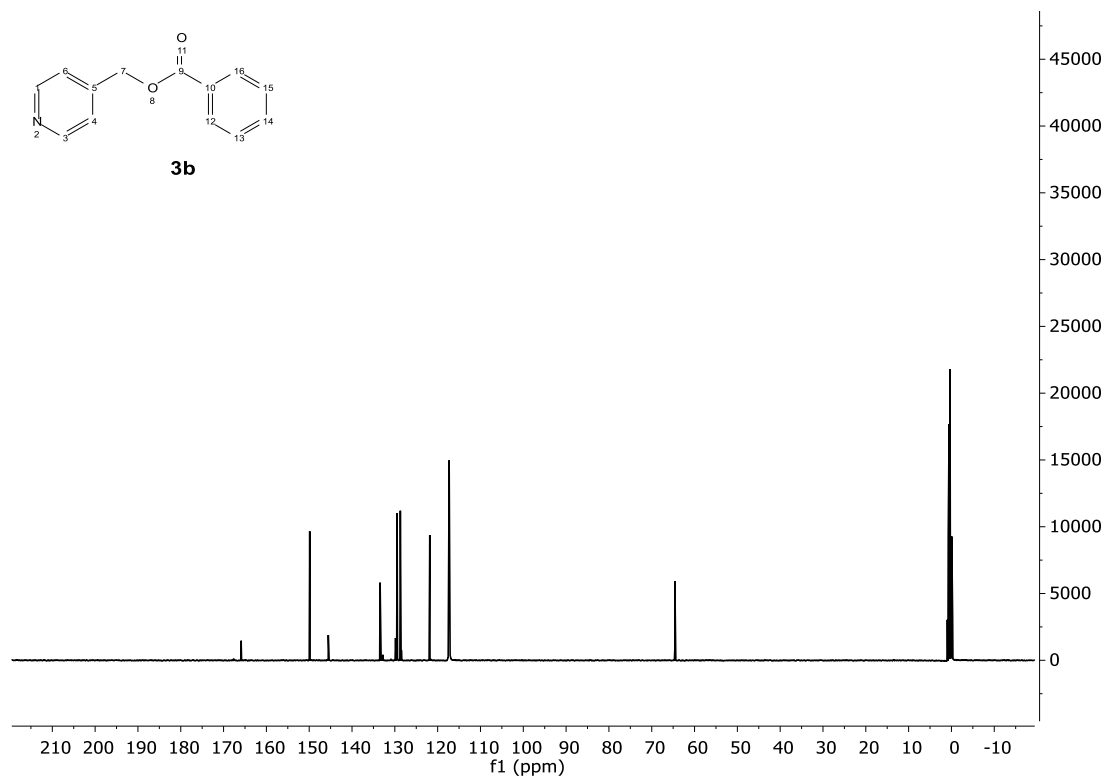
Figure A16. ^{13}C NMR spectra of **2b**.

^{13}C NMR (101 MHz, Chloroform-*d*) δ 168.38, 135.36, 133.25, 131.41, 128.99.

Figure A17. MS spectra of **2b**.

Figure A 18. ^1H NMR spectra of **3b**.

^1H NMR (400 MHz, Chloroform-*d*) δ 8.66 (d, 2H), 8.13 (d, 2H), 7.61 (dd, 1H), 7.57 – 7.44 (m, 2H), 7.37 (d, 2H), 5.40 (s, 2H).

Figure A19. ^{13}C NMR spectra of **3b**.

^{13}C NMR (101 MHz, Acetonitrile- d_3) δ 165.89, 149.88, 145.54, 133.44, 129.83, 129.47, 128.71, 121.84, 64.59.

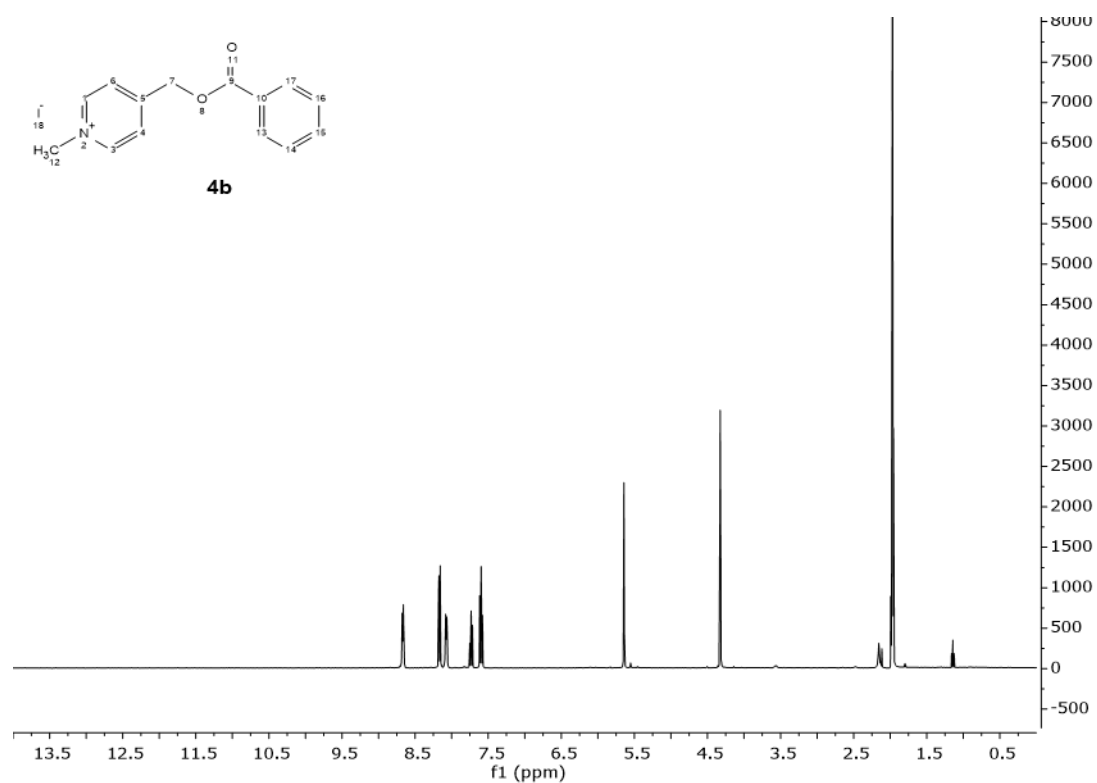


Figure A20. ^1H NMR spectra of **4b**.

^1H NMR (400 MHz, Acetonitrile- d_3) δ 8.67 (d, 2H), 8.16 (d, 2H), 8.07 (d, $J = 6.3$ Hz, 2H), 7.73 (dd, 1H), 7.65 – 7.55 (m, 2H), 5.64 (s, 2H), 4.33 (s, 2H).

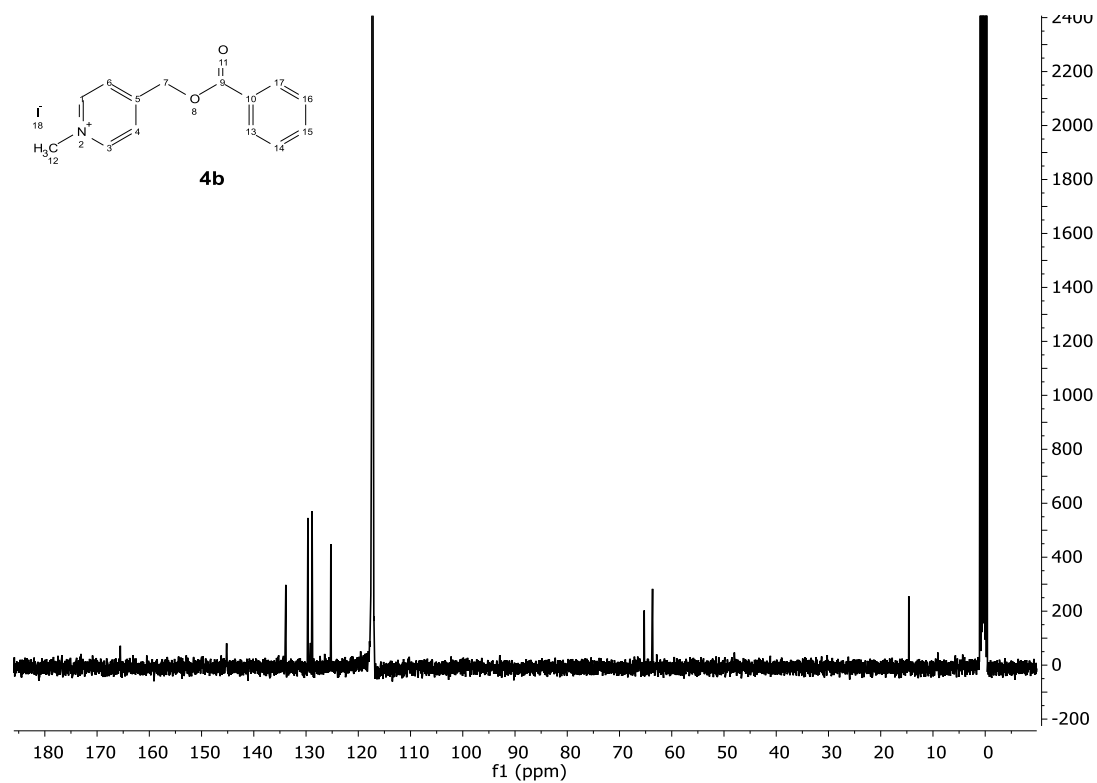
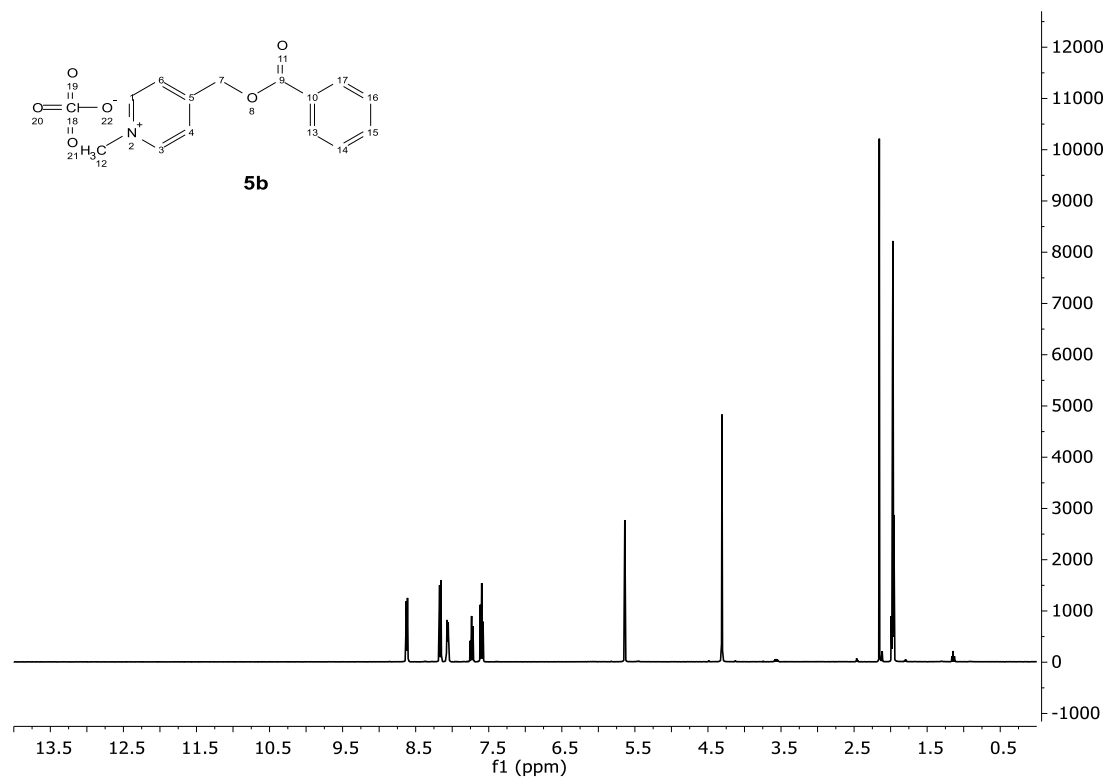
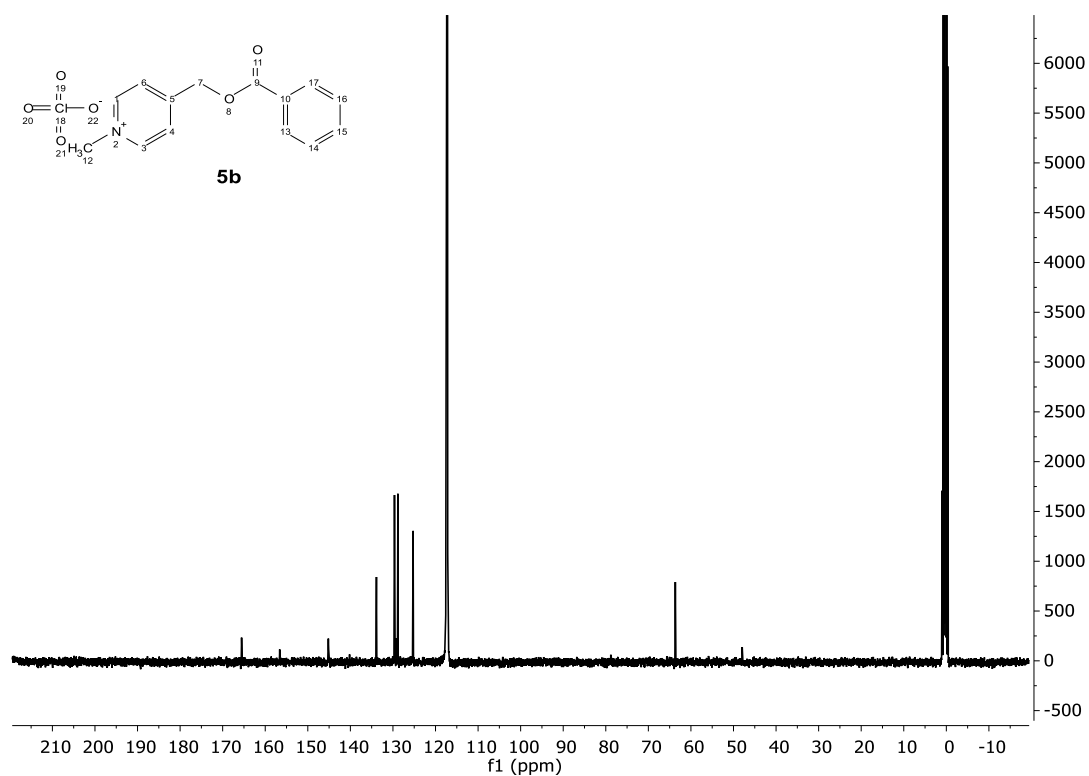


Figure A21. ^{13}C NMR spectra of **4b**.

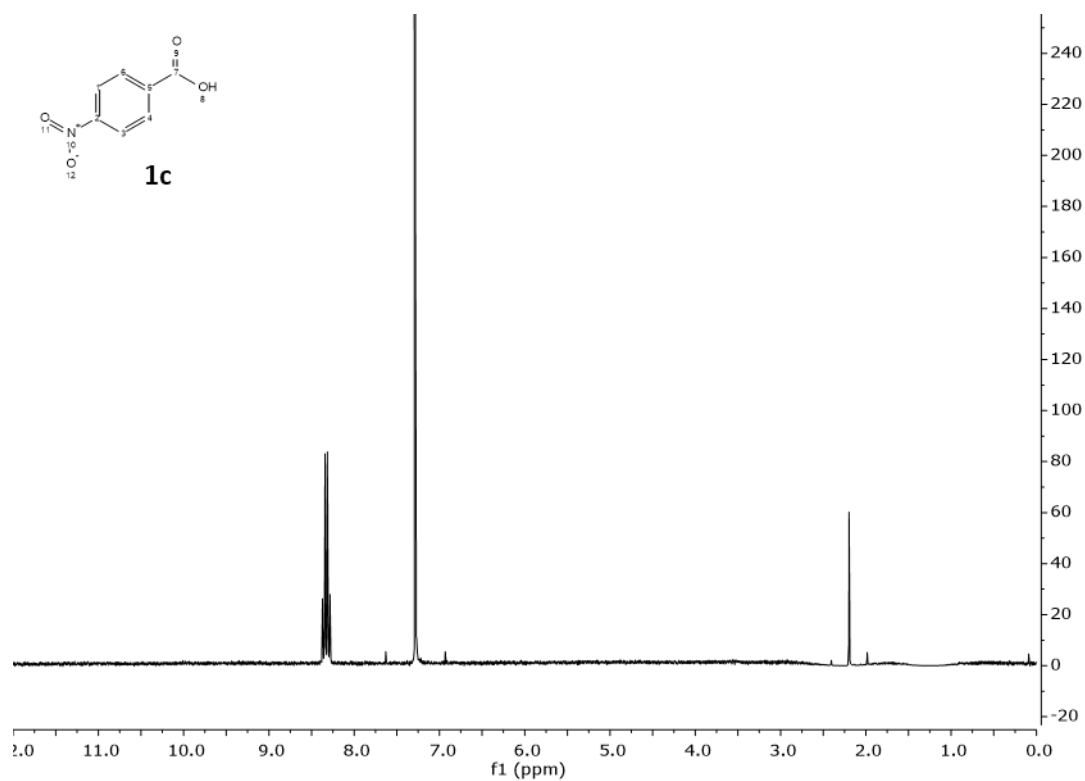
^{13}C NMR (101 MHz, Acetonitrile- d_3) δ 165.55, 152.93, 145.20, 133.87, 129.65, 129.14, 128.84, 125.26, 65.27, 48.00, 14.63.

**Figure A22.** ^1H NMR spectra of **5b**.

^1H NMR (400 MHz, Acetonitrile- d_3) δ 8.62 (d, 2H), 8.16 (d, 2H), 8.06 (d, $J = 6.3$ Hz, 2H), 7.73 (d, 1H), 7.65 – 7.55 (m, 2H), 5.64 (s, 2H), 4.31 (s, 3H).

Figure A23. ¹³C NMR spectra of **5b**.

¹³C NMR (101 MHz, Acetonitrile-*d*₃) δ 165.55, 156.60, 145.57 – 144.63 (m), 133.88, 129.64, 129.14, 128.84, 125.26, 63.66, 47.95.

Figure A24. ¹H NMR spectra of **1c**.

^1H NMR (300 MHz, Chloroform-d) δ 8.40 – 8.25 (m, 4H).

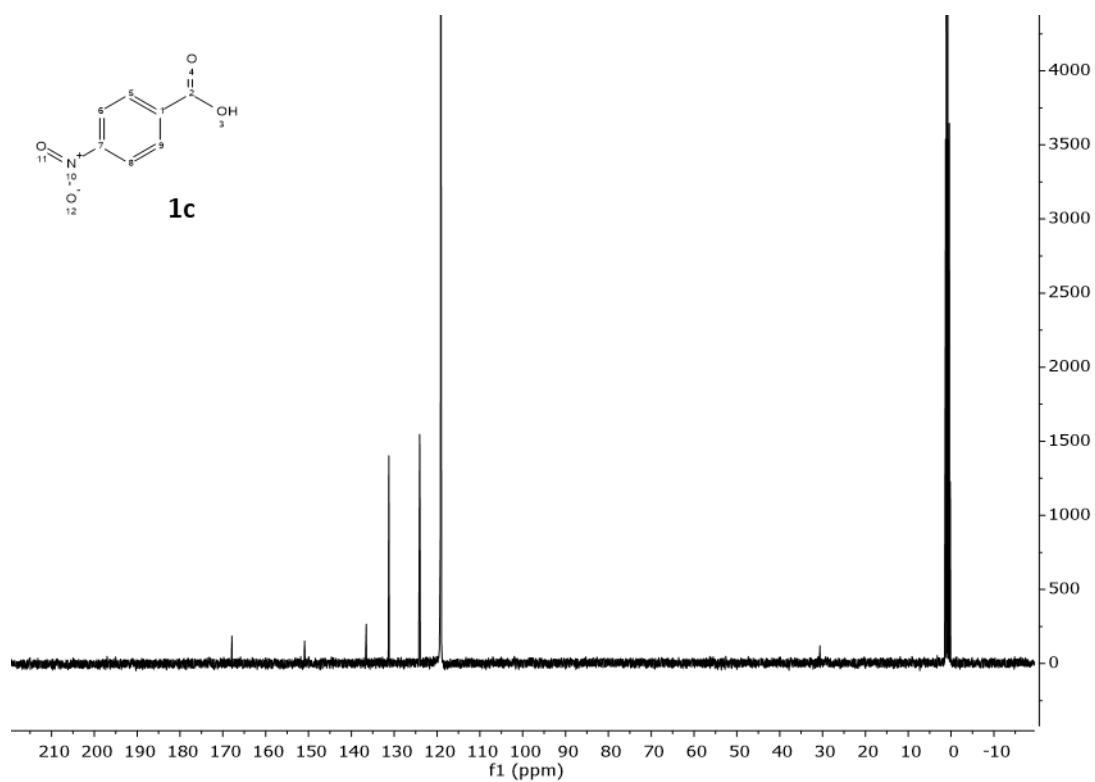


Figure A25. ^{13}C NMR spectra of **1c**.

^{13}C NMR (101 MHz, CD $_3$ CN/D $_2$ O) δ 167.88, 150.91, 136.52, 131.26, 124.06.

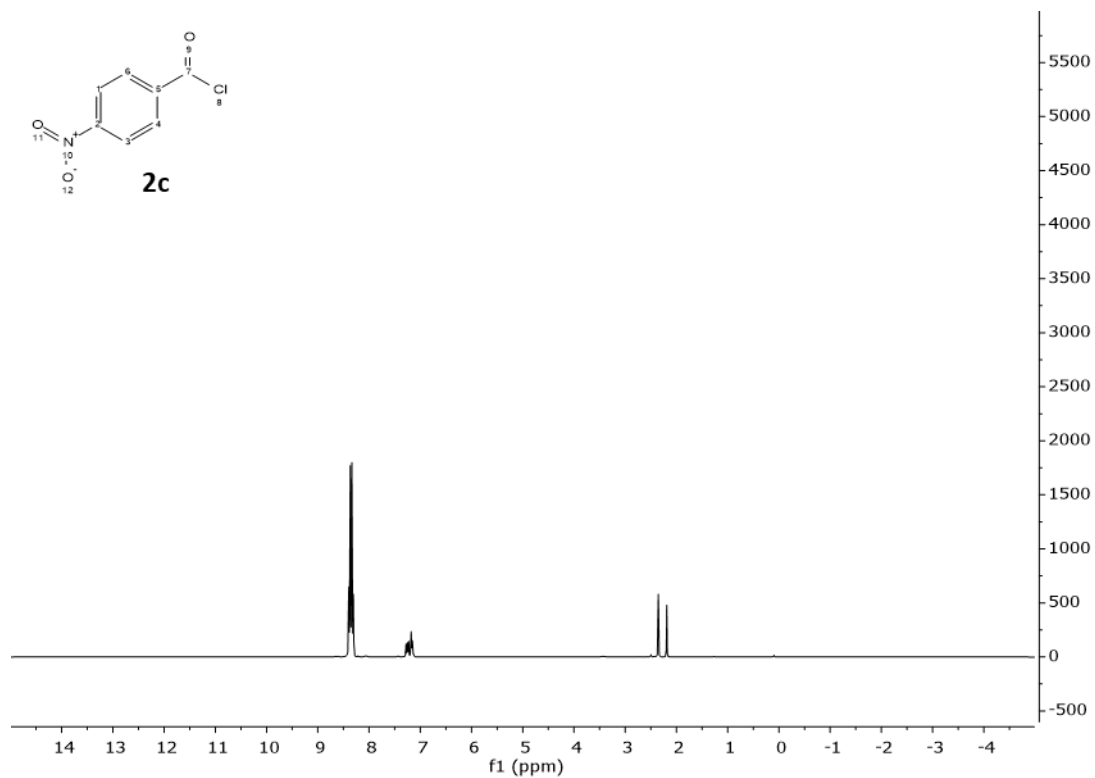
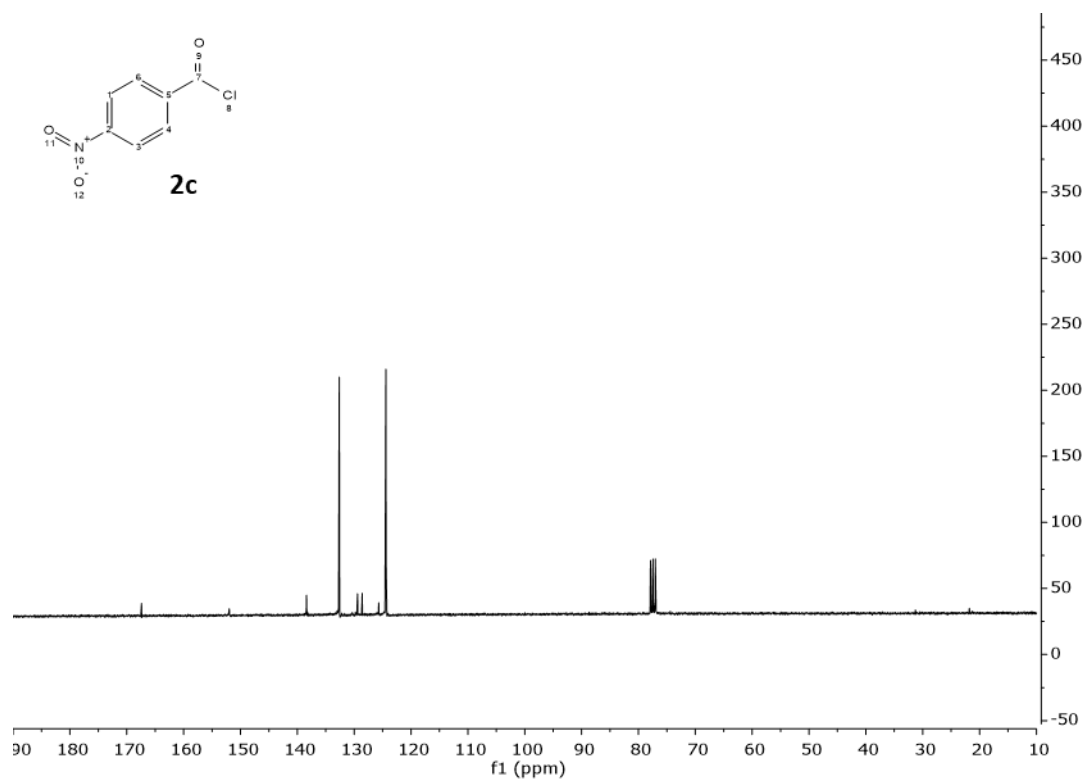
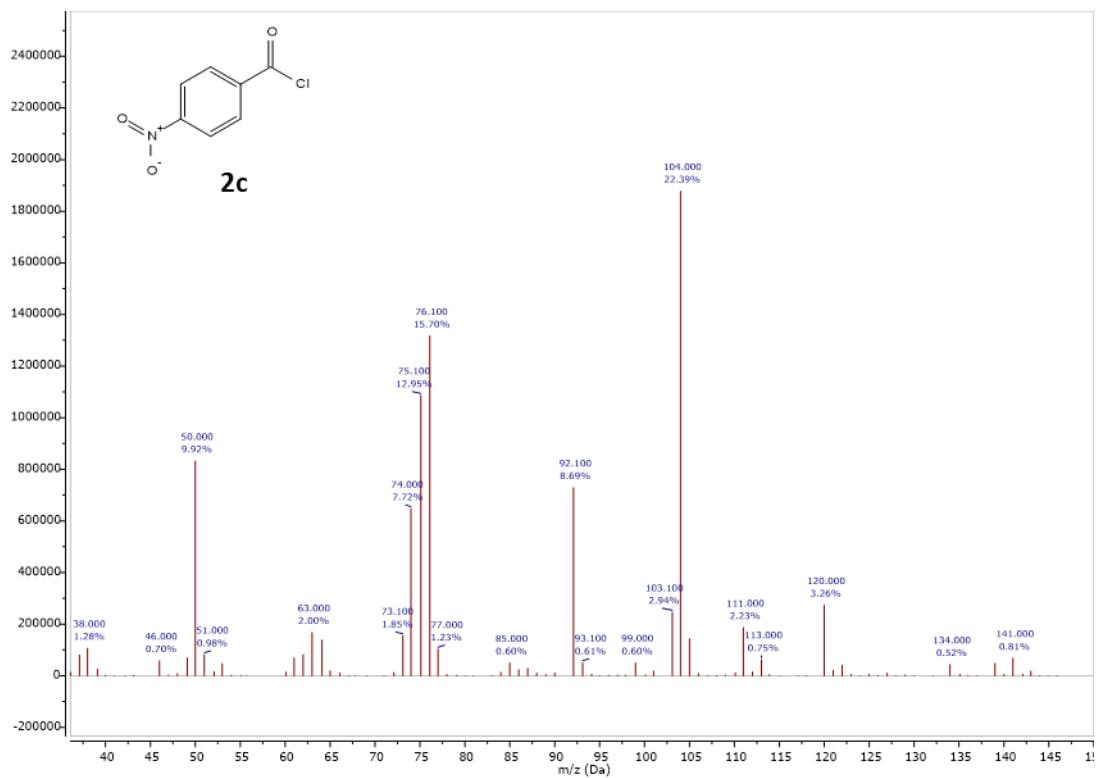


Figure A26. ^1H NMR spectra of **2c**.

^1H NMR (300 MHz, Chloroform-d) δ 8.43 – 8.26 (m, 4H).

Figure A27. ¹³C NMR spectra of **2c**.

¹³C NMR (75 MHz, Chloroform-*d*) δ 167.41, 151.98, 138.38, 132.62, 124.43.

Figure A28. MS spectra of **2c**.

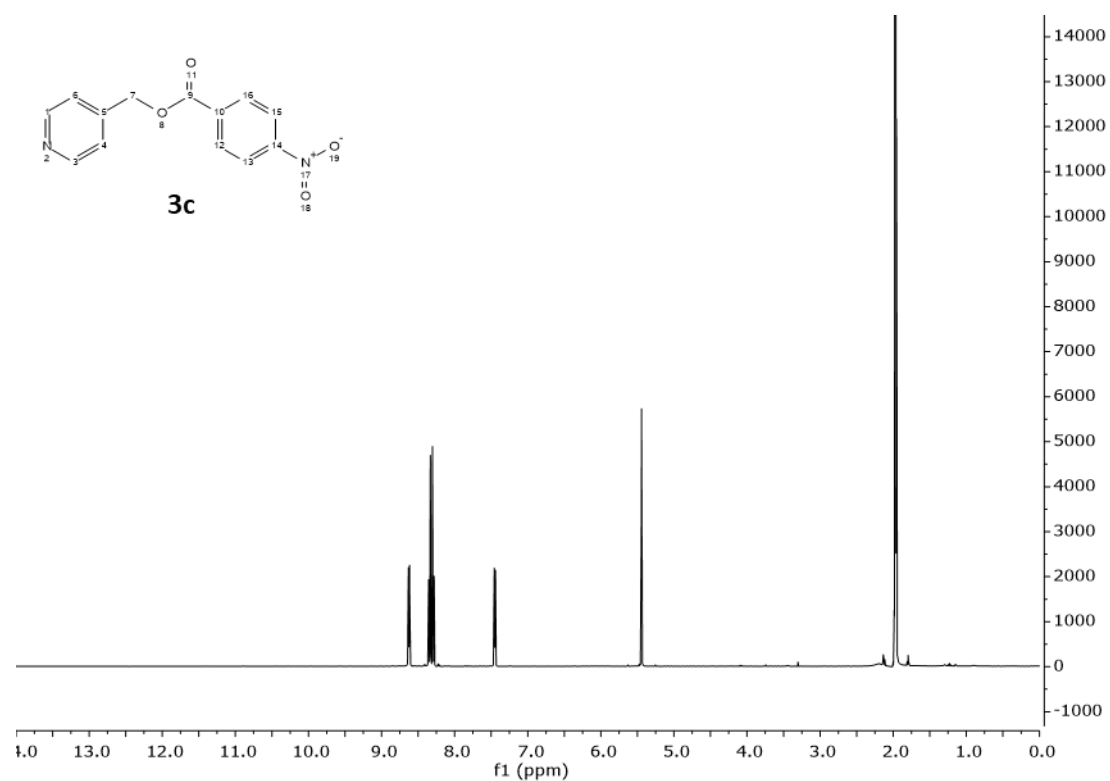


Figure A29. ^1H NMR spectra of **3c**.

^1H NMR (400 MHz, Acetonitrile- d_3) δ 8.62 (d, 2H), 8.39 – 8.25 (m, 4H), 7.45 (d, J = 4.4, 1.6, 0.7 Hz, 2H), 5.44 (s, 2H).

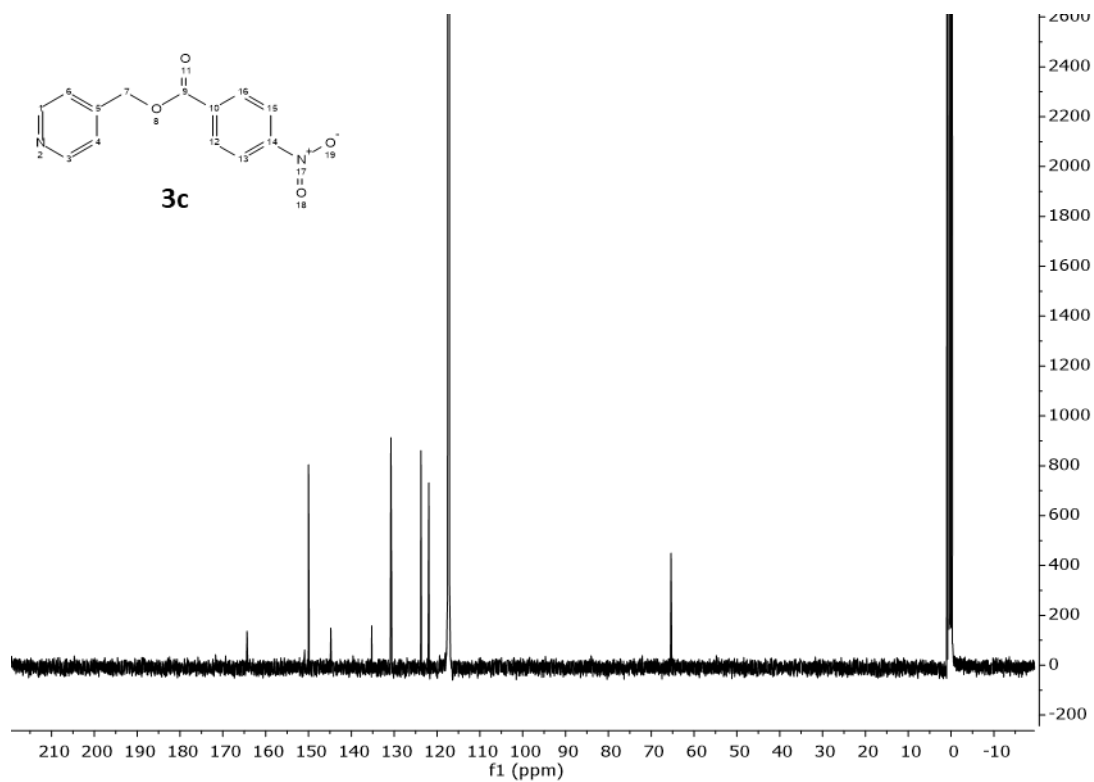


Figure A30. ^{13}C NMR spectra of **3c**.

^{13}C NMR (101 MHz, Acetonitrile- d_3) δ 164.36, 150.90, 150.00, 144.81, 135.25, 130.77, 123.75, 121.92, 65.37.

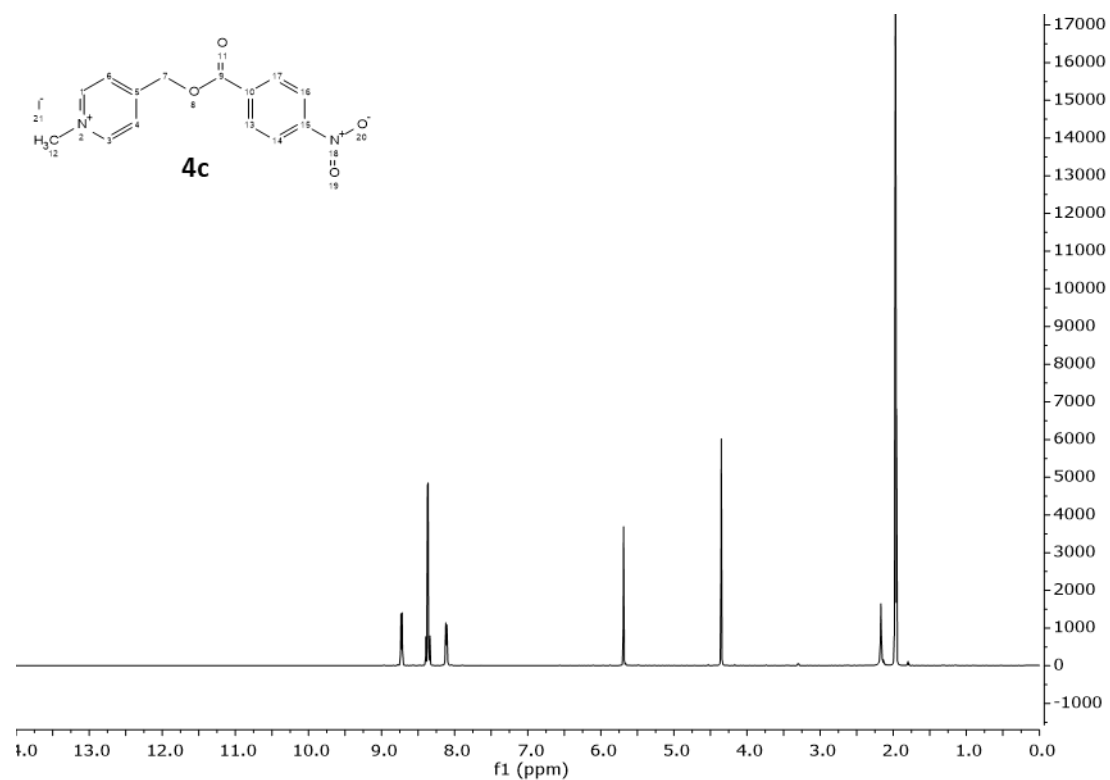


Figure A31. ^1H NMR spectra of **4c**.

^1H NMR (400 MHz, Acetonitrile- d_3) δ 8.72 (d, 2H), 8.42 – 8.31 (m, 4H), 8.11 (d, $J = 6.3$ Hz, 2H), 5.69 (s, 2H), 4.35 (s, 3H).

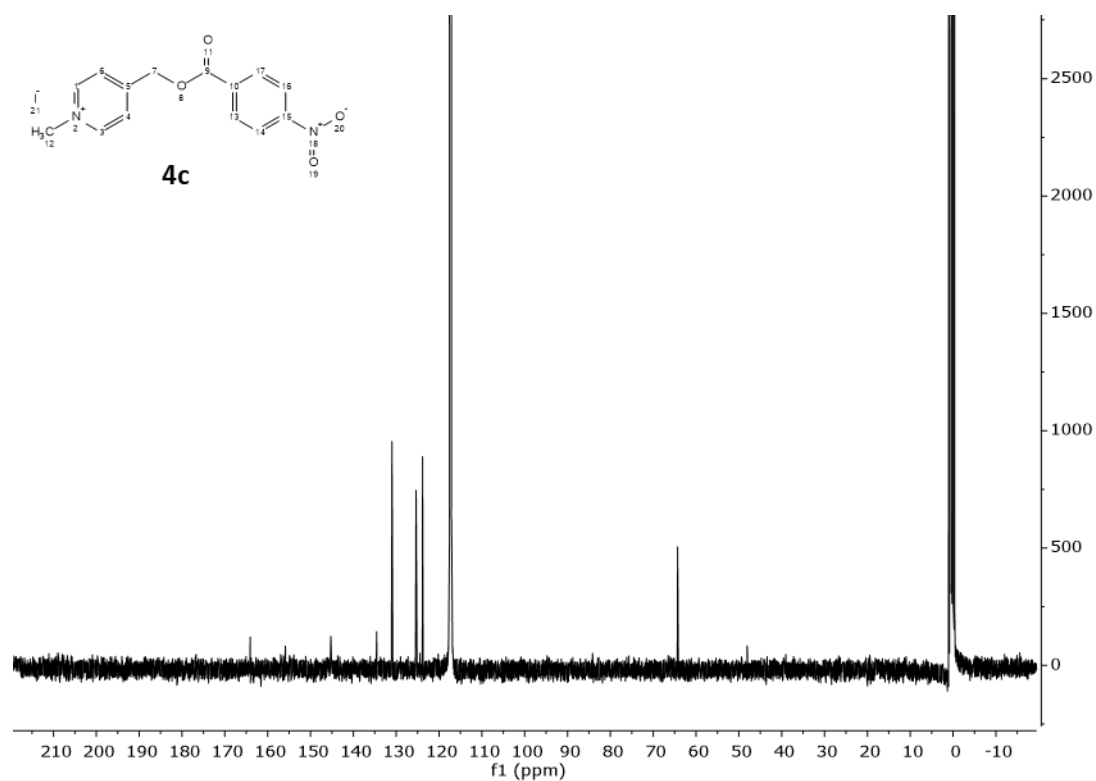
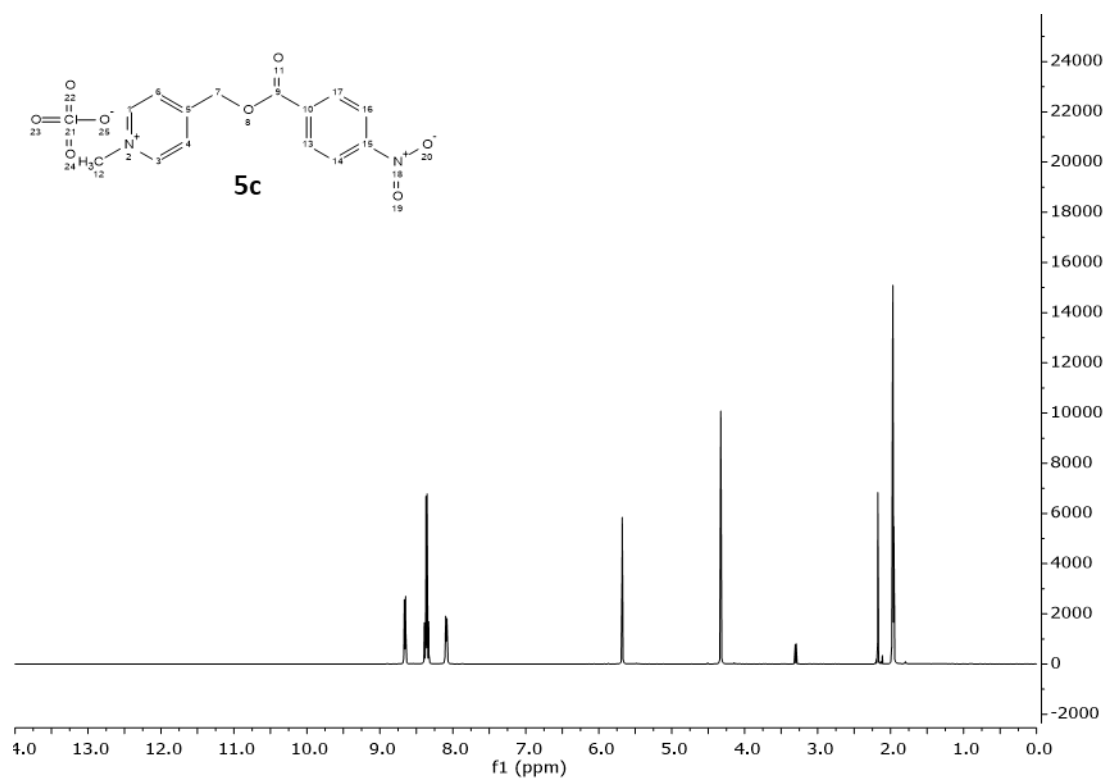
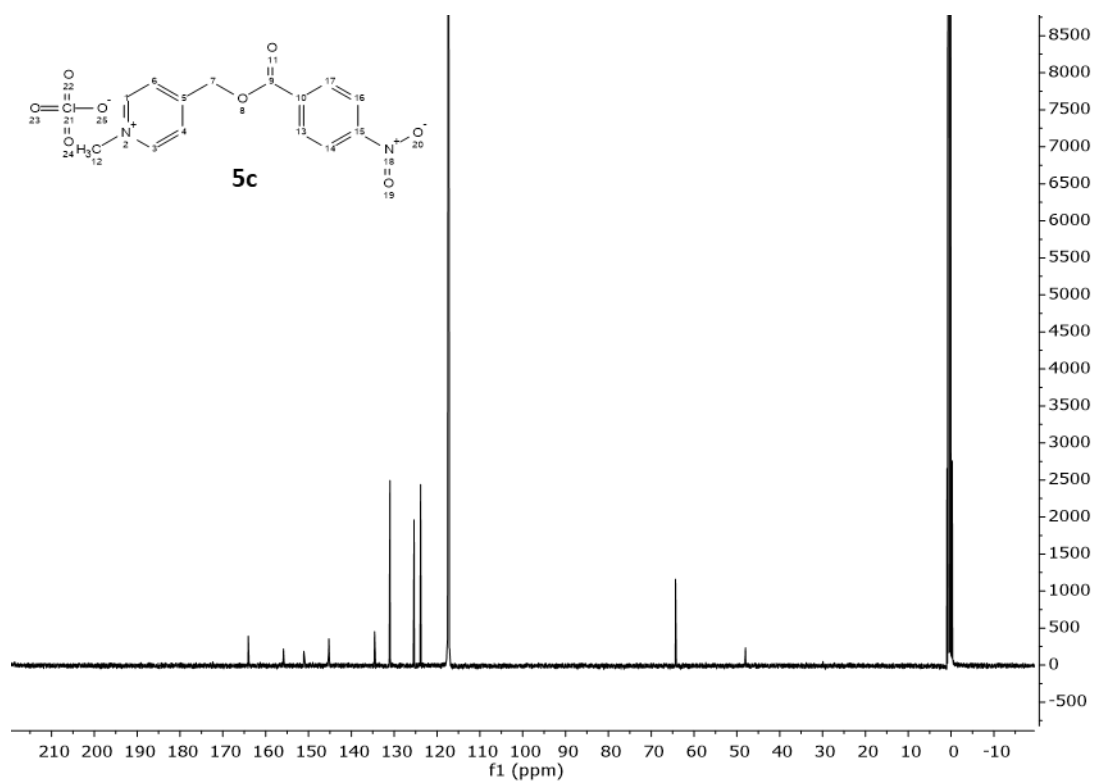


Figure A32. ^{13}C NMR spectra of **4c**.

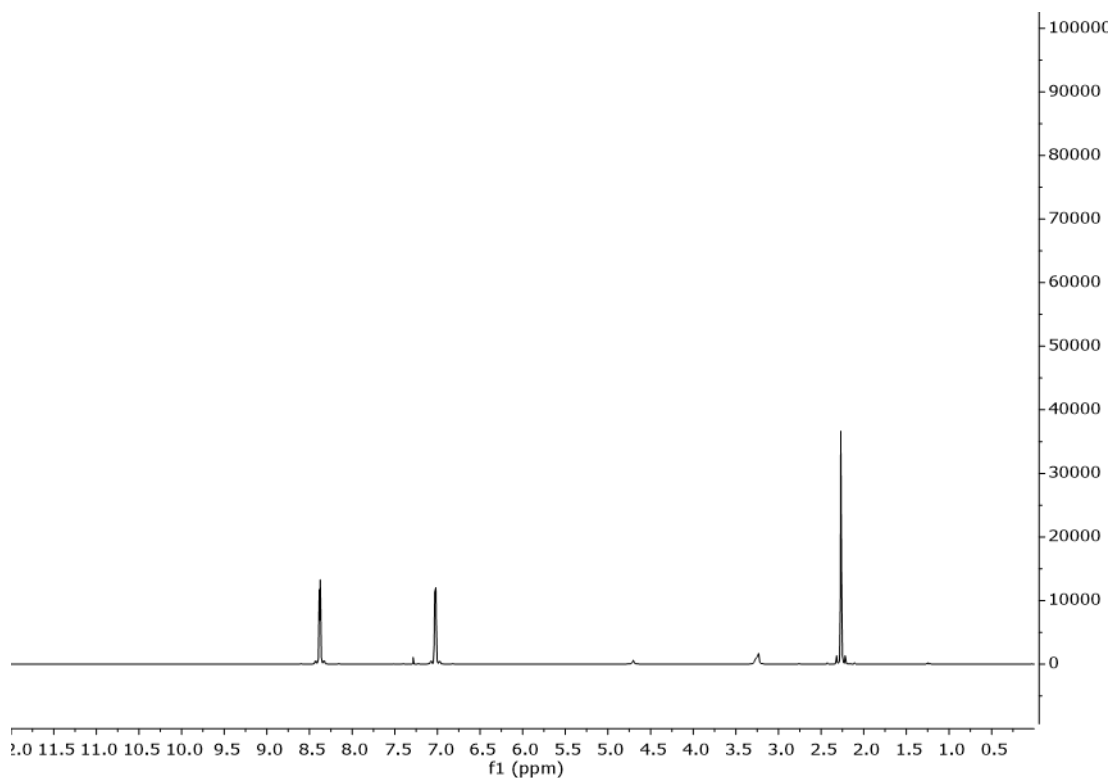
^{13}C NMR (101 MHz, Acetonitrile- d_3) δ 164.07, 155.87, 151.12, 147.17 – 143.86 (m), 134.55, 130.99, 125.36, 123.85, 64.31, 48.05.

**Figure A33.** ^1H NMR spectra of **5c**.

^1H NMR (400 MHz, Acetonitrile- d_3) δ 8.69 – 8.62 (m, 2H), 8.42 – 8.30 (m, 4H), 8.09 (d, $J = 6.3$ Hz, 2H), 5.68 (d, $J = 1.1$ Hz, 2H), 4.33 (s, 3H).



^{13}C NMR (101 MHz, Acetonitrile- d_3) δ 164.07, 155.85, 151.10, 146.27 – 144.53 (m), 134.58, 130.99, 125.36, 123.84, 64.32, 48.78 – 47.05 (m).



^1H NMR (400 MHz, Chloroform- d) δ 8.38 (d, 4H), 7.03 (d, 4H), 2.27 (s, 6H).

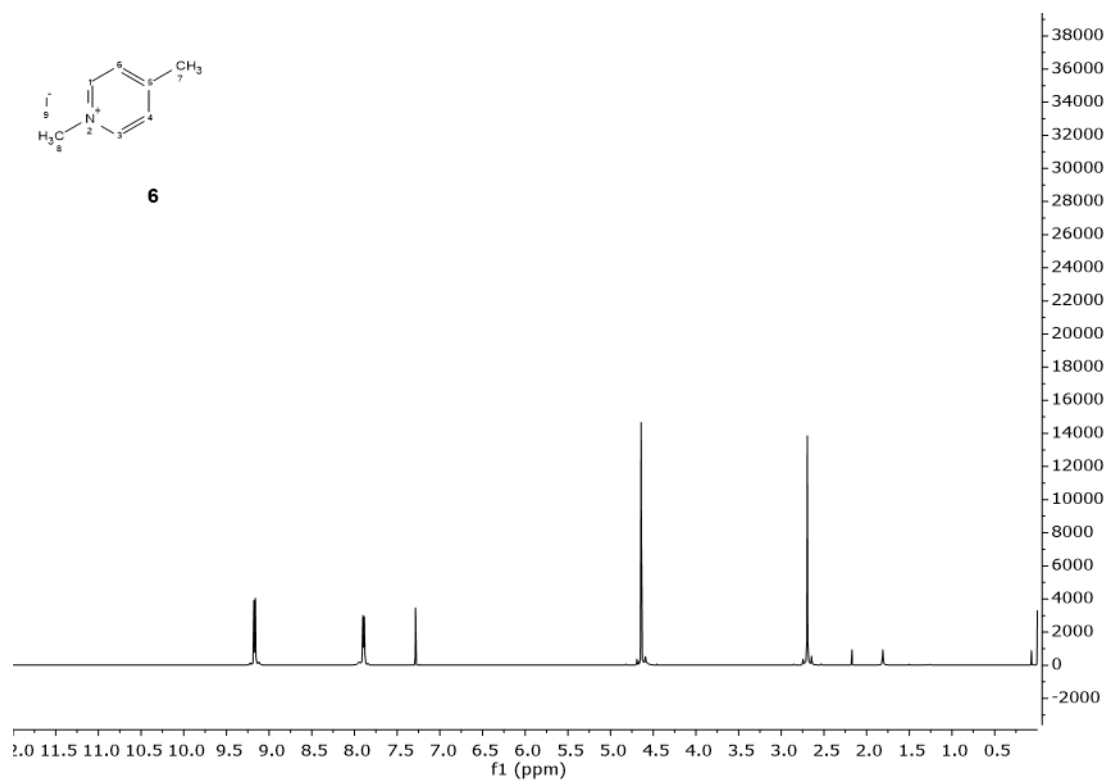


Figure A36. ¹H NMR spectra of 6.

¹H NMR (400 MHz, Chloroform-*d*) δ 9.17 (d, 2H), 7.89 (d, *J* = 6.2 Hz, 2H), 4.64 (s, 2H), 2.70 (s, 3H).

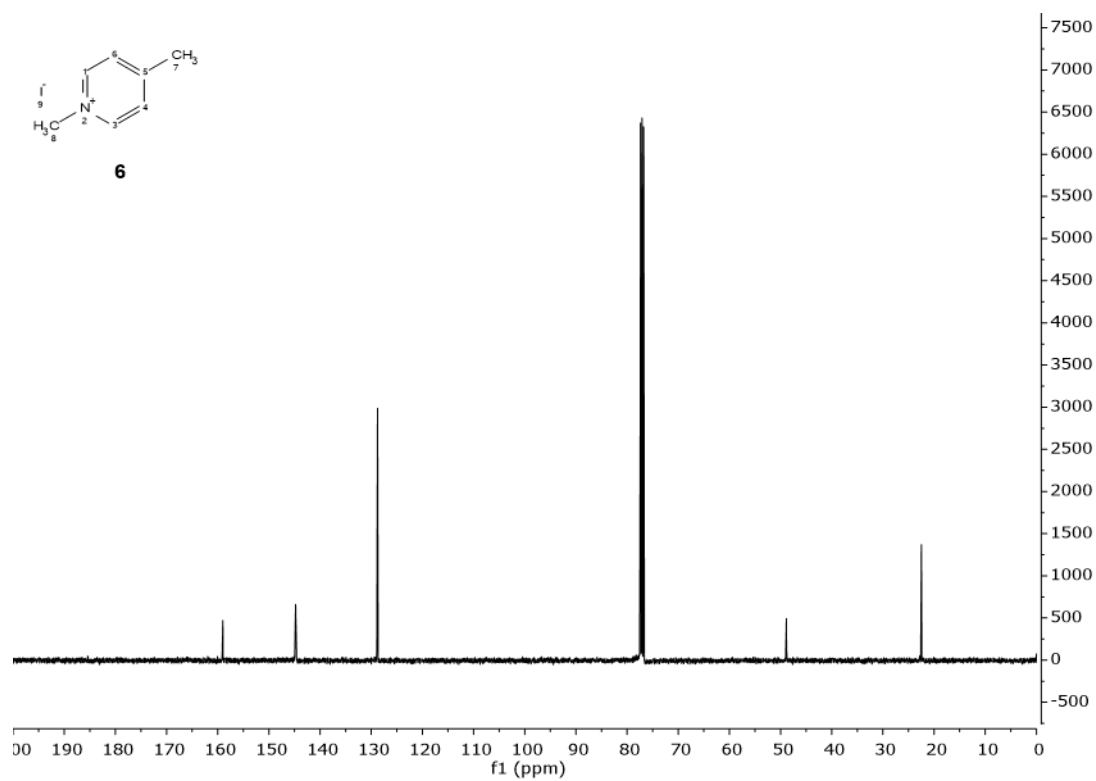


Figure A37. ¹³C NMR spectra of 6.

¹³C NMR (101 MHz, Chloroform-*d*) δ 159.00, 146.27 – 143.18 (m), 128.76, 48.87, 22.47.

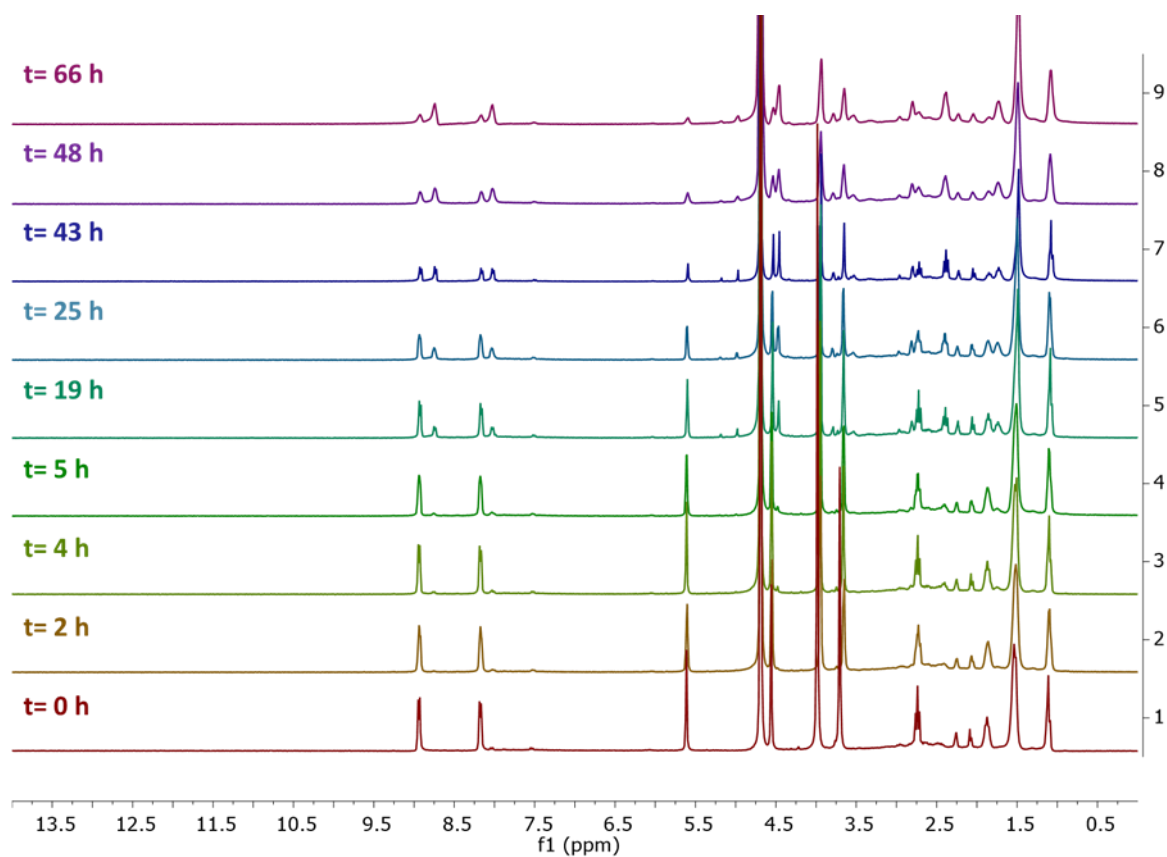


Figure A38. Evolution of the photodeprotection of octanoic acid with g-CDs.

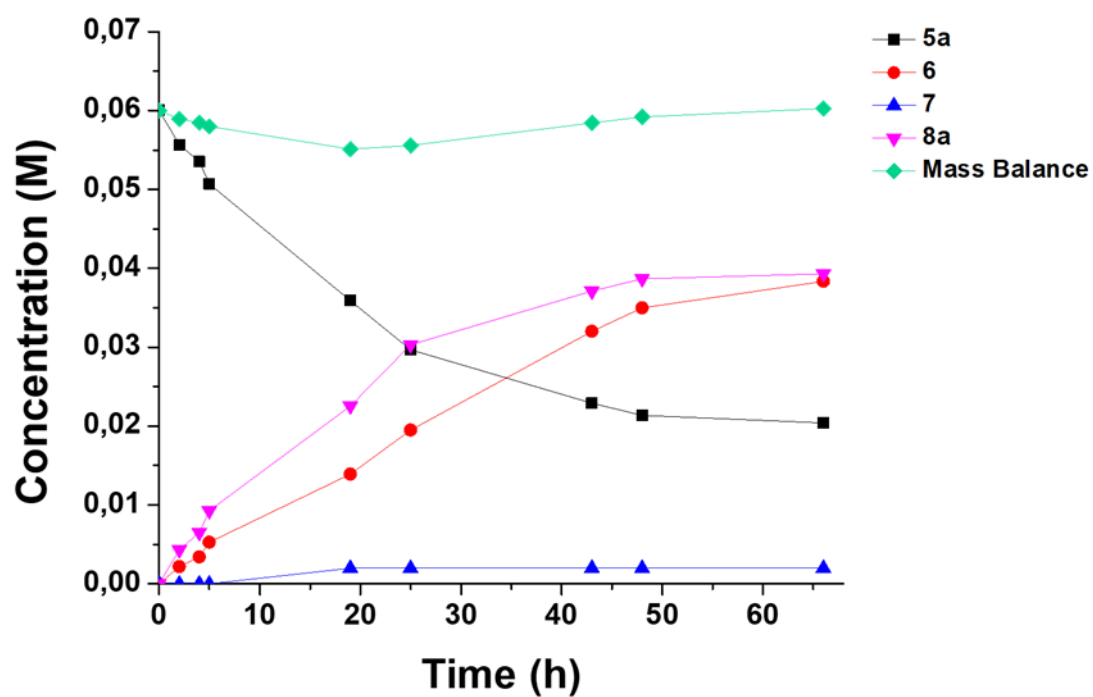


Figure A39. Concentration profiles of reagent and products in the photodeprotection of 5a with g-CDs.

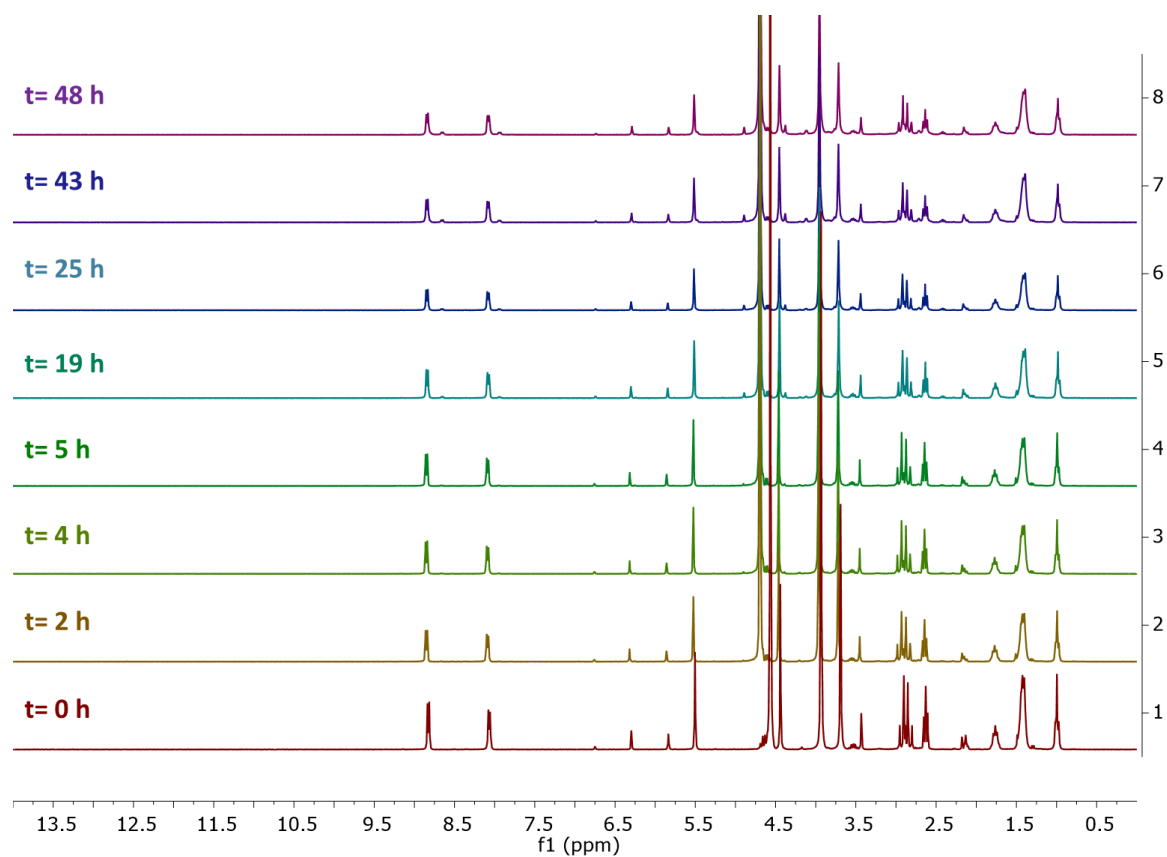


Figure A40. Evolution of the photodeprotection of octanoic acid with α -CDs.

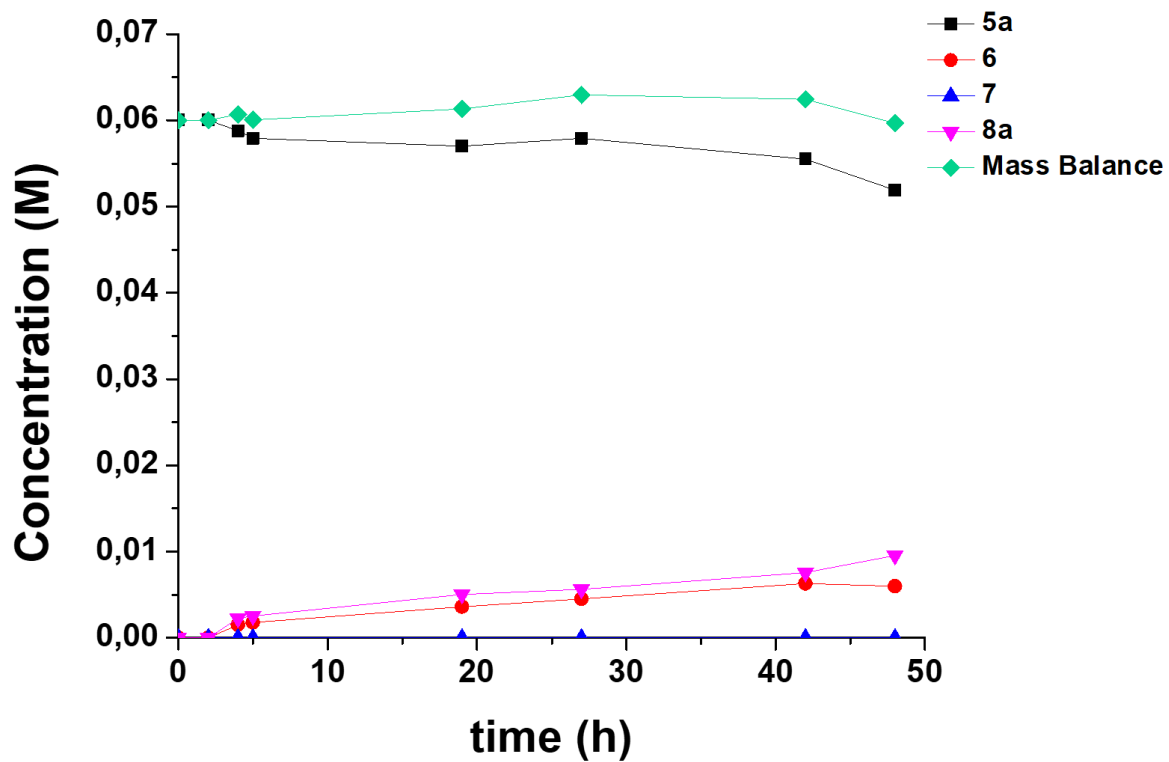


Figure A41. Concentration profiles of reagent and products in the photodeprotection of 5a with a-CDs.

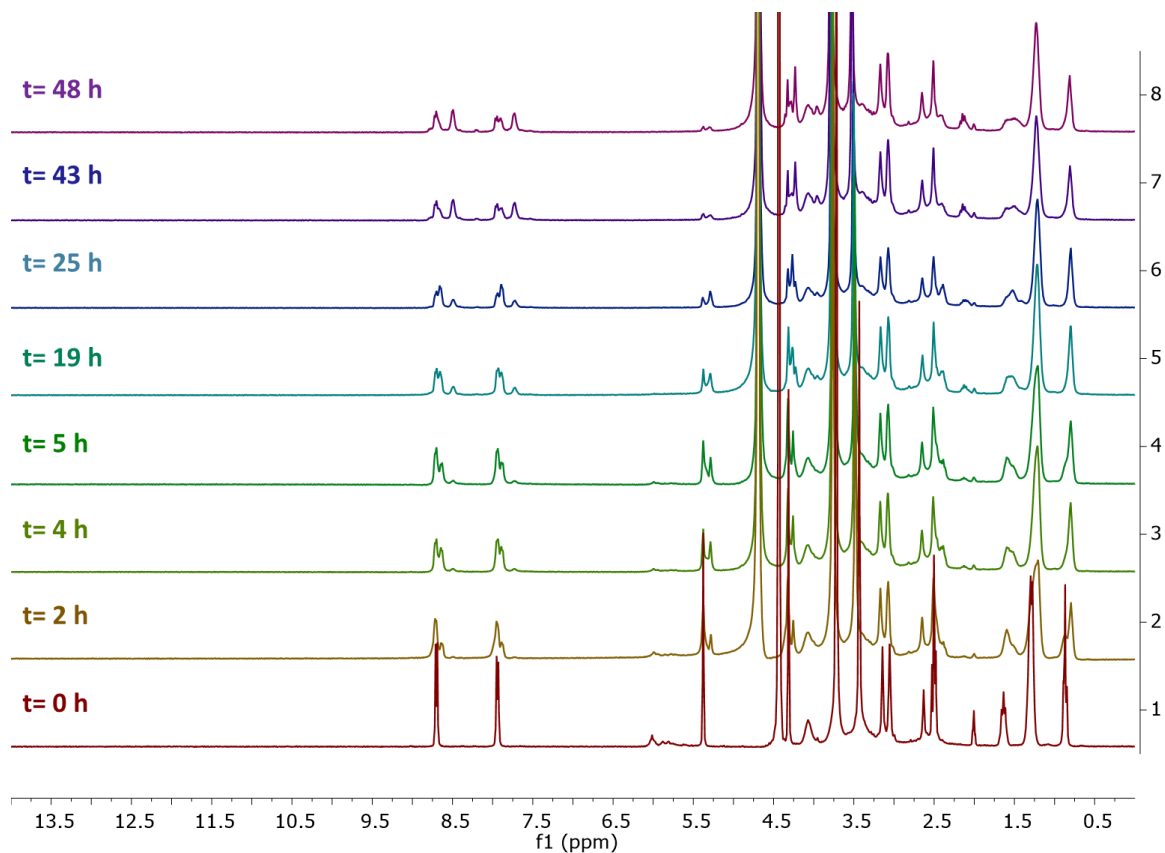


Figure A42. Evolution of the photodeprotection of octanoic acid with g-N-CDs.

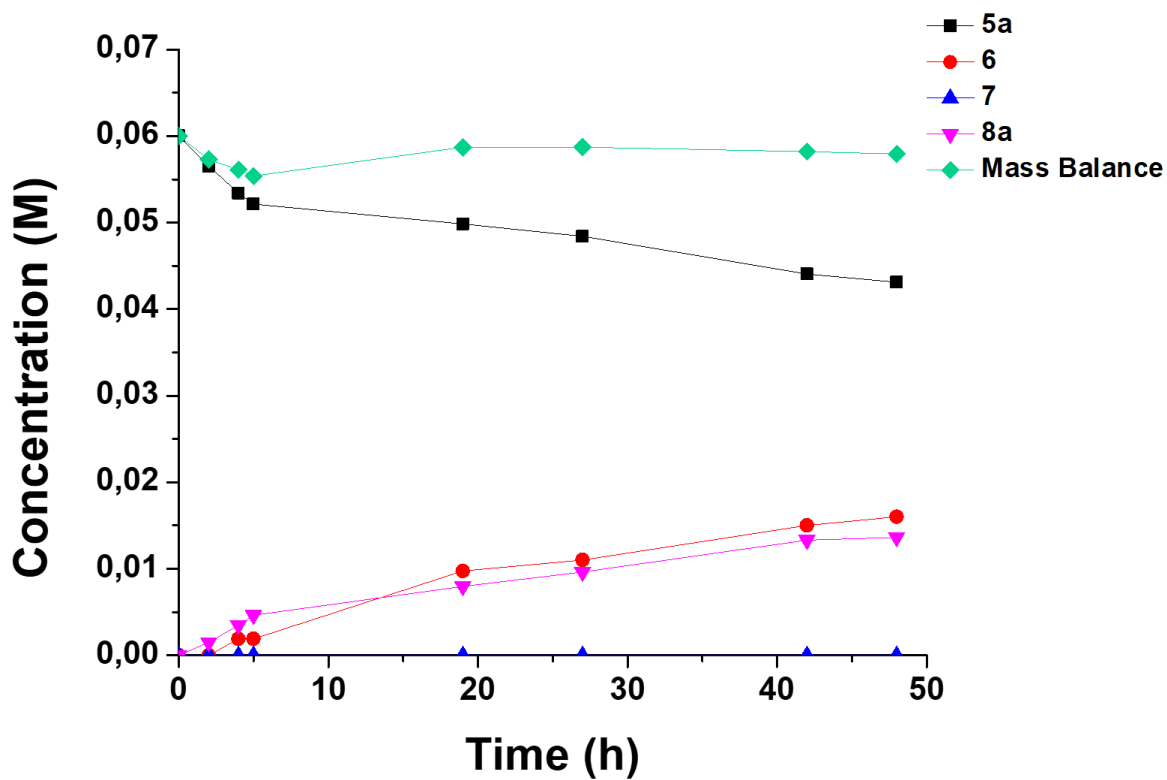


Figure A43. Concentration profiles of reagent and products in the photodeprotection of **5a** with **g-N-CDs**.

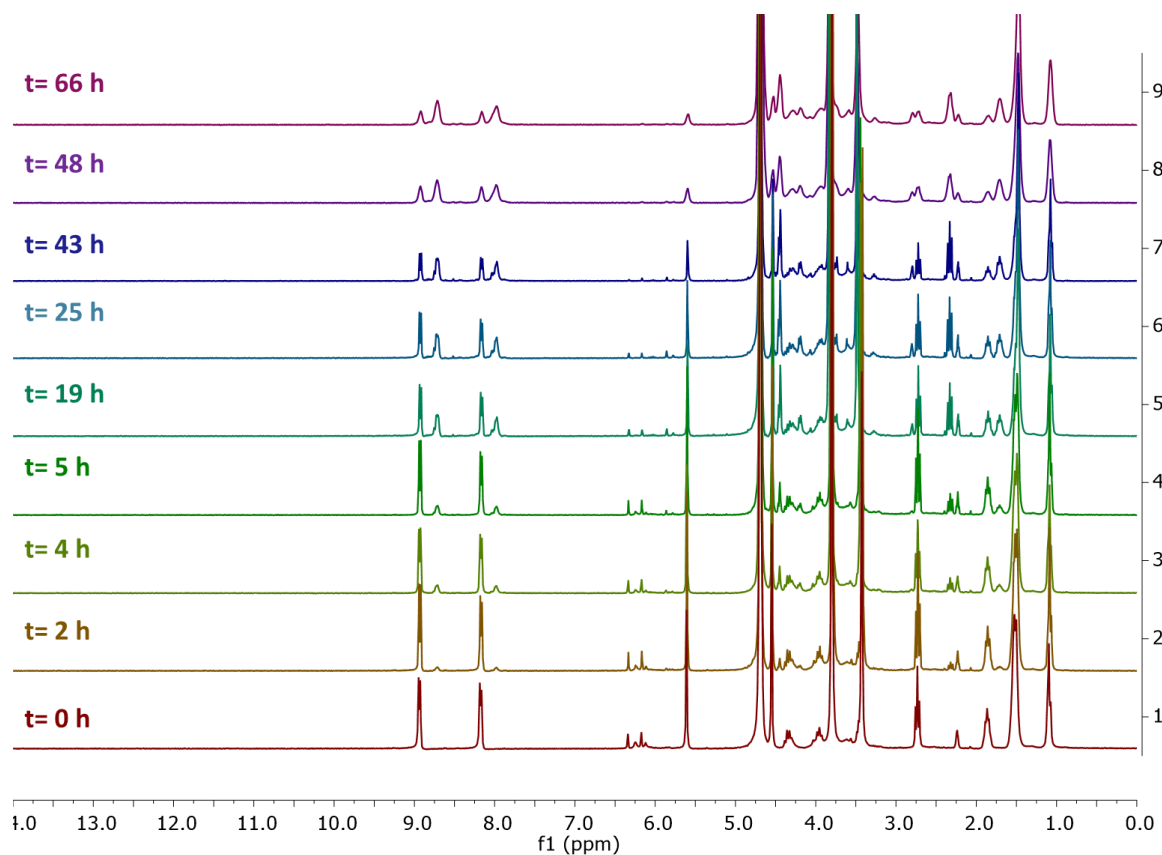


Figure A44. Evolution of the photodeprotection of octanoic acid with **a-N-CDs**.

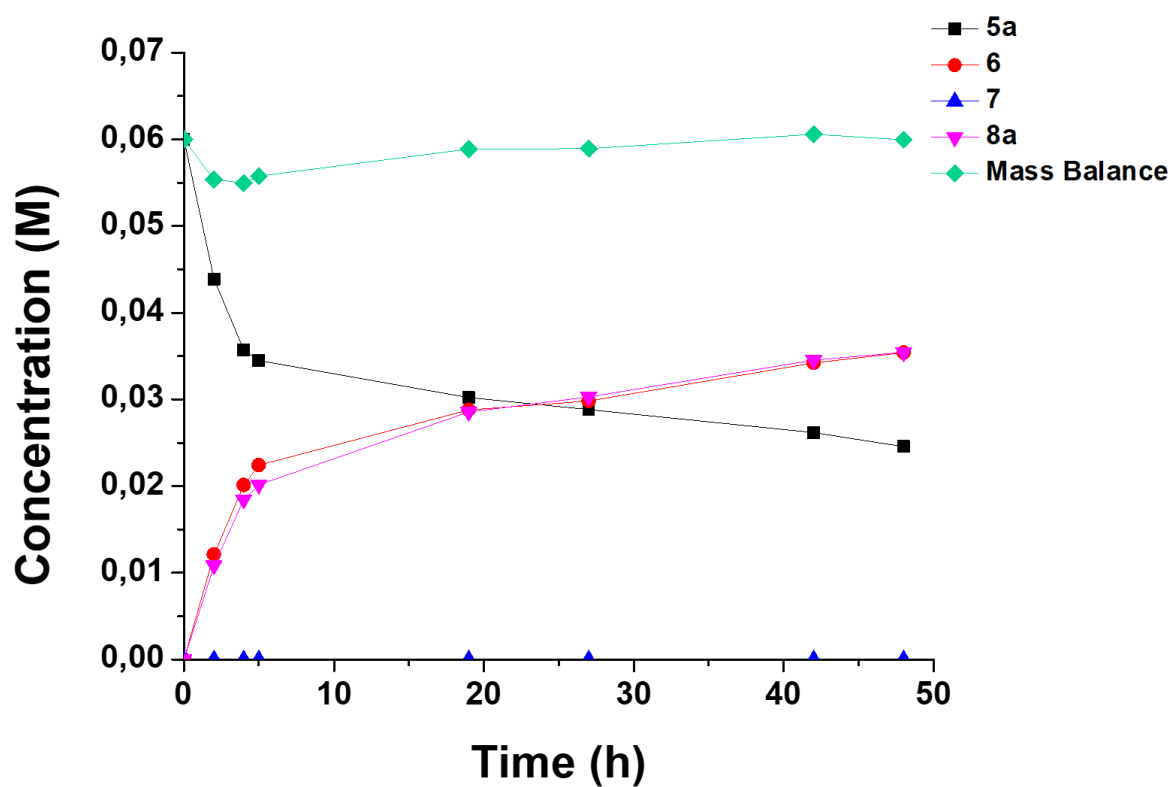


Figure A45. Concentration profiles of reagent and products in the photodeprotection of **5a** with α -N-CDs.

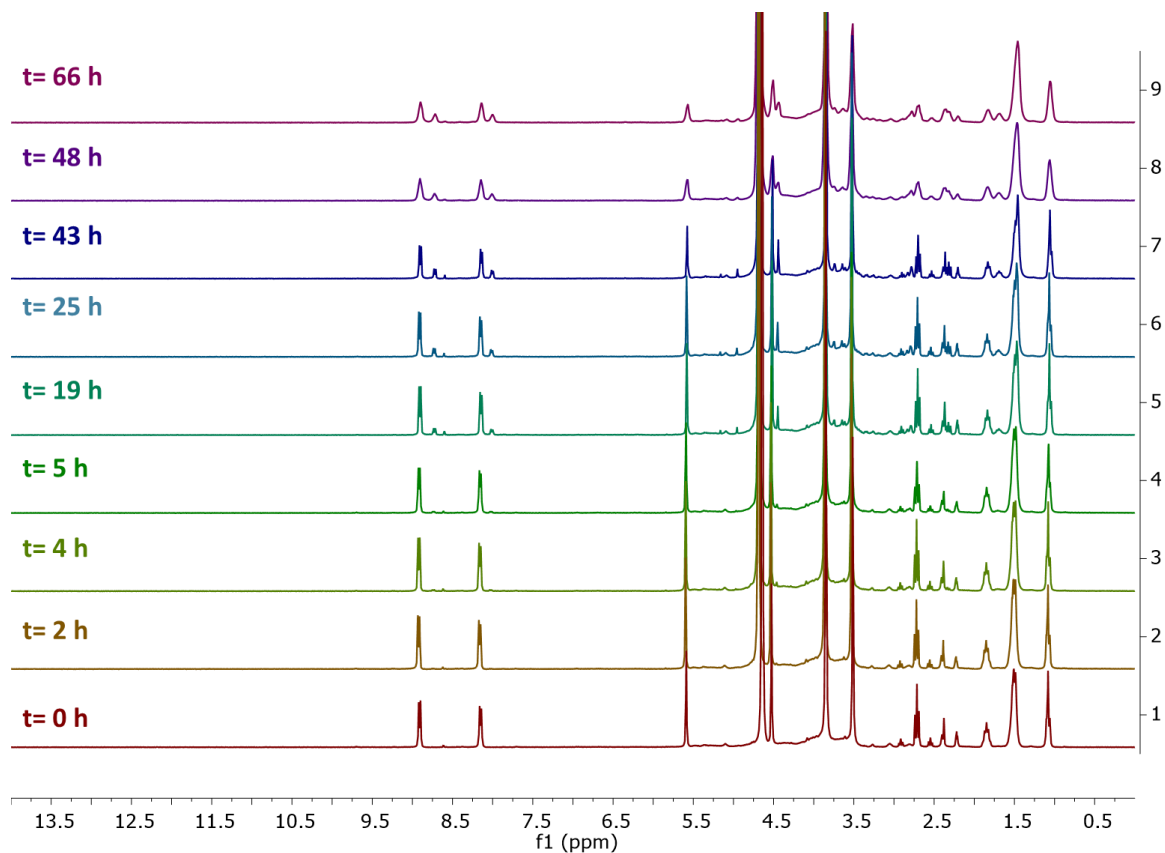


Figure A46. Evolution of the photodeprotection of octanoic acid with α -Glu-CDs.

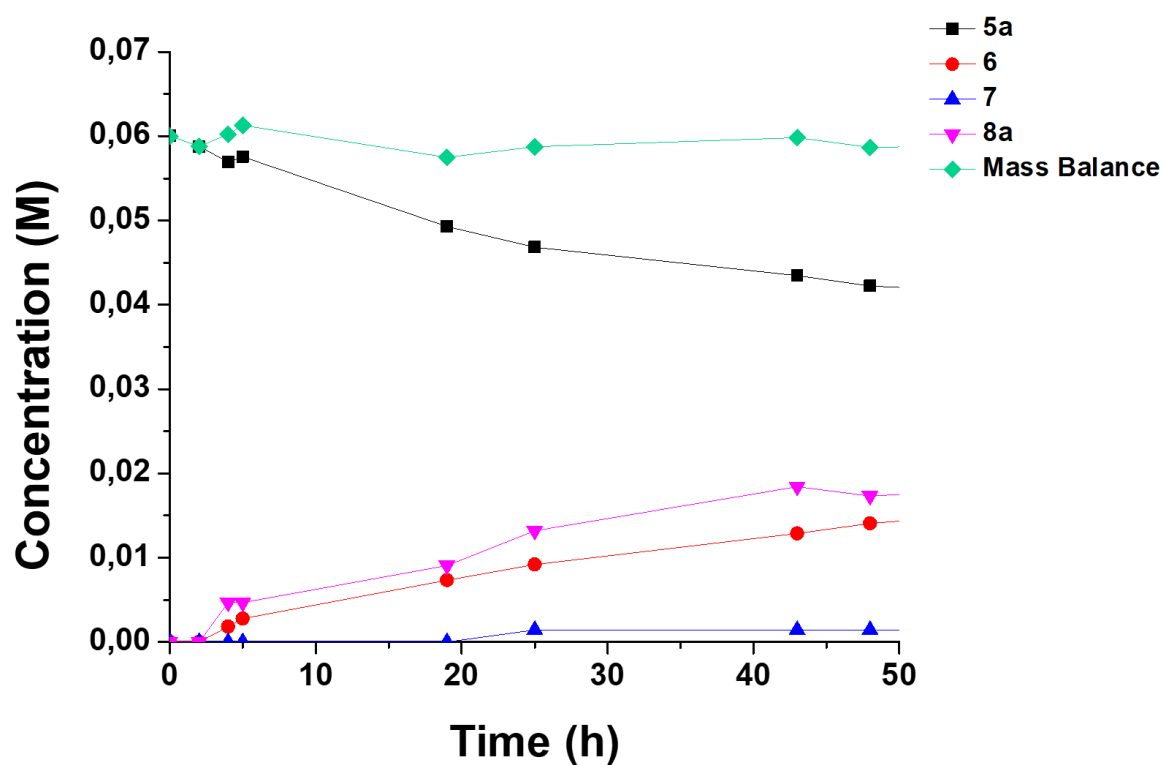


Figure A47. Concentration profiles of reagent and products in the photodeprotection of **5a** with α -Glu-CDs.

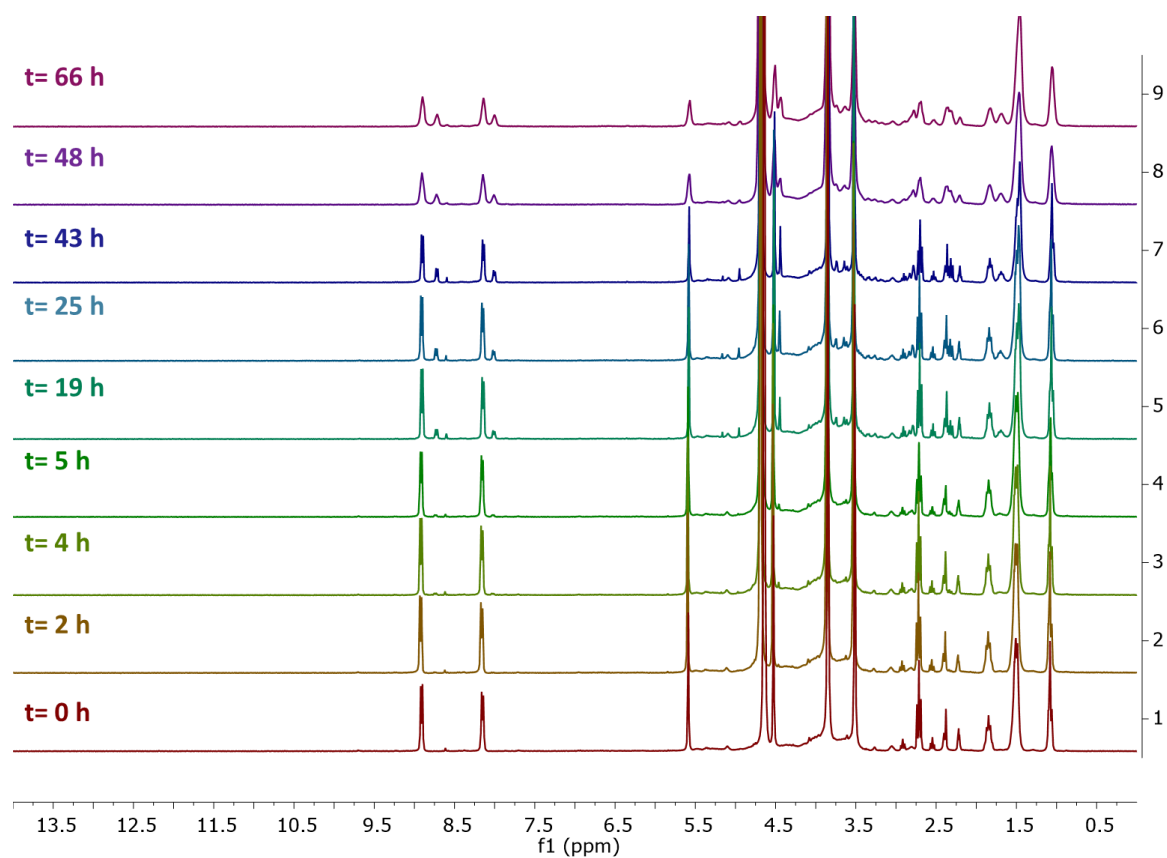


Figure A48. Evolution of the photodeprotection of octanoic acid with α -Glu-CDs.

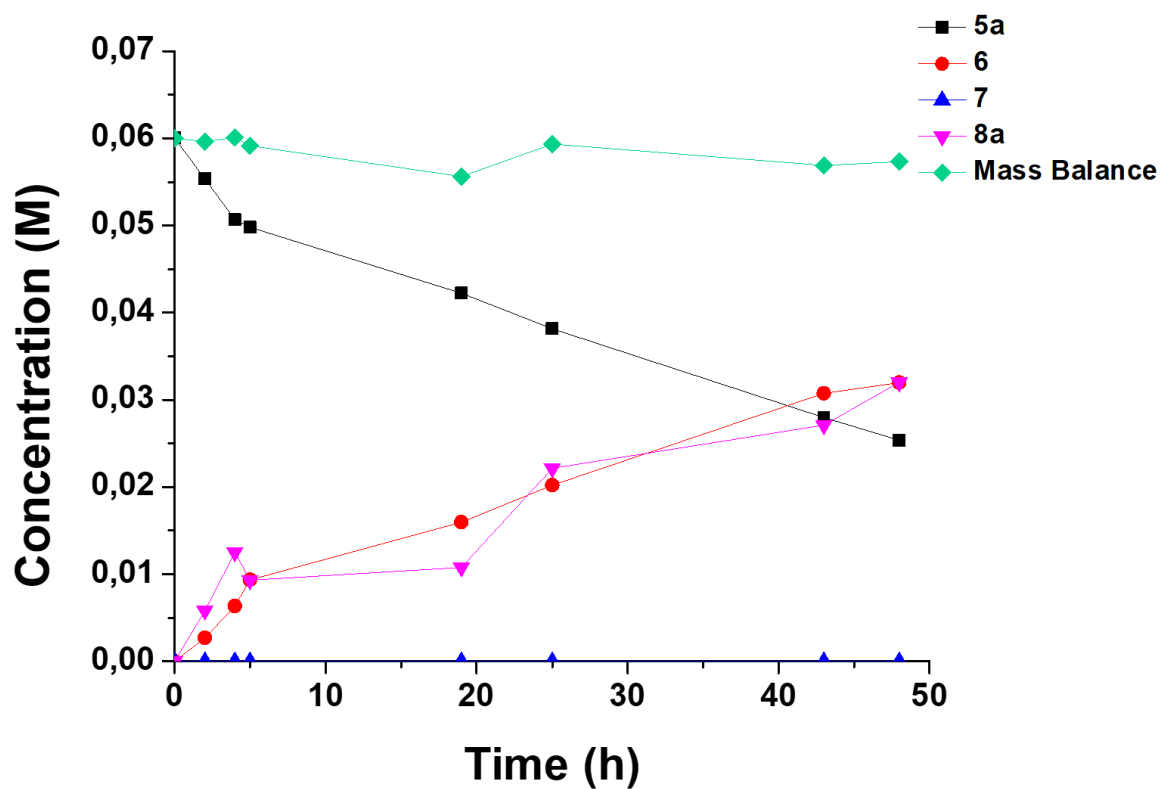


Figure A49. Concentration profiles of reagent and products in the photodeprotection of **5a** with *g*-Glu-CDs.

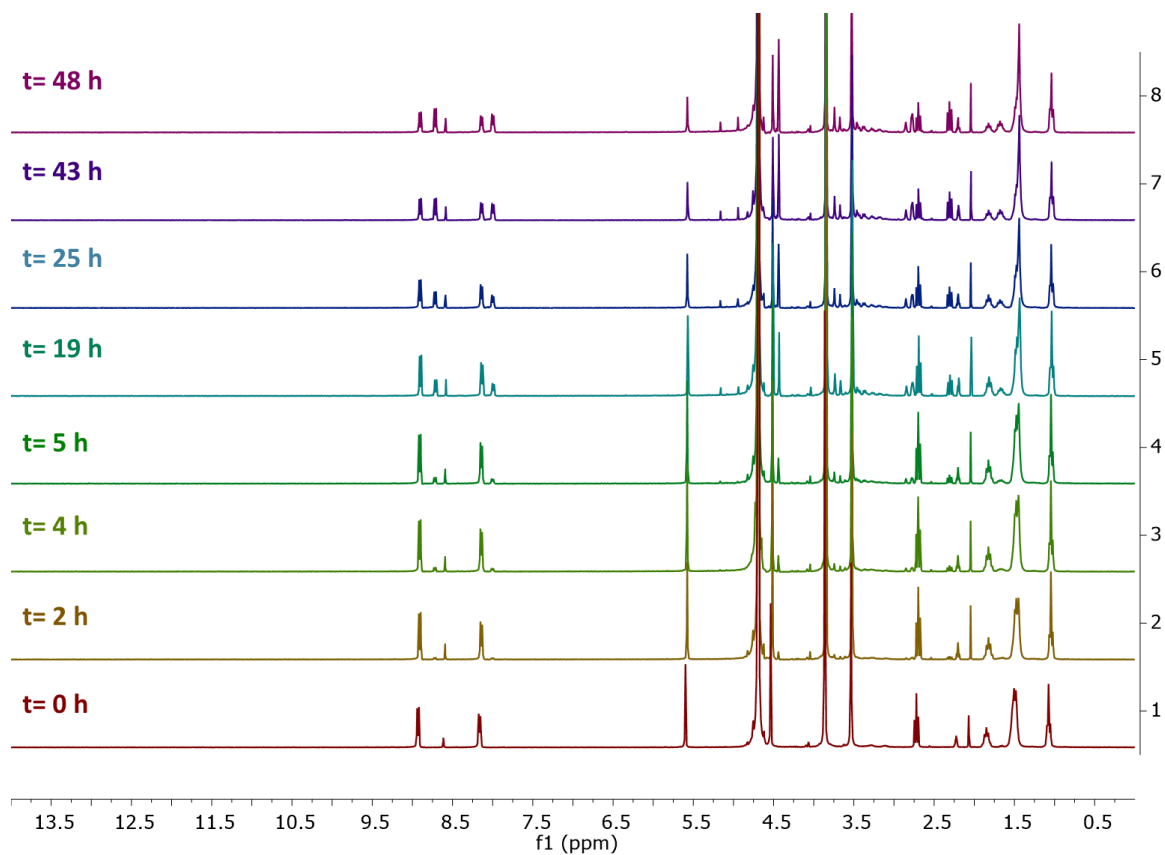


Figure A50. Evolution of the photodeprotection of octanoic acid with g-Glu-N-CDs.

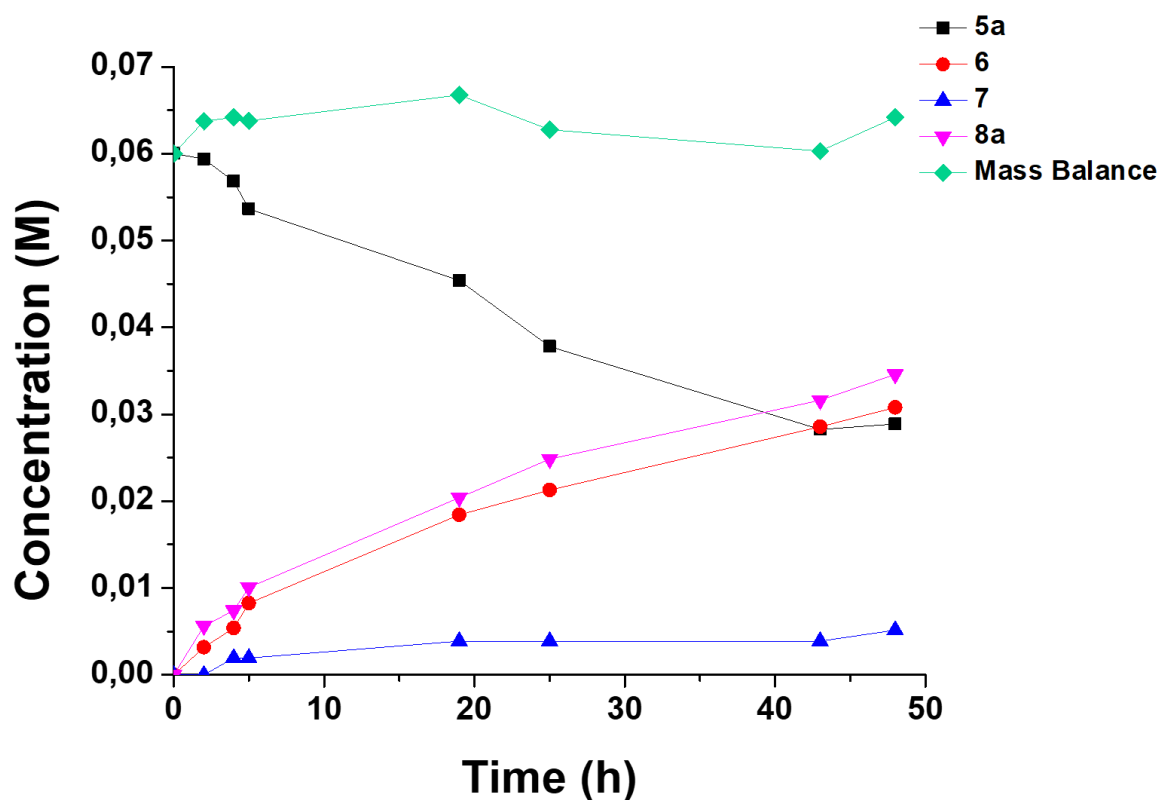


Figure A51. Concentration profiles of reagent and products in the photodeprotection of 5a with g-Glu-N-CDs

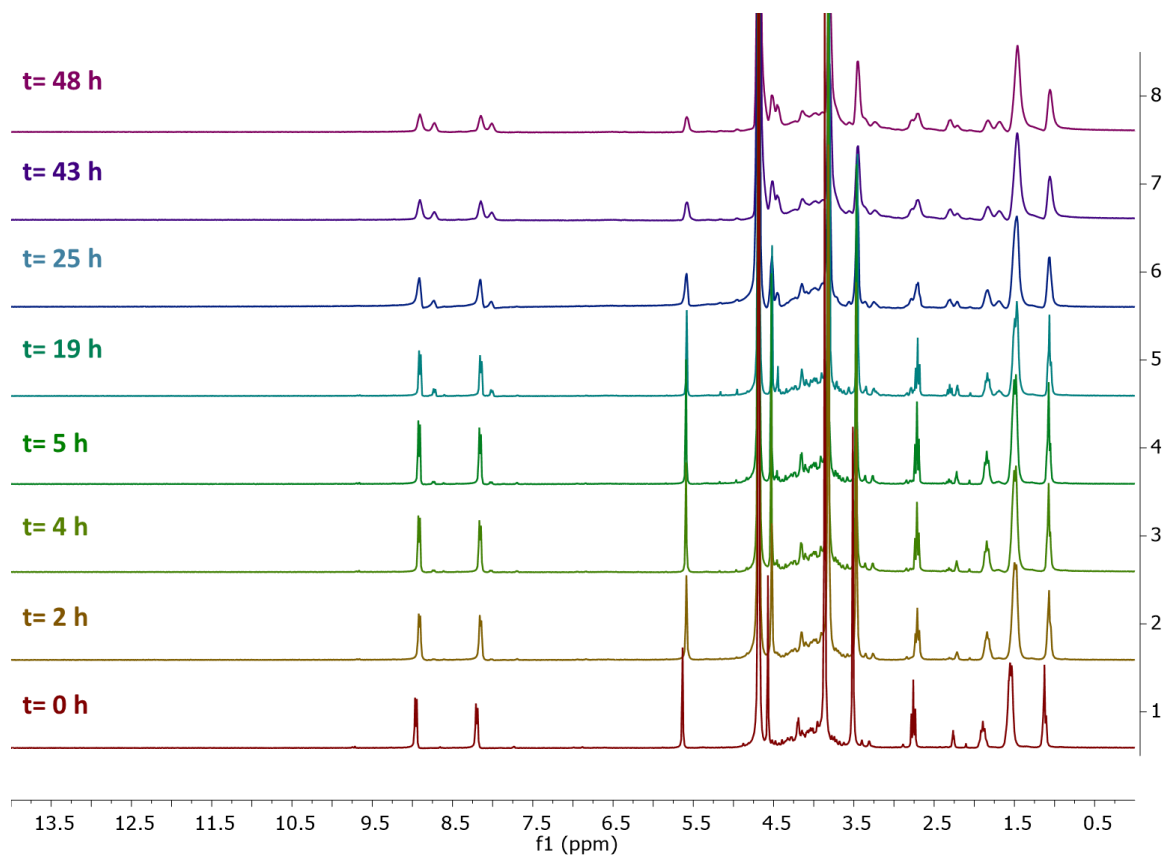


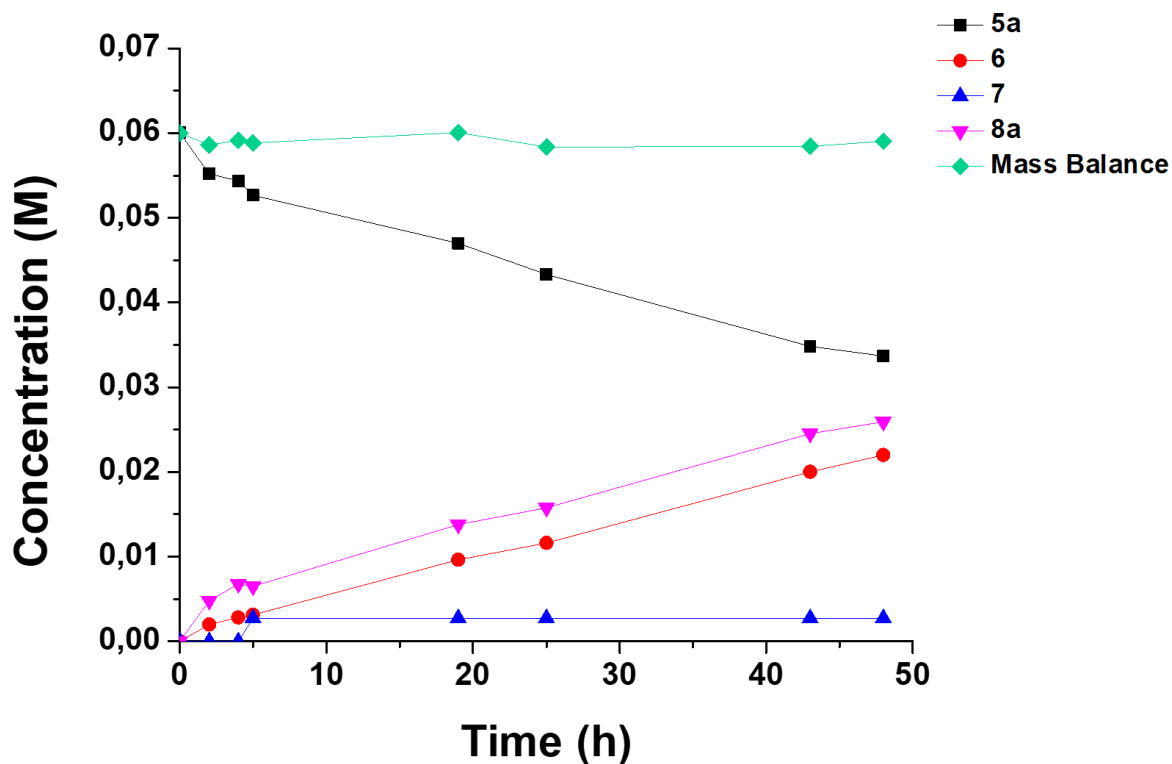
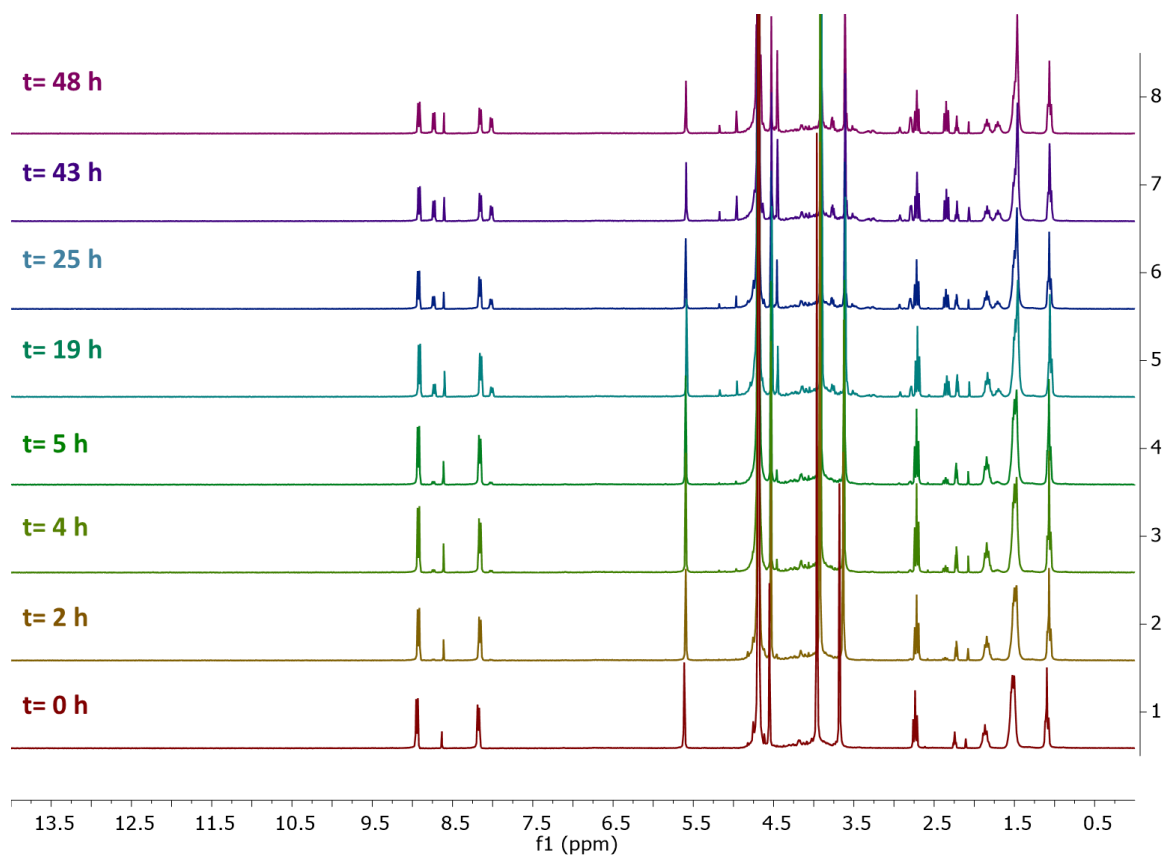
Figure A52. Evolution of the photodeprotection of octanoic acid with α -Fru-CDs.Figure A53. Concentration profiles of reagent and products in the photodeprotection of 5a with α -Fru-CDs.

Figure A54. Evolution of the photodeprotection of octanoic acid with g-Fru-CDs.

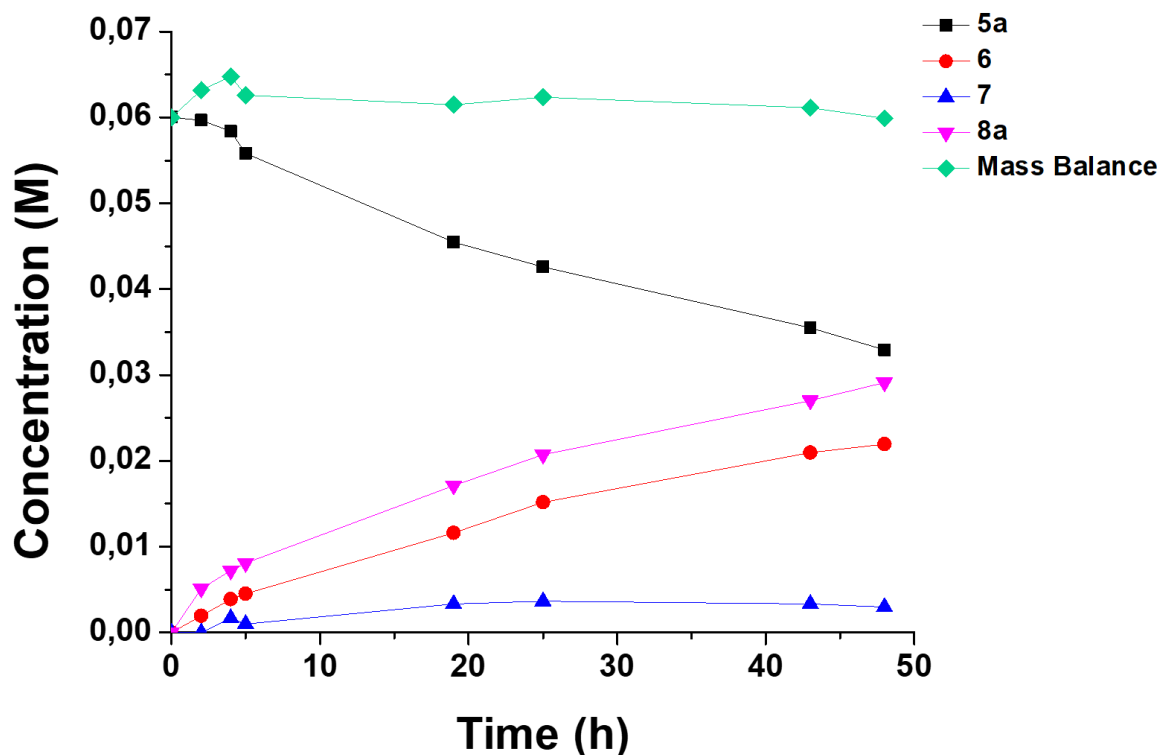


Figure A55. Concentration profiles of reagent and products in the photodeprotection of 5a with g-Fru-CDs.

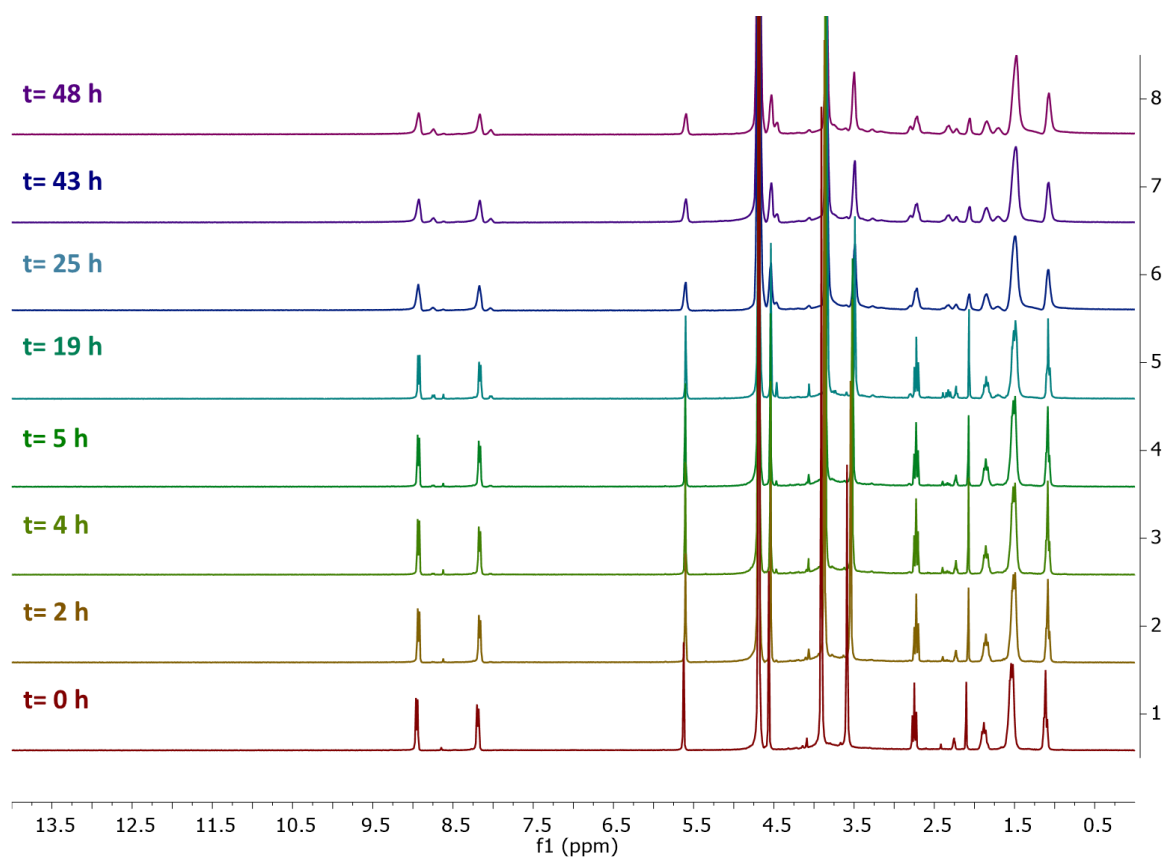


Figure A56. Evolution of the photodeprotection of octanoic acid with g-Fru-N-CDs

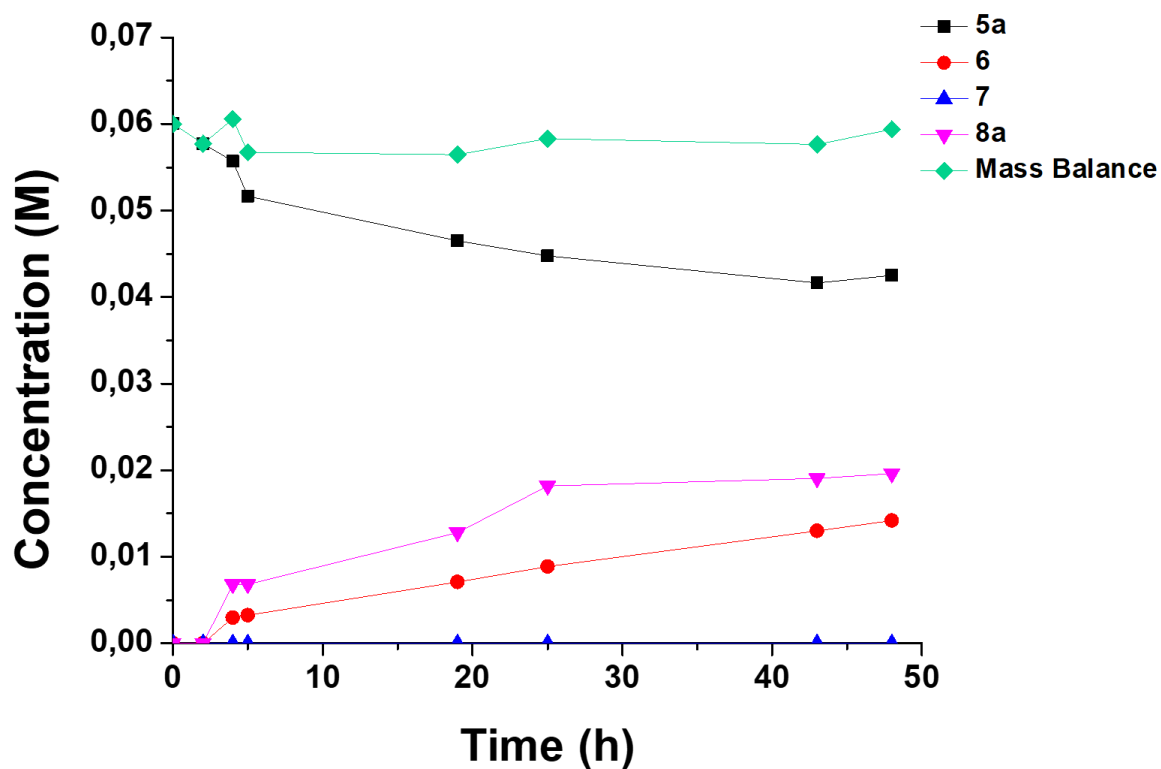


Figure A57. Concentration profiles of reagent and products in the photodeprotection of 5a with g-Fru-N-CDs.

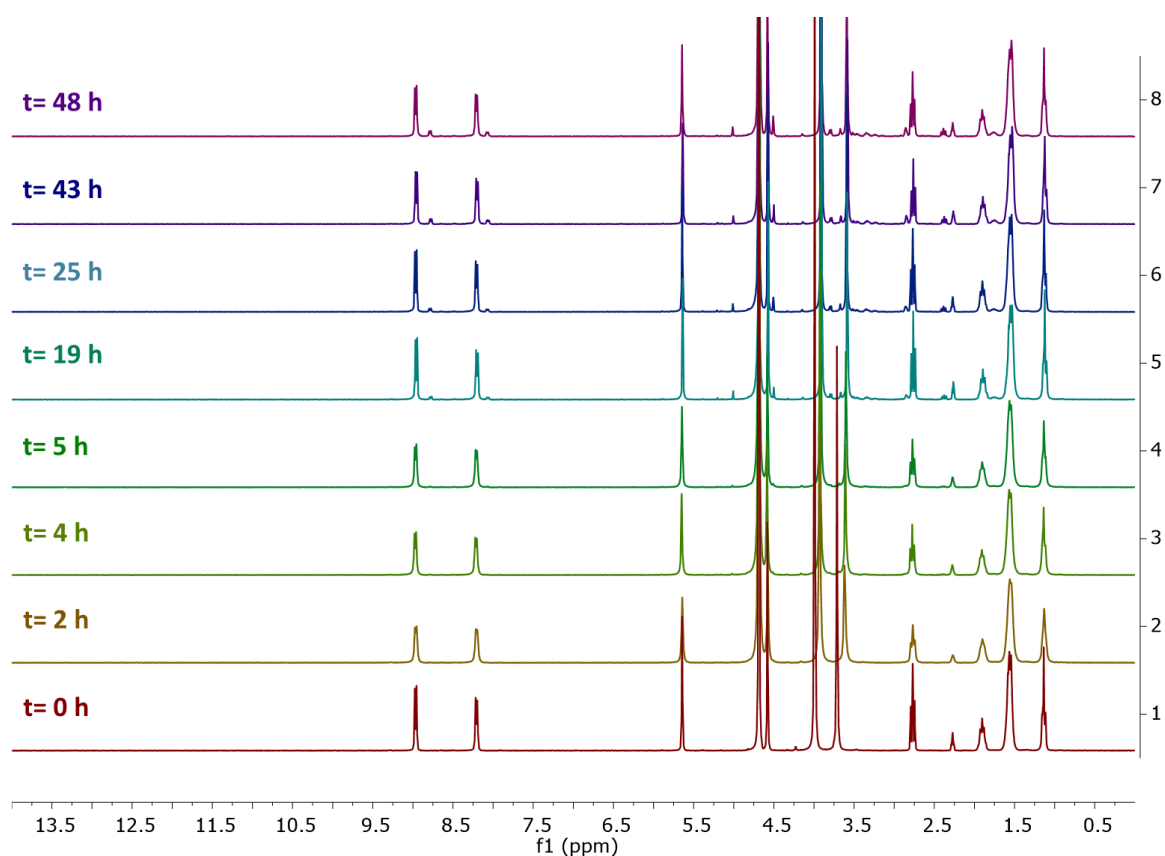


Figure A58. Evolution of the photodeprotection of octanoic acid in standard conditions without CDs.

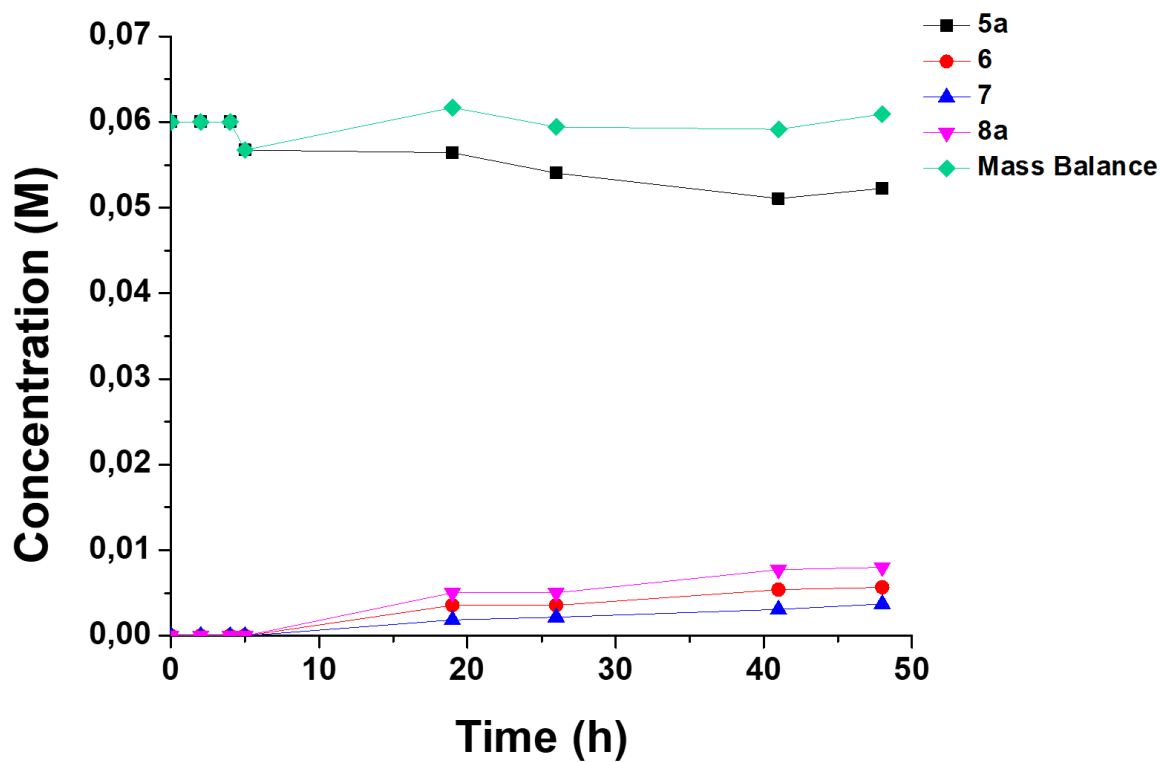


Figure A59. Concentration profiles of reagent and products in the photodeprotection of **5a** in standard conditions without CDs.

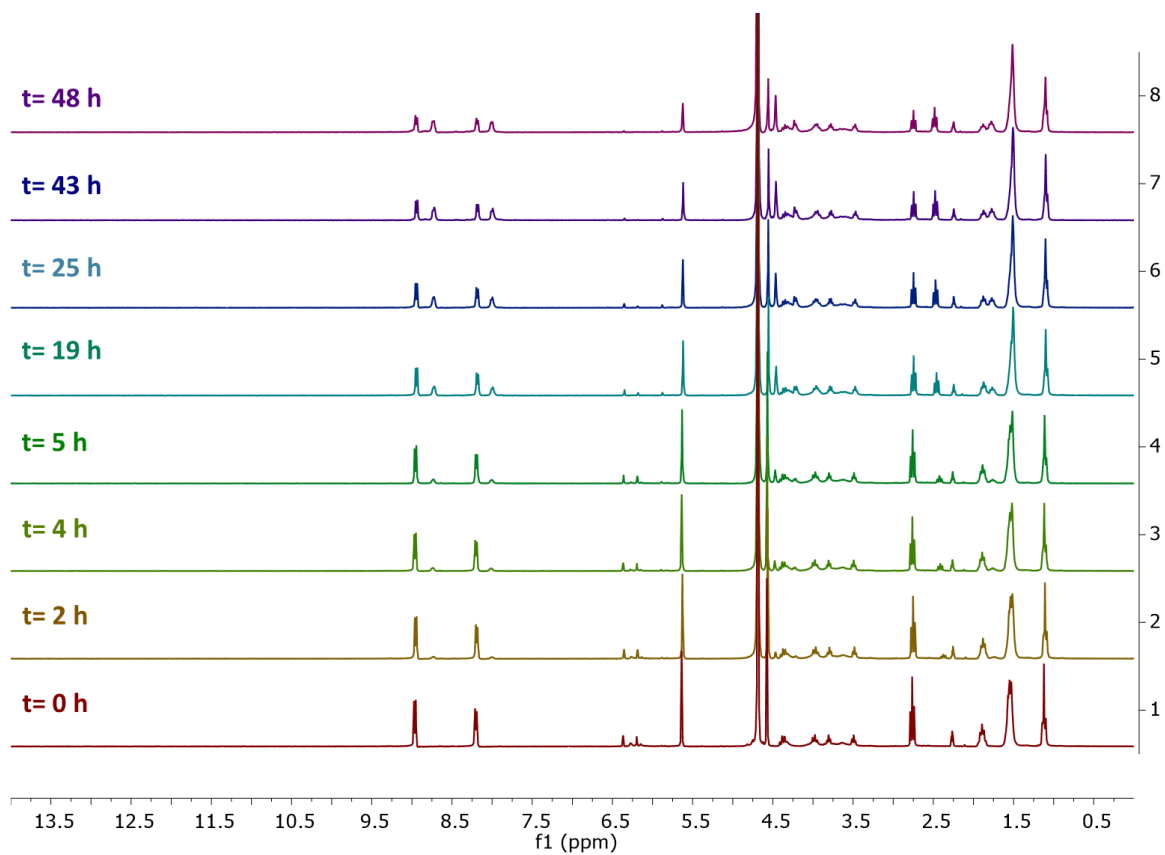


Figure A60. Evolution of the photodeprotection of octanoic acid in standard conditions without EDTA.

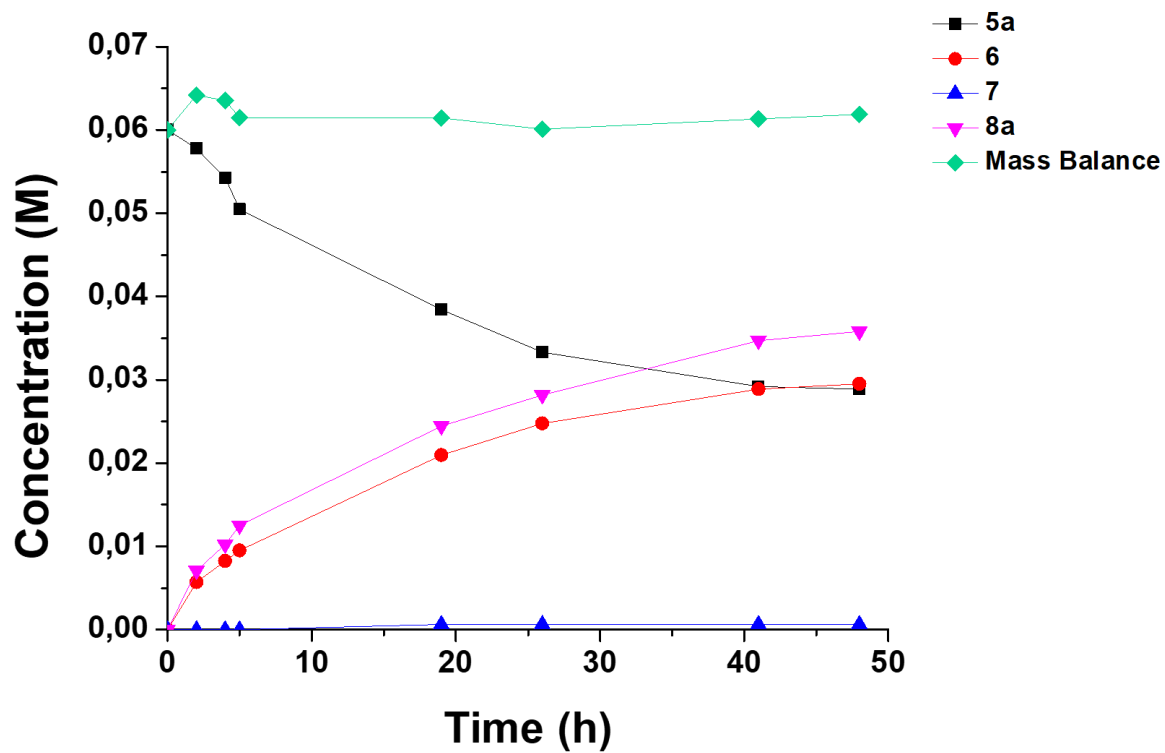


Figure A61. Concentration profiles of reagent and products in the photodeprotection of **5a** in standard conditions without EDTA.

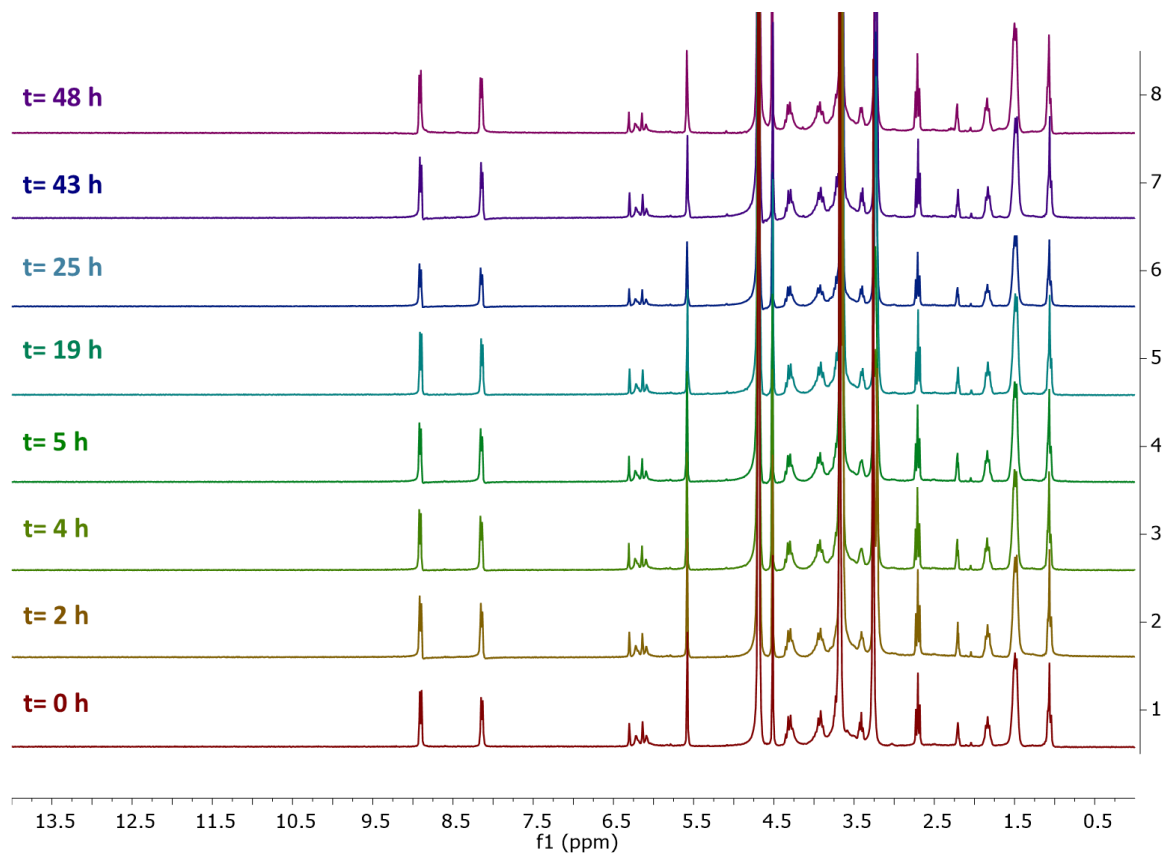


Figure A62. Evolution of the photodeprotection of octanoic acid in standard conditions without light.

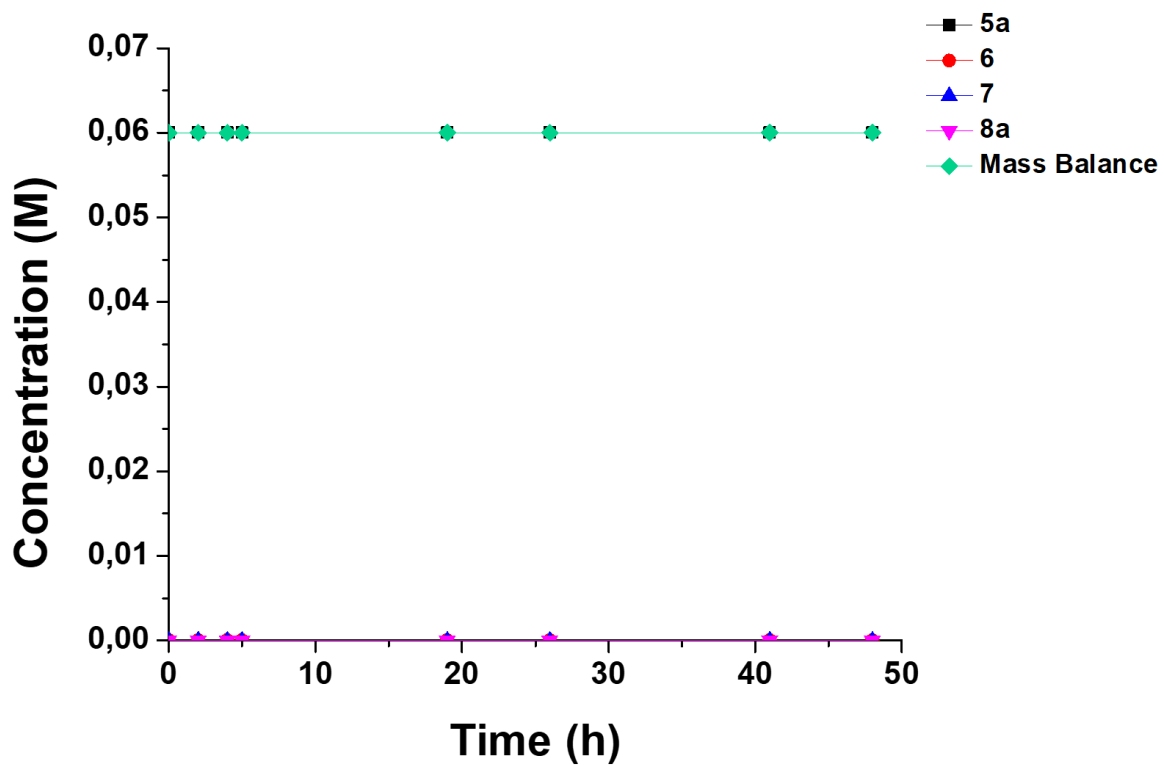


Figure A63. Concentration profiles of reagent and products in the photodeprotection of **5a** in standard conditions without light

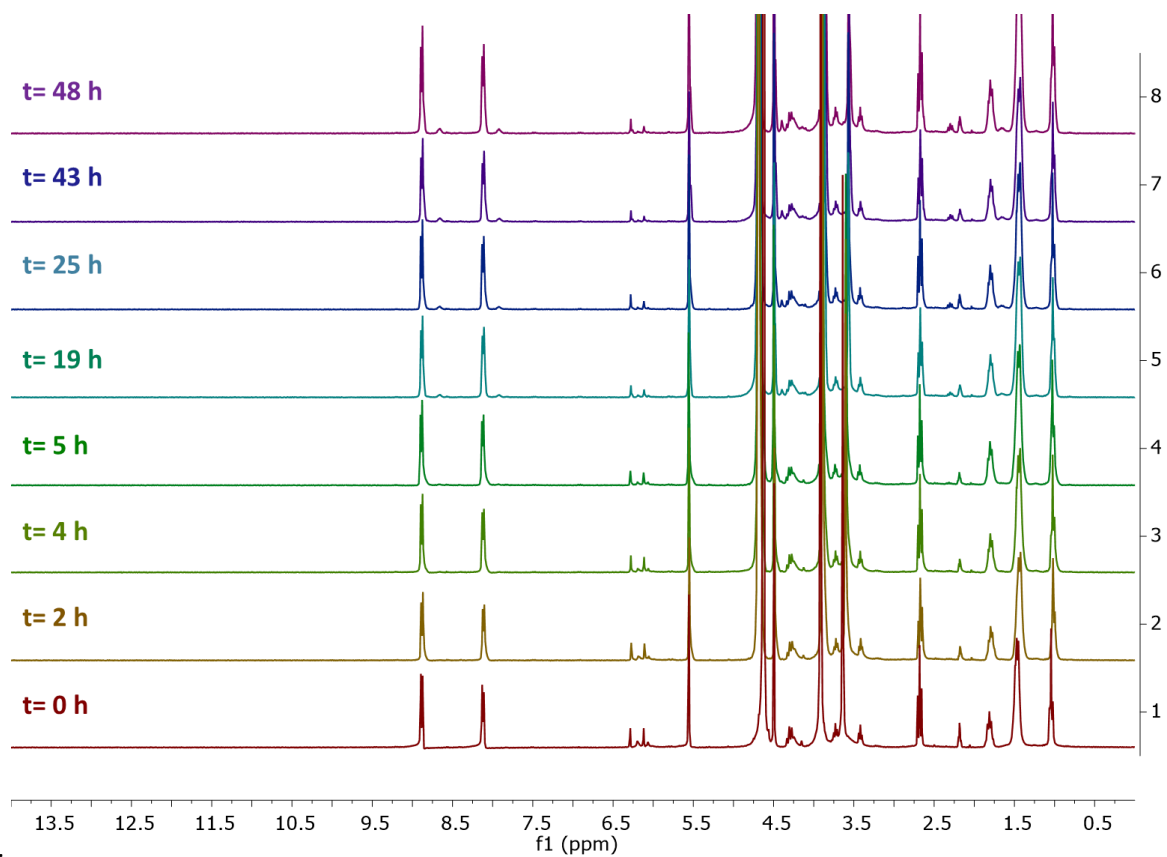


Figure A64. Evolution of the photodeprotection of octanoic acid in standard conditions with visible light.

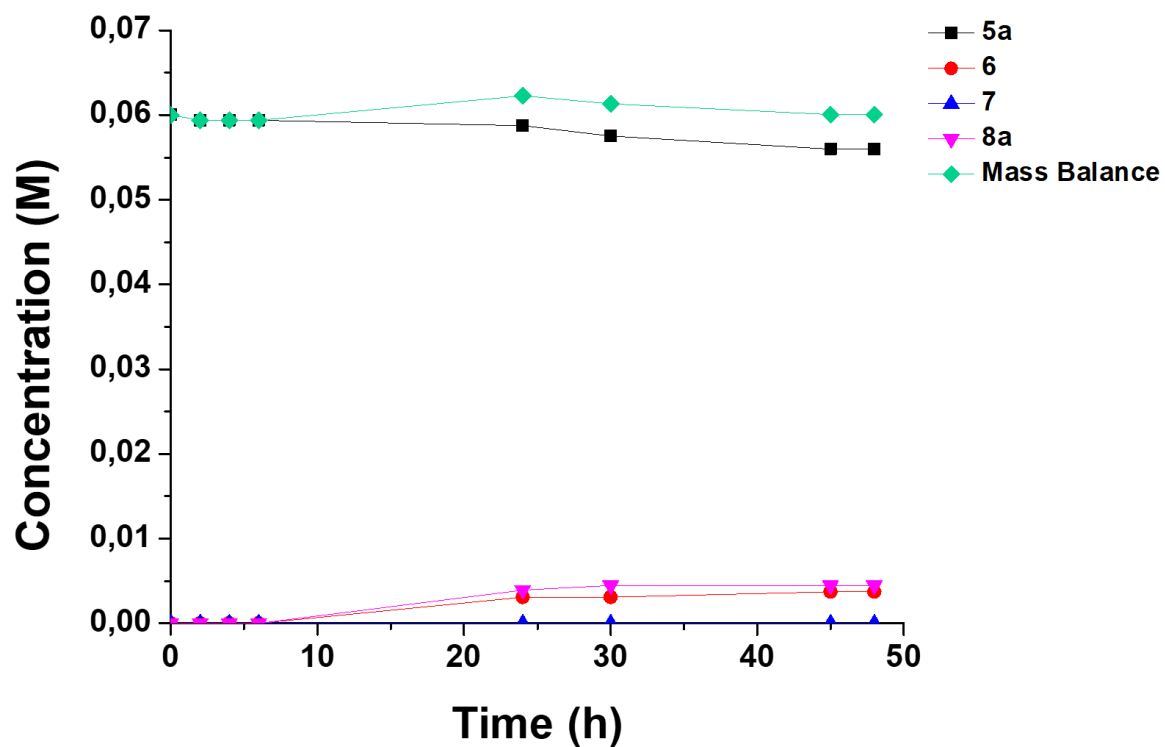


Figure A65. Concentration profiles of reagent and products in the photodeprotection of 5a in standard conditions with visible light.

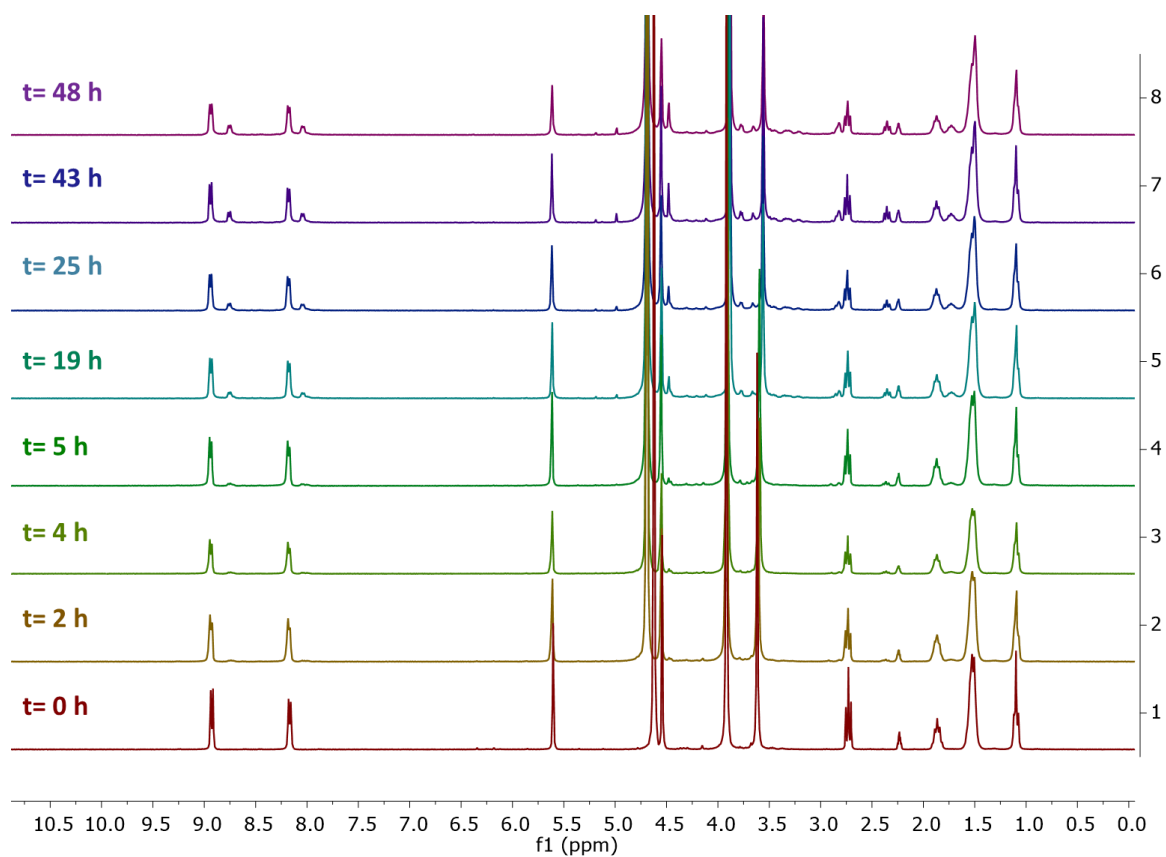


Figure A66. Evolution of the photodeprotection of octanoic acid in standard conditions with 1 mg/mL of α -N-CDs.

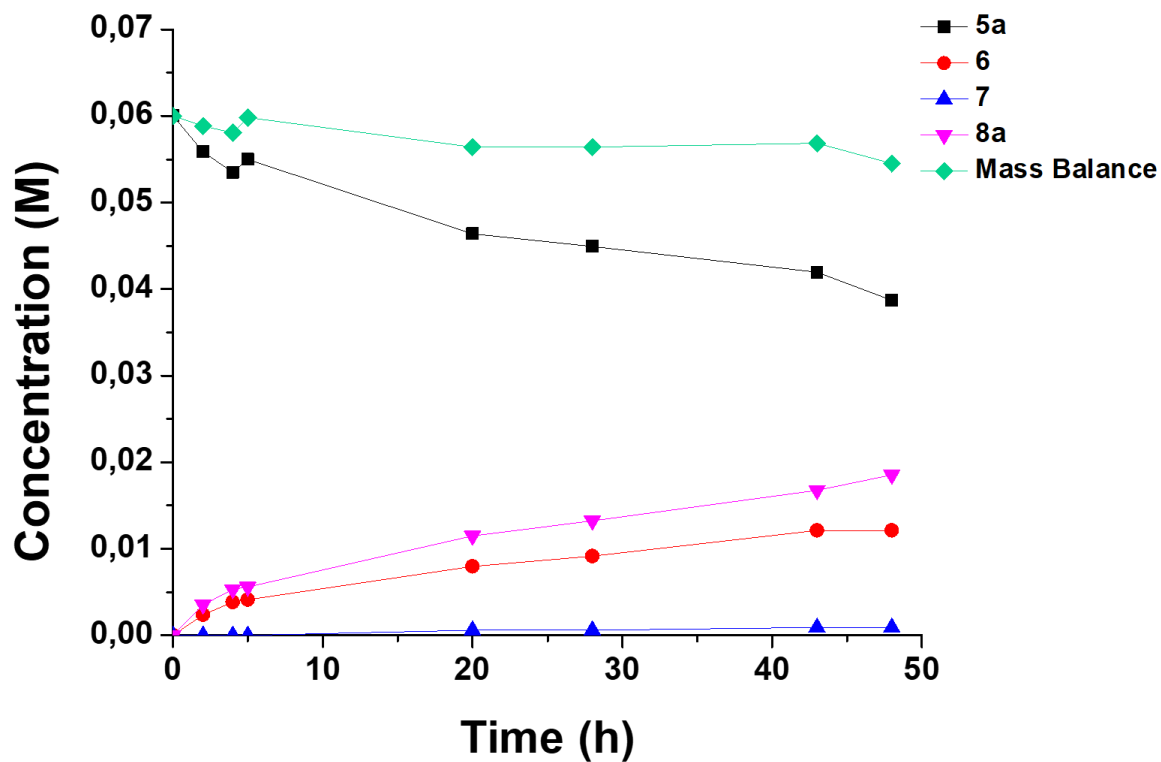


Figure A67. Concentration profiles of reagent and products in the photodeprotection of **5a** in standard conditions with 1 mg/mL of **α -N-CDs**.

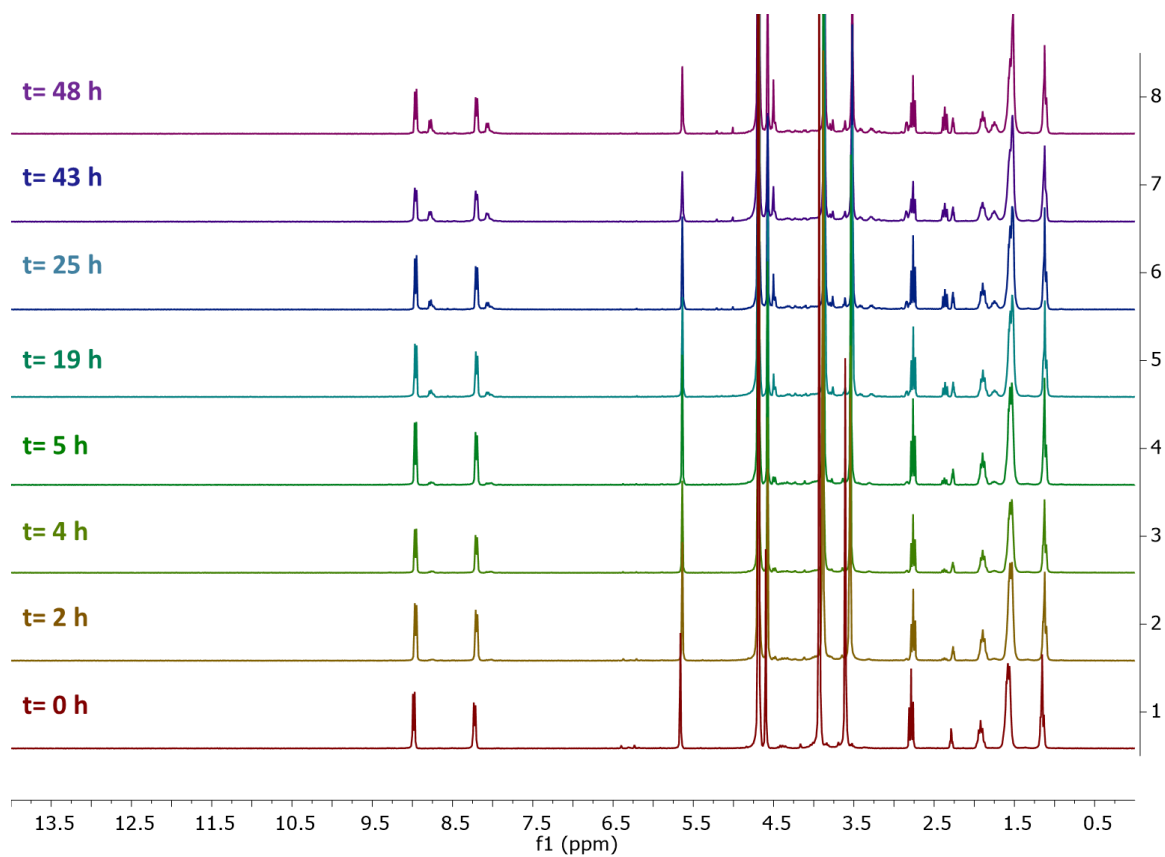


Figure A68. Evolution of the photodeprotection of octanoic acid in standard conditions with 5 mg/mL of **α -N-CDs**.

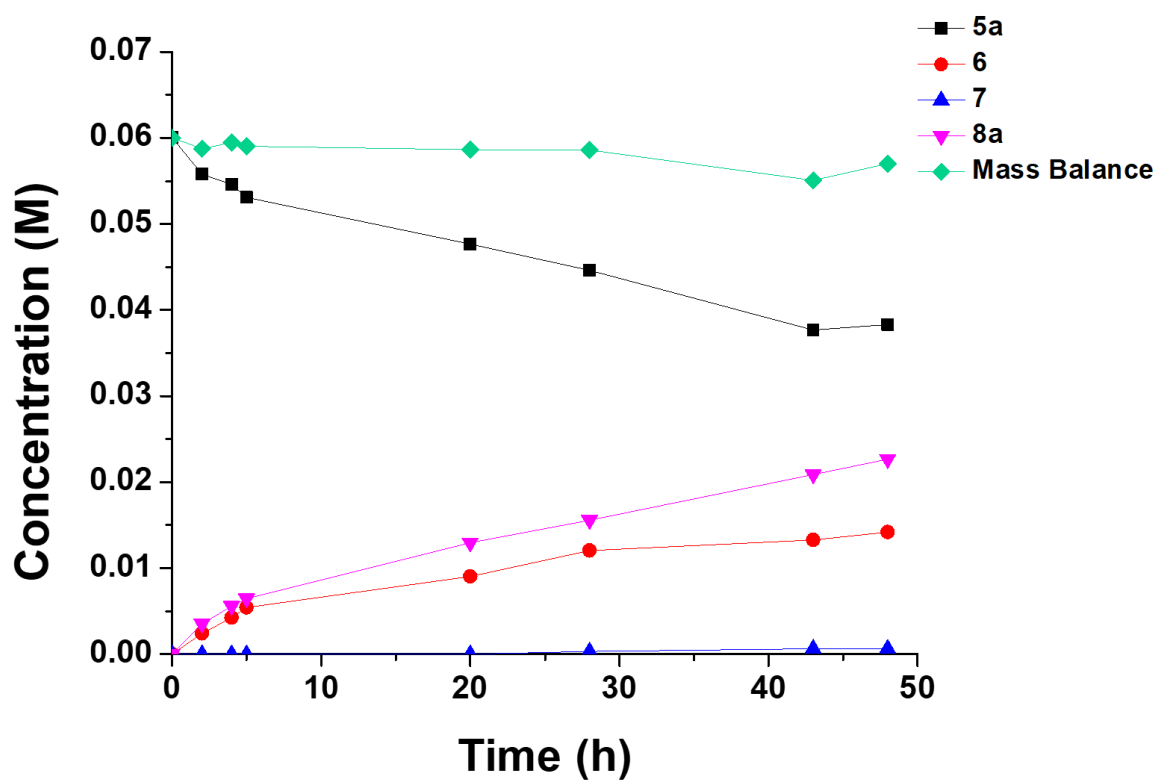


Figure A69. Concentration profiles of reagent and products in the photodeprotection of 5a in standard conditions with 5 mg/mL of α -N-CDs.

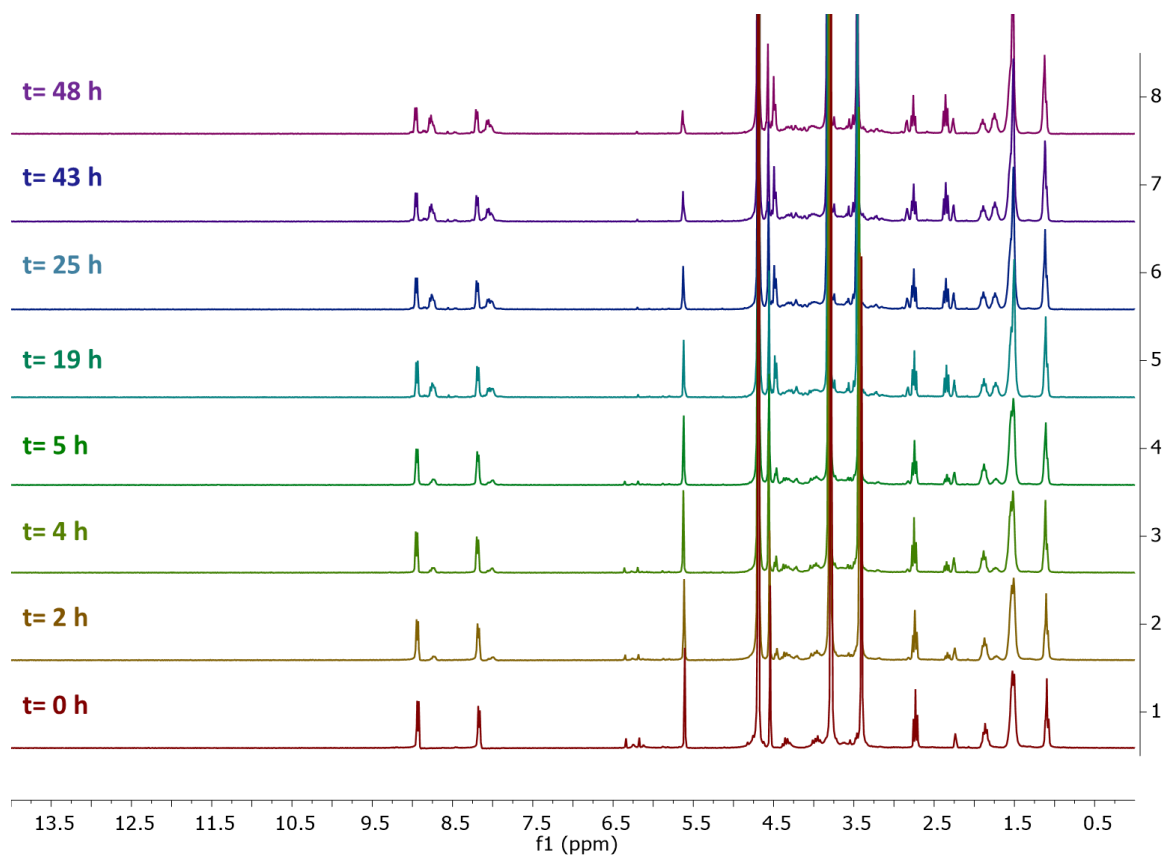


Figure A70. Evolution of the photodeprotection of octanoic acid in standard conditions with 10 mg/mL of α -N-CDs.

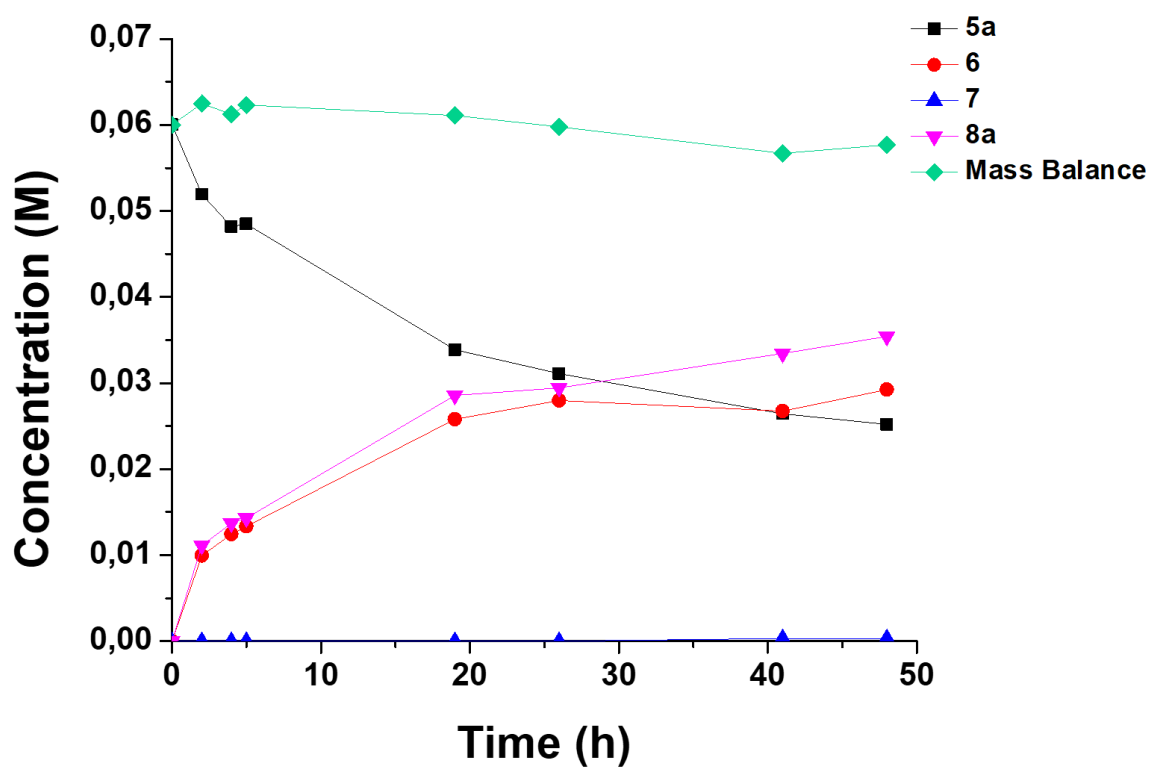


Figure A71. Concentration profiles of reagent and products in the photodeprotection of 5a in standard conditions with 10 mg/mL of α -N-CDs.

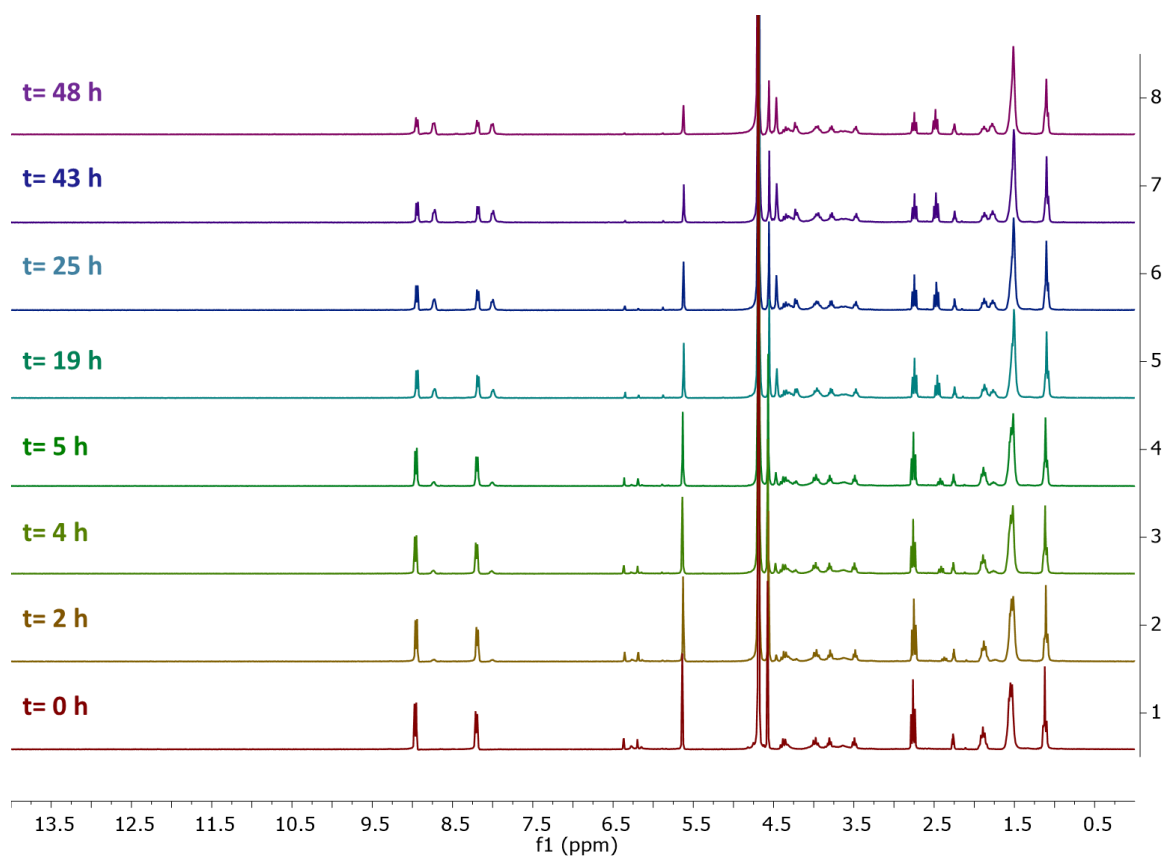


Figure A72. Evolution of the photodeprotection of octanoic acid with 20 mg/mL of α -N-CDs and without EDTA.

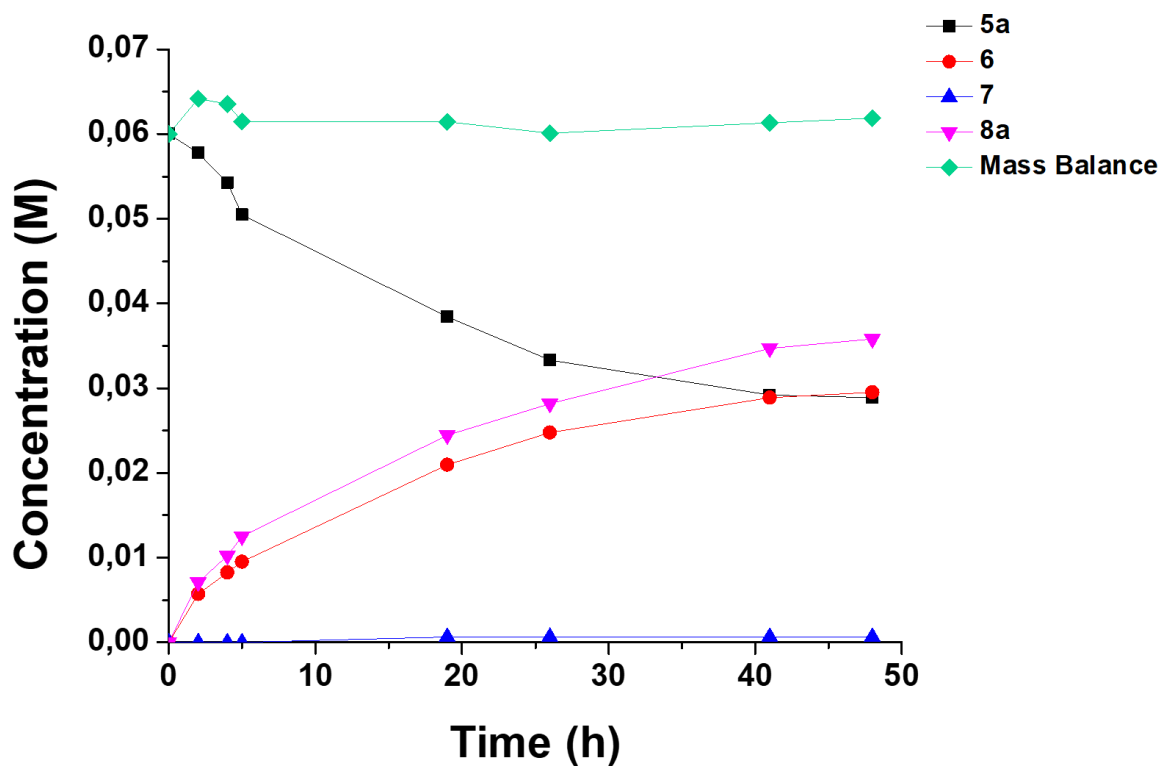


Figure A73. Concentration profiles of reagent and products in the photodeprotection of **5a** with 20 mg/mL of **α -N-CDs** and without EDTA.

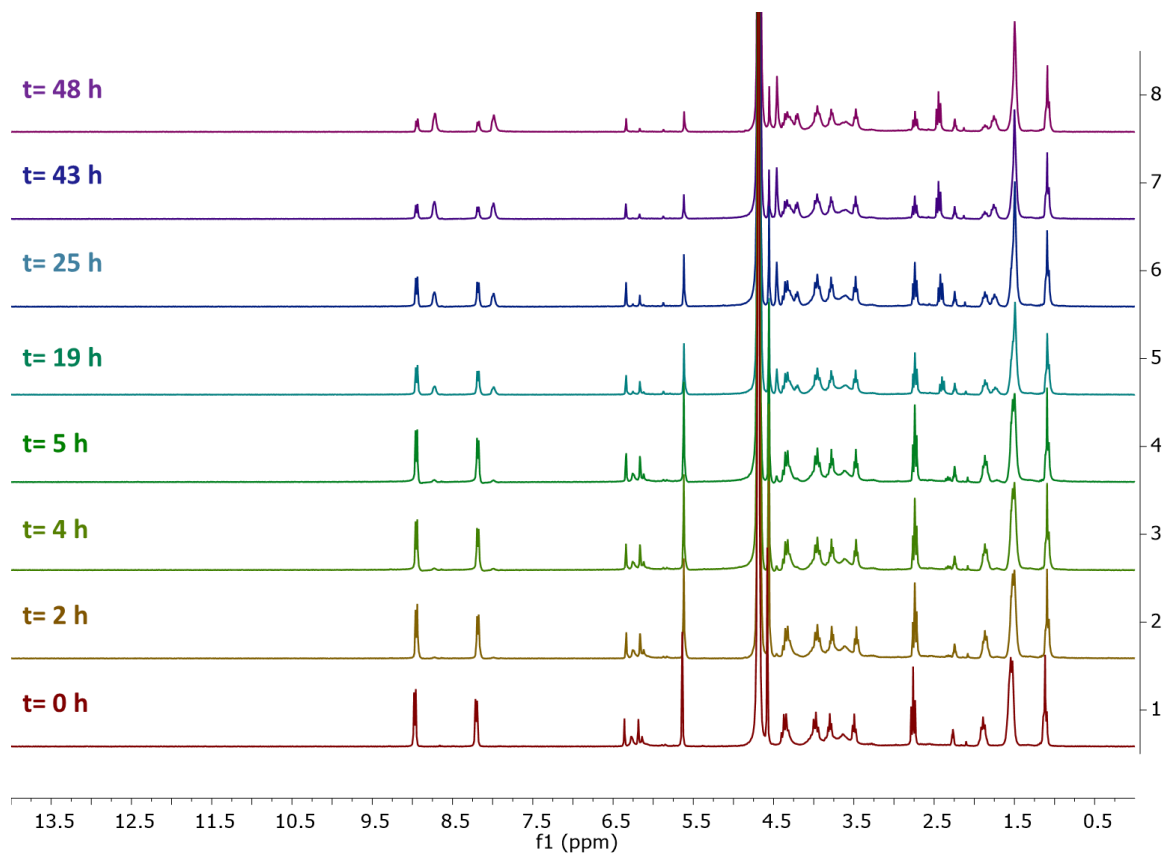


Figure A74. Evolution of the photodeprotection of octanoic acid with 50 mg/mL of **α -N-CDs** and without EDTA.

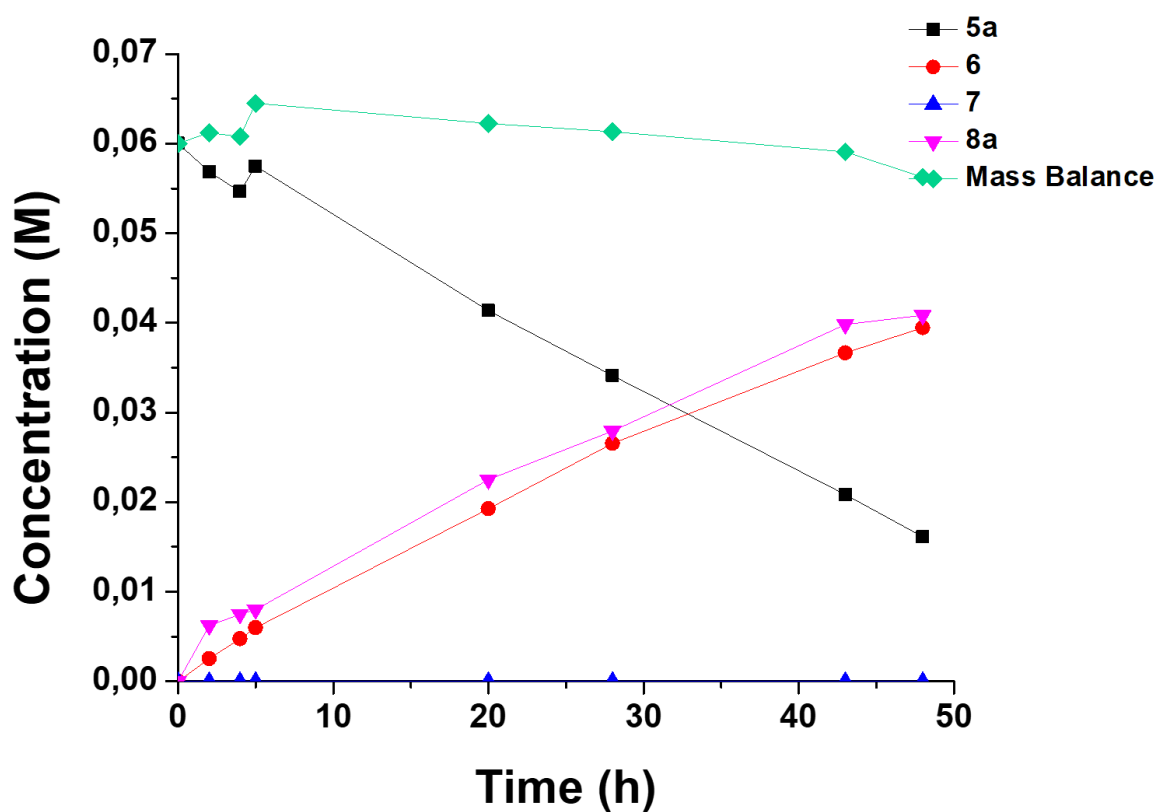


Figure A75. Concentration profiles of reagent and products in the photodeprotection of **5a** with 50 mg/mL of **a-N-CDs** and without EDTA

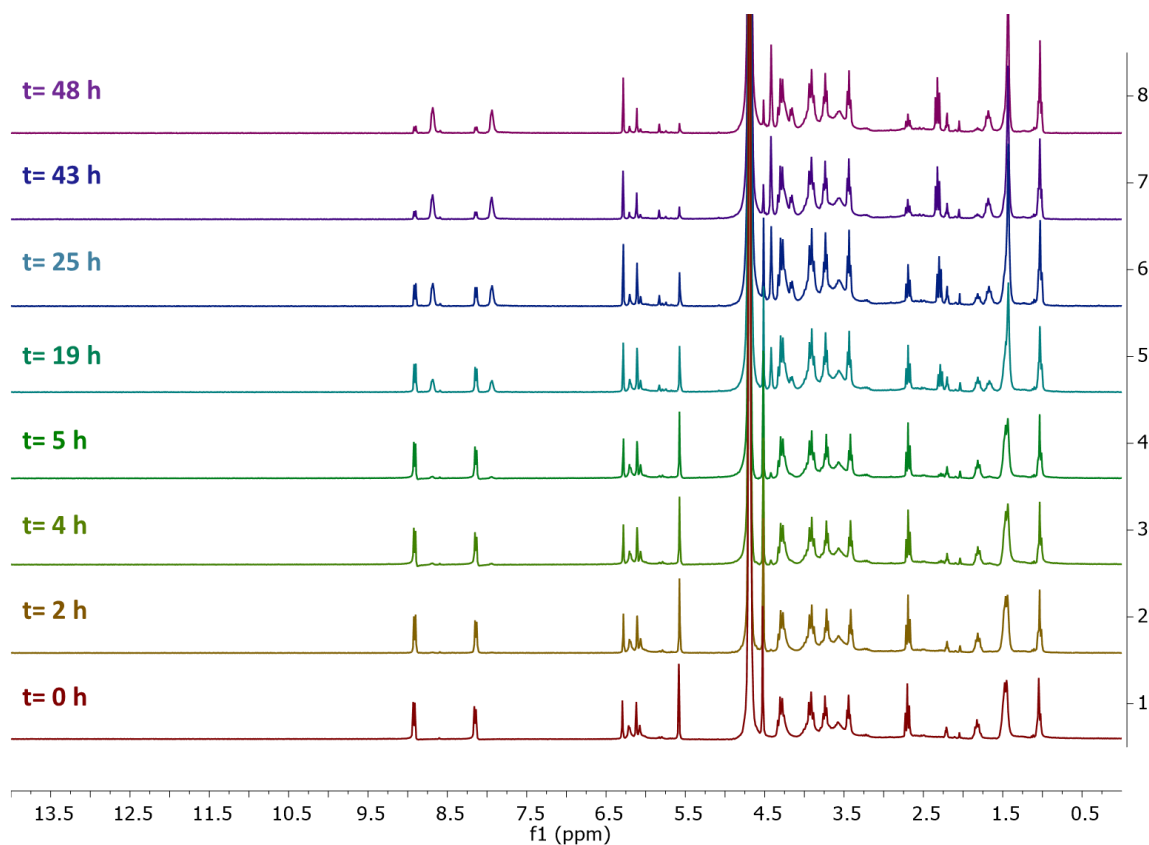


Figure A76. Evolution of the photodeprotection of octanoic acid with 50 mg/mL of a-N-CDs and without EDTA.

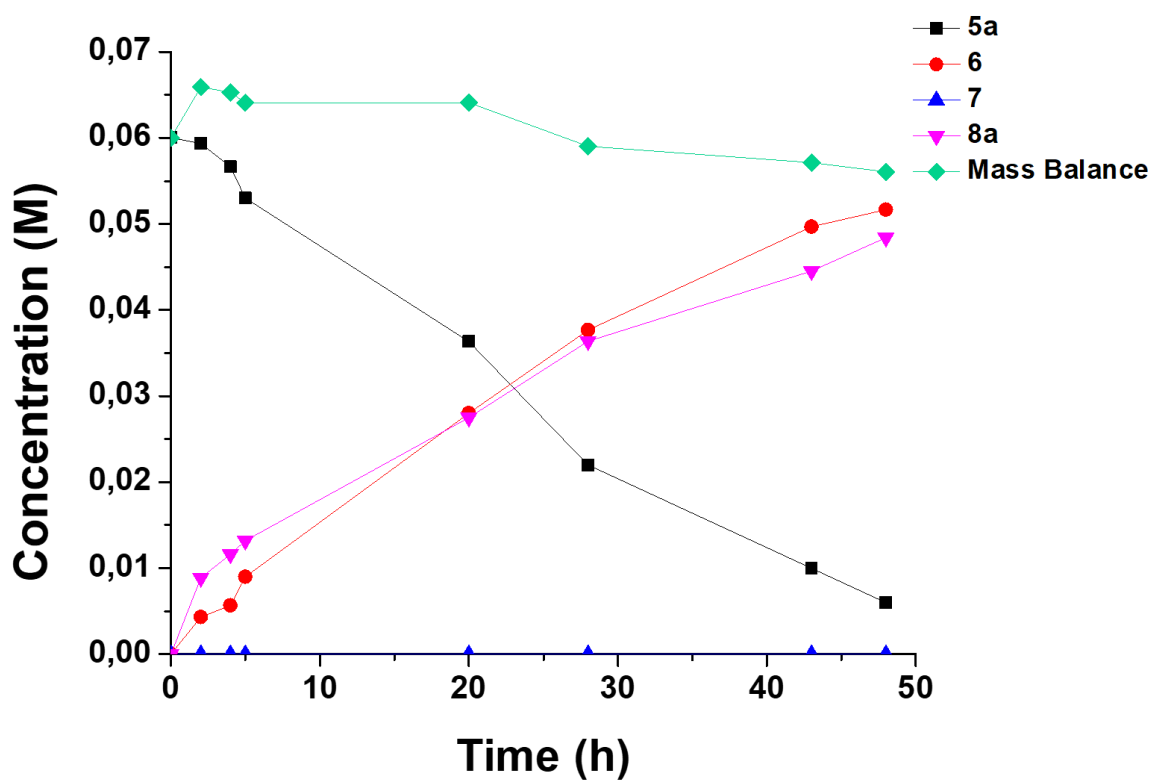


Figure A77. Concentration profiles of reagent and products in the photodeprotection of 5a with 100 mg/mL of a-N-CDs and without EDTA.

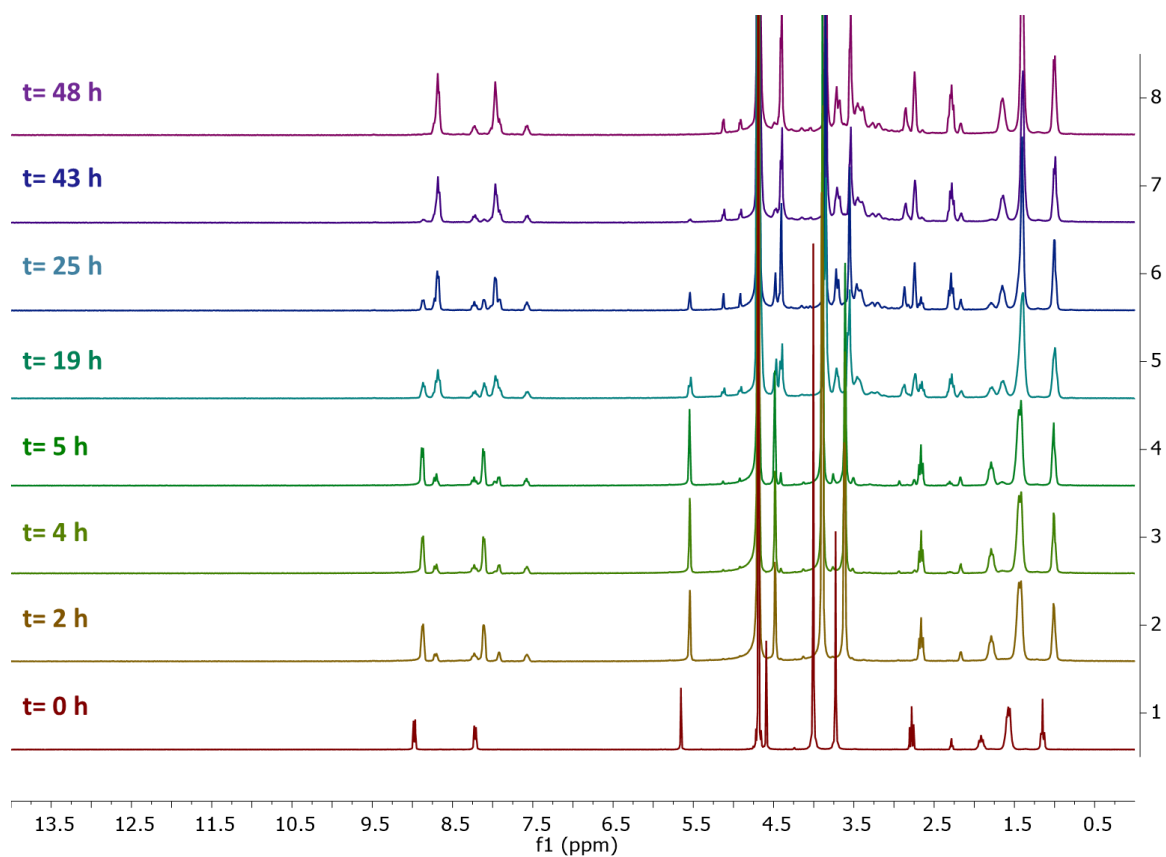


Figure A78. Evolution of the photodeprotection of octanoic acid with $\text{Ru}(\text{bpy})_3^{2+}$.

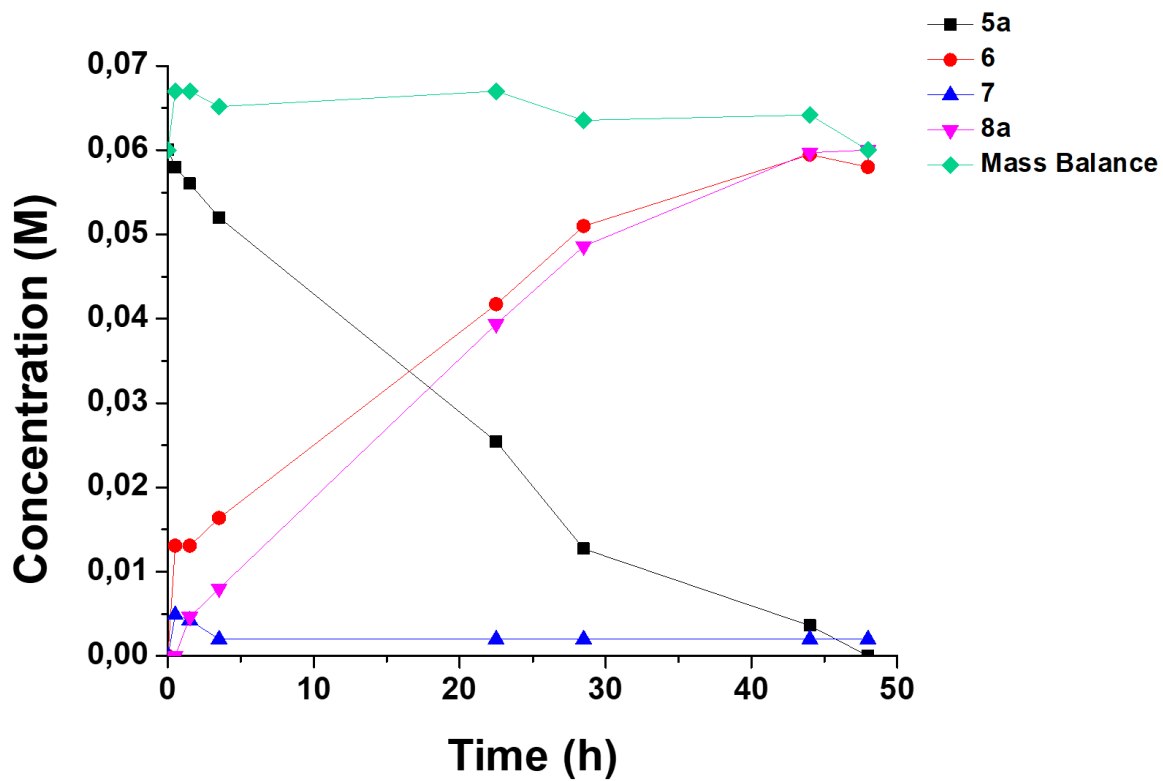


Figure A79. Concentration profiles of reagent and products in the photodeprotection of **5a** with $\text{Ru}(\text{bpy})_3^{2+}$.

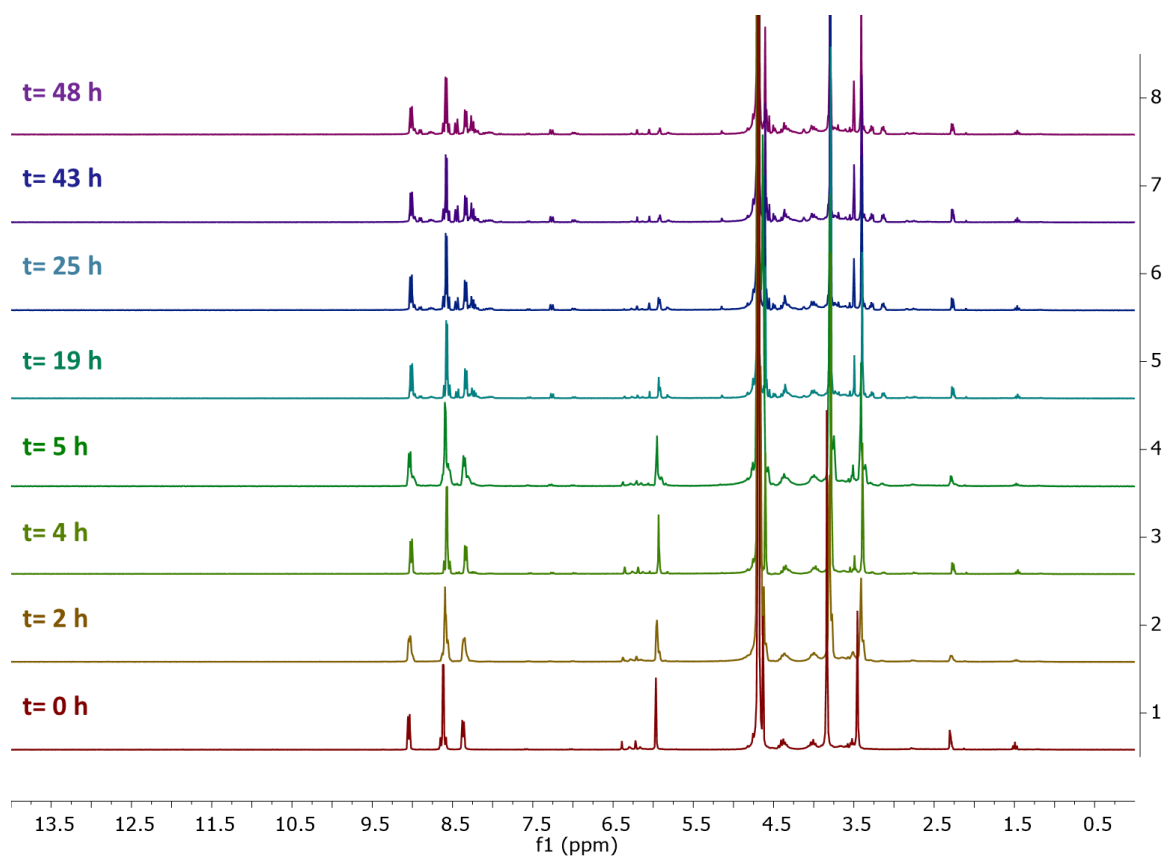


Figure A80. Evolution of the photodeprotection reaction of 5b with a-N-CDs.

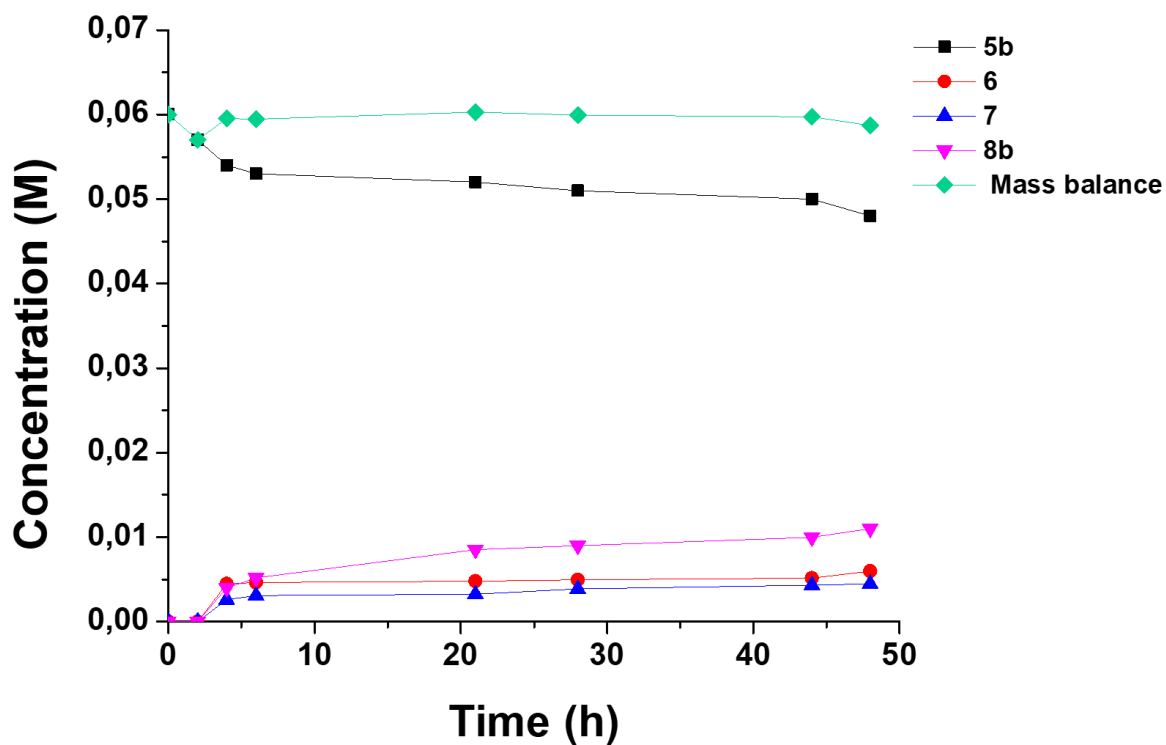


Figure A81. Concentration profiles of reagent and products in the photodeprotection of 5b.

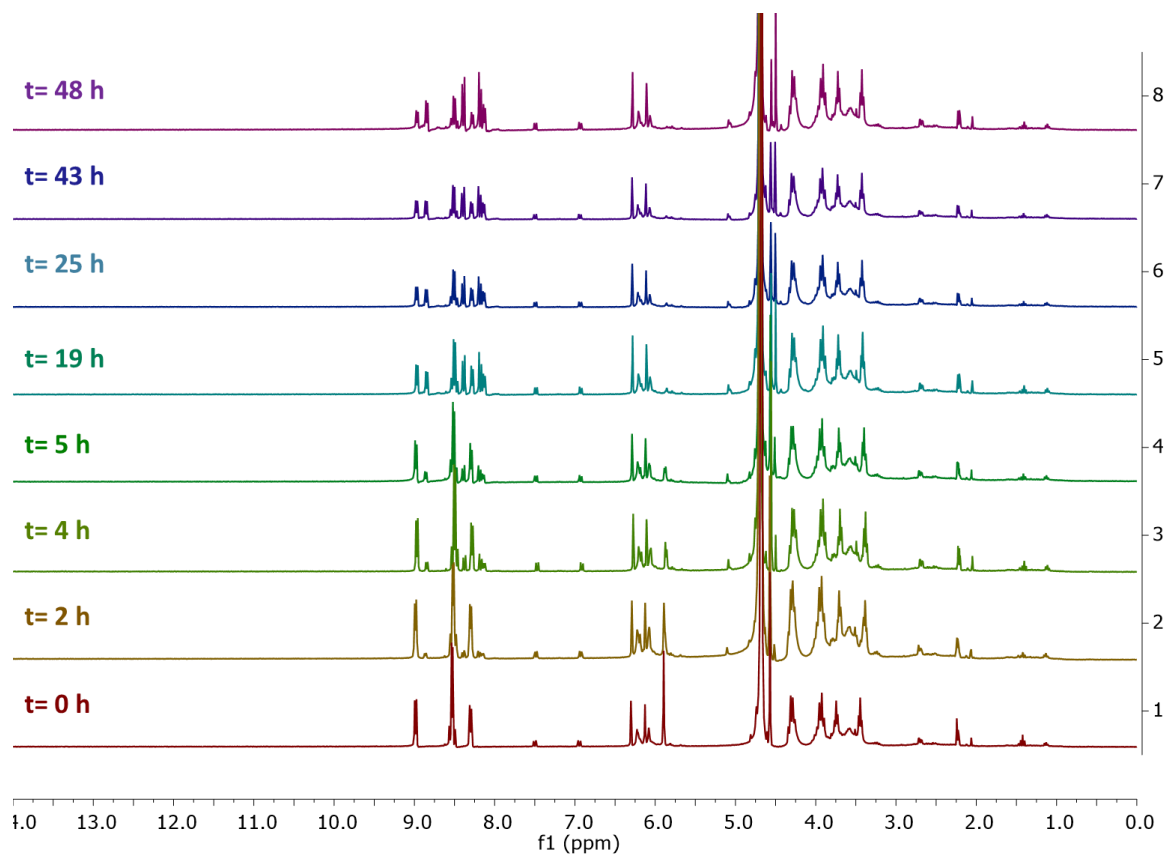


Figure A82. Evolution of the photodeprotection reaction of **5b** with 100mg of α -N-CDs and without EDTA.

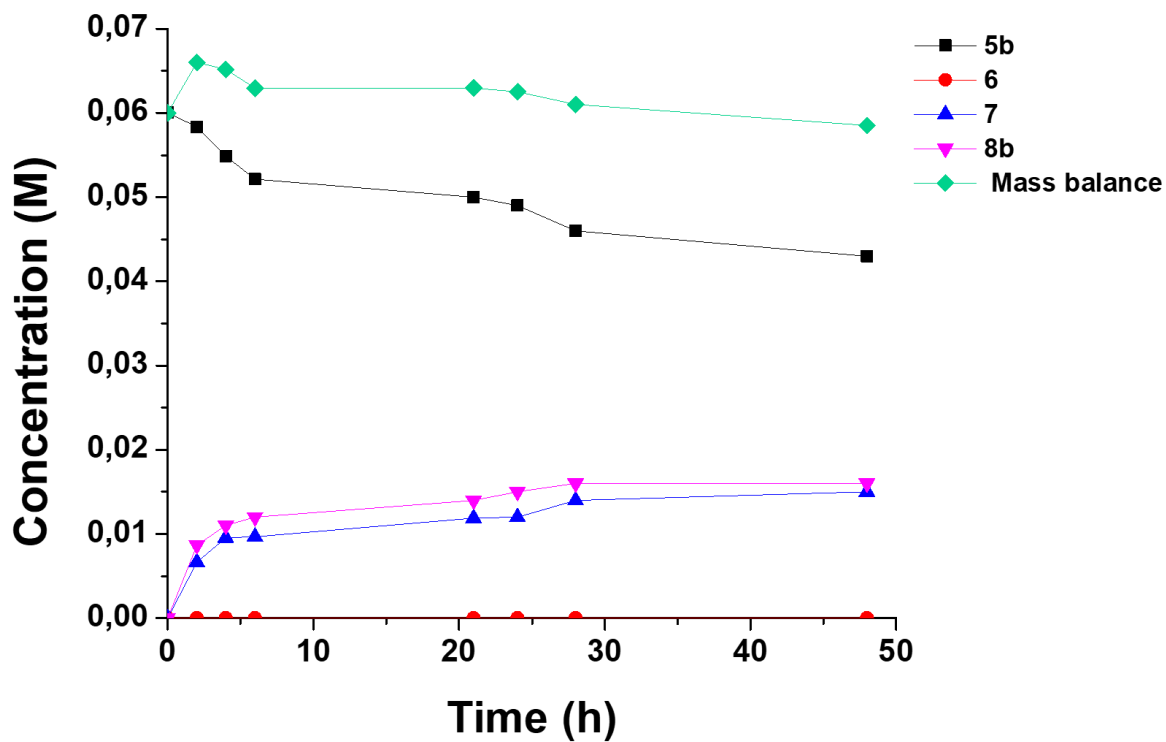


Figure A83. Concentration profiles of reagent and products in the photodeprotection of **5b** with 100mg of **a-N-CDs** and without EDTA.

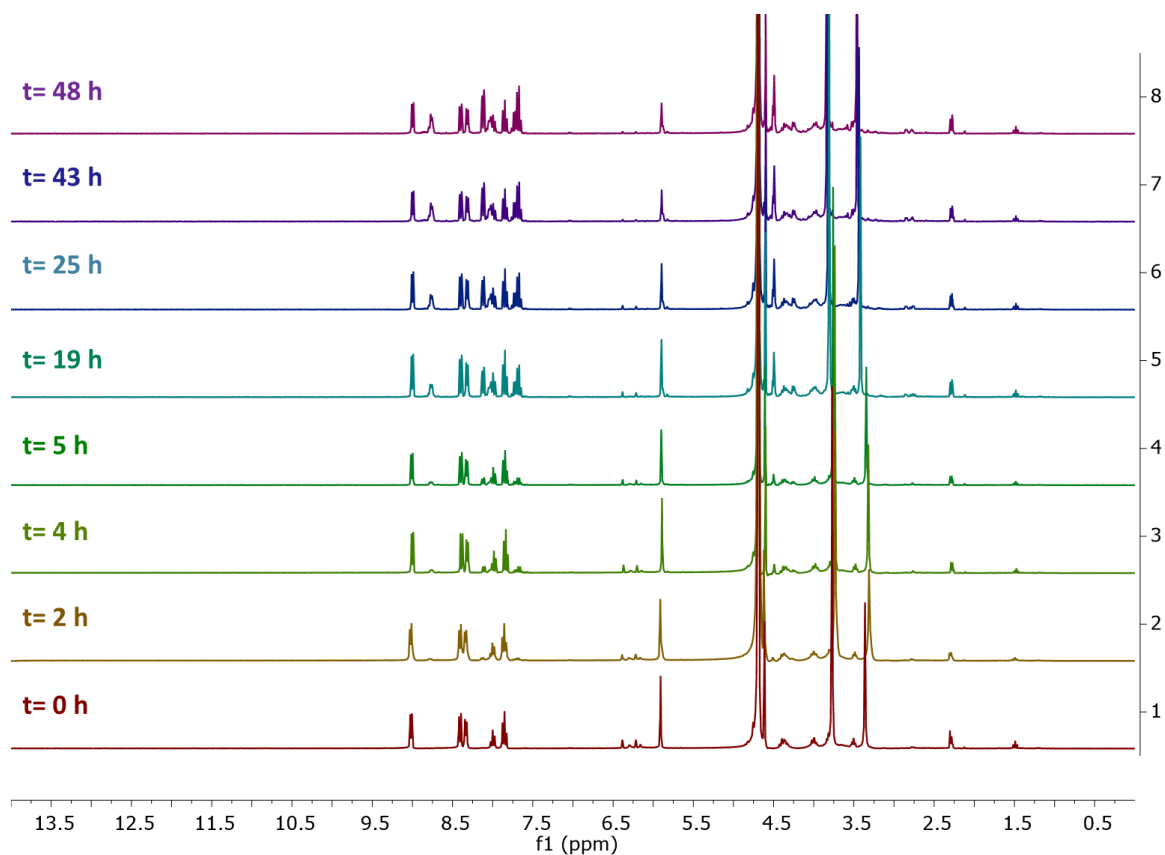


Figure A84. Evolution of the photodeprotection reaction of **5c** with **a-N-CDs**.

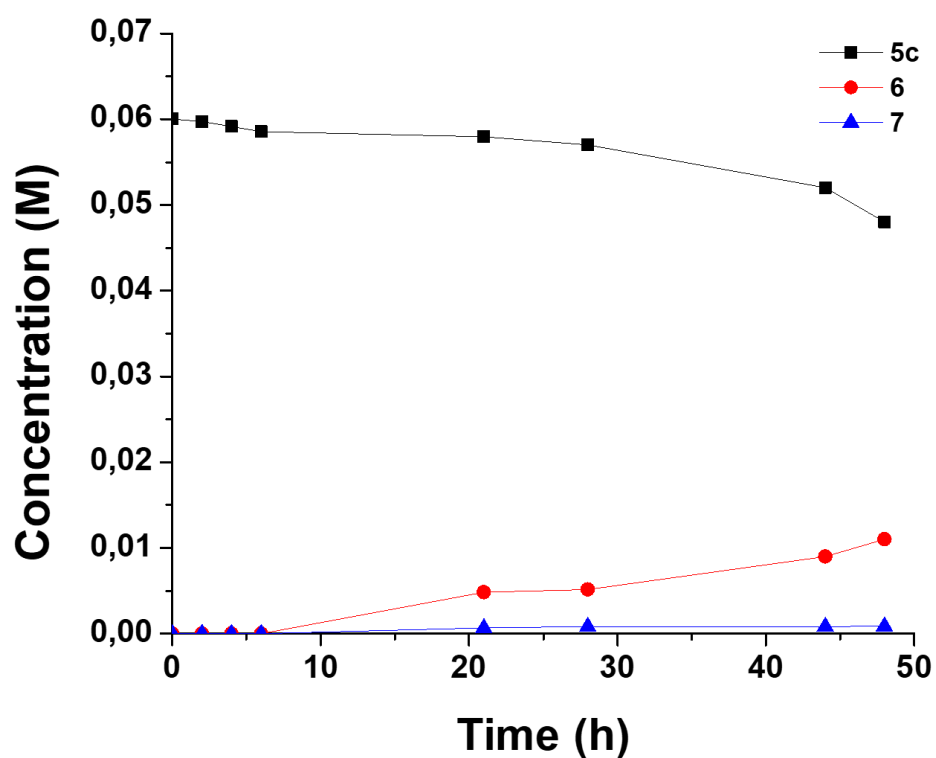
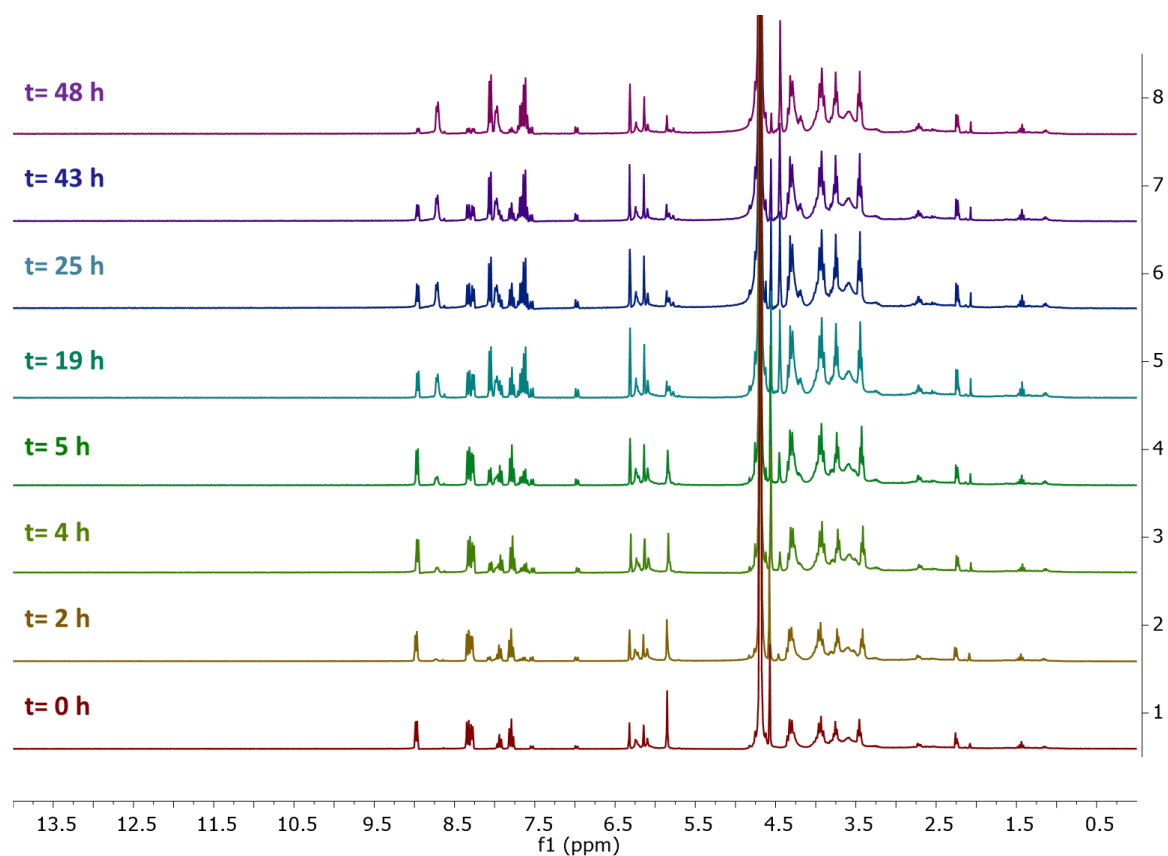


Figure A85. Concentration profiles of reagent and products in the photodeprotection of **5c**.**Figure A86.** Evolution of the photodeprotection reaction of **5c** with 100mg of **a-N-CDs** and without EDTA.

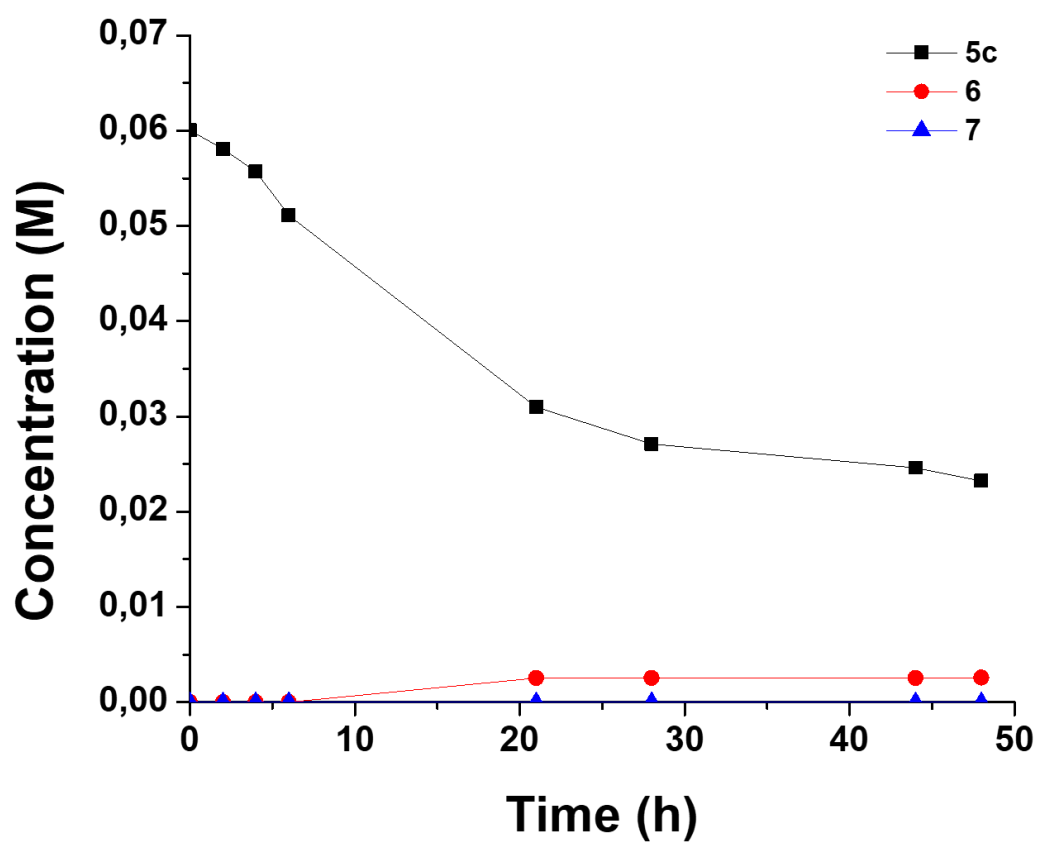


Figure A87. Concentration profiles of reagent and products in the photodeprotection of 5c with 100mg of **a-N-CDs** and without EDTA.